UNIVERSITÀ DEGLI STUDI DI CATANIA

IN CONVENZIONE CON

UNIVERSITÀ DEGLI STUDI DI PALERMO

DOTTORATO DI RICERCA IN

SCIENZA DEI MATERIALI E NANOTECNOLOGIE - XXXII CICLO

GIULIANA GIULIANO

HYBRID PEROVSKITE SOLAR CELLS:

SEMITRANSPARENT DESIGN AND INTERFACE

OPTIMIZATION

TUTOR: DR. TIZIANA FIORE

CO-TUTOR: PROF. BRUNO PIGNATARO

COORDINATORE: PROF. MARIA GRAZIA GRIMALDI

TESI PER IL CONSEGUIMENTO DEL TITOLO DI DOTTORE DI RICERCA

Acknowledgement

Abstract

Over the last 10 years, the emergence of a new thin-film PV family – the perovskite solar cells (PSCs) – has stunned the scientific community with its extraordinary performance and rapid progress in a very short time. An astonishing increase in power conversion efficiency (PCE) has been achieved from 3.8% in 2009 to 24.2% in 2019, thanks to the unique optoelectronic properties of hybrid perovskite materials and the intense research efforts devoted to optimizing film deposition methods, interfacial materials and device structures. In addition to the high performances, PSCs are easy to produce via low-cost thin-film deposition techniques and display a great potential for unconventional PV applications, such as building-integrated photovoltaics (BIPVs) and tandem PV devices, allowing color and transparency.

Whilst many advances have been made in the field of PSCs, there is still much work to be done in order to enable a large-scale commercialization. This thesis aims to assist in moving towards this objective by investigating ways to overcome some of the key challenges concerning the operation, composition, cost, and stability of the devices. More specifically, the research work presented in this thesis explores new strategies for the fabrication of cost-effective, semitransparent (ST) PSCs in the prospect of BIPV applications, as well as alternative charge-transport materials, solvent additives and interface engineering approaches for effective defect passivation and performance enhancement, both in terms of efficiency and stability.

First, a novel multilayer dielectric/metal/dielectric (DMD) transparent electrode based on nonprecious copper (Cu) and molybdenum suboxide (MoO_x) is developed and incorporated as a top anode in planar n-i-p ST-PSCs. The formation of a continuous and percolative 9.5 nm thick copper film on top of an ultrathin Au seed layer is confirmed by various in-depth investigations. The gold seed layer is also proved to act as an effective Cu diffusion barrier. Whilst silver and gold are typically used in such DMD structures, their replacement with copper allows for a substantial cost reduction without sacrificing the device performance. Through this strategy, PCEs as high as 12.5%, along with acceptable transparency levels, are successfully achieved.

Then, the attention is moved towards the effect of the perovskite layer morphology and crystallinity on the device performance and stability by using different solution-based deposition approaches. It is demonstrated that the incorporation of a small amount of α-terpineol, a non-toxic

and easily accessible monoterpene alcohol, into the one-step perovskite precursor solution as a solvent additive is capable of producing more uniform and highly crystalline perovskite films with fewer defects and trap states. Through this approach, the PCE of PSCs is boosted from 13.9% to 15.4% with reduced hysteresis and improved stability.

Lastly, this thesis investigates the role of selective charge-transport materials on the performance of planar and mesoscopic n-i-p PSCs. The potential of three different conjugated copolymers as alternative dopant-free hole-transport layers is explored for the first time. Improved PCEs are successfully demonstrated for one of the three copolymers compared to traditional solution-processed hole-transport layers, which typically require the use of stability-adverse dopants to reach appreciable conductivity. Preliminary studies on the development and optimization of mesoporous titania (TiO_2) electron-transport layers are also presented. Specifically, Ti^{3+}-containing blue-titania nanoparticulate (NP) films are successfully prepared and used as mesoporous scaffolds in mesoscopic n-i-p PSCs. Furthermore, a 10% PCE enhancement is demonstrated by doping the blue-titania with nitrogen element. In parallel, one-dimensional (1D) TiO_2 nanorod (NR) arrays are grown by hydrothermal method and tested for the same role. The autoclaving time is opportunely optimized to achieve the best PCE.

Table of Contents

Chapter 1

Introduction

This chapter describes the broad motivation for research and investment into renewable energy and photovoltaic technologies. Specifically, it provides background information on hybrid perovskite solar cells, their current status and challenges. Special attention is given to the recent advances in interface engineering and semitransparent design of perovskite cells for modern applications, including building-integrated photovoltaics, flexible optoelectronics, and multi-junction tandem solar cells.
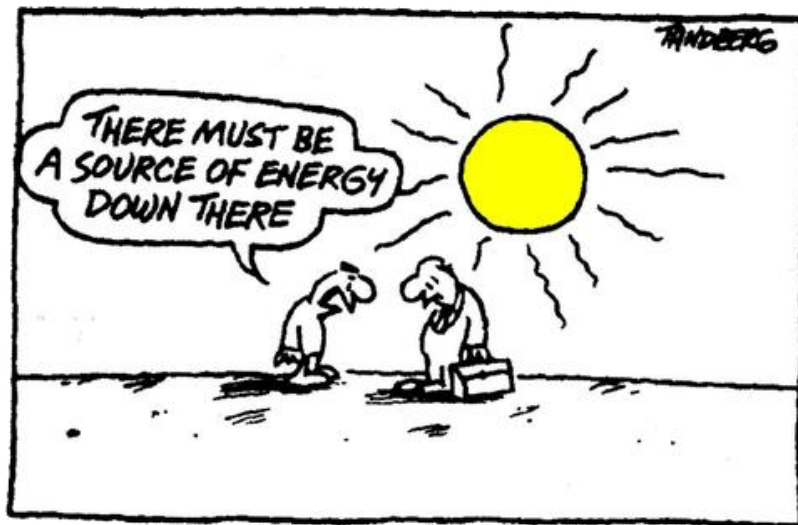
1.1. Motivation and Overview of Photovoltaics

1.1.1. Global Warming and Fossil Fuels

Scientific evidence for global warming, the general increase in the Earth's surface and ocean temperatures, is striking and unequivocal: data collected by several major institutions and temperature monitoring stations spread around the world, including NASA's Goddard Institute for Space Studies (GISS), show that the average global temperature has risen more than 0.9 degrees Celsius (°C) over the last 150 years (see **Figure 1.1**).[1] The most accurate climate change models predict dangerous and potentially catastrophic consequences: as temperatures increase, there will be severe risks of wildlife extinctions, melting of the polar ice caps, sea level rise, extreme weather events, coral bleaching and disintegration, floods and droughts, disease, economic disaster, and more (see **Figure 1.2**). Some of these changes are already occurring: heat waves and intense rain events have increased in frequency during the last decades, while the mean sea level is raising at an average annual rate of 1.7 mm, with arctic ice thinned by 40% since the 1950s.[2] This makes global warming one of the most pressing issues of our time.
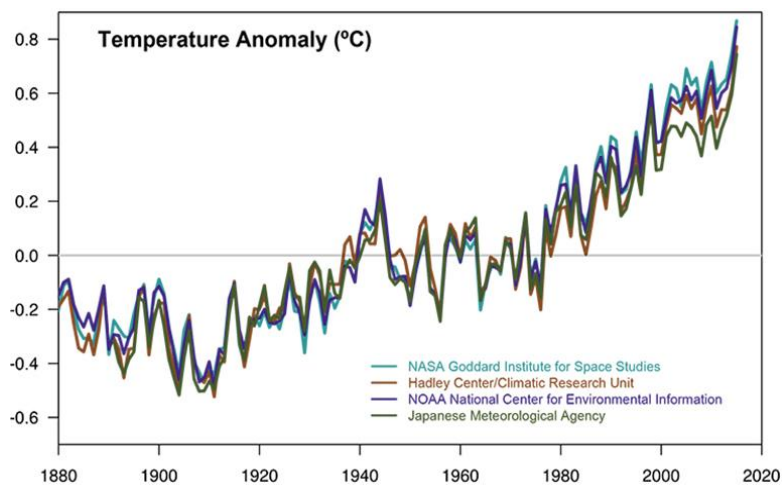
Figure 1.1. *Changes in global temperatures over the years. The different lines show the data collected by separate research centre. Source: NASA.*[1]

Natural mechanisms such as volcanic eruptions and changes in solar radiation levels have been estimated to contribute less than 5 percent to the recent warming effect.[3] On the other hand, there is international scientific consensus that most of the warming observed over the last 50 years is

attributable to anthropogenic factors. Every day, enormous amounts of greenhouse gases such as carbon dioxide (CO_2), methane (CH_4), chlorofluorocarbons (CFCs), and nitrous oxide (N_2O) are released by human activities (combustion of fossil fuels, forestry, agriculture). Their increasing concentration in the atmosphere is acting to trap heat radiated from Earth's surface, boosting the so-called "greenhouse effect". A recent report by UN Intergovernmental Panel on Climate Change (IPCC) states that, as long as the atmosphere remains overloaded with heat-trapping gases, the planet will reach the crucial threshold of 1.5 °C above pre-industrial levels by as early as 2030, precipitating the risks for ecosystems, human health, and economy.[4]

Figure 1.2. *Potential future effects of global warming include wildlife extinctions, melting of the polar ice caps, long periods of drought, and extreme weather events. Source: NASA.*[5]

Carbon dioxide accounts for about 76 percent of total man-made greenhouse emissions.[6] Since the beginning of the Industrial Revolution, the atmospheric concentration of CO_2 has dramatically increased from approximately 280 parts per millions (ppm) to more than 400 ppm at a rate that is unprecedented over decades to millennia (see **Figure 1.3**).[7] Even though CO_2 has a lower heat-trapping ability than other greenhouse gases, it is identified as the key driver of climate change since it lingers into the atmosphere for hundreds of years and hence constitutes a threat over the long term. Most of the anthropogenic CO_2 emissions come from the burning of fossil fuels for electricity and heat generation, industry, and transportation. These sectors emit more than 32.5 Gigatons of CO_2 per year.[8] This is why the current energy reliance on such high-carbon fossil resources is blamed to be the main contributor to human-induced global warming.

Despite global efforts to address climate change, including the landmark 2015 Paris climate agreement,[9] CO_2 emissions from fossil fuels continue to rise driven by the sustained growth in

global population and economic activities. Within this scenario, quicker and more decisive action is needed to restrain heat-trapping pollution and to prevent dangerous human interference with the climate system if the serious negative impacts of global warming are to be avoided. In particular, the role of energy in social and economic development must be balanced, with the need of reducing our reliance on fossil fuels and switching to less carbon-intensive sources of energy.[6]
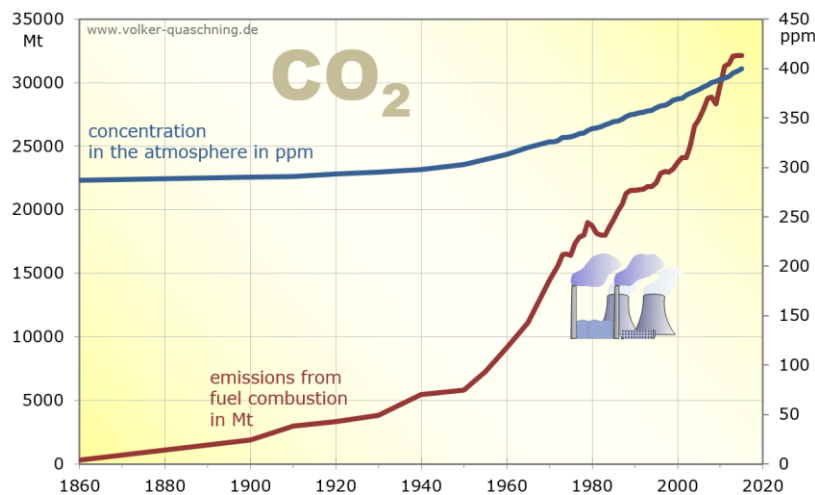
Figure 1.3. *Global CO₂ atmospheric concentrations (in parts per millions, ppm) and emissions from fuel combustion (in Megatons, Mt) over time.*

In addition to the environmental impact, the current energy economy primarily based on finite fossil energy carriers has social and geopolitical implications which should also be taken into account, starting from the following considerations: fossil fuels are non-renewable sources of energy as they take millions of years to form and cannot be replenished on a human timescale once they are fully used; the known viable reserves are limited, and they are depleting at an ever-faster rate due to the increasing energy demand; these reserves are distributed very unequally over the globe, more than 70% of the mineral oil and natural gas deposits being concentrated within the 'strategic ellipse' of countries extending from Saudi Arabia, over Iraq and Iran, up to Russia.[10] Given these premises, it is evident how dangerous the situation may become in an 'energy-hungry' future. The costs of fossil fuels are expected to grow very rapidly because of the gradual reduction of their provisions. As fossil fuels become scarcer and more expensive, international tensions and fighting over remaining supplies, especially of oil and gas, are likely to become more heated, thereby leading to an increased frequency of armed conflicts and wars. Such an "energy-centric"

scenario, where control over fossil fuel reserves translates into geopolitical dominance for some and economic vulnerability for others, contributes to establish disparities and iniquities in human society.[11] A clear evidence of this is the huge gap in energy consumption between industrialized and developing countries, that becomes even more extreme when looking at individual countries, with China (a newly industrialized country) and the United States being by far the world's largest energy consumers (see **Figure 1.4**).[12] Today, more than three quarters of the conventional fossil energy carriers are used, often inefficiently, by one quarter of the world's population in the industrialized countries, resulting in a global situation which is far from social sustainability.

Below 50   50 to 100   100 to 500   500 to 2000   Above 2000   Source Enerdata
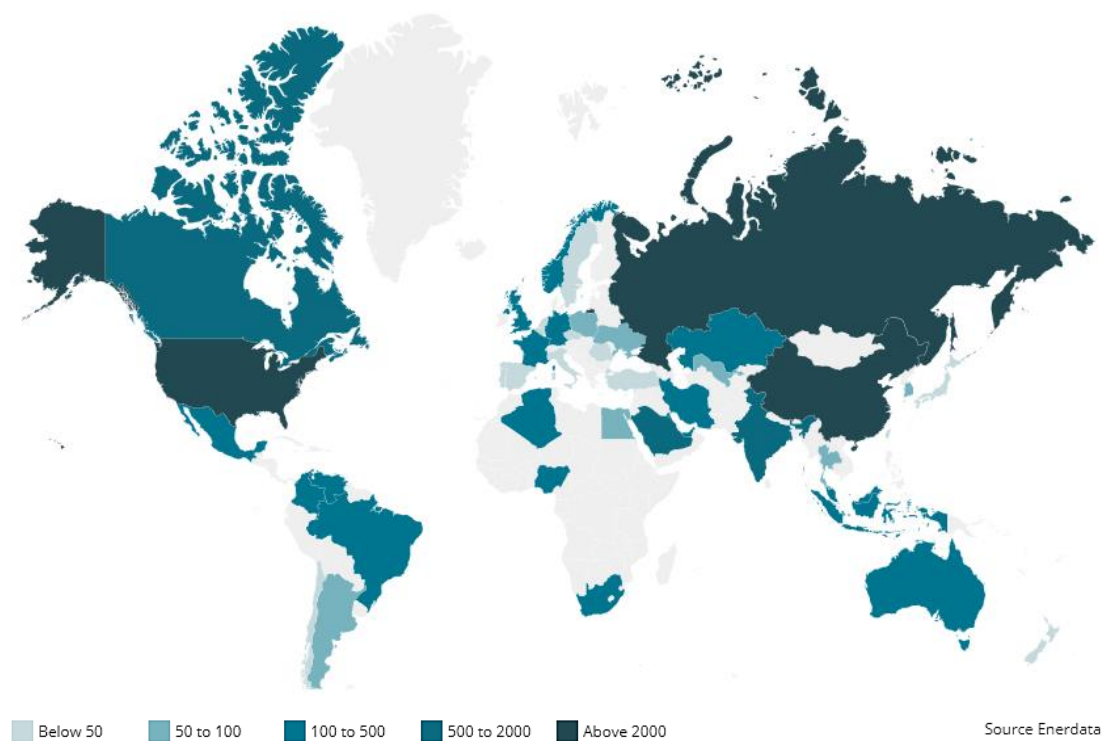
Figure 1.4. *World 2018 energy consumption per country (in million metric tons of oil equivalent, Mtoe). Source: Enerdata.*[12]

All these factors, together with evidence of human-induced climate change, constitute the major alarms of an impending energy crisis. To prevent this crisis from turning into a global depression, a shift away from the current reliance on fossil fuels is necessary and inevitable. To quote Vincenzo Balzani,[10] the current energy and climate crisis should be taken as "an opportunity to move away from fossil fuels, reduce disparities, increase international cooperation, and lead humanity to an innovative concept of prosperity".

1.1.2. Renewable Energy for Sustainable Development

Against this background of imminent global collapse, "sustainable development" is the only path that can secure a better and safer future for all. A sustainable development can be defined as "a development that meets the needs of the present without compromising the ability of future generations to meet their own needs". This term began to gain acceptance in the late 1980s, after its appearance in *Our Common Future*, also known as *The Brundtland Report*, a landmark report by UN World Commission on Environment and Development (WCED).[13] At the core of the sustainability paradigm is the need to consider three strategic 'pillars' together: society, the economy, and the environment. If any one of these pillars is weak, then the system as a whole is unsustainable (**Figure 1.5**). Therefore, sustainable development can only be pursued if economic growth, environmental protection, and social well-being are guaranteed at the same time.
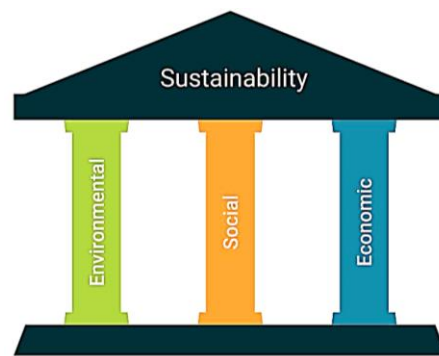
Figure 1.5. *The three pillars of sustainability.*

Sustainable development is not possible without sustainable energy. There is widespread recognition that the current energy system dominated by fossil fuels is unsustainable on all levels (environmental, social, economic). The environmental 'pillar' is the one that is triggering the most concern, being seriously threatened by global warming. Hence, transforming the global energy sector constitutes an absolute priority from a sustainable development perspective. Ensuring "access to affordable, reliable, sustainable and modern energy for all" is one of the 17 *Global Goals for Sustainable Development* set by the UN General Assembly in 2015 and will be key in achieving almost all the other goals, especially the one concerning climate action.[14,15] Strategies for sustainable energy development typically involve two main changes: (i) a decrease in energy use through energy efficiency measures; (ii) a shift from fossil fuels to renewable energy sources.

In particular, expanding the share of renewables in the supply system constitutes the major challenge and stands at the core of the transition to a sustainable energy future.[16]

Renewable energy sources are resources of energy that can replenish themselves naturally on a human timescale. Typical examples are solar, hydropower, wind, tidal, ocean wave, biomass, and geothermal energies. These resources and their technologies are considered key tools for sustainable development as they can enhance access to affordable and reliable energy, provide opportunities for mitigating greenhouse gas emissions, improve human health, and boost world energy security through resource diversification. In recent years, they have played an important role on the global economy, reducing the dependency on fossil fuels to some extent. According to the REN21's *Renewables 2018* global status report, renewable energy accounted for an estimated 18.2% of global total final energy consumption in 2016, with modern renewables (excluding traditional use of biomass) representing 10.4%, displacing conventional fuels in four important areas: electricity generation, heating and cooling, transportation, and rural (off-grid) energy services.[17] The penetration of renewables is highest in the electricity sector with a share of 26.5%, most of it coming from hydropower (16.4%), followed by wind (5.6%) (see **Figure 1.6**). With falling technology costs and rising fossil fuel prices, renewable energy technologies are increasingly competitive and are expected to continue their expansion in the next years, as forecasted by the International Energy Agency (IEA).[18]
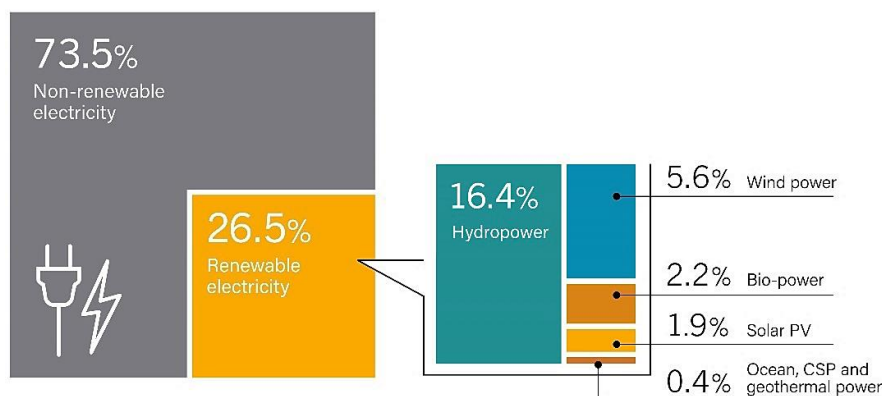
Figure 1.6. *Estimated renewable energy share of global electricity production, end-2017. Source: REN21, Renewables 2018 Global Status Report.*[17]

Despite tremendous progress in some renewable sectors, the overall share of renewable energy is increasing relatively slowly. A primary reason is the continued growth in overall energy demand.

Other key barriers to the widespread implementation of renewables include climate change denial, government constraints, and efforts to impede renewable energy by the fossil-fuel industry. To meet long-term climate and other sustainability goals, renewable energy development in the heat, electricity and transport sectors must accelerate. A number of initiatives and technologies, including energy storage, heat pumps, and electric vehicles, are now helping to integrate renewable energy into the electricity sector and to facilitate the coupling of renewables with the thermal and transport sectors. But greater supportive government measures, appropriate market design, and new technological solutions are needed for a timely energy transition.

1.1.3. Solar Energy and Photovoltaic Technology

Solar energy, among other renewable sources of energy, has enormous potential as a clean, ubiquitous, very abundant and freely available energy source for managing long-term issues in energy crisis.[19,20] Around 23000 Terawatts (TW) of solar energy strikes the Earth's emerged continents continuously (assuming 65% losses by atmosphere and clouds), an amount of energy which far exceeds both the world's total primary energy demand (16 TW in 2009) and that predicted for 2050 (27 TW).[19] By contrast, energy outputs from other renewable and conventional sources seem to be on a much smaller scale, as shown in **Figure 1.7**. It follows that harvesting solar energy will most likely be the major part of the sustainable energy infrastructure in the future.
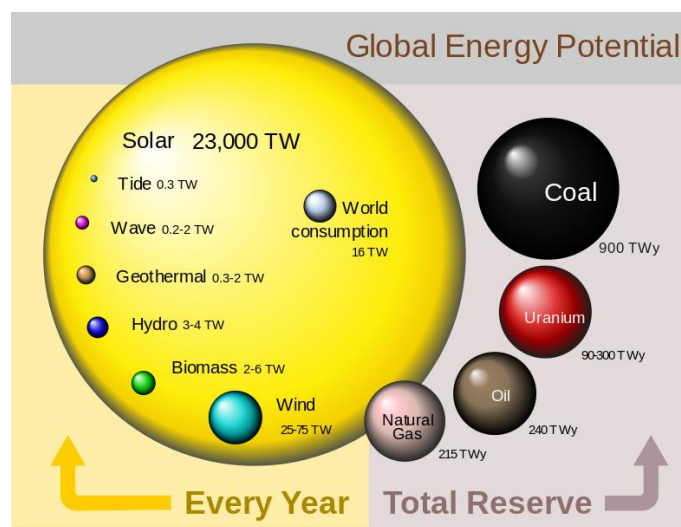
Figure 1.7. *Estimate of the yearly energy potential of renewables in Terawatts (TW) and of the total known reserves of finite sources in Terawatt-year (TWy).*[19]

To exploit the unlimited power of the Sun, its electromagnetic radiation must be captured and converted into useful forms of energy. Since solar energy is extremely dilute (average solar flux of 170 W m^{-2}) and intermittent (due to diurnal cycles and atmospheric conditions), conversion should involve concentration and storage. A number of routes and technologies have been developed to convert sunlight into heat, electricity, and fuel, including photovoltaics (PVs), concentrated solar power (CSP), solar heating and cooling (SHC) systems, and artificial photosynthesis.[21] In particular, converting sunlight directly into electricity by means of PV systems represents one of the most promising and effective strategy for harnessing solar energy power. The potential of solar PV is substantial: it has been estimated that the total primary energy supply could be fulfilled if only 4% of the desert areas on Earth were used for PV implementation.[22]

A conventional PV system employs solar panels, each comprising a number of solar cells, which are solid-state semiconductor devices that can convert incident light into direct current (DC) electricity through the photovoltaic effect.[23] When photons in the incoming sunlight are absorbed by the semiconductor material, electron-hole pairs are generated. The electrons and holes are then separated and transported to the opposite terminals of the device, driven by a certain "asymmetry" inside the structure that assists directional extraction. If an electrical load is connected to the cell between the front and back contacts, charge carriers will complete the circuit through this load, constituting an electrical current in it. As a result, solar energy is partly converted into electrical energy consumed by this load. The fraction of incident power that is effectively converted into electricity corresponds to the power conversion efficiency (PCE) of the solar cell. This process is illustrated in **Figure 1.8** for the typical solar cells in use today, whose operation relies upon the asymmetry associated with a p-n junction.[24] In these junction devices, charge separation occurs because of a pre-existing built-in potential, arising from the contact between two electronically dissimilar semiconductor materials, p-type (which contains an excess of holes) and n-type (which contains an excess of electrons). Many other junctions such as Schottky barrier, p-i-n, and metal-insulator-semiconductor have been studied and used to extract charge carriers from a solar cell. More details about the operating principles of solar cells will be given below.

Solar PV has become object of steadily growing interest in both academic and industrial areas during the last decades. The main attraction of PV systems is that they produce electric power without harming the environment (their operation produces no pollution and no greenhouse gas emissions), by directly transforming a free inexhaustible source of energy into electricity. They

hence constitute a key technology option for realizing a decarbonized power sector and sustainable energy supply.[25,26] In recent years, solar PV has experienced exponential growth all over the world thanks to both dramatic cost reductions, mainly driven by technological improvements and scaling up of manufacturing, and supportive government policies. The continuing increase in the performance/cost ratio as well as the ever-higher levels of investment involved have boosted the role of photovoltaics in the global energy market. Currently, solar PV makes an important contribution to the growing share of renewables in electricity generation, accounting for nearly 55% of newly installed renewable power capacity in 2017. Based on the REN21's report,[17] more solar PV capacity was added in 2017 than the net additions of fossil fuels and nuclear power combined, up to a total global capacity of 402 Gigawatts (see **Figure 1.9**). By 2050, the IEA foresees solar PV to reach 4.7 TW under its "high renewables" scenario, making solar power the world's largest source of electricity.[27]
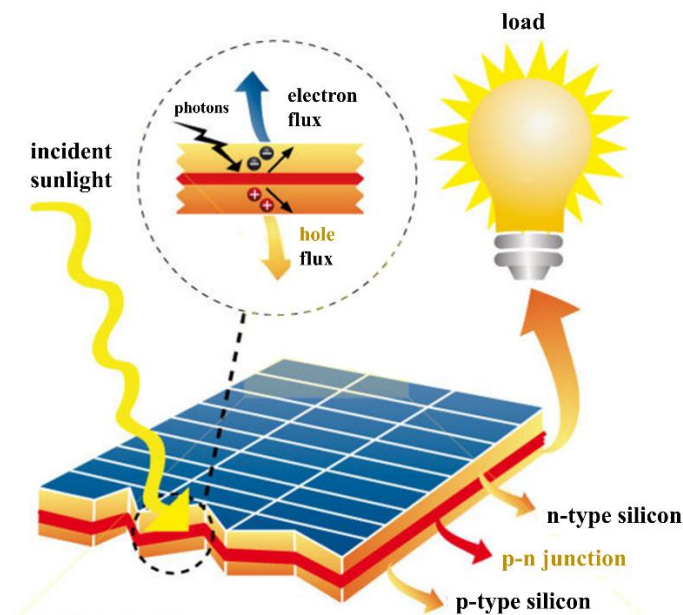
Figure 1.8. *Scheme of a typical silicon solar cell based on a p-n junction.*

Despite this promising scenario, solar PV is at present still a minor player in the global power sector, contributing less than 2% to the global electricity generation (see Figure 1.6). A wider and faster expansion of photovoltaics is mainly hindered by the high costs of production compared with other conventional fuels. Indeed, PV market is currently dominated by crystalline silicon solar cells (90% market share), which are relatively expensive from a manufacturing standpoint. New

PV technologies and materials are continuously being developed in order to reduce costs and increase efficiency, as described in the next sub-section. Nevertheless, the road to PV competitiveness remains complex. Hopefully, more efforts from researchers, industries, and governments will be dedicated to solar PV in the coming years, in order to help the technology to become further established as a marketable and economically viable product.[28]
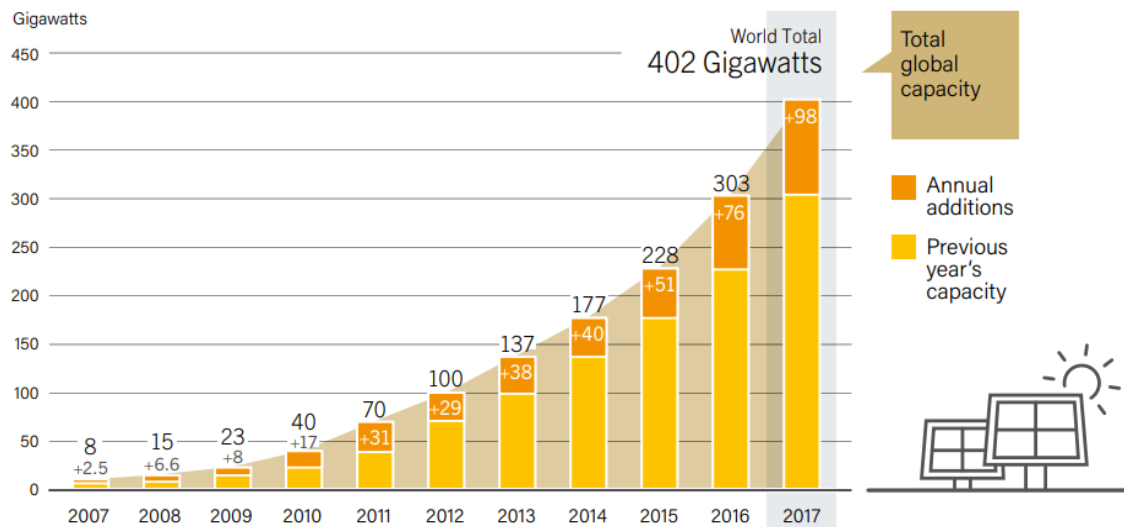
Figure 1.9. *Solar PV Global Capacity and Annual Additions, 2007-2017. Source: REN21, Renewables 2018 Global Status Report.*[17]

1.1.4. Towards Third-Generation Photovoltaics

The photovoltaic effect was first discovered by Bequerel in 1839 while experimenting with electrolytic cells.[29] But a long period was required to reach the first landmark achievement in PV technology: the production in 1954 of the first practical silicon solar cell with 6% PCE by Chapin et al. at Bell Laboratories.[30] Since then, solar PV industry has developed several more materials and module anatomies with the aim of reducing the production costs for large-scale use.[31] Today, there is a wide variety of PV technologies in the marketplace that can be generally classified into two categories: wafer-based and thin-film solar cells (see **Figure 1.10**).

Wafer-based solar cells are fabricated on semiconductor wafers. Three primary examples are:

- Crystalline silicon (c-Si) solar cells, in the single-crystalline (sc-Si) or multi-crystalline (mc-Si) form, are the most mature of all PV technologies. In the early years, silicon-based PV

technology was favored by different factors such as the abundance of silica on the Earth's crust and the advances in silicon processing for integrated circuits. Cylindrical single crystals are typically grown through the Czochralski process (the standard process used for the needs of microelectronics),[32] while mc-Si blocks are formed by casting. The resulting ingots are sliced into wafers prior to cell processing. The higher crystal quality in sc-Si cells improves charge extraction and conversion efficiency at the expense of more expensive wafers and material processing. Record research-cell efficiencies stand at 26.1% for sc-Si and 22.3% for mc-Si.[33] A key disadvantage of c-Si is its relatively poor ability to absorb light, which requires the use of thick (100-200 μm), rigid, impurity-free, and expensive wafers. This shortcoming translates to high manufacturing costs and constrained module form factors. Today, c-Si solar cells are the leading deployed PV technology with a market share of 90%, but their costs are still too high, impairing the deployment of such devices on a Terawatt scale.

- Gallium arsenide (GaAs) solar cells are the highest efficiency single-junction PV devices, with a record PCE of 29.1%.[33] GaAs cells use thin films but require wafers as templates for crystal growth. GaAs is almost perfectly suited for solar energy harvesting, with strong absorption across the solar spectrum, direct bandgap, and low non-radiative energy loss. Unfortunately, high material costs limit the large-scale deployment of GaAs-based devices.

- III-V multi-junction (MJ) solar cells are the leading PV technology for space applications. These devices use a stack of two or more single-junction cells which contain exotic semiconducting compounds of group III (Al, Ga, In) and group V (N, P, As, Sb) in the form of high-quality crystalline films. III-V MJ solar cells have reached efficiencies as high as 39.2% (46% with sunlight concentration),[33] but complex manufacturing processes and high material costs make them prohibitively expensive for large-area terrestrial applications.

Although wafer-based c-Si PV devices are market leaders at present, there is a general consensus that significant cost reductions in the future will primarily be achieved through the development of thin-film solar cells.[34] Thin-film PV technology involves the deposition of one or more thin layers (from a few nanometers to a few microns) of photovoltaic material on an inexpensive substrate (glass, plastic, metal) through low-cost solution-based or vapor phase deposition techniques. In this way, materials usage and manufacturing costs are severely reduced. Some common materials used in commercial thin-film solar cells are hydrogenated amorphous silicon (a-Si:H), cadmium telluride (CdTe), and copper indium gallium selenide (CIGS). These materials

generally absorb light 10-1000 times more efficiently than c-Si, allowing the use of much thinner devices compared to silicon wafers. Record certified cell efficiencies have reached 14%, 22.1%, and 22.9% for a-Si:H, CdTe, and CIGS solar cells, respectively.[33] These devices have been marketed but have not gained the success of c-Si solar cells due to several technological limitations. The deposited thin films generally contain high densities of crystal defects, resulting in limited device efficiency and lifetime. Moreover, most of the applied semiconductors are generally very rare (tellurium, indium), highly toxic (cadmium), and environmental unfriendly. For all of these reasons, commercial thin-film solar cells still own a small market share (10% of the total PV market).[31]
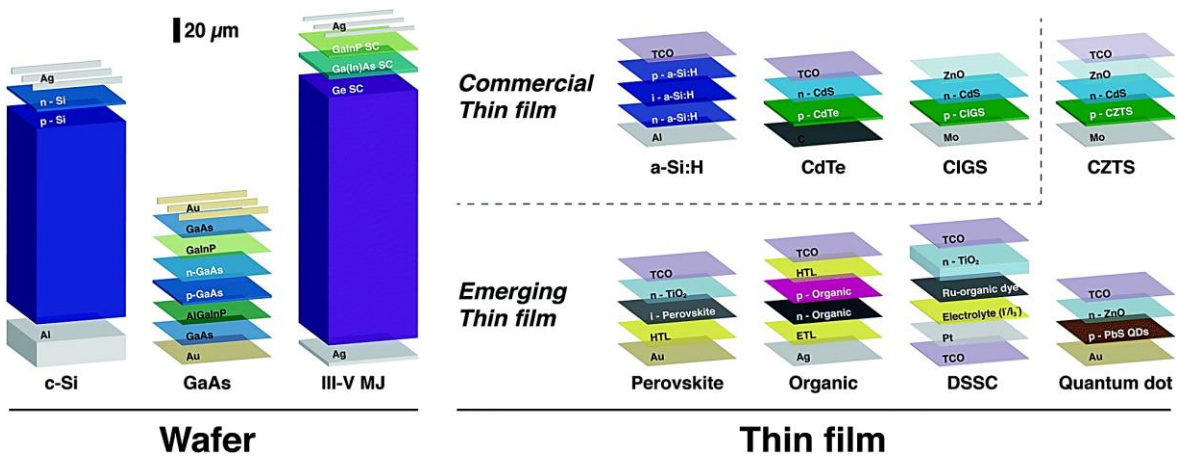
Figure 1.10. *Typical solar PV devices, divided into wafer-based and thin-film technologies. Primary absorber layers are labeled in white. (adapted with permission from Ref.* [31]*)*

Nowadays, new-generation thin-film PV technologies based on innovative concepts and nano-structured materials are making inroads.[31,35] Most of them are still in the research and development phase and have not yet been commercialized. Despite their still poor performance and stability, these technologies have the potential to overcome many of the limitations of today's applied PV devices as they can theoretically achieve high conversion efficiencies while still using thin films and low-cost deposition methods. This is especially represented in the use of roll-to-roll (R2R) compatible printing techniques. Moreover, they offer potentially unique properties, such as visible transparency, high weight-specific power [W g^{-1}], and flexible form factors, that could open the door to novel, unconventional PV applications. Key emerging thin-film PV technologies are:

- Organic Solar Cells (OSCs), which are built from thin films (typically 100 nm) of organic semiconductors, including polymers and small molecules.[36]

- Dye Sensitized Solar Cells (DSSCs), in which a metal-organic dye is employed as light harvester and sensitizer on a mesoporous layer of nano-particulate titanium dioxide (TiO_2); the circuit is completed by a redox couple in a solid or liquid electrolyte medium.[37]

- Quantum Dot Solar Cells (QDSCs), which are based on the DSSC architecture but employ low-bandgap semiconductor nanoparticles (quantum dots) as light absorbers.[38]

- Perovskite Solar Cells (PSCs), which include a perovskite-structured compound, most commonly a hybrid organic-inorganic lead halide-based material, as the light harvester.[39]

In particular, the PSC technology has received tremendous attention since it has shown an astonishing growth in a very short time (see the next section). Record certified cell efficiency for PSCs has recently reached 24.2%, much higher than those shown by other emerging thin-film solar cells and very close to those of conventional wafer-based PV technologies (see **Figure 1.11**).[33]
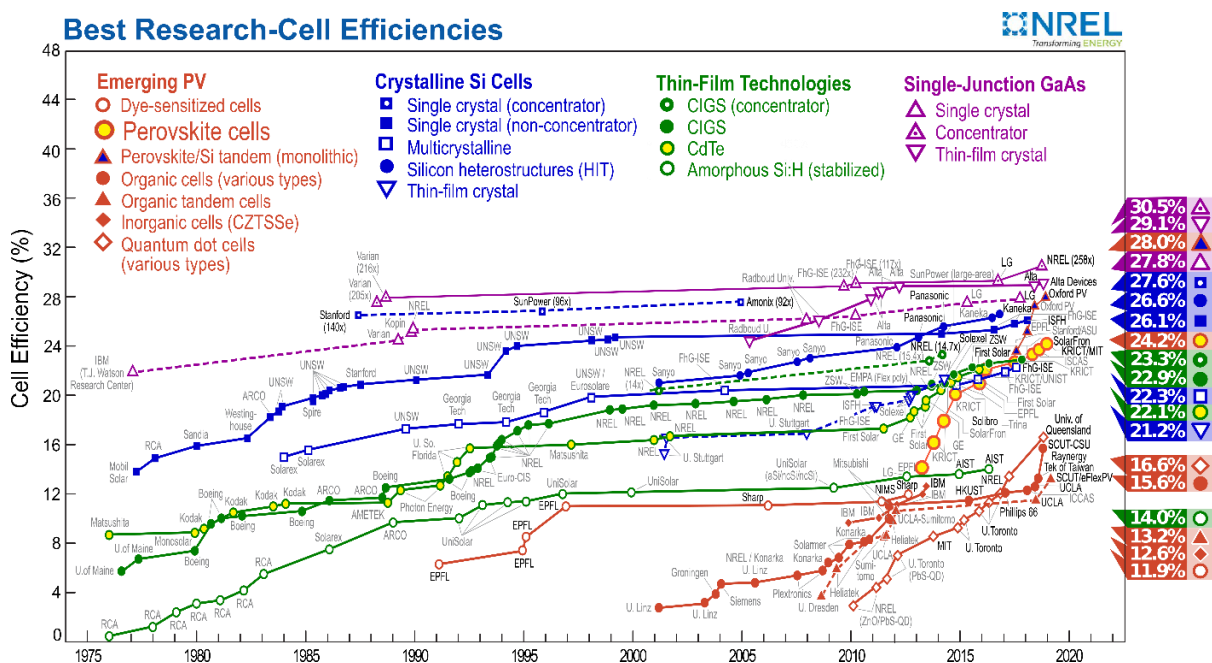
Figure 1.11. *Evolution of the record research-cell efficiencies of the different PV technologies (wafers, thin films, and emerging thin films) since 1975. Source: NREL.*[33]

Another widely used classification scheme for PV technologies delineates three distinct generations, depending on the raw material used and the level of commercial maturity:

14

- First-generation (I) PV technologies (fully commercial) consist of wafer-based solar cells of c-Si and GaAs;

- Second-generation (II) technologies consist of thin-film solar cells based on conventional inorganic semiconductors, including a-Si:H, CdTe, and CIGS;

- Third-generation (III) technologies include all the emerging thin-film devices (OSCs, DSSCs, PSCs, *etc*.) which are still in demonstration, along with a variety of innovative concepts, including multi-junction devices, hot-carrier collection, and thermophotovoltaics.[40,41]

The three generations are commonly represented as shadow regions on a plot of efficiency vs. cost. **Figure 1.12** shows these regions as originally defined in 2001.[40] This diagram clearly suggests that the research and development of third-generation PV technologies, including perovskite solar cells, is the most promising pathway towards achieving a significant role for solar photovoltaics in the future energy system.
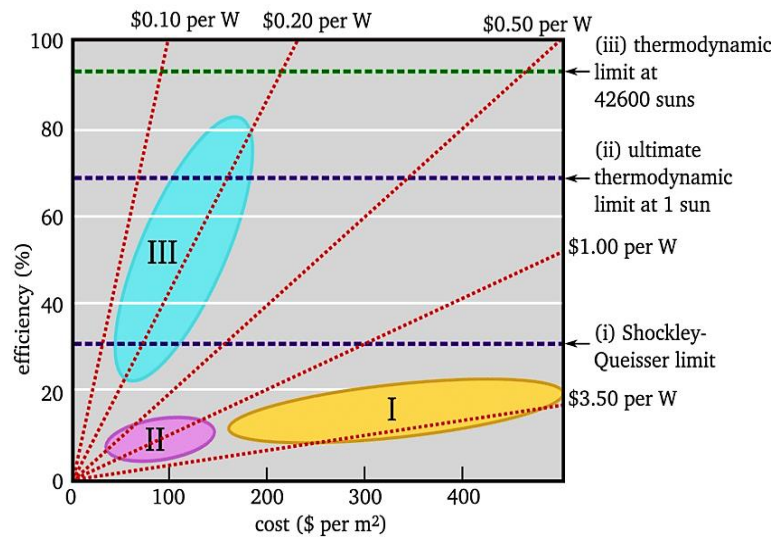
Figure 1.12. *Efficiency and cost projections for first-, second-, and third-generation PV technologies.*[40]

1.2. Perovskite Solar Cells: Basics and Challenges

1.2.1. Origin of Perovskite Semiconductor

Among third-generation photovoltaics, perovskite solar cells have drawn tremendous research interest during the last decade as they have emerged as one of the most standout PV technology in terms of efficiency (see Figure 1.11). These devices are exceptional in a way that they can achieve PCEs as high as 24.2%, while utilizing inexpensive fabrication processes and introducing useful additional features such as flexibility and semitransparency. Such an extraordinary photovoltaic performance is attributable to the unique combination of optoelectronic properties and solution processability shown by the constituent perovskite materials.[42–45]

The term "perovskite" refers to the mineral form of calcium titanate ($CaTiO_3$) first discovered by Gustav Rose in 1839 and named in honor of Russian mineralogist Lev Perovski (1792-1856). Today, this term is widely used to describe any material with the same crystal structure as $CaTiO_3$ and general formula ABX_3, where A and B are cations of different sizes, and X is an anion. The ideal perovskite structure, which is illustrated in **Figure 1.13**, is a cubic lattice and consists of corner-sharing BX_6 octahedra in three dimensions, with A cations occupying the cuboctahedral cavities in each unit cell and neutralizing the charge of the octahedral networks.
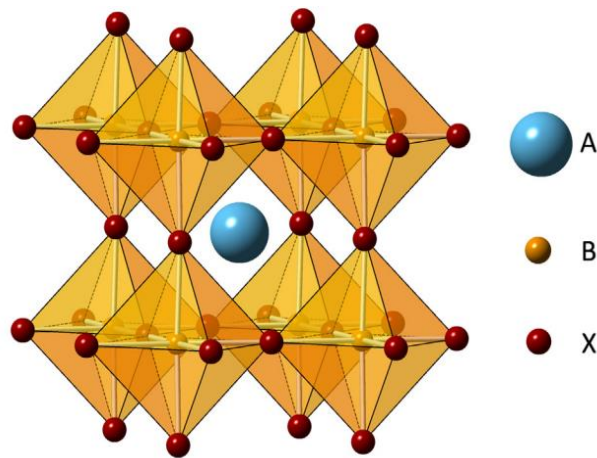
Figure 1.13. *Ideal cubic structure of perovskite (ABX_3).*

Such a three-dimensional (3D) perovskite lattice can only form for certain combinations of anions and cations, depending on their dimensions. To predict whether a certain composition would form

a stable perovskite structure, Goldschmidt's tolerance factor t can be used as a guide and calculated using the following equation:[46,47]

$$t = \frac{R_A + R_X}{\sqrt{2}(R_B + R_X)} \qquad \{1.1\}$$

where R_A, R_B, and R_X are the effective ionic radii of the A, B, and X components of the perovskite lattice. t = 1 corresponds to a perfectly packed and stable cubic 3D structure, while t < 1 or t > 1 suggest crystallographic distortion. In practice, a cubic 3D phase will likely form if 0.85 < t < 1, while lower-symmetry distorted variants (orthorhombic, rhombohedral, tetragonal, or trigonal phases) are likely to occur when 0.75 < t < 0.85, resulting from the tilting and rotation of the BX_6 octahedra. For t values below 0.75 or above 1.11, formation of the 3D perovskite structure will become unfavorable. In particular, when t >> 1, two-dimensional (2D) or one-dimensional (1D) perovskites can be obtained as a result of the 3D framework destabilization by excessively large A cations. More than one structure is usually found for a perovskite material with a given chemical composition, and reversible phase transitions can be induced by external stimuli such as electric field, temperature, and pressure.

Although almost all known perovskites have t values between 0.75 and 1.11, for some systems with t within the most favorable range (0.8- 0.9) no perovskite structure is stable. This means that the t criterion is not by itself a sufficient condition for the formation of the perovskite structure. More recently, octahedral factor μ was introduced to better estimate the formability of perovskites. The μ factor is focused on the stability of the BX_6 octahedron, and it is defined as the ratio of the ionic radii of B (R_B) and X ions (R_X):

$$\mu = \frac{R_B}{R_X} \qquad \{1.2\}$$

It has been found that the μ values between 0.41 and 0.73, along with permissible t values, are favorable for perovskite structure stability.[47]

Perovskites represent a vast and unique class of materials across condensed matter physics and solid-state chemistry, showing high versatility and a multitude of intriguing features from both the theoretical and the application point of view. Examples of piezoelectric, insulating, semiconducting, conducting, magnetic, ferroelectric and superconducting perovskites are known. Their composition as well as their distortion in geometry from ideal structure play a crucial role in tuning their physical properties such as the bandgap (energy difference between the valence band

maximum, VBM, and the conduction band minimum, CBM). Historically, inorganic oxide-based perovskites ($CaTiO_3$, $BaTiO_3$, $LaMnO_3$, etc.) have been most actively studied for various applications due to their superior ferroelectric and superconducting properties. However, their wide bandgaps limit their use in solar applications as they utilize a mere 8-20% of the solar spectrum.[45] Instead, the perovskites of interest for photovoltaic purposes are halide-based perovskites (ABX_3, with $X = I^-$, Cl^-, Br^-), which are generally solution-processable semiconductors. Halide perovskite structure was first observed in $CsPbX_3$ in 1958.[48] Since then, a number of A, B, and X ions have been investigated in the halide perovskite family to better understand the structural versatility and diversity of these compounds. Typical inorganic A site cations that can form 3D perovskites include Li^+, Na^+, Rb^+, K^+ and Cs^+, while the B site can be occupied by any divalent metal cation, the most relevant for optoelectronic purposes being Pb^{2+}, Sn^{2+}, Ge^{2+}, and Eu^{2+}. The replacement of the inorganic A site cation with an organic cation leads to the formation of hybrid organic-inorganic halide perovskites, a class of perovskites that has attracted huge attention since the 1970s due to their improved optical and electrical properties. Aside from a clear difference in A species between inorganic and hybrid perovskites, there is also a change in symmetry of the A site component from spherical (inorganic) to non-spherical (organic), this being particularly important in terms of polarization and orientational disorder.[49] Owing to the limited space in the 3D perovskite lattice, only small-size organic cations with three or less C−C/ C−N bonds can be incorporated within the voids. The most commonly investigated hybrid halide perovskites to date have been based on methylammonium ($CH_3NH_3^+$, also referred to as MA^+) or formamidinium ($NH_2CHNH_2^+$, FA^+) as the organic cation.[50]

The perovskite compound that first excited the PV research field was methylammonium lead tri-iodide ($CH_3NH_3PbI_3$, also known as $MAPbI_3$). With $t = 0.83$ and $\mu = 0.54$ (from $R_A = 1.8$ Å, $R_B = 1.19$ Å, $R_X = 2.2$ Å), $MAPbI_3$ adopts a black tetragonal perovskite phase at room temperature (see **Figure 1.14**).[51] The great interest in this material is due to its favorable optoelectronic properties, which are rarely seen in solution-processable materials. Indeed, $MAPbI_3$ is a semiconductor with a direct bandgap of about 1.55 eV and a broad light absorption spectrum up to 800 nm, which are nearly optimal conditions for solar PV purposes (1.1—1.4 eV is the optimal bandgap range dictated by the Shockley-Queisser limit for a single-junction solar cell).[52] Additionally, it is characterized by a large absorption coefficient (up to 10^5 cm^{-1}), allowing for a reduced thickness necessary to efficiently absorb light, and by a low exciton binding energy, which means that

photogenerated charges can separate readily at room temperature. Finally, it displays long charge carrier diffusion lengths (up to 100 nm) and sufficiently high charge mobilities. This indicates that the charges can efficiently diffuse to the electrodes before recombining. Theoretical studies have shown that these superior photovoltaic properties are originated from the combination of high perovskite symmetry, high electronic dimensionality, the unique electronic configuration of Pb, including the Pb $6s^2$ lone pair that causes strong Pb 6s – I 5p antibonding coupling, the inactive Pb 6p, the strong spin–orbit coupling (SOC), and the arrangement of the polar organic cations.[53]
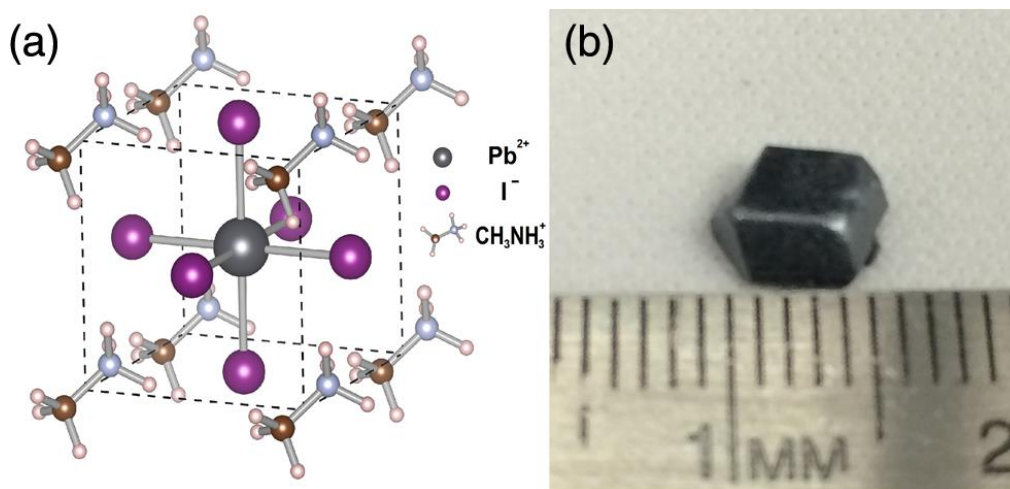
Figure 1.14. (a) Crystal structure of MAPbI₃ perovskite, and (b) photograph of a MAPbI₃ single crystal. (adapted with permission from Ref. [51])

MAPbI₃ was first utilized in solar PV devices as recently as in 2009 by Kojima et al., who used it as the sensitizer in liquid electrolyte DSSCs and achieved a maximum efficiency of 3.8%.[54] Since then, the highest efficiencies reported for perovskite solar cells have been obtained most frequently using this perovskite material, or its mixed iodide-chloride analogue ($CH_3NH_3PbI_{3-x}Cl_x$ or $MAPbI_{3-x}Cl_x$), as the light absorber. The small addition of Cl^- anions to the organolead tri-iodide was first proposed in 2012 by H. J. Snaith et al., who found that this leads to a striking increase in the electron-hole diffusion lengths (up to 1 μm) and carrier lifetimes.[55,56] It has been demonstrated that in MAPbI₃-based PSCs holes are much more efficiently extracted than electrons, thus explaining the necessity of a mesoporous titania scaffold (mp-TiO₂, an electron conductor) to achieve high efficiencies. On the contrary, $MAPbI_{3-x}Cl_x$-based devices are characterized by long and balanced diffusion lengths for both electrons and holes, and therefore perform well even

without a mp-TiO$_2$ scaffold. This means that the MAPbI$_{3-x}$Cl$_x$ perovskite itself can sustain sufficient electron transport to enable highly efficient charge collection. Mesoporous scaffold-free architectures are desirable for applications where low-temperature processing (e.g. flexible solar cells) or maximized optical transmittance (e.g. semitransparent solar cells) are required, as will be discussed below. From a structural point of view, mixed MAPbI$_{3-x}$Cl$_x$ have shown to produce highly oriented crystalline structures (in contrast to the MAPbI$_3$ non-oriented structures), exemplified through the strong X-ray diffraction (XRD) peaks along the (110), (220), and (330) planes attributed to the tetragonal phase.[57] On the other hand, the partial Cl inclusion has a small impact on the bandgap, with both the VBM and CBM shifted upward by ca. 0.1-0.2 eV.

During the last years, several other compositional modifications of MAPbI$_3$ have been proposed, resulting in color variation and PCE modulation.[58] One of the key attributes of perovskite materials is that they possess excellent tunability of the bandgap, achievable through rational compositional engineering (see **Figure 1.15**). This is a very attractive feature for solar cell applications, since it allows for devices with a specific color, or for semitransparent solar cells that can be used as top cells in tandem devices (see Section 1.2.6). Bromide has been most effectively used to tune the bandgap of hybrid perovskites. Noh et al.[59] were first to investigate the effects of mixed iodide-bromide MAPbI$_{3-x}$Br$_x$ compositions, realizing a tunable bandgap between 1.5 and 2.2 eV and a wide variety of film color. Interestingly, bromide-containing perovskites were also found to display better stability under moist air conditions. In 2014, Pellet et al.[60] demonstrated an improved PCE using mixed cation lead tri-iodide perovskites by gradually substituting MA with FA cations. The improved performance compared to pure MAPbI$_3$ was due to greater absorption in the red region of the spectrum (narrower bandgap), resulting in higher photocurrent. Even though the nature of the organic cation does not directly affect the electronic band structure of perovskites (the valence and the conduction band of the MAPbI$_3$ are formed exclusively from Pb and I orbitals), it can regulate the bandgap by changing the crystal geometry. Numerous other reports of (MA)$_x$(FA)$_{1-x}$PbI$_3$-based devices with respectful PCEs have been documented.[61–63] Another way of changing the bandgap of perovskite is by replacing toxic Pb^{2+} with alternative homovalent metal species (Sn^{2+}, Ge^{2+}) at the B site. Mixed MASn$_{1-x}$Pb$_x$I$_3$ devices have been studied by Zuo et al.[64] and Ogomi et al.,[65] demonstrating bandgap tuning through varying Pb:Sn ratios. Tin-based perovskites have promising photovoltaic properties like narrower bandgap (1.2-1.4 eV) and higher carrier mobility. However, they suffer from rapid degradation as a result of the inherent instability

of the Sn^{2+} state, which is readily oxidized to Sn^{4+} upon contact with air. This effect is even more prominent for the case of Ge^{2+}, inevitably reducing the performance of the corresponding PV devices.[66] More recent approaches consist in doping lead-based perovskites with other homovalent (Co^{2+}, Cu^{2+}, Mg^{2+}, Mn^{2+}, Ni^{2+}, and Zn^2) or heterovalent (Bi^{3+}, Au^{3+}, In^{3+}, Ag^+, Cu^+, Na^+) metal ions. For instance, it was shown by Nayak et al.[67] that Bi^{3+} doping results in tunable bandgap of MAPbI$_3$ and enhanced charge carrier lifetime.
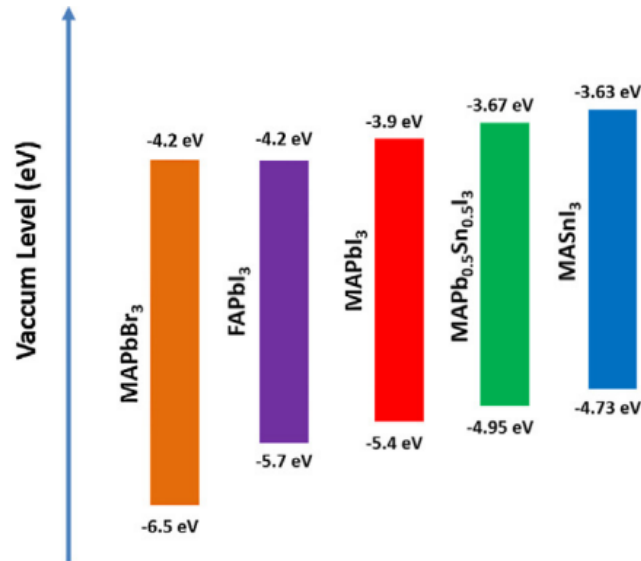
Figure 1.15. Energy bands of commonly employed hybrid perovskites. (adapted from Ref. [45])

1.2.2. Operating Principles and Charge Dynamics

Light absorption, charge separation, charge transport, and charge collection are general working processes in solar cells, including perovskite cells.[68] PSCs are most commonly designed as a p-i-n (or n-i-p) heterojunction architecture, where the intrinsic (i-type) perovskite semiconductor serves as the light absorber for photogeneration of charge carriers, while n- and p-type materials are introduced in the device to provide the built-in potential and assist directional extraction. A typical PSC comprises a front transparent conducting electrode (TCE), which allows for the passage of light in the heart of the cell, a perovskite photo-active layer sandwiched between a hole-transporting layer (HTL) and an electron-transporting layer (ETL), and a metal reflective back contact. The ETL is normally made of TiO$_2$, an n-type material which forms a n-i junction selective

to the passage of electrons, while the HTL is a p-type material that forms a i-p junction selective to the holes transport. During exposure to sunlight, photons are absorbed by the perovskite layer, leading to excitation of electrons from valence to conduction band of perovskite and the generation of excitons (bound electron-hole pairs). The charges dissociate readily thanks to the low exciton binding energy of perovskite absorbers and become free to move across the device. This non-excitonic nature of the charge generation is one of the main advantages of PSCs, since in excitonic solar cells like OSCs significant losses in energy occur through exciton migration and dissociation. The free electrons and holes can efficiently diffuse through the perovskite layer, thanks to the relatively high charge mobilities and long charge diffusion lengths, and reach the ETL/perovskite or perovskite/HTL interface respectively, driven by the built-in electric field. At the interface, charge transfer (CT) process takes place either by injection of electrons into ETL or injection of holes into HTL. For an efficient CT process, the band alignment of the perovskite with the HTL and the ETL materials is essential: the conduction band edge (or LUMO, lowest unoccupied molecular orbital, in organic semiconductors) of the ETL must be lower than the perovskite conduction band, and the valence band edge (or HOMO, highest occupied molecular orbital, in organic semiconductors) of the HTL must be higher than the perovskite valence band (see **Figure 1.16**).[68] After interfacial charge transfer, charge transport processes occur in the ETL (HTL), where high electron (hole) mobility can guarantee efficient electron (hole) transport toward the electrode.
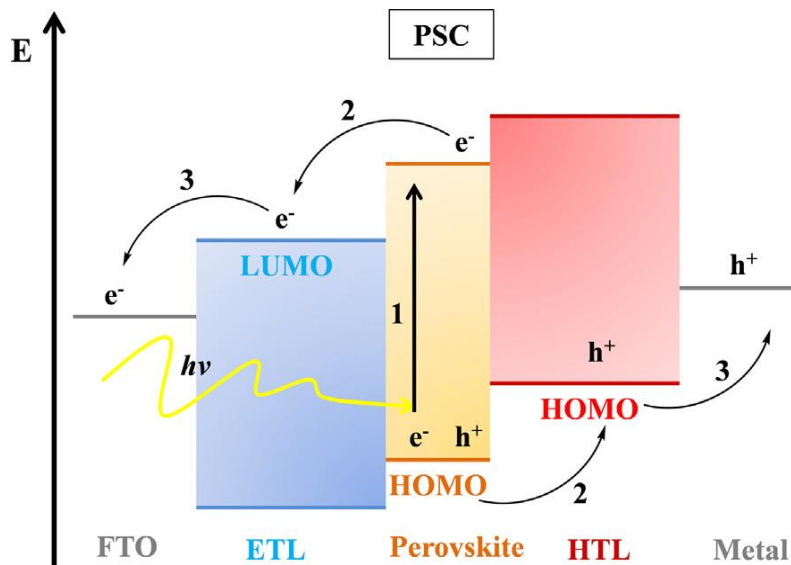
Figure 1.16. *Band diagram and main processes in a typical PSC: 1) absorption of photon and free charge generation; 2) charge transport; 3) charge extraction. (adapted from Ref. [68])*

However, it was shown that the superior charge transport capabilities of perovskite materials permit effective charge collection even without ETL and HTL by making p-n homojunction devices.[69] Lastly, selective contacts with appropriate work function (WF) are important prerequisite for an efficient extraction of electrons from the ETL or holes from the HTL. The formation of a quasi-ohmic contact, in contrast to a Schottky contact, is commonly preferred to alleviate interfacial energy barriers. A p-type (n-type) semiconductor forms a Schottky contact with a low (high) WF metal and an ohmic contact with a high (low) WF metal, where "high" and "low" refers to the absolute value difference between the vacuum level and the Fermi level of the electrode. Therefore, the difference between the Fermi level of the electrode and the VBM (or HOMO) of the HTL or the CBM (or LUMO) of the ETL should be as small as possible to reduce the carrier injection barrier at the interface. Additional measures such as interfacial buffer layers or doping of the charge transport layers can be utilized to reduce interfacial barriers, as will be discussed below. In contrast to OSCs, where the cell's built-in potential is strongly influenced by the anode-cathode WF difference, in PSCs the voltage output is mainly dominated by the quasi-Fermi levels of the photoexcited perovskite due to the low exciton binding energy and excellent transport properties of perovskites. This in turn widens the choice of possible electrode materials, an advantage that has been widely exploited in this thesis (see Chapter 3).

Each mentioned step in the operation of PSCs is subject to potential loss mechanisms that limit the overall PCE. One of these mechanisms is radiative band-to-band recombination of electron-hole pairs, which occurs when part of the energy absorbed by the semiconductor material is released by spontaneous light emission or luminescence (see **Figure 1.17**). This process is unavoidable, because it is the time-reversed process of light absorption. Therefore, it is already taken into account in the calculation of the theoretical Shockley-Queisser (SQ) efficiency limit.[70] The SQ limit is commonly used to estimate the limit PCE of single-junction solar cells and can be described as the ideal case in which recombination of electron-hole pairs is only radiative (with no other source of recombination) in a single bandgap semiconductor. In practice, there are several other loss mechanisms that may take place, including: i) optical losses, mainly coming from photon reflection and absorption in poorly responding cell regions; ii) electrical losses, originating from series and shunt resistances (see Chapter 2, Section 3); iii) non-radiative recombination losses, including Auger recombination and trap-assisted Shockley-Read-Hall (RSH) recombination losses (see Figure 1.17); iv) interface recombination losses, stemming from all of the interfaces involved

in the device. This explains why the presently achieved 24.2% for PSCs is still far from the theoretical SQ limit of 30.5% (for a bandgap of 1.6 eV). Researchers have recently found that the main PCE losses in PSCs are from RSH recombination, deriving from defects or trap states induced by poor film quality, and from interface recombination, mainly occurring at charge-transport layers/perovskite interfaces: electron (hole) injected into ETL (HTL) recombines with hole (electron) in perovskite.[71] Actually, defect-related bulk and interface recombination can affect not only PCE but also hysteresis along with long-term stability, as will be discussed below. Therefore, it is an important direction for further improvement of solar cell performance to minimize the above recombination losses. One of the most promising way to do this is to improve the device architecture through rational interface engineering and defect passivation strategies.
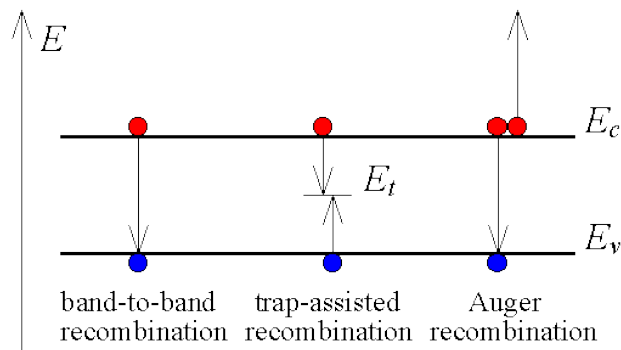
Figure 1.17. Carrier recombination mechanisms in semiconductors.

1.2.3. Architecture Evolution of PSCs

Advances in the design of device architecture are one of the main factors that drove the evolution of PSCs.[72] After having recognized the relevance of hybrid perovskites as potentially high-efficiency photovoltaic materials, researchers focused their efforts on optimizing the PSC structure. PSCs were initially fabricated in the conventional DSSC architecture, whose operating principle is shown in **Figure 1.18**.[73] A typical DSSC is constructed on a glass substrate and comprises a transparent conductive oxide (TCO) layer – most commonly fluorine-doped tin oxide (FTO) – which serves as the bottom (front-side) electrode, a thin compact TiO_2 (c-TiO_2) hole-blocking layer, a several micron thick mp-TiO_2 layer sensitized with organic dyes (e.g. N719), a liquid electrolyte, and a metal counter electrode (back-side, Pt/TCO/glass). The photoexcitation of

the dye results in the excitation of electrons and their subsequent injection into the conduction band of mp-TiO$_2$, and then to the front electrode. This process leaves the photosensitizer in an oxidized state, which is reduced back to the ground state by the reductants (e.g. I$^-$) in the liquid electrolyte. Lastly, the deactivated reductants (e.g., I$_3^-$) diffuse to the metal counter electrode, where they are regenerated by the electrons collected from the external circuit. This complete electron flow creates a photocurrent in DSSCs. In 2009, Kojima et al.[54] replaced the conventional dyes with MAPbI$_3$ and MAPbBr$_3$ perovskites by means of a one-step spin-coating technique (see Section 1.2.4), demonstrating PCEs of 3.8% and 3.1%, respectively. However, their work did not receive much attention due to the relatively low efficiency of the devices along with instability in liquid electrolyte where organometal halide perovskite easily decomposes. Two years later, Im et al.[74] fabricated perovskite-based DSSCs with an improved PCE of 6.5% using thinner TiO$_2$ layer (from 8-12 µm to 3 µm) and MAPbI$_3$ quantum dots as the photosensitizer. Despite a considerable increase in PCE, these devices still showed very poor stability due to the quick dissolution of the perovskite QDs in the liquid electrolyte medium.
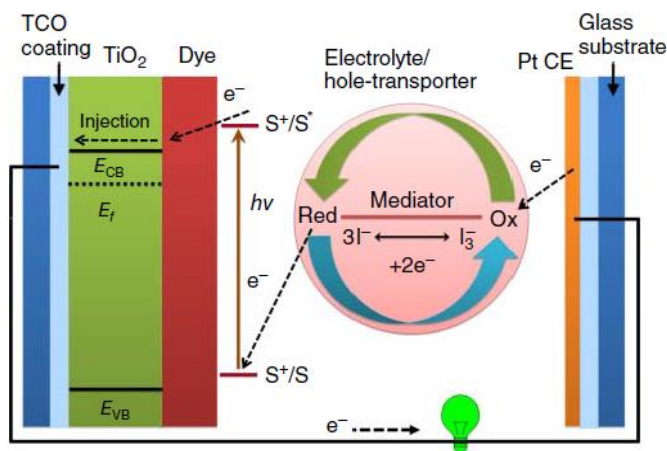
Figure 1.18. *Working principle of a DSSC. (adapted with permission from Ref.* [73]*)*

In 2012, instability issues associated with the liquid electrolyte in perovskite-sensitized solar cells was simply solved by replacing it with the solid 2, 2', 7, 7'-tetrakis (*N, N*-p-dimethoxy-phenylamino)-9, 9'-spirobifluorene (spiro-MeOTAD) hole-transport material (HTM). Park et al.[75] proposed a solid-state mesoscopic PSC architecture (see **Figure 1.19**) based on MAPbI$_3$ nanocrystals, spiro-MeOTAD, and merely 0.6 µm thick mp-TiO$_2$ film, achieving a maximum PCE of 9.7%. Similar PCEs can be obtained from N719-sensitized cells with 10 µm thick mp-TiO$_2$

layers. Comparable efficiency with sub-micron thick TiO_2 film is due to the much higher absorption coefficient of $MAPbI_3$, which is a key factor for fabricating high-efficiency solar cells. In this device configuration, part of the solid-state HTM penetrates into the pores of mp-TiO_2, making direct contact with the perovskite photosensitizer. The remaining spiro-MeOTAD forms a dense capping layer that covers the mp-TiO_2, preventing shunts between the electron transport material (ETM) and the back contact. In contrast to the liquid electrolyte that suffered from low charge carrier mobility, the solid-state spiro-MeOTAD enables holes to move more efficiently. It also allows for a more efficient hole extraction from the perovskite layer, thanks to the better alignment of its HOMO level (-5.22 eV) with the valence band of $MAPbI_3$ (-5.43 eV). In addition to the PCE enhancement, the stability of the device was also dramatically improved.
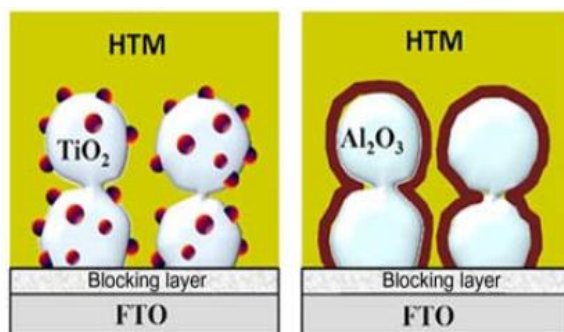
Figure 1.19. *Schematics of solid-state mesoscopic (left) and meso-superstructured (right) PSCs.*

Analogous to the mesoscopic architecture, Snaith's group invented the meso-superstructured configuration by replacing the mp-TiO_2 with the insulating Al_2O_3, as shown in Figure 1.19. This device configuration was very similar to the mesoscopic structure, but the perovskite materials formed a continuous, extremely thin absorber (ETA) layer on the surface of the mesoporous metal oxide. The charge transport mechanism in meso-superstructured PSCs differ from that of the mesoscopic cells in one critical way: unlike the case of mp-TiO_2, injection of electrons from the perovskite layer into Al_2O_3 is energetically unfavorable due to the higher conduction band of Al_2O_3; moreover, Al_2O_3 is electrically insulating. Therefore, in this device architecture, Al_2O_3 merely serves as a mesoporous scaffold for the perovskite absorber. This implies that the perovskite material can transport electrons by itself in the absence of adjacent ETM. In 2012, Lee et al.[55] fabricated meso-superstructured PSCs based on the mixed halide $MAPbI_{3-x}Cl_x$ instead of the pure $MAPbI_3$, and their champion device with the porous Al_2O_3 layer achieved a PCE of

10.9%, significantly higher than the 7.6% PCE exhibited by the best control device with mp-TiO$_2$. These results confirmed the superior optoelectronic properties of the mixed halide perovskite, even without mp-TiO$_2$ assistance.

In principle, increasing the thickness of the absorber layer can improve light absorption and prevent direct shunts between the HTM and the ETM. Accordingly, PSCs rapidly evolved towards improved mesoscopic structures featuring thicker and dense perovskite films. In 2013, Heo et al.[76] reported high-performance mesoscopic PSCs based on MAPbI$_3$, mp-TiO$_2$, polytriarylamine (PTAA) as the HTM, and Au as the back contact. They found that devices with a 600 nm thick mp-TiO$_2$ exhibited the best PCE (12%) due to the formation of a perovskite capping layer (or overlayer) between the mp-TiO$_2$ and the HTM. Currently, this type of mesoscopic n-i-p structure is widely adopted by PV researchers and thus is called the "regular" structure due its popularity (see **Figure 1.20**a). The further progress in the design of regular PSCs was propelled by the advances in film deposition techniques, enabling thicker and uniform perovskite layers to be deposited on a thinner mesoporous scaffold. For instance, Burschka et al.[77] fabricated PSCs with the best PCE of 15% by depositing a smooth perovskite capping layer on top of a 300 nm thick mp-TiO$_2$ layer using a two-step sequential deposition method (see Section 1.2.4). One year later, Im et al.[78] employed the same deposition technique to fabricate PSCs on a thinner (100 nm) mp-TiO$_2$, resulting in the increased thickness of the perovskite capping layer and the improved efficiency (17%) of the devices. To date, the state-of-the-art PSCs with the record PCEs are predominantly fabricated in the regular n-i-p mesoscopic configuration.
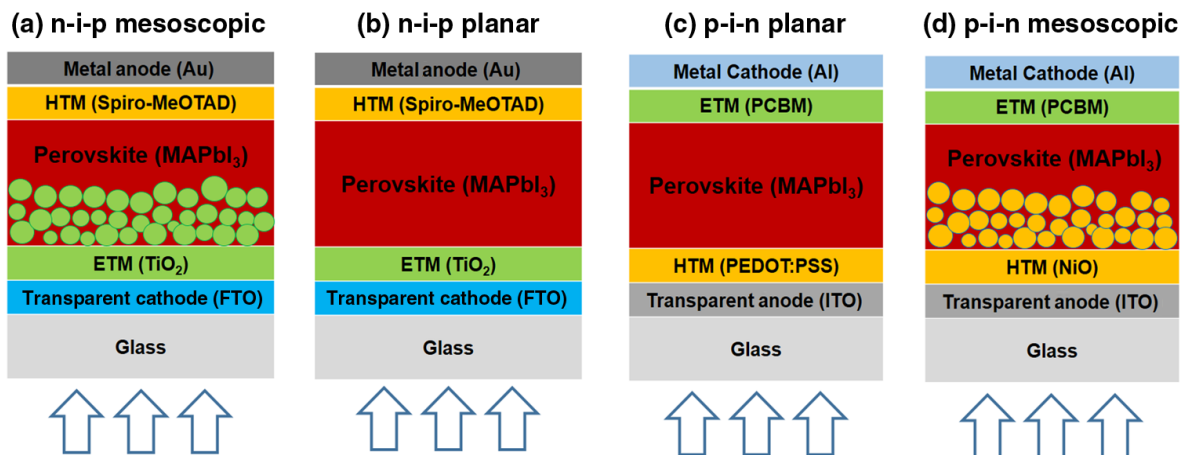
Figure 1.20. *Schematics of the major PSC architectures: regular n-i-p (a) mesoscopic and (b) planar; inverted p-i-n (c) planar and (d) mesoscopic. (adapted with permission from Ref.[72])*

The good electric properties of meso-superstructured PSCs based on insulating Al_2O_3 suggested that perovskite solar cells could be fabricated without the mesoporous TiO_2 scaffold. This led to the development of planar n-i-p heterojunction PSCs. As schematized in Figure 1.20b, planar n-i-p devices are comprised of a TCO bottom electrode, an intrinsic perovskite layer, which serves only as light absorber without mp-TiO_2 assistance, an n-type ETM (typically c-TiO_2), a p-type HTM, and a metal (Ag, Au) top electrode. The absence of a mesoporous metal oxide layer leads to an overall simpler architecture. However, this structure requires a better control of the formation of the perovskite layer and suitable choice of the HTM and ETM materials. While Snaith et al.[55] only achieved a PCE of 1.8% for their preliminary planar n-i-p heterojunction device (likely due to the incomplete surface coverage of the $MAPbI_{3-x}Cl_x$ film), high-performance solar cells were realized in the following years after the advances in film deposition techniques, interface engineering, and defect passivation. The present state-of-the-art planar PSCs prepared by solution deposition techniques yield average PCEs of around 21%.[79] Although the traditional mesoporous PSC generally show higher PCEs compared with the planar architecture, the latter can be fabricated with a low-temperature process (a high-temperature calcination step is generally required to prepare the mesoporous scaffold), a great advantage for applications in the context of flexible optoelectronics. Additionally, planar devices can provide reduced optical transmittance losses, which makes them better suited for semitransparent applications (see Section 1.2.6).

In addition to the regular and planar n-i-p configurations, the planar p-i-n heterojunction architecture derived from OSCs was also adopted by the PSC community as an alternative. This structure is often referred to as the "inverted" structure, since it has an opposite sequence of HTM and ETM than the regular configuration (see Figure 1.20c). The prototype of planar p-i-n PSC was reported by Jeng et al.[80] in 2013 and featured the following structure: glass / indium tin oxide (ITO) as the anode / poly(3,4-ethylenedioxythiophene) polystyrene sulfonate (PEDOT:PSS) as the HTL / $MAPbI_3$ as the light absorber / C_{60} fullerene as the ETL / bathocuproine (BCP) as a buffer layer / Al as the cathode. The best device yielded a PCE of 1.6%, which improved to 3.9% when C_{60} was replaced by phenyl-C_{61}-butyric acid methyl ester ($PC_{61}BM$). In the following years, the performance of planar p-i-n PSCs rapidly progressed towards PCEs exceeding 21%.[81] In addition to the high efficiency, planar p-i-n devices generally offer low-temperature processing and negligible hysteresis behavior. In recent years, high-performance p-i-n mesoscopic PSCs were also

fabricated using suitable oxide HTMs such as NiO$_x$ as the mesoporous scaffold in place of the PEDOT:PSS.[82] The device configuration is schematized in Figure 1.20d.

As previously mentioned, the ETL/HTL helps to provide interfaces for selective charge extraction. Interestingly, working PSCs were also demonstrated even when one charge-transport layer was omitted. Successful removal of the HTL was reported by several groups, thanks to the ambipolar nature and excellent transport properties of perovskite.[83] ETL-free devices with respectable PCEs were also obtained.[84] These structures are promising against conventional PSCs since they require simpler and cheaper fabrication processes. Such an extraordinary versatility in adopting various device configurations confirms the remarkable potential of perovskites in PV applications.

1.2.4. Thin Film Fabrication Approaches

Perovskite Layer Deposition

As the PSC technology progressed, preparation of high-quality perovskite films with controlled morphology and crystallinity became essential for fabricating high-efficiency devices. The morphological evolution and crystallization behavior of perovskite film were found to strongly affect non-radiative recombination dynamics, charge dissociation efficiency, and carrier diffusion lengths in resultant PSCs.[85] The film thickness is also a key parameter: if the film is too thin, then it will not absorb sufficient sunlight; if the film is too thick, the electron and hole diffusion lengths will be shorter than the film thickness and the charges will not be collected efficiently. Furthermore, the presence of pinholes or other inhomogeneities in the perovskite layer will result in direct contact between the p-type and n-type materials, leading to shunting paths and consequently lower PCE. In summary, it is critically important to have a uniform, dense, highly crystalline and pinhole-free perovskite film with high surface coverage and optimized thickness in order to achieve high PCE and reproducibility. Such a high quality can only be obtained through a delicate control of the deposition method, precursor stoichiometry, thermal treatment, solvents/additives used, and surrounding environment.

Various deposition approaches were developed to build up high-quality perovskite films, primarily: one-step or two-step solution processing, thermal vapor deposition, and hybrid vapor-assisted solution process (see **Figure 1.21**).[86] In early works, high-performance PSCs were achieved by vacuum deposition processes. In 2013, Liu et al.[87] successfully applied a dual-source

thermal evaporation technique to deposit the MAPbI$_{3-x}$Cl$_x$ perovskite absorber and obtained a maximum PCE of 15.4%. In their work, organic MAI and inorganic PbCl$_2$ precursor salts were evaporated simultaneously from different sources (co-evaporation) on top of a rotated substrate at 10^{-5} mbar with an as-deposited molar ratio of 4:1, followed by thermal annealing to drive the reaction and crystallization. The perovskite films prepared with this method showed better uniformity and coverage compared to solution-processed films, resulting in higher efficiencies and excellent reproducibility. Other similar methods, such as layer-by-layer sequential vacuum sublimation and chemical vapor deposition, were also reported.[88,89] However, there is a fundamental limitation associated with these techniques: they require high vacuum conditions, which involve high costs and thus mass production is not feasible. To circumvent this issue, Yang et al.[90] demonstrated a hybrid deposition technique, known as vapor-assisted solution process (VASP), which builds up high-quality MAPbI$_3$ film through chemical reaction of solution-processed PbI$_2$ film with MAI vapor. Other hybrid fabrication approaches combining both solution and vapor processes were developed, but due to their higher complexity, they are still not the mainstream for PSC fabrication.
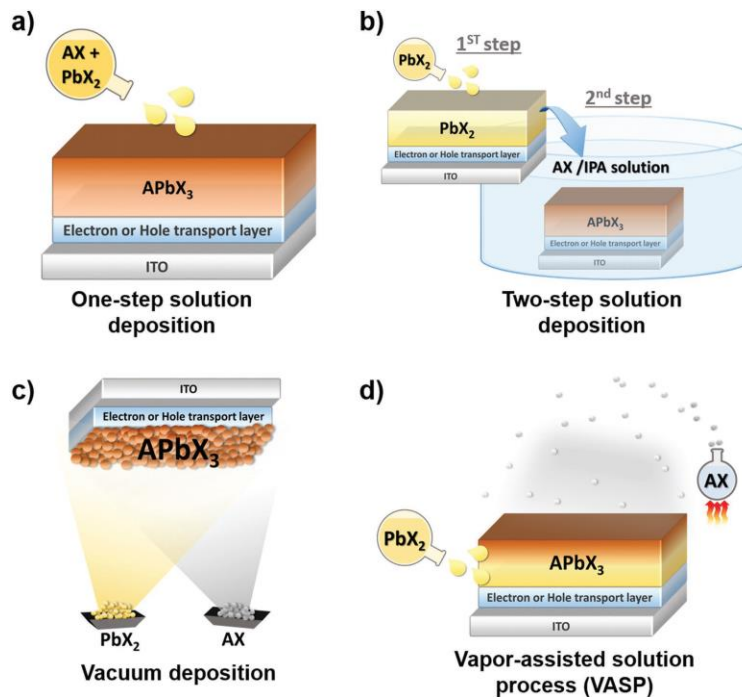
Figure 1.21. *General deposition methods of perovskite film: (a) one-step solution deposition; (b) two-step solution deposition; (c) vacuum deposition; (d) vapor-assisted solution process (VASP). (adapted with permission from Ref.* [91]*)*

Due to the easier operation and low cost, solution processing routes are the most attractive for perovskite film fabrication in the prospect of future PSC commercialization. Various thin-film solution deposition technologies were employed, such as spin-coating, doctor blading, slot-die coating, ink-jet printing, screen printing, and spray-coating (see **Figure 1.22**), most of which are compatible with roll-to-roll (R2R) processing for industrial large-scale production.[92] Among them, the spin-coating technique (which will be described in Chapter 2) is the most widely used in research laboratories to deposit small-area perovskite films. Two primary solution processing routes are available: one-step deposition and two-step (spin-spin or spin-dip) sequential deposition. In the one-step solution process, the precursor solution is typically prepared by dissolving organic halide MAX and metal halide PbX_2 in 1:1 stoichiometric or 3:1 non-stoichiometric molar ratio in a polar aprotic solvent such as N,N-dimethylformamide (DMF), dimethyl sulfoxide (DMSO), γ-butyrolactone (GBL), or a mixture of them. This single solution is deposited in a single step onto the substrate by a suitable technique such as spin-coating. A post-deposition annealing step at temperatures ranging from 80 to 150 °C is then used to convert the precursors into the final $MAPbX_3$ perovskite film. The conversion is typically very obvious to the eye, since it involves a transition from a bright yellow to a dark brown/black color. Generally, both the solution deposition and the thermal annealing step are performed in nitrogen-filled glove boxes with H_2O and O_2 contents less than 5 ppm to prevent perovskite degradation (see Section 1.2.7). The one-step approach was extensively used in the early days of PSCs to fabricate performing $MAPbI_3$ and $MAPbI_{3-x}Cl_x$ films. A great starting point for solution-processed $MAPbI_{3-x}Cl_x$ films was reported by Lee and co-workers,[55] who demonstrated a PCE of 10.9%. In their work, a mixture of MAI and $PbCl_2$ in a molar ratio of 3:1 was dissolved in DMF, and the perovskite film was formed after 30 s of spin-coating and 100 °C thermal annealing. A similar processing route has been selected in this work of thesis for its simplicity, low cost, and effectiveness (see Chapter 2, Section 2).

Despite the ease of processing, one-step precursors usually result in a relatively high density of pinholes in the coated perovskite film, thus reducing the amount of photogenerated charges and increasing the probability of shunts in the device. In order to improve the film coverage, a two-step coating technique was developed by Gratzel's group in 2013,[77] leading to a PCE of more than 15%. They used a process in which a PbI_2 film was first deposited by spin-coating and then dipped into a solution of MAI dissolved in isopropyl alcohol (IPA), followed by thermal annealing at 70-100 °C to drive the inter-diffusion between the two layers and form the $MAPbI_3$ perovskite film.

Alternatives include deposition of an organic halide layer onto the PbI$_2$ by spin-coating or spray coating.[93,94] The perovskite films prepared with the two-step method were found, in general, to show better coverage, improved morphology with larger crystals, and more effective infiltration into the mesoporous scaffolds, leading to higher performances and PCEs comparable to those achieved by vapor deposition. However, because of the challenges associated with perovskite conversion in the sequential process, the one-step deposition method is typically easier to control and less time-consuming.
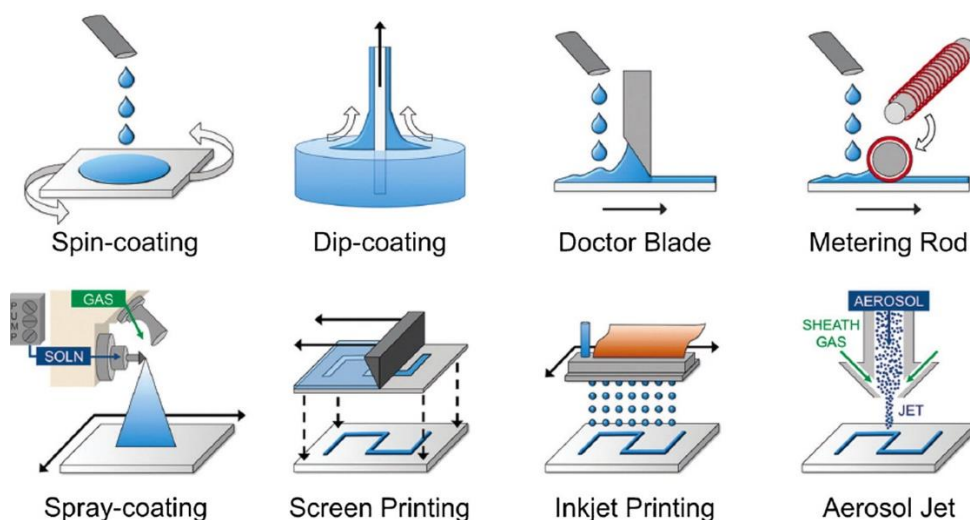
Figure 1.22*. Illustration of various solution deposition technologies employed to fabricate small- and large-area perovskite films. (adapted with permission from Ref.* [92]*)*

Even though all processing conditions (solution concentration, precursor stoichiometry, annealing temperature, atmosphere) have been considered, solution-processed perovskite film quality is often poor, with a high density of pinholes and small grain sizes. To further improve the quality of solution-processed perovskite films, several strategies have been proposed, including: incorporation of more than one organic or inorganic precursors,[95] anti-solvent dripping (ASD) treatment,[96] use of binary solvent systems,[97] hot-casting,[98] multi-step thermal annealing,[99] solvent annealing,[100] various substrate pre-treatments, and use of additives.[101] In particular, additive engineering strategy was extensively adopted to finely tune the crystallization process and minimize the SRH non-radiative recombination losses by increasing grain size, passivating defects and improving charge transport and separation in resultant perovskite films. For instance, Liang et al.[102] proposed the incorporation of 1,8-diiodioctane (DIO) as a solvent additive into the precursor

solution to facilitate nucleation and modulate the kinetics of perovskite crystal growth. Their approach led to the formation of MAPbI$_{3-x}$Cl$_x$ films with more uniform and highly oriented crystals and an improved surface coverage due to the enhanced solubility of PbCl$_2$ (as a result of chelation of Pb^{2+} with DIO). These features resulted in solar cells with reduced non-radiative recombination and enhanced PCEs (from 9.0 to 11.8% with the addition of 1% DIO). Other rationally chosen additives with higher boiling point (to balance dissolution and recrystallization process during the annealing treatment) or stronger Lewis basicity (to promote stronger interaction with Pb^{2+} Lewis acid)[103] than that of DMF have been successfully applied.

Fabrication of Other Components in PSCs

Apart from the perovskite film, the PSC architectures incorporate other components, including charge-transport layers, bottom electrode and top electrode, the deposition of which is also critical for obtaining high-performance devices. Laboratory-scale PSCs typically start with a glass (or plastic) substrate coated with a TCO layer, which will serve as the bottom electrode. TCO-coated substrates are typically prepared by magnetron sputtering and are commercially available from a number of companies. Some researchers have tried to deposit the TCO layer themselves using alternative techniques[104] or to replace it with other transparent conducting materials.[105] The trade-off between transparency and conductivity, as well as the morphology of the bottom electrode will strongly affect the overall performance of the device. The subsequent steps of PSC fabrication involve the sequential deposition of electron-transport, absorber (perovskite), and hole-transport layers. High-quality perovskite films can be obtained by a variety of solution-based, vacuum-based and/or hybrid processes, as described above. Concerning the charge-transport layers, a number of organic and inorganic semiconductor materials have been successfully implemented as ETMs or HTMs in PSCs, as will be discussed in the next sub-section. These materials are typically processable from solution and therefore can be deposited by spin-coating or other simple solution-based techniques.[106] In this regard, it is necessary to use solvents that are orthogonal to the underlying materials, such that the underlayers are not solvated during the deposition of the charge-transport layer. Examples of solvents orthogonal to the perovskite materials are chlorobenzene (CB), dichlorobenzene (DCB), and toluene. Apart from conventional solution processing routes, vacuum-based deposition methods have also been used to deposit organic small molecules and/or metal oxides in order to achieve higher performances, at the expense of manufacturing costs. It is

also important to mention that conventional methods for fabrication of metal oxide compact/mesoporous layers (e.g. c-TiO$_2$ and mp-TiO$_2$) typically involve the deposition of a metal alkoxide precursor solution (e.g. titanium (IV) isopropoxide) by spin-coating or spray-pyrolysis followed by a high-temperature (> 400 °C) sintering step, which increases the costs and hampers the fabrication of flexible devices. Very recently, alternative low-temperature processing routes have been proposed, leading to encouraging efficiencies of up to 18.2%.[107] Finally, the last fabrication step consists in depositing the metal top electrode by thermal evaporation. Thermal evaporation is a mature and scalable technology, but it requires high vacuum (see Chapter 2, Section 1). Recently, alternative vacuum-free methods have been developed and fully solution-processed perovskite solar cells with printed back electrodes (e.g. inkjet-printed silver nanowires) have been successfully fabricated.[108] As in the case of perovskite film, several strategies have been proposed to enhance the quality and performance of each PSC component, including doping strategies, nano-design, and additive engineering, as discussed below.

1.2.5. Interface Engineering for High-Performance PSCs

In addition to the advances in the perovskite film fabrication, the progress in ETMs and HTMs also played an essential role in the evolution of PSCs. The charge-transport layers are directly relevant to the performance of PSCs. The photogenerated electron-hole pairs in the perovskite layer would experience charge separation at the interfaces between the perovskite absorber and the ETL or HTL, as previously described. In this regard, a proper energy level alignment is vital. Suitable band offsets (~0.2 eV) need to be provided for both ETL/perovskite and perovskite/HTL interfaces to ensure efficient charge extraction and minimize carrier recombination. Therefore, the HTM and ETM should be selected with energy levels well matched to the perovskite material. In addition, the work functions of the two electrodes should match the energy levels of the charge-transport layers in order to facilitate charge collection. **Figure 1.23** shows the band energy levels for the most commonly used materials in PSCs. Lastly, the ETM/HTM should ensure efficient and selective charge transport (high electron or hole mobility, as well as adequate bandgap to block the opposite charge carriers) and should be stable enough to prolong the device lifetime.

Engineering the interface between the perovskite layer and the charge-transport layers has become an important method for improving the charge extraction and reducing the gap between theoretical

and practical PCEs. In addition to poor aligned energetics, interface losses may largely result from defects and trap states, which would cause non-radiative recombination and poor stability. The passivation of the defects on the surface of the perovskite film and at the junctions between perovskite and HTL or ETL by chemical doping, compositional engineering, use of additives, and/or insertion of interfacial buffer layers is now regarded as a valid strategy to reduce the interfacial losses and boost the efficiency towards the theoretical SQ limit.[109]
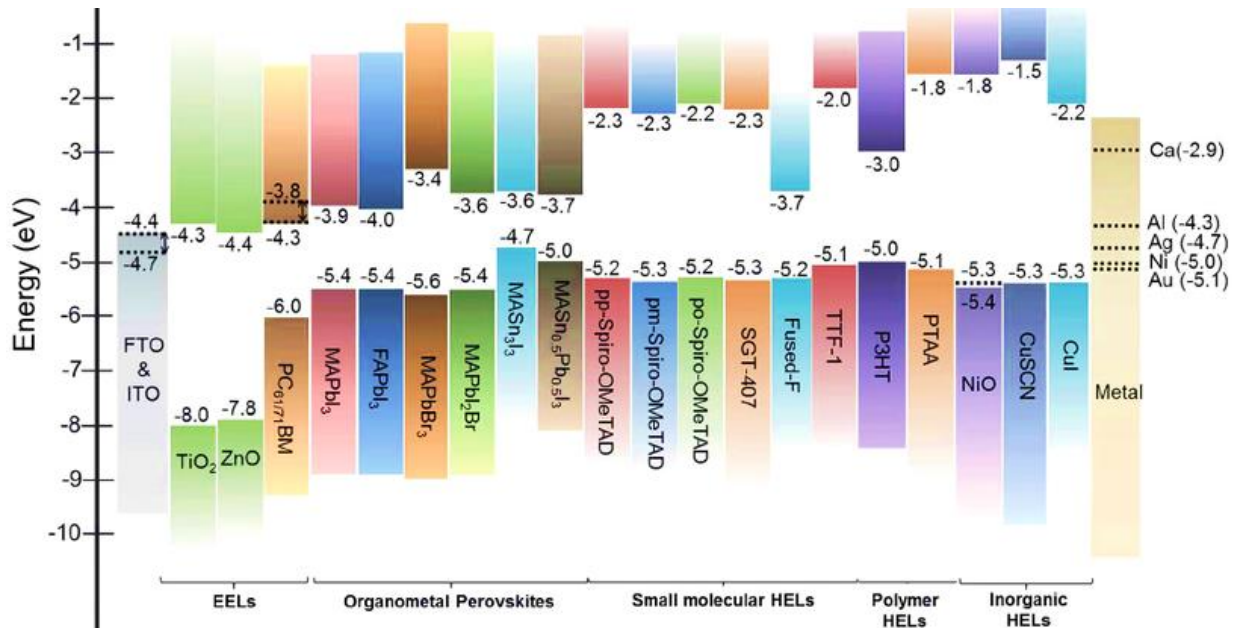
Figure 1.23. *Schematic energy level diagram of the most commonly used materials in PSCs. (adapted with permission from Ref.* [106])

The ETL/Perovskite Interface

In PSCs, the role of ETM is to extract photoexcited electrons and transport them to the electrode while blocking holes from perovskite. Since the early development stages of PSCs, TiO$_2$ has been widely used as the compact and mesoporous ETM in the conventional n-i-p device configuration due to its excellent electron transport properties, well-matched energy levels, and suitable bandgap. However, trap states and defects present at TiO$_2$ surfaces have generally provided non-radiative recombination pathways at the ETL/perovskite interface, reducing the voltage output and the electron injection rate.[110] Various attempts have been made to passivate the TiO$_2$ surface, for example via insertion of self-assembled monolayers (SAMs) or through doping strategies. In

particular, it has been demonstrated that titania doping, either by replacing the Ti^{4+} cation or the O^{2-} anion with other metal (Y, Nb, Li, Mg, Al, Ru) or non-metal (F, N) ions, could be a promising way to enhance the electronic properties of TiO_2 (see Chapter 5). For example, Zhang et al.[111] synthesized N-doped titania nanorod arrays with hydrothermal method and used them as the ETL in mesoporous n-i-p PSCs. Their best device yielded a PCE of 11.1%, which was 14.7% higher than that of devices based on undoped TiO_2. The efficiency enhancement was ascribed to faster electron transfer and lower resistance in the device based on N-doped TiO_2.

Besides TiO_2, other materials such as ZnO, SnO_2, CdSe, and CdS have been used as efficient ETMs in n-i-p PSCs.[112] On the other hand, fullerene derivatives such as $PCB_{61}M$ and $PCB_{71}M$ are among the commonly used organic ETMs in the p-i-n device configuration. These materials can be processed at low temperatures, enabling the potential for roll-to-roll manufacturing on flexible substrates. Also, combinations of organic-inorganic ETLs have been reported in inverted devices.

The Perovskite/HTL Interface

HTMs are also critical for a good PV performance. Their function is to block electrons and transport holes. PSCs benefited from a wide selection of HTMs that have been continually investigated during the last years, including inorganic crystals, organic small molecules and semiconducting polymers. The chemical structures of commonly employed organic HTMs are illustrated in **Figure 1.24**. Spiro-MeOTAD is the most used organic HTM in regular PSCs, while PEDOT:PSS is extensively employed in inverted solar cell structures due to its excellent transparency, work function, and conductivity. Spiro-MeOTAD is considered as the standard HTM for n-i-p PSCs as it leads to devices with record efficiencies (> 20% PCEs) thanks to its special physical and chemical characteristics, well-matched HOMO level (see Figure 1.23) and remarkable electron-blocking property. However, there are many issues associated with its production on a commercial scale such as its multi-step synthesis, laborious purification steps, and high cost. Moreover, it exhibits a quite low hole mobility ($- 4 \times 10^{-5}$ cm^2 V^{-1} s^{-1}), mainly ascribed to the lack of molecular ordering in the film, which limits the performance of pure solution-processed spiro-MeOTAD films. Several p-type dopants and additives have been reported to improve the electrical properties of spiro-MeOTAD, but their use is generally associated with stability issues, especially after exposure to humidity. For example, it has been reported that the commonly used lithium bis(trifluoromethanesulfonyl)imide (Li-TFSI) and 4-*tert*-butylpyridine

(TBP) dopants tend to accelerate the degradation of PSCs due to their hygroscopic nature (see Section 1.2.7).[113]
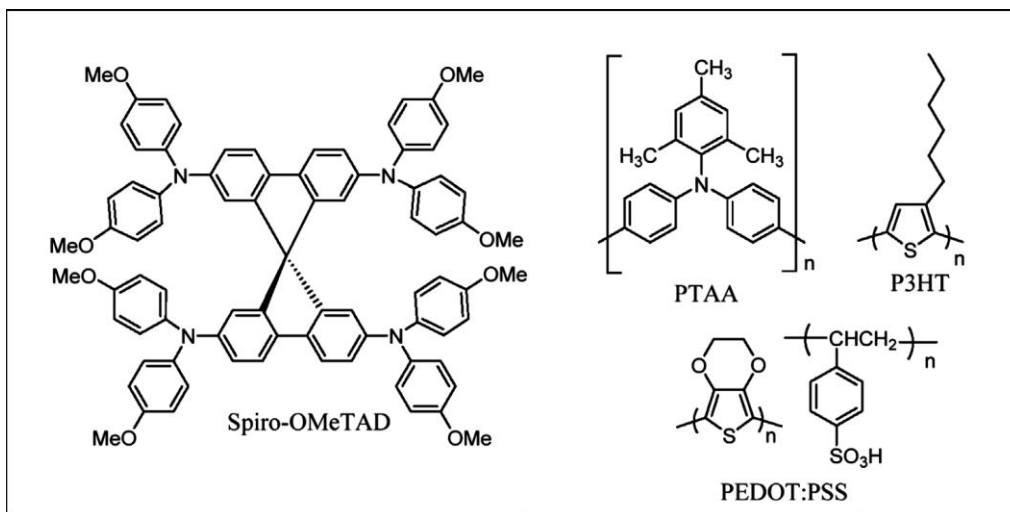
Figure 1.24. Chemical structure of organic HTMs commonly used in PSCs.

Several other HTMs such as PTAA,[76] poly(3-hexylthiophene-2,5-diyl) (P3HT),[114] and triazatruxene derivatives[115] have been investigated as alternatives to spiro-MeOTAD. Among them, PTAA and triazatruxene derivatives showed competitive PCEs and improved stability. On the other hand, P3HT-based devices initially yielded lower efficiencies of around 12-16% due to additional non-radiative recombination at the perovskite/P3HT interface.[71] Very recently, Jung et al.[116] have demonstrated P3HT-based PSCs yielding PCEs as high as 22.7% by introducing a wide-bandgap halide (WBH) layer prior to P3HT deposition. During the last years, tremendous efforts have been dedicated to develop novel dopant-free HTLs in order to enhance the device stability (see Chapter 5). For instance, a dopant-free HTM of IDF-SFXPh, which is a derivative of 6,12-dihydroindeno[1,2-b]fluorine (IDF), has been used by Liu et al.[117] to achieve efficient (17.6% PCE) and stable devices. Another possible solution to the high cost and instability of the standard organic HTMs is employing cost-effective and more stable inorganic HTMs, such as NiO_x, CuO, CuSCN, and Cu_2O, which have recently led to respectable PCEs.[118] In addition to the investigation of different HTMs, several interface engineering strategies have been developed to achieve effective passivation of hole trapping states located at the perovskite/HTM interface. For example, Abate et al.[119] introduced iodopentafluorobenzene (IPFB) at the interface through supramolecular

halogen bonding in order to saturate the under-coordinated halide anions on the surface of perovskite, and their approach led to fast and efficient hole extraction. Noel et al.[120] demonstrated that the under-coordinated Pb atoms can be passivated via treatment of the perovskite surface with Lewis bases such as thiophene and pyridine, resulting in reduced non-radiative recombination.

The Electrode Interfaces

Interface engineering across the electrodes has also attracted considerable attention. Introducing proper interfacial layers to modify the electrode/ETL and HTL/electrode interfaces is an important approach to improve PSCs performance. FTO (WF = 4.4 eV) and ITO (WF = 4.7 eV) are the most commonly used materials as transparent bottom electrodes. To engineer the interface between the TCO layer and the ETL or HTL, highly transparent and conductive interlayers are required. For instance, Snaith et al.[121] proposed graphene as interfacial material between FTO and TiO_2. The optoelectronic properties and band position of graphene are well suited for electron cascade, leading to enhanced PV performance. Regarding the ITO-based devices, the intermediate work function of this material makes it possible for ITO to be used both in regular and inverted structures to collect either electrons or holes (see Figure 1.23). In the inverted architecture, it is generally coated with a PEDOT:PSS layer, which will serve as the HTL. In the normal structure, a compact TiO_2 layer is generally deposited on top of ITO to prevent direct contact between the ITO and HTM. A Schottky barrier exists at the ITO/TiO_2 junction, which may lead to detrimental effects on the device performance. To circumvent this issue, Yang et al.[122] introduced an ultrathin (highly transparent) polyethyleneimine ethoxylated (PEIE) layer between the ITO and the TiO_2 to tune the energy level alignment. An interfacial dipole was found to contribute to the change in WF, which decreased to 4.0 eV, as a result of an electron transfer from the amine-containing molecules to the electrode surface. Great efforts were also devoted to the optimization of the charge-transport layer/metal top electrode interface. In inverted PSCs, bathocuproine (BCP) is one of the well-known interfacial materials used between fullerene derivatives and metal electrodes.[123] Rhodamine 101,[124] 4,7-diphenyl-1,10-phenanthroline (Bphen),[125] and metal acetylacetonates[126] were also proved to work well as electrode interlayers. In numerous studies, the hole extraction efficiency at the HTL/metal electrode interface was enhanced by inserting a thin molybdenum (VI) suboxide (MoO_x) buffer layer.[127] Thermally evaporated MoO_x films were found to have WF at 5.4 eV,[128] which aligns well with the HOMO level of the spiro-MeOTAD. Despite the strong n-type nature

and very low-lying valence band, MoO_x can extract holes from the adjacent p-type semiconductor through oxygen-vacancy-induced gap states close to its Fermi level, leading to a better contact.

1.2.6. Semitransparent PSCs: Design and Applications

Among others, one beauty of PSCs that outshines conventional PV technologies is their possibility to be made semitransparent. Recently, semitransparent (ST) solar cells have opened up new perspectives for energy conversion and sustainable development thanks to their great potential in a variety of applications, including building-integrated photovoltaics (BIPVs), solar-powered automotive/wearable electronics, and tandem multijunction solar cells.[129–131] Their integration into buildings as power-generating solar windows, façades, or other aesthetic architectural elements constitutes one of the most intriguing perspectives (see **Figure 1.25**). In view of these applications, the opaque and bulky nature of silicon-based panels has led to a greater focus on emerging thin-film solar cells that can be made truly semitransparent, such as DSSCs, OSCs, and PSCs.[132] Among them, semitransparent perovskite solar cells (ST-PSCs) have rapidly taken the lead owing to their superior performances and easy processing.

The state-of-the-art PSCs are usually nontransparent due to the use of opaque, highly reflective metal counter electrodes (typically 100 nm thick Au, Ag, or Al) and the strong absorption of the ~400 nm thick perovskite film. To enable practical ST applications, specific transparency requirements must be fulfilled. For example, an average visible transmittance (AVT) of at least 25% is generally taken as a benchmark for solar windows.[133] To realize the desired semitransparency, ST-PSCs need to employ transparent top electrodes (TTEs) and thinner or opportunely engineered perovskite layers which can only absorb a part of incident light. Such inherent trade-off between absorbed light and transmitted light is the main reason for the lower efficiencies typically observed in ST-PSCs compared to their opaque counterparts. Investigations on ST-PSCs began with the milestone work by Eperon et al.[134] in 2014, who fabricated a neutral-colored ST-PSC showing a PCE of 3.5% and an AVT of 30%. The authors made use of incomplete surface coverage and dewetting of spin-coated $MAPbI_{3-x}Cl_x$ films to form micro-structured arrays of perovskite "islands". The perovskite islands were thick enough to absorb all visible light, whereas the "dewet" regions were visibly transparent. As the TTE, they simply utilized a thin (10 nm), thermally evaporated Au film. Due to the discontinuous nature of the perovskite film,

shunting paths via direct contact between spiro-OMeTAD and c-TiO$_2$ led to a quite low voltage output. In the same year, Roldàn-Carmona et al.[135] proposed an alternative device layout, where the thickness of continuous perovskite films was precisely controlled by thermal evaporation and an additional 100 nm thick LiF layer was deposited on top of the Au electrode as an antireflective (AR) coating. As a result, PCEs as high as 6.4% with AVT close to 29% were achieved.

Figure 1.25. *Dye solar cell façade at SwissTech convention center at EPFL, by Solaronix.*

Another effective way to provide the semitransparency is to simply thin the solution-processed perovskite film and opportunely engineer the electrode for maximum optical transmittance. This concept is schematized in **Figure 1.26** for a typical n-i-p planar architecture. The key point is the selection of an appropriate TTE with high transparency, high electrical conductivity, robust chemical stability, low cost, and proper work function. Moreover, the TTE should be processable without damaging the underlying temperature- and solvent-sensitive layers in the device. To date, transparent conductive oxides like ITO and FTO dominate the current use of transparent electrodes in the optoelectronic industry. Unfortunately, TCOs can hardly be employed as top electrodes because they generally need high-energy deposition techniques (e.g. magnetron sputtering), which may damage the underlying absorber and charge-transport layers.[136] Moreover, their increasing prices and poor mechanical properties are undesirable for applications in modern and flexible optoelectronic devices. For these reasons, there has been a growing research interest in alternative materials to serve as TTEs, such as ultrathin metal (UTM) films,[137] multilayer dielectric/metal/dielectric (DMD) structures,[138–140] metal nanowires,[141] conductive polymers,[142] graphene,[143] and carbon nanotubes.[144] Recently, the development of DMD structures has offered

a compelling approach for the pursuit of high-performance ST-PSCs. Such composite electrodes are made of an optically thin metal film (< 12nm) embedded between two dielectric materials with high refractive indexes. They exhibit ideal characteristics to serve as TTEs, such as high electrical conductivity, enhanced transparency compared with UTM films, low-temperature and solvent-free deposition, mechanical flexibility, and tunable optoelectronic properties. As an example, Della Gaspera et al.[138] applied a $MoO_x/Au/MoO_x$ DMD top electrode to the fabrication of regular ST-PSCs in 2015, and their devices showed PCEs of 5.3-13.6% with the corresponding AVTs of 31-7%.
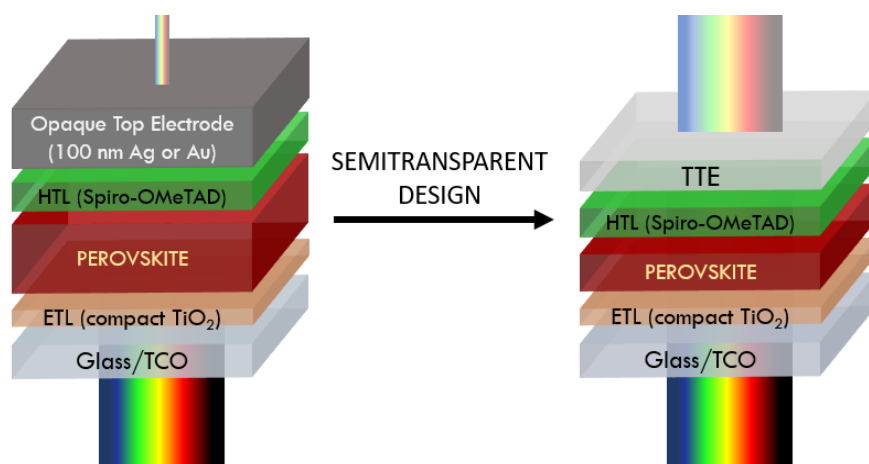
Figure 1.26. *Schematic device design of a regular planar ST-PSCs.*

Another way of fabricating ST-PSCs consists in using a wide bandgap perovskite, of which there are many known examples (see Section 1.2.1). This strategy proved to be particularly beneficial for tandem applications. Tandem or multijunction solar cells make use of two or more absorber layers with different bandgaps to boost PCEs over the limits imposed by the SQ theory.[145] The working principle of tandem PV devices is based on the combination/stacking of different sub-cells, each of them able to absorb a different portion of the solar spectrum, which allows to minimize energy losses and reach higher PCEs (see **Figure 1.27**). In a standard double-junction configuration, the highest-energy photons are captured by the material with the largest bandgap in the front cell, whereas the lower-energy photons are allowed to pass through the front cell and reach the smaller-bandgap semiconductor rear cell, enabling a more efficient use of photon energy. To date, high-efficiency tandem solar cells have been demonstrated by combining conventional

PV technologies (c-Si, CIGS, and CdTe solar cells) with perovskite solar cells of different bandgaps into 2-terminal (2T) or 4-terminal (4T) configurations.[131,139] In particular, perovskite/c-Si tandem solar cells have recently achieved an outstanding record PCE of 28%, certified by the National Renewable Energy Agency (NREL).[33] Also, all-perovskite tandem photovoltaics are attracting great attention since they could deliver lower fabrications costs while still enabling an efficient harvest of solar energy. Recently, Eperon et al.[146] have achieved a breakthrough on perovskite-perovskite tandem photovoltaics using perovskite materials with ideally matched bandgaps, demonstrating efficiencies as high as 17% for 2-T devices and 20.3% for 4-T devices.
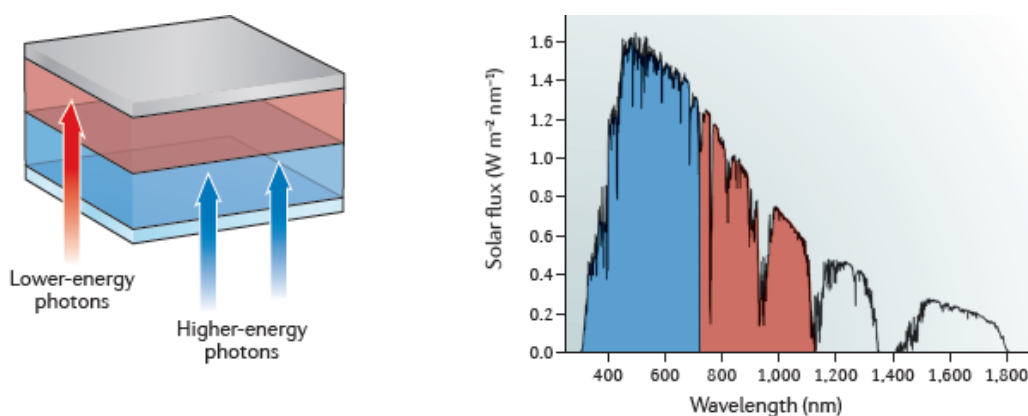
Figure 1.27. *Working principle of a tandem solar cell. The front cell absorbs the higher-energy photons only, while the lower-energy photons of the solar spectrum can reach the rear cell, where they can be absorbed and converted. (adapted with permission from Ref.[145])*

1.2.7. Current Issues and Future Outlook

Despite the astonishing progresses achieved in the last years in terms of power conversion efficiency, the PSC technology is still facing some challenging issues with regard to the operation, composition and stability of devices that need to be addressed before commercialization. Some of these challenges are discussed point-by-point here below.

Stability of materials

The biggest obstacle to the large-scale commercialization of PSCs is their rapid performance degradation, especially when stored under ambient conditions.[147,148] The intrinsic instability of hybrid halide perovskites associated with their ionic nature, as well as their degradation induced

by the permeation of oxygen and moisture from the atmosphere are the major reasons. A proposed degradation mechanism induced by humidity and oxygen is the following:

a) $CH_3NH_3PbI_3$ (s) $\leftrightarrow$ PbI_2 (s) + CH_3NH_3I (aq)

b) CH_3NH_3I (aq) $\leftrightarrow$ CH_3NH_2 (aq) + HI (aq)

c)   4HI (aq) + O_2 (g) $\leftrightarrow$ $2I_2$ (s) + $2H_2O$ (l)
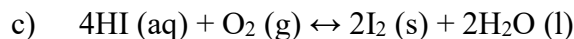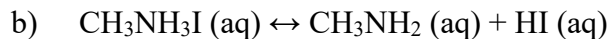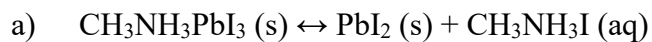
According to this mechanism, the highly hygroscopic MA^+ cation could be removed from the perovskite lattice upon contact with moisture and then could combine with iodine to reform aqueous MAI and solid PbI_2 (step a). Next, the MAI may decompose into aqueous methylamine and HI (step b), followed by degradation of HI by a redox reaction with O_2 (step c), producing H_2O and I_2. The Gibbs free energy associated with the third step is largely negative, indicating that this reaction is highly favorable and highlighting the relevance of this step in the decomposition process. Other proposed mechanisms involve the formation of hydrated products ($MAPbI_3 \cdot H_2O$) or photoinduced reactive peroxide or superoxide species. Due to such side effects from oxygen and moisture, the perovskite materials are typically processed inside the glove box. However, some studies curiously showed that proper humidity levels could be helpful on enlarging perovskite crystal sizes towards higher performance and improved stability.[149]

In addition, the high temperature would also lead to perovskite decomposition. Several groups reported the low thermal conductivity of $MAPbI_3$.[150] Moreover, the decomposition of $MAPbX_3$ (X=Cl, Br, I) was observed starting from 130 °C, confirmed by the emergence of new peaks in the XRD patterns.[151] Therefore, these materials would most likely suffer a PCE degradation during the long-term device operation due to accumulated heat inside the film. The degradation of perovskites may also derive from the interaction with ultraviolet (UV) light at the TiO_2 layer.[152] Assisted by UV light, TiO_2 could interact with I^- and form I_2 in the same way as it occurs in typical DSSCs. Therefore, it could destroy the perovskite crystal structure with detrimental effects on the device performance. Applying a proper UV-filter was suggested by several groups.[153]

The stability issue of the perovskite solar cells may not only come from the intrinsic instability of perovskites, but also from adjacent materials and interfaces. In fact, PSCs are composed of several layers with different compositions, and the possible corrosion or formation of complexes induced by chemical interactions must also be taken into account. As previously mentioned, common HTL additives such as LiTFSI and TBP can facilitate device degradation by interacting with moisture

(LiTFSI is highly hygroscopic) or forming complexes with PbI$_2$ (TBP can dissolve PbI$_2$, forming PbI$_2$·TBP complexes).[113] Recently, Kato et al.[154] detected iodine from the perovskite at the Ag electrode after aging in the dark under inert atmosphere and proposed a mechanism for AgI formation. They also observed that the corrosion was even more severe when the devices were aged under humidity, thermal stressing, and light soaking. Thus, a careful choice of materials and interfaces is necessary to prolong device lifetime. Moreover, it was found that the defects and trap states from perovskite grain boundaries (GBs) and at the interfaces also play a critical role in decomposition of PSCs, accelerating the aforementioned degradation mechanisms.[155] Therefore, suppressing trap-assisted non-radiative recombination and reducing defect density could be beneficial not only in terms of power conversion efficiency, as previously discussed, but also for long-term device stability.

Toxicity issues

The most used metal cation in PSCs is lead, which has proven to be the superior constituent, both in terms of performance and stability. However, the environmental impact of its usage due to its toxicity is becoming an important issue for commercial PSC development. Even though it has been demonstrated that the possible contamination from PSCs would be relatively insignificant compared to other lead pollutions,[156] and that using lead from daily waste can produce solar cells with the same efficiency as those fabricated using pristine material purchased from commercial suppliers,[157] studies on lead-free PSCs cannot be neglected. In recent years, substantial research efforts have been focused on considering the replacement of toxic Pb^{2+} with other more environmentally friendly metal cations, without compromising on efficiency and stability.[158] The first material identified as promising for this substitution was Sn. As previously mentioned, a partial substitution of lead by tin was reported by Zuo et al., who demonstrated a PCE of 10.1%.[64] However, the complete substitution of lead is difficult because tin-based perovskites are extremely reactive, with Sn^{2+} oxidation state being chemically unstable and easily oxidizing to Sn^{4+}. Another intensively studied candidate is bismuth, which can form a stable (MA)$_3$Bi$_3$I$_9$ perovskite material.[159] This material shows several advantages, such as non-toxicity, ambient stability, and low-temperature solution processability. Unfortunately, (MA)$_3$Bi$_3$I$_9$-based devices could only be able to reach PCEs of less than 1%. Other types of lead-free perovskites such as MAGeI$_3$, MASrI$_3$, and MACaI$_3$, have also been reported, although with poor results.[160–162] It is discouraging to note

that the performances achieved until now by completely lead-free perovskite devices are very low, with a maximum PCE of 6.22% yielded by $FASnI_3$-based devices.[163] Therefore, investigation of new lead-free perovskite solar cells and development of new strategies to enhance their PV performance still remain open challenges.

Hysteresis Effects

Another challenging issue of PSCs is the presence of hysteresis in the current-voltage (I-V) output, consisting in the irreproducibility of the I-V curve depending on the voltage scan direction and speed. First reported by Dualeh et al. in 2014,[164] the hysteretic behavior generally manifests itself in an improvement in apparent device performance under reverse scan (forward bias to reverse bias) as compared to forward scan (reverse bias to forward bias) and is observed most at moderate scan speeds. Understanding the cause of hysteresis is essential to avoid ambiguities in the PSCs characterization and to improve the stability of the device.

A number of mechanisms have been proposed to explain the observed hysteresis in perovskite solar cells. The three most discussed processes are: (1) charge trapping and detrapping dynamics resulting from a large defect density in the perovskite film and/or at the interfaces; (2) ferroelectric polarization of the perovskite material induced by the applied electric field; (3) ion migration for which excess ions could accumulate at interfaces and modify the built-in potential.[165] In support of the first mechanism, it has been demonstrated by several groups that perovskite crystals with larger grain sizes show less prominent hysteresis effects due to the reduced amount of grain boundaries.[166] At present, there is no single universally accepted mechanism behind hysteresis, and it is of course possible that the aforementioned processes occur concurrently. The lack of a complete understanding demands further investigation in the future.

Manufacturing Challenges

To fabricate marketable large-area PSC devices, researchers also need to mitigate the costs associated with manufacturing and to scale up the constituent layers while maintaining high efficiency and reproducibility. As widely discussed above, solution processability is one of the key advantages of perovskite solar cells over traditional PV devices, as this property allows for the use of low-cost solution-based fabrication techniques. However, some of the PSC components, such as spiro-MeOTAD, are very expensive, at least at the laboratory scale. Most of the organic HTMs

used in PSCs are synthesized by coupling reaction using palladium, which is an expensive metal, as a catalyst, and this consequently increases the manufacturing costs. Therefore, alternative materials or protocols should be developed in the prospect of future commercialization. Similarly, the fabrication costs of ETMs and perovskite materials should be reduced, for example by replacing the conventional sintering procedure of TiO_2 with other low-temperature processes.

In addition to cost, the other important challenge in PSC manufacturing is the scaling up. The spin-coating technique has achieved great success in fabricating small-area PSCs, leading to the highest efficiencies reported to date. However, the deposition of uniform and high-quality perovskite films over large areas using spin-coating is very challenging. The same issue is valid for the other layers. Several scalable techniques such as slot-die coating, doctor blading, and inkjet printing have been explored as an alternative, and fully-printable PSCs yielding respectable PCEs have been demonstrated. In addition to the uniformity and quality of the perovskite and charge-transport layers, the conductivity of the TCO layer is vital to maintain high performances, and this could be an issue over large-area substrates that needs to be addressed.[91]

Future Outlook

Efficiency, cost and stability are the three main pillars for starting an effective commercialization of a given PV technology. Despite the high efficiencies and low-cost fabrication protocols of PSCs, the poor stability of the hybrid perovskite under ambient conditions is still a major issue that has to be addressed. A substantial research emphasis is being placed on developing new strategies to avoid both intrinsic and extrinsic degradation mechanisms, and considerable advances are being achieved through rational compositional engineering, defect passivation, and hermetic encapsulation solutions. The PV community is also aware about the toxicity associated with the lead content in PSCs. Alternative lead-free perovskite absorbers have been extensively explored, but the corresponding devices generally suffer from poor performances. Anyway, it has been calculated that the possible contamination from lead-based PSCs would be relatively insignificant compared to the amount of lead released by other human activities, for example though a coal burning power station. In addition, it has been demonstrated that high-efficiency PSCs can also be fabricated using lead from recycled lead-acid batteries or isolating PbI_2 from previous devices, an encouraging result from a recycling and lifecycle perspective. Concerning the anomalous hysteresis observed for hybrid perovskites, it has been proposed that the grain size of perovskite

crystals should be larger while the defects located at the interfaces should be passivated in order to reduce the charge trapping/detrapping dynamics behind this phenomenon. Other hypothesized mechanisms, such as ion migration and ferroelectric polarization, are still under scrutiny. The complete elimination of hysteresis would enable a more correct characterization of the devices and the fabrication of long-term stable PSCs. Lastly, there is also a substantial progress in fabricating large-area PSC devices through scalable solution-based fabrication techniques, which is of interest for the practical applications.

In summary, the current limitations impeding the commercialization of PSCs are now well known and tackled by numerous research groups around the world. Recent advances and perspectives are encouraging, especially in terms of efficiency/cost ratio. Very recently, Song et al.[167] reported a comprehensive study evaluating the direct manufacturing cost of a perovskite module. Based on their results, the PSC technology seems to have all the trumps to emerge as a cost leader in the future energy PV market.

1.3. Aim and Outline of the Thesis

The present Ph.D. thesis is a report of over three years of work carried out at the Department of Physics and Chemistry of the University of Palermo on the topic of hybrid organic-inorganic PSCs. More specifically, the aim of the work was to develop new strategies for the fabrication of cost-effective, semitransparent PSCs in the prospect of BIPV and tandem applications, as well as to explore alternative charge-transport materials, solvent additives and interface engineering approaches towards effective defect passivation and performance enhancement, both in terms of efficiency and stability. The experimental methods and measurement setups used in this thesis to fabricate and characterize the solar cells are detailed in **Chapter 2**.

In **Chapter 3**, a novel DMD multilayer transparent electrode with high transparency and conductivity based on non-precious copper and molybdenum suboxide is developed and successfully incorporated as the hole-collecting top electrode in planar n-i-p ST-PSCs yielding PCEs as high as 12.5%. A fine tuning of the perovskite layer thickness is also carried out to further enhance the device transparency up to a maximum AVT approaching the benchmark of 25% for solar window applications. This work is believed to be the first example of the fabrication of planar n-i-p ST-PSCs using a Cu-based DMD top electrode and hence constitutes an important step forward in the replacement of the conventional Au- and Ag-based DMD structures, which are generally much more expensive (Au) and/or less stable (Ag).

Chapter 4 presents the improvements achieved in perovskite layer morphology and crystallinity by using α-terpineol as a solvent additive in the precursor solution. The impact of these improvements on the PSC performance and stability is thoroughly evaluated. In particular, a significant PCE enhancement from 13.9% to 15.4%, as well as an improved stability under inert conditions are demonstrated and justified in terms of reduced non-radiative recombination.

Lastly, **Chapter 5** focuses on the role of selective charge-transport materials on the device performance. Specifically, the first part of this chapter explores the potential of three different copolymers as alternative dopant-free HTLs in planar n-i-p PSCs. Improved PCEs are demonstrated for one of the three copolymers compared to pure solution-processed spiro-MeOTAD and P3HT films. In the second part of Chapter 5, doped TiO_2 nanoparticles as well as one-dimensional (1D) TiO_2 nanorod arrays are successfully prepared in the form of thin films. Their potential as mesoporous scaffolds in regular mesoscopic PSCs is investigated and discussed.

1.4. References

(1) National Aeronautics and Space Administration (NASA). Scientific Consensus: Earth's Climate is Warming. https://climate.nasa.gov/scientific-consensus/ (accessed Sep 17, 2019).

(2) Intergovernmental Panel on Climate Change (IPCC). *AR5 Climate Change 2014: Impacts, Adaptation, and Vulnerability*; Cambridge University Press: New York, 2014.

(3) Intergovernmental Panel on Climate Change (IPCC). *AR5 Climate Change 2013: The Physical Science Basis*; Cambridge University Press: Cambridge, United Kingdom and New York, 2013.

(4) Intergovernmental Panel on Climate Change (IPCC). *Global Warming of 1.5°C*; Geneva, 2018.

(5) National Aeronautics and Space Administration (NASA). The Effects of Climate Change. https://climate.nasa.gov/effects/ (accessed Sep 17, 2019).

(6) Intergovernmental Panel on Climate Change (IPCC). *AR5 Climate Change 2014: Mitigation of Climate Change*; Cambridge University Press: New York, 2014.

(7) NOAA Earth System Research Laboratory. Trends in Atmospheric Carbon Dioxide. https://www.esrl.noaa.gov/gmd/ccgg/trends/ (accessed Sep 17, 2019).

(8) International Energy Agency (IEA). *CO_2 Emissions from Fuel Combustion 2018*; 2018.

(9) UNFCC. Report of the Conference of the Parties on its Twenty-First Session FCCC/CP/2015/10/Add.1. http://unfccc.int/resource/docs/2015/cop21/eng/10a01.pdf.

(10) Armaroli, N.; Balzani, V. The Future of Energy Supply: Challenges and Opportunities. *Angew. Chem. Int. Ed.* **2007**, *46* (1–2), 52–66. https://doi.org/10.1002/anie.200602373.

(11) Capellán-Pérez, I.; Mediavilla, M.; de Castro, C.; Carpintero, Ó.; Miguel, L. J. Fossil Fuel Depletion and Socio-Economic Scenarios: An Integrated Approach. *Energy* **2014**, *77*, 641–666. https://doi.org/10.1016/j.energy.2014.09.063.

(12) Enerdata. World Energy Consumption Statistics. https://yearbook.enerdata.net/total-energy/world-consumption-statistics.html (accessed Sep 18, 2019).

(13) World Commission on Environment and Development (WCED). *The Brundtland Report: Our Common Future*; Oxford University Press: Oxford and New York, 1987.

(14) United Nations Department of Economic and Social Affairs (UN DESA). Sustainable Development Goal 7: Ensure Access to Affordable, Reliable, Sustainable and Modern Energy for All. https://sustainabledevelopment.un.org/sdg7 (accessed Sep 18, 2019).

(15) Nerini, F. F.; Tomei, J.; To, L. S.; Bisaga, I.; Parikh, P.; Black, M.; Borrion, A.; Spataru, C.; Broto, V. C.; Anandarajah, G.; et al. Mapping Synergies and Trade-Offs between Energy and the Sustainable Development Goals. *Nat. Energy* **2018**, *3* (1), 10–15. https://doi.org/10.1038/s41560-017-0036-5.

(16) Gielen, D.; Boshell, F.; Saygin, D.; Bazilian, M. D.; Wagner, N.; Gorini, R. The Role of Renewable Energy in the Global Energy Transformation. *Energy Strategy Rev.* **2019**, *24*, 38–50. https://doi.org/10.1016/j.esr.2019.01.006.

(17) REN21. *Renewables 2018 Global Status Report*; 2018.

(18) International Energy Agency (IEA). Renewables 2018: Market Analysis and Forecast from 2018 to 2023. https://www.iea.org/renewables2018/ (accessed Sep 18, 2019).

(19) Perez, R. and M. Perez. A Fundamental Look at Energy Reserves for the Planet. *Int. Energy Agency SHC Programme Sol. Update* **2009**, *50*, 2–3.

(20) Kabir, E.; Kumar, P.; Kumar, S.; Adelodun, A. A.; Kim, K.-H. Solar Energy: Potential and Future Prospects. *Renew. Sustain. Energy Rev.* **2018**, *82*, 894–900. https://doi.org/10.1016/j.rser.2017.09.094.

(21) Yinghao Chu; Peter Meisen. *Review and Comparison of Different Solar Energy Technologies*; Global Energy Network Institute (GENI): San Diego, 2011.

(22) Kurokawa, K.; Komoto, K.; Vleuten, P. V. D. *Energy from the Desert: Practical Proposals for Very Large Scale Photovoltaic Systems*; Earthscan, 2007.

(23) Hersch, P.; Zweibel, K. *Basic Photovoltaic Principles and Methods*; Technical Information Office, Solar Energy Research Institute, 1982.

(24) Shockley, W. The Theory of p-n Junctions in Semiconductors and p-n Junction Transistors. *Bell Syst. Tech. J.* **1949**, *28* (3), 435–489. https://doi.org/10.1002/j.1538-7305.1949.tb03645.x.

(25) Breyer, C.; Bogdanov, D.; Gulagi, A.; Aghahosseini, A.; Barbosa, L. S. N. S.; Koskinen, O.; Barasa, M.; Caldera, U.; Afanasyeva, S.; Child, M.; et al. On the Role of Solar Photovoltaics in Global Energy Transition Scenarios. *Prog. Photovolt. Res. Appl.* **2017**, *25* (8), 727–745. https://doi.org/10.1002/pip.2885.

(26) Creutzig, F.; Agoston, P.; Goldschmidt, J. C.; Luderer, G.; Nemet, G.; Pietzcker, R. C. The Underestimated Potential of Solar Energy to Mitigate Climate Change. *Nat. Energy* **2017**, *2* (9), 17140. https://doi.org/10.1038/nenergy.2017.140.

(27) International Energy Agency (IEA). *Technology Roadmap: Solar Photovoltaic Energy*; Paris, 2014.

(28) Haegel, N. M.; Margolis, R.; Buonassisi, T.; Feldman, D.; Froitzheim, A.; Garabedian, R.; Green, M.; Glunz, S.; Henning, H.-M.; Holder, B.; et al. Terawatt-Scale Photovoltaics: Trajectories and Challenges. *Science* **2017**, *356* (6334), 141–143. https://doi.org/10.1126/science.aal1288.

(29) Bequerel, A. E. Recherches Sur Les Effets de La Radiation Chimique de La Lumiere Solaire Au Moyen Des Courants Electriques. *Comptes Rendus L′Academie Sci.* **1839**, *9*, 145–149.

(30) Chapin, D. M.; Fuller, C. S.; Pearson, G. L. A New Silicon p-n Junction Photocell for Converting Solar Radiation into Electrical Power. *J. Appl. Phys.* **1954**, *25* (5), 676–677. https://doi.org/10.1063/1.1721711.

(31) Jean, J.; Brown, P. R.; Jaffe, R. L.; Buonassisi, T.; Bulović, V. Pathways for Solar Photovoltaics. *Energy Environ. Sci.* **2015**, *8* (4), 1200–1219. https://doi.org/10.1039/C4EE04073B.

(32) Czochralski, J. A New Method for the Measurement of the Crystallization Rate of Metals. *Z. Für Phys. Chem.* **1918**, *92*, 219–221.

(33) National Renewable Energy Laboratory (NREL). Best Research-Cell Efficiency Chart. https://www.nrel.gov/pv/assets/pdfs/best-research-cell-efficiencies.20190802.pdf (accessed Sep 18, 2019).

(34) Lee, T. D.; Ebong, A. U. A Review of Thin Film Solar Cell Technologies and Challenges. *Renew. Sustain. Energy Rev.* **2017**, *70*, 1286–1297. https://doi.org/10.1016/j.rser.2016.12.028.

(35) Almosni, S.; Delamarre, A.; Jehl, Z.; Suchet, D.; Cojocaru, L.; Giteau, M.; Behaghel, B.; Julian, A.; Ibrahim, C.; Tatry, L.; et al. Material Challenges for Solar Cells in the Twenty-First Century: Directions in Emerging Technologies. *Sci. Technol. Adv. Mater.* **2018**, *19* (1), 336–369. https://doi.org/10.1080/14686996.2018.1433439.

(36) Liu, X.; Chen, H.; Tan, S. Overview of High-Efficiency Organic Photovoltaic Materials and Devices. *Renew. Sustain. Energy Rev.* **2015**, *52*, 1527–1538. https://doi.org/10.1016/j.rser.2015.08.032.

(37) Gong, J.; Sumathy, K.; Qiao, Q.; Zhou, Z. Review on Dye-Sensitized Solar Cells (DSSCs): Advanced Techniques and Research Trends. *Renew. Sustain. Energy Rev.* **2017**, *68*, 234–246. https://doi.org/10.1016/j.rser.2016.09.097.

(38) Chebrolu, V. T.; Kim, H.-J. Recent Progress in Quantum Dot Sensitized Solar Cells: An Inclusive Review of Photoanode, Sensitizer, Electrolyte, and the Counter Electrode. *J. Mater. Chem. C* **2019**, *7* (17), 4911–4933. https://doi.org/10.1039/C8TC06476H.

(39) Park, N.-G. Perovskite Solar Cells: An Emerging Photovoltaic Technology. *Mater. Today* **2015**, *18* (2), 65–72. https://doi.org/10.1016/j.mattod.2014.07.007.

(40) Green, M. A. Third Generation Photovoltaics: Ultra-High Conversion Efficiency at Low Cost. *Prog. Photovolt. Res. Appl.* **2001**, *9* (2), 123–135. https://doi.org/10.1002/pip.360.

(41) Green, M. A. Third Generation Photovoltaics: Solar Cells for 2020 and Beyond. *Phys. E Low-Dimens. Syst. Nanostructures* **2002**, *14*, 65–70. https://doi.org/10.1016/S1386-9477(02)00361-2.

(42) *Organic-Inorganic Halide Perovskite Photovoltaics: From Fundamentals to Device Architectures*; Park, N.-G., Grätzel, M., Miyasaka, T., Eds.; Springer International Publishing, 2016.

(43) Jena, A. K.; Kulkarni, A.; Miyasaka, T. Halide Perovskite Photovoltaics: Background, Status, and Future Prospects. *Chem. Rev.* **2019**, *119* (5), 3036–3103. https://doi.org/10.1021/acs.chemrev.8b00539.

(44) Petrus Michiel L.; Schlipf Johannes; Li Cheng; Gujar Tanaji P.; Giesbrecht Nadja; Müller-Buschbaum Peter; Thelakkat Mukundan; Bein Thomas; Hüttner Sven; Docampo Pablo. Capturing the Sun: A Review of the Challenges and Perspectives of Perovskite Solar Cells. *Adv. Energy Mater.* **2017**, *7* (16), 1700264. https://doi.org/10.1002/aenm.201700264.

(45) Chen, Q.; De Marco, N.; Yang, Y. (Michael); Song, T.-B.; Chen, C.-C.; Zhao, H.; Hong, Z.; Zhou, H.; Yang, Y. Under the Spotlight: The Organic–Inorganic Hybrid Halide Perovskite for Optoelectronic Applications. *Nano Today* **2015**, *10* (3), 355–396. https://doi.org/10.1016/j.nantod.2015.04.009.

(46) Goldschmidt, V. M. Die Gesetze Der Krystallochemie. *Naturwissenschaften* **1926**, *14*, 477–485. https://doi.org/10.1007/BF01507527.

(47) Li, C.; Lu, X.; Ding, W.; Feng, L.; Gao, Y.; Guo, Z. Formability of ABX$_3$ (X = F, Cl, Br, I) Halide Perovskites. *Acta Crystallogr. B* **2008**, *64* (Pt 6), 702–707. https://doi.org/10.1107/S0108768108032734.

(48) Møller, C. K. Crystal Structure and Photoconductivity of Cæsium Plumbohalides. *Nature* **1958**, *182* (4647), 1436–1436. https://doi.org/10.1038/1821436a0.

(49) Selig, O.; Sadhanala, A.; Müller, C.; Lovrincic, R.; Chen, Z.; Rezus, Y. L. A.; Frost, J. M.; Jansen, T. L. C.; Bakulin, A. A. Organic Cation Rotation and Immobilization in Pure and Mixed Methylammonium Lead-Halide Perovskites. *J. Am. Chem. Soc.* **2017**, *139* (11), 4068–4074. https://doi.org/10.1021/jacs.6b12239.

(50) El-Ghtami, H.; Laref, A.; Laref, S. Electronic and Optical Behaviors of Methylammonium and Formamidinium Lead Trihalide Perovskite Materials. *J. Mater. Sci. Mater. Electron.* **2019**, *30* (1), 711–720. https://doi.org/10.1007/s10854-018-0340-2.

(51) Saidaminov, M. I.; Abdelhady, A. L.; Murali, B.; Alarousu, E.; Burlakov, V. M.; Peng, W.; Dursun, I.; Wang, L.; He, Y.; Maculan, G.; et al. High-Quality Bulk Hybrid Perovskite Single

Crystals within Minutes by Inverse Temperature Crystallization. *Nat. Commun.* **2015**, *6* (1), 1–6. https://doi.org/10.1038/ncomms8586.

(52) Rühle, S. Tabulated Values of the Shockley–Queisser Limit for Single Junction Solar Cells. *Sol. Energy* **2016**, *130*, 139–147. https://doi.org/10.1016/j.solener.2016.02.015.

(53) Xiao, Z.; Yan, Y. Progress in Theoretical Study of Metal Halide Perovskite Solar Cell Materials. *Adv. Energy Mater.* **2017**, *7* (22), 1701136. https://doi.org/10.1002/aenm.201701136.

(54) Kojima, A.; Teshima, K.; Shirai, Y.; Miyasaka, T. Organometal Halide Perovskites as Visible-Light Sensitizers for Photovoltaic Cells. *J. Am. Chem. Soc.* **2009**, *131* (17), 6050–6051. https://doi.org/10.1021/ja809598r.

(55) Lee, M. M.; Teuscher, J.; Miyasaka, T.; Murakami, T. N.; Snaith, H. J. Efficient Hybrid Solar Cells Based on Meso-Superstructured Organometal Halide Perovskites. *Science* **2012**, *338* (6107), 643–647. https://doi.org/10.1126/science.1228604.

(56) Stranks, S. D.; Eperon, G. E.; Grancini, G.; Menelaou, C.; Alcocer, M. J. P.; Leijtens, T.; Herz, L. M.; Petrozza, A.; Snaith, H. J. Electron-Hole Diffusion Lengths Exceeding 1 Micrometer in an Organometal Trihalide Perovskite Absorber. *Science* **2013**, *342* (6156), 341–344. https://doi.org/10.1126/science.1243982.

(57) Luo, S.; Daoud, W. A. Crystal Structure Formation of $CH_3NH_3PbI_{3-X}Cl_X$ Perovskite. *Materials* **2016**, *9* (3). https://doi.org/10.3390/ma9030123.

(58) Prakash, J.; Singh, A.; Sathiyan, G.; Ranjan, R.; Singh, A.; Garg, A.; Gupta, R. K. Progress in Tailoring Perovskite Based Solar Cells through Compositional Engineering: Materials Properties, Photovoltaic Performance and Critical Issues. *Mater. Today Energy* **2018**, *9*, 440–486. https://doi.org/10.1016/j.mtener.2018.07.003.

(59) Noh, J. H.; Im, S. H.; Heo, J. H.; Mandal, T. N.; Seok, S. I. Chemical Management for Colorful, Efficient, and Stable Inorganic–Organic Hybrid Nanostructured Solar Cells. *Nano Lett.* **2013**, *13* (4), 1764–1769. https://doi.org/10.1021/nl400349b.

(60) Pellet, N.; Gao, P.; Gregori, G.; Yang, T.-Y.; Nazeeruddin, M. K.; Maier, J.; Grätzel, M. Mixed-Organic-Cation Perovskite Photovoltaics for Enhanced Solar-Light Harvesting. *Angew. Chem. Int. Ed.* **2014**, *53* (12), 3151–3157. https://doi.org/10.1002/anie.201309361.

(61) Chen, J.; Xu, J.; Xiao, L.; Zhang, B.; Dai, S.; Yao, J. Mixed-Organic-Cation (FA)x(MA)1–XPbI3 Planar Perovskite Solar Cells with 16.48% Efficiency via a Low-Pressure Vapor-Assisted Solution Process. *ACS Appl. Mater. Interfaces* **2017**, *9* (3), 2449–2458. https://doi.org/10.1021/acsami.6b13410.

(62) Zhang, Y.; Grancini, G.; Feng, Y.; Asiri, A. M.; Nazeeruddin, M. K. Optimization of Stable Quasi-Cubic $FA_xMA_{1-x}PbI_3$ Perovskite Structure for Solar Cells with Efficiency beyond 20%. *ACS Energy Lett.* **2017**, *2* (4), 802–806. https://doi.org/10.1021/acsenergylett.7b00112.

(63) Mateen, M.; Arain, Z.; Liu, C.; Yang, Y.; Liu, X.; Ding, Y.; Shi, P.; Ren, Y.; Wu, Y.; Dai, S.; et al. High-Quality $(FA)_x(MA)_{1-x}PbI_3$ for Efficient Perovskite Solar Cells via a Facile Cation-Intermixing Technique. *ACS Sustain. Chem. Eng.* **2019**, *7* (13), 11760–11768. https://doi.org/10.1021/acssuschemeng.9b02031.

(64) Zuo, F.; Williams, S. T.; Liang, P.-W.; Chueh, C.-C.; Liao, C.-Y.; Jen, A. K.-Y. Binary-Metal Perovskites Toward High-Performance Planar-Heterojunction Hybrid Solar Cells. *Adv. Mater.* **2014**, *26* (37), 6454–6460. https://doi.org/10.1002/adma.201401641.

(65) Ogomi, Y.; Morita, A.; Tsukamoto, S.; Saitho, T.; Fujikawa, N.; Shen, Q.; Toyoda, T.; Yoshino, K.; Pandey, S. S.; Ma, T.; et al. $CH_3NH_3Sn_xPb_{(1-x)}I_3$ Perovskite Solar Cells

Covering up to 1060 Nm. *J. Phys. Chem. Lett.* **2014**, *5* (6), 1004–1011. https://doi.org/10.1021/jz5002117.

(66) Ju, M.-G.; Dai, J.; Ma, L.; Zeng, X. C. Lead-Free Mixed Tin and Germanium Perovskites for Photovoltaic Application. *J. Am. Chem. Soc.* **2017**, *139* (23), 8038–8043. https://doi.org/10.1021/jacs.7b04219.

(67) Nayak, P. K.; Sendner, M.; Wenger, B.; Wang, Z.; Sharma, K.; Ramadan, A. J.; Lovrinčić, R.; Pucci, A.; Madhu, P. K.; Snaith, H. J. Impact of Bi3+ Heterovalent Doping in Organic–Inorganic Metal Halide Perovskite Crystals. *J. Am. Chem. Soc.* **2018**, *140* (2), 574–577. https://doi.org/10.1021/jacs.7b11125.

(68) Marinova, N.; Valero, S.; Delgado, J. L. Organic and Perovskite Solar Cells: Working Principles, Materials and Interfaces. *J. Colloid Interface Sci.* **2017**, *488*, 373–389. https://doi.org/10.1016/j.jcis.2016.11.021.

(69) Cui, P.; Wei, D.; Ji, J.; Huang, H.; Jia, E.; Dou, S.; Wang, T.; Wang, W.; Li, M. Planar p–n Homojunction Perovskite Solar Cells with Efficiency Exceeding 21.3%. *Nat. Energy* **2019**, *4* (2), 150–159. https://doi.org/10.1038/s41560-018-0324-8.

(70) Shockley, W.; Queisser, H. J. Detailed Balance Limit of Efficiency of p-n Junction Solar Cells. *J. Appl. Phys.* **1961**, *32* (3), 510–519. https://doi.org/10.1063/1.1736034.

(71) Stolterfoht, M.; Caprioglio, P.; Wolff, C. M.; Márquez, J. A.; Nordmann, J.; Zhang, S.; Rothhardt, D.; Hörmann, U.; Redinger, A.; Kegelmann, L.; et al. The Perovskite/Transport Layer Interfaces Dominate Non-Radiative Recombination in Efficient Perovskite Solar Cells. *Energy Environ. Sci.* **2019**, *12* (9), 2778–2788. https://doi.org/10.1039/c9ee02020a.

(72) Song, Z.; Watthage, S. C.; Phillips, A. B.; Heben, M. J. Pathways toward High-Performance Perovskite Solar Cells: Review of Recent Advances in Organo-Metal Halide Perovskites for Photovoltaic Applications. *J. Photonics Energy* **2016**, *6* (2), 022001. https://doi.org/10.1117/1.JPE.6.022001.

(73) Yun, S.; Freitas, J. N.; Nogueira, A. F.; Wang, Y.; Ahmad, S.; Wang, Z.-S. Dye-Sensitized Solar Cells Employing Polymers. *Prog. Polym. Sci.* **2016**, *59*, 1–40. https://doi.org/10.1016/j.progpolymsci.2015.10.004.

(74) Im, J.-H.; Lee, C.-R.; Lee, J.-W.; Park, S.-W.; Park, N.-G. 6.5% Efficient Perovskite Quantum-Dot-Sensitized Solar Cell. *Nanoscale* **2011**, *3* (10), 4088–4093. https://doi.org/10.1039/C1NR10867K.

(75) Kim, H.-S.; Lee, C.-R.; Im, J.-H.; Lee, K.-B.; Moehl, T.; Marchioro, A.; Moon, S.-J.; Humphry-Baker, R.; Yum, J.-H.; Moser, J. E.; et al. Lead Iodide Perovskite Sensitized All-Solid-State Submicron Thin Film Mesoscopic Solar Cell with Efficiency Exceeding 9%. *Sci. Rep.* **2012**, *2*, 591. https://doi.org/10.1038/srep00591.

(76) Heo, J. H.; Im, S. H.; Noh, J. H.; Mandal, T. N.; Lim, C.-S.; Chang, J. A.; Lee, Y. H.; Kim, H.; Sarkar, A.; Nazeeruddin, M. K.; et al. Efficient Inorganic–Organic Hybrid Heterojunction Solar Cells Containing Perovskite Compound and Polymeric Hole Conductors. *Nat. Photonics* **2013**, *7* (6), 486–491. https://doi.org/10.1038/nphoton.2013.80.

(77) Burschka, J.; Pellet, N.; Moon, S.-J.; Humphry-Baker, R.; Gao, P.; Nazeeruddin, M. K.; Grätzel, M. Sequential Deposition as a Route to High-Performance Perovskite-Sensitized Solar Cells. *Nature* **2013**, *499* (7458), 316–319. https://doi.org/10.1038/nature12340.

(78) Im, J.-H.; Jang, I.-H.; Pellet, N.; Grätzel, M.; Park, N.-G. Growth of CH3NH3PbI3 Cuboids with Controlled Size for High-Efficiency Perovskite Solar Cells. *Nat. Nanotechnol.* **2014**, *9* (11), 927–932. https://doi.org/10.1038/nnano.2014.181.

(79) Luan, Y.; Yi, X.; Mao, P.; Wei, Y.; Zhuang, J.; Chen, N.; Lin, T.; Li, C.; Wang, J. High-Performance Planar Perovskite Solar Cells with Negligible Hysteresis Using 2,2,2-Trifluoroethanol-Incorporated SnO$_2$. *iScience* **2019**, *16*, 433–441. https://doi.org/10.1016/j.isci.2019.06.004.

(80) Jeng, J.-Y.; Chiang, Y.-F.; Lee, M.-H.; Peng, S.-R.; Guo, T.-F.; Chen, P.; Wen, T.-C. CH3NH3PbI3 Perovskite/Fullerene Planar-Heterojunction Hybrid Solar Cells. *Adv. Mater.* **2013**, *25* (27), 3727–3732. https://doi.org/10.1002/adma.201301327.

(81) Wang, Y.; Chen, W.; Wang, L.; Tu, B.; Chen, T.; Liu, B.; Yang, K.; Koh, C. W.; Zhang, X.; Sun, H.; et al. Dopant-Free Small-Molecule Hole-Transporting Material for Inverted Perovskite Solar Cells with Efficiency Exceeding 21%. *Adv. Mater.* **2019**, *31* (35), 1902781. https://doi.org/10.1002/adma.201902781.

(82) Wang, T.; Ding, D.; Wang, X.; Zeng, R.; Liu, H.; Shen, W. High-Performance Inverted Perovskite Solar Cells with Mesoporous NiO$_x$ Hole Transport Layer by Electrochemical Deposition. *ACS Omega* **2018**, *3* (12), 18434–18443. https://doi.org/10.1021/acsomega.8b02612.

(83) Tsai, K.-W.; Chueh, C.-C.; Williams, S. T.; Wen, T.-C.; Jen, A. K. Y. High-Performance Hole-Transporting Layer-Free Conventional Perovskite/Fullerene Heterojunction Thin-Film Solar Cells. *J. Mater. Chem. A* **2015**, *3* (17), 9128–9132. https://doi.org/10.1039/C5TA01343G.

(84) Huang, C.; Lin, P.; Fu, N.; Liu, C.; Xu, B.; Sun, K.; Wang, D.; Zeng, X.; Ke, S. Facile Fabrication of Highly Efficient ETL-Free Perovskite Solar Cells with 20% Efficiency by Defect Passivation and Interface Engineering. *Chem. Commun.* **2019**, *55* (19), 2777–2780. https://doi.org/10.1039/C9CC00312F.

(85) Salim, T.; Sun, S.; Abe, Y.; Krishna, A.; Grimsdale, A. C.; Lam, Y. M. Perovskite-Based Solar Cells: Impact of Morphology and Device Architecture on Device Performance. *J. Mater. Chem. A* **2015**, *3* (17), 8943–8969. https://doi.org/10.1039/C4TA05226A.

(86) Dubey, A.; Adhikari, N.; Mabrouk, S.; Wu, F.; Chen, K.; Yang, S.; Qiao, Q. A Strategic Review on Processing Routes towards Highly Efficient Perovskite Solar Cells. *J. Mater. Chem. A* **2018**, *6* (6), 2406–2431. https://doi.org/10.1039/C7TA08277K.

(87) Liu, M.; Johnston, M. B.; Snaith, H. J. Efficient Planar Heterojunction Perovskite Solar Cells by Vapour Deposition. *Nature* **2013**, *501* (7467), 395–398. https://doi.org/10.1038/nature12509.

(88) Chen, C.-W.; Kang, H.-W.; Hsiao, S.-Y.; Yang, P.-F.; Chiang, K.-M.; Lin, H.-W. Efficient and Uniform Planar-Type Perovskite Solar Cells by Simple Sequential Vacuum Deposition. *Adv. Mater.* **2014**, *26* (38), 6647–6652. https://doi.org/10.1002/adma.201402461.

(89) Luo, P.; Zhou, S.; Xia, W.; Cheng, J.; Xu, C.; Lu, Y. Chemical Vapor Deposition of Perovskites for Photovoltaic Application. *Adv. Mater. Interfaces* **2017**, *4* (8), 1600970. https://doi.org/10.1002/admi.201600970.

(90) Chen, Q.; Zhou, H.; Hong, Z.; Luo, S.; Duan, H.-S.; Wang, H.-H.; Liu, Y.; Li, G.; Yang, Y. Planar Heterojunction Perovskite Solar Cells via Vapor-Assisted Solution Process. *J. Am. Chem. Soc.* **2014**, *136* (2), 622–625. https://doi.org/10.1021/ja411509g.

(91) Jung, Y.-S.; Hwang, K.; Heo, Y.-J.; Kim, J.-E.; Vak, D.; Kim, D.-Y. Progress in Scalable Coating and Roll-to-Roll Compatible Printing Processes of Perovskite Solar Cells toward Realization of Commercialization. *Adv. Opt. Mater.* **2018**, *6* (9), 1701182. https://doi.org/10.1002/adom.201701182.

(92) Chilvery, A.; Das, S.; Guggilla, P.; Brantley, C.; Sunda-Meya, A. A Perspective on the Recent Progress in Solution-Processed Methods for Highly Efficient Perovskite Solar Cells. *Sci. Technol. Adv. Mater.* **2016**, *17* (1), 650–658. https://doi.org/10.1080/14686996.2016.1226120.

(93) Xu, Y.; Zhu, L.; Shi, J.; Lv, S.; Xu, X.; Xiao, J.; Dong, J.; Wu, H.; Luo, Y.; Li, D.; et al. Efficient Hybrid Mesoscopic Solar Cells with Morphology-Controlled $CH_3NH_3PbI_{3-x}Cl_x$ Derived from Two-Step Spin Coating Method. *ACS Appl. Mater. Interfaces* **2015**, *7* (4), 2242–2248. https://doi.org/10.1021/am5057807.

(94) Mohammadian, N.; Alizadeh, A. H.; Moshaii, A.; Gharibzadeh, S.; Alizadeh, A.; Mohammadpour, R.; Fathi, D. A Two-Step Spin-Spray Deposition Processing Route for Production of Halide Perovskite Solar Cell. *Thin Solid Films* **2016**, *616*, 754–759. https://doi.org/10.1016/j.tsf.2016.09.039.

(95) Tombe, S.; Adam, G.; Heilbrunner, H.; Yumusak, C.; Apaydin, D. H.; Hailegnaw, B.; Ulbricht, C.; Arendse, C. J.; Langhals, H.; Iwuohaa, E.; et al. The Influence of Perovskite Precursor Composition on the Morphology and Photovoltaic Performance of Mixed Halide $MAPbI_{3-x}Cl_x$ Solar Cells. *Sol. Energy* **2018**, *163*, 215–223. https://doi.org/10.1016/j.solener.2018.01.083.

(96) Konstantakou, M.; Perganti, D.; Falaras, P.; Stergiopoulos, T. Anti-Solvent Crystallization Strategies for Highly Efficient Perovskite Solar Cells. *Crystals* **2017**, *7* (10), 291. https://doi.org/10.3390/cryst7100291.

(97) Zhang, J.; Zhang, L.; Li, X.; Zhu, X.; Yu, J.; Fan, K. Binary Solvent Engineering for High-Performance Two-Dimensional Perovskite Solar Cells. *ACS Sustain. Chem. Eng.* **2019**, *7* (3), 3487–3495. https://doi.org/10.1021/acssuschemeng.8b05734.

(98) Liao, H.-C.; Guo, P.; Hsu, C.-P.; Lin, M.; Wang, B.; Zeng, L.; Huang, W.; Soe, C. M. M.; Su, W.-F.; Bedzyk, M. J.; et al. Enhanced Efficiency of Hot-Cast Large-Area Planar Perovskite Solar Cells/Modules Having Controlled Chloride Incorporation. *Adv. Energy Mater.* **2017**, *7* (8), 1601660. https://doi.org/10.1002/aenm.201601660.

(99) Jiang, Y.; Pan, L.; Wei, D.; Li, W.; Li, S.; Yang, S.-E.; Shi, Z.; Guo, H.; Xia, T.; Zang, J.; et al. The Modified Multi-Step Thermal Annealing Process for Highly Efficient $MAPbI_3$-Based Perovskite Solar Cells. *Sol. Energy* **2018**, *174*, 218–224. https://doi.org/10.1016/j.solener.2018.09.016.

(100) Xiao, Z.; Dong, Q.; Bi, C.; Shao, Y.; Yuan, Y.; Huang, J. Solvent Annealing of Perovskite-Induced Crystal Growth for Photovoltaic-Device Efficiency Enhancement. *Adv. Mater.* **2014**, *26* (37), 6503–6509. https://doi.org/10.1002/adma.201401685.

(101) Li, T.; Pan, Y.; Wang, Z.; Xia, Y.; Chen, Y.; Huang, W. Additive Engineering for Highly Efficient Organic–Inorganic Halide Perovskite Solar Cells: Recent Advances and Perspectives. *J. Mater. Chem. A* **2017**, *5* (25), 12602–12652. https://doi.org/10.1039/C7TA01798G.

(102) Liang, P.-W.; Liao, C.-Y.; Chueh, C.-C.; Zuo, F.; Williams, S. T.; Xin, X.-K.; Lin, J.; Jen, A. K.-Y. Additive Enhanced Crystallization of Solution-Processed Perovskite for Highly Efficient Planar-Heterojunction Solar Cells. *Adv. Mater.* **2014**, *26* (22), 3748–3754. https://doi.org/10.1002/adma.201400231.

(103) Cao, X. B.; Li, C. L.; Zhi, L. L.; Li, Y. H.; Cui, X.; Yao, Y. W.; Ci, L. J.; Wei, J. Q. Fabrication of High Quality Perovskite Films by Modulating the Pb–O Bonds in Lewis Acid–Base Adducts. *J. Mater. Chem. A* **2017**, *5* (18), 8416–8422. https://doi.org/10.1039/C7TA00539C.

(104)   Tanaka, T.; Hashimoto, N.; Furuya, E.; Nakagawa, M.; Kakehi, Y.; Mori, T.; Yamada, Y.; Kondo, Y. Fabrication of Perovskite Solar Cells with ITO Deposited at a High Rate by Activated Reactive Evaporation Using a Pressure-Gradient-Type Plasma Gun. *Jpn. J. Appl. Phys.* **2019**, *58* (6), 068010. https://doi.org/10.7567/1347-4065/ab241c.

(105)   Ou, X.-L.; Xu, M.; Feng, J.; Sun, H.-B. Flexible and Efficient ITO-Free Semitransparent Perovskite Solar Cells. *Sol. Energy Mater. Sol. Cells* **2016**, *157*, 660–665. https://doi.org/10.1016/j.solmat.2016.07.010.

(106)   Chueh, C.-C.; Li, C.-Z.; Jen, A. K.-Y. Recent Progress and Perspective in Solution-Processed Interfacial Materials for Efficient and Stable Polymer and Organometal Perovskite Solar Cells. *Energy Environ. Sci.* **2015**, *8* (4), 1160–1189. https://doi.org/10.1039/C4EE03824J.

(107)   Schulze, P. S. C.; Bett, A. J.; Winkler, K.; Hinsch, A.; Lee, S.; Mastroianni, S.; Mundt, L. E.; Mundus, M.; Würfel, U.; Glunz, S. W.; et al. Novel Low-Temperature Process for Perovskite Solar Cells with a Mesoporous TiO_2 Scaffold. *ACS Appl. Mater. Interfaces* **2017**, *9* (36), 30567–30574. https://doi.org/10.1021/acsami.7b05718.

(108)   Han, K.; Xie, M.; Zhang, L.; Yan, L.; Wei, J.; Ji, G.; Luo, Q.; Lin, J.; Hao, Y.; Ma, C.-Q. Fully Solution Processed Semi-Transparent Perovskite Solar Cells with Spray-Coated Silver Nanowires/ZnO Composite Top Electrode. *Sol. Energy Mater. Sol. Cells* **2018**, *185*, 399–405. https://doi.org/10.1016/j.solmat.2018.05.048.

(109)   Yang, Z.; Babu, B. H.; Wu, S.; Liu, T.; Fang, S.; Xiong, Z.; Han, L.; Chen, W. Review on Practical Interface Engineering of Perovskite Solar Cells: From Efficiency to Stability. *Sol. RRL* **2019**. https://doi.org/10.1002/solr.201900257.

(110)   Abdi-Jalebi, M.; Dar, M. I.; Sadhanala, A.; Senanayak, S. P.; Giordano, F.; Zakeeruddin, S. M.; Grätzel, M.; Friend, R. H. Impact of a Mesoporous Titania–Perovskite Interface on the Performance of Hybrid Organic–Inorganic Perovskite Solar Cells. *J. Phys. Chem. Lett.* **2016**, *7* (16), 3264–3269. https://doi.org/10.1021/acs.jpclett.6b01617.

(111)   Zhang, Z.-L.; Li, J.-F.; Wang, X.-L.; Qin, J.-Q.; Shi, W.-J.; Liu, Y.-F.; Gao, H.-P.; Mao, Y.-L. Enhancement of Perovskite Solar Cells Efficiency Using N-Doped TiO_2 Nanorod Arrays as Electron Transfer Layer. *Nanoscale Res. Lett.* **2017**, *12* (1), 43. https://doi.org/10.1186/s11671-016-1811-0.

(112)   Mahmood, K.; Sarwar, S.; Mehran, M. T. Current Status of Electron Transport Layers in Perovskite Solar Cells: Materials and Properties. *RSC Adv.* **2017**, *7* (28), 17044–17062. https://doi.org/10.1039/C7RA00002B.

(113)   Wang, S.; Huang, Z.; Wang, X.; Li, Y.; Günther, M.; Valenzuela, S.; Parikh, P.; Cabreros, A.; Xiong, W.; Meng, Y. S. Unveiling the Role of TBP–LiTFSI Complexes in Perovskite Solar Cells. *J. Am. Chem. Soc.* **2018**, *140* (48), 16720–16730. https://doi.org/10.1021/jacs.8b09809.

(114)   Nia, N. Y.; Matteocci, F.; Cina, L.; Di Carlo, A. High-Efficiency Perovskite Solar Cell Based on Poly(3-Hexylthiophene): Influence of Molecular Weight and Mesoscopic Scaffold Layer. *ChemSusChem* **2017**, *10* (19), 3854–3860. https://doi.org/10.1002/cssc.201700635.

(115)   Connell, A.; Wang, Z.; Lin, Y.-H.; Greenwood, P. C.; Wiles, A. A.; Jones, E. W.; Furnell, L.; Anthony, R.; Kershaw, C. P.; Cooke, G.; et al. Low Cost Triazatruxene Hole Transporting Material for >20% Efficiency Perovskite Solar Cells. *J. Mater. Chem. C* **2019**, *7* (18), 5235–5243. https://doi.org/10.1039/C8TC04231D.

(116)   Jung, E. H.; Jeon, N. J.; Park, E. Y.; Moon, C. S.; Shin, T. J.; Yang, T.-Y.; Noh, J. H.; Seo, J. Efficient, Stable and Scalable Perovskite Solar Cells Using Poly(3-Hexylthiophene). *Nature* **2019**, *567* (7749), 511–515. https://doi.org/10.1038/s41586-019-1036-3.

(117)   Liu, F.; Wu, F.; Tu, Z.; Liao, Q.; Gong, Y.; Zhu, L.; Li, Q.; Li, Z. Hole Transport Materials Based on 6,12-Dihydroindeno[1,2-b]Fluorine with Different Periphery Groups: A New Strategy for Dopant-Free Perovskite Solar Cells. *Adv. Funct. Mater.* **2019**, *29* (24), 1901296. https://doi.org/10.1002/adfm.201901296.

(118)   Gil, B.; Yun, A. J.; Lee, Y.; Kim, J.; Lee, B.; Park, B. Recent Progress in Inorganic Hole Transport Materials for Efficient and Stable Perovskite Solar Cells. *Electron. Mater. Lett.* **2019**, *15* (5), 505–524. https://doi.org/10.1007/s13391-019-00163-6.

(119)   Abate, A.; Saliba, M.; Hollman, D. J.; Stranks, S. D.; Wojciechowski, K.; Avolio, R.; Grancini, G.; Petrozza, A.; Snaith, H. J. Supramolecular Halogen Bond Passivation of Organic–Inorganic Halide Perovskite Solar Cells. *Nano Lett.* **2014**, *14* (6), 3247–3254. https://doi.org/10.1021/nl500627x.

(120)   Noel, N. K.; Abate, A.; Stranks, S. D.; Parrott, E. S.; Burlakov, V. M.; Goriely, A.; Snaith, H. J. Enhanced Photoluminescence and Solar Cell Performance via Lewis Base Passivation of Organic–Inorganic Lead Halide Perovskites. *ACS Nano* **2014**, *8* (10), 9815–9821. https://doi.org/10.1021/nn5036476.

(121)   Wang, J. T.-W.; Ball, J. M.; Barea, E. M.; Abate, A.; Alexander-Webber, J. A.; Huang, J.; Saliba, M.; Mora-Sero, I.; Bisquert, J.; Snaith, H. J.; et al. Low-Temperature Processed Electron Collection Layers of Graphene/TiO_2 Nanocomposites in Thin Film Perovskite Solar Cells. *Nano Lett.* **2014**, *14* (2), 724–730. https://doi.org/10.1021/nl403997a.

(122)   Zhou, Y.; Fuentes-Hernandez, C.; Shim, J.; Meyer, J.; Giordano, A. J.; Li, H.; Winget, P.; Papadopoulos, T.; Cheun, H.; Kim, J.; et al. A Universal Method to Produce Low-Work Function Electrodes for Organic Electronics. *Science* **2012**, *336* (6079), 327–332. https://doi.org/10.1126/science.1218829.

(123)   Yuan, D.-X.; Yuan, X.-D.; Xu, Q.-Y.; Xu, M.-F.; Shi, X.-B.; Wang, Z.-K.; Liao, L.-S. A Solution-Processed Bathocuproine Cathode Interfacial Layer for High-Performance Bromine-Iodine Perovskite Solar Cells. *Phys. Chem. Chem. Phys. PCCP* **2015**, *17* (40), 26653–26658. https://doi.org/10.1039/c5cp03995a.

(124)   Ciro, J.; Mesa, S.; Uribe, J. I.; Mejía-Escobar, M. A.; Ramirez, D.; Montoya, J. F.; Betancur, R.; Yoo, H.-S.; Park, N.-G.; Jaramillo, F. Optimization of the Ag/PCBM Interface by a Rhodamine Interlayer to Enhance the Efficiency and Stability of Perovskite Solar Cells. *Nanoscale* **2017**, *9* (27), 9440–9446. https://doi.org/10.1039/C7NR01678F.

(125)   Jiang, L.-L.; Cong, S.; Lou, Y.-H.; Yi, Q.-H.; Zhu, J.-T.; Ma, H.; Zou, G.-F. Interface Engineering toward Enhanced Efficiency of Planar Perovskite Solar Cells. *J. Mater. Chem. A* **2015**, *4* (1), 217–222. https://doi.org/10.1039/C5TA09231K.

(126)   Chen, W.; Xu, L.; Feng, X.; Jie, J.; He, Z. Metal Acetylacetonate Series in Interface Engineering for Full Low-Temperature-Processed, High-Performance, and Stable Planar Perovskite Solar Cells with Conversion Efficiency over 16% on 1 cm^2 Scale. *Adv. Mater.* **2017**, *29* (16), 1603923. https://doi.org/10.1002/adma.201603923.

(127)   Sanehira, E. M.; Tremolet de Villers, B. J.; Schulz, P.; Reese, M. O.; Ferrere, S.; Zhu, K.; Lin, L. Y.; Berry, J. J.; Luther, J. M. Influence of Electrode Interfaces on the Stability of Perovskite Solar Cells: Reduced Degradation Using MoO_x/Al for Hole Collection. *ACS Energy Lett.* **2016**, *1* (1), 38–45. https://doi.org/10.1021/acsenergylett.6b00013.

(128)   Sun, Y.; Takacs, C. J.; Cowan, S. R.; Seo, J. H.; Gong, X.; Roy, A.; Heeger, A. J. Efficient, Air-Stable Bulk Heterojunction Polymer Solar Cells Using MoO_x as the Anode Interfacial Layer. *Adv. Mater.* **2011**, *23* (19), 2226–2230. https://doi.org/10.1002/adma.201100038.

(129)   Traverse, C. J.; Pandey, R.; Barr, M. C.; Lunt, R. R. Emergence of Highly Transparent Photovoltaics for Distributed Applications. *Nat. Energy* **2017**, *2* (11), 849. https://doi.org/10.1038/s41560-017-0016-9.

(130)   Xue, Q.; Xia, R.; Brabec, C. J.; Yip, H.-L. Recent Advances in Semi-Transparent Polymer and Perovskite Solar Cells for Power Generating Window Applications. *Energy Environ. Sci.* **2018**, *11* (7), 1688–1709. https://doi.org/10.1039/C8EE00154E.

(131)   Bailie, C. D.; Christoforo, M. G.; Mailoa, J. P.; Bowring, A. R.; Unger, E. L.; Nguyen, W. H.; Burschka, J.; Pellet, N.; Lee, J. Z.; Grätzel, M.; et al. Semi-Transparent Perovskite Solar Cells for Tandems with Silicon and CIGS. *Energy Environ. Sci.* **2015**, *8* (3), 956–963. https://doi.org/10.1039/C4EE03322A.

(132)   Tai, Q.; Yan, F. Emerging Semitransparent Solar Cells: Materials and Device Design. *Adv. Mater.* **2017**, *29* (34), 1700192. https://doi.org/10.1002/adma.201700192.

(133)   Chen, K.-S.; Salinas, J.-F.; Yip, H.-L.; Huo, L.; Hou, J.; Jen, A. K.-Y. Semi-Transparent Polymer Solar Cells with 6% PCE, 25% Average Visible Transmittance and a Color Rendering Index Close to 100 for Power Generating Window Applications. *Energy Environ. Sci.* **2012**, *5* (11), 9551. https://doi.org/10.1039/c2ee22623e.

(134)   Eperon, G. E.; Burlakov, V. M.; Goriely, A.; Snaith, H. J. Neutral Color Semitransparent Microstructured Perovskite Solar Cells. *ACS Nano* **2014**, *8* (1), 591–597. https://doi.org/10.1021/nn4052309.

(135)   Roldán-Carmona, C.; Malinkiewicz, O.; Betancur, R.; Longo, G.; Momblona, C.; Jaramillo, F.; Camacho, L.; Bolink, H. J. High Efficiency Single-Junction Semitransparent Perovskite Solar Cells. *Energy Env. Sci* **2014**, *7* (9), 2968–2973. https://doi.org/10.1039/C4EE01389A.

(136)   Cao, W.; Li, J.; Chen, H.; Xue, J. Transparent Electrodes for Organic Optoelectronic Devices: A Review. *J. Photonics Energy* **2014**, *4* (1), 040990. https://doi.org/10.1117/1.JPE.4.040990.

(137)   Yun, J. Ultrathin Metal Films for Transparent Electrodes of Flexible Optoelectronic Devices. *Adv. Funct. Mater.* **2017**, *27* (18), 1606641. https://doi.org/10.1002/adfm.201606641.

(138)   Della Gaspera, E.; Peng, Y.; Hou, Q.; Spiccia, L.; Bach, U.; Jasieniak, J. J.; Cheng, Y.-B. Ultra-Thin High Efficiency Semitransparent Perovskite Solar Cells. *Nano Energy* **2015**, *13*, 249–257. https://doi.org/10.1016/j.nanoen.2015.02.028.

(139)   Yang, Y. (Michael); Chen, Q.; Hsieh, Y.-T.; Song, T.-B.; Marco, N. D.; Zhou, H.; Yang, Y. Multilayer Transparent Top Electrode for Solution Processed Perovskite/Cu(In,Ga)(Se,S)$_2$ Four Terminal Tandem Solar Cells. *ACS Nano* **2015**, *9* (7), 7714–7721. https://doi.org/10.1021/acsnano.5b03189.

(140)   Rahmany, S.; Layani, M.; Magdassi, S.; Etgar, L. Fully Functional Semi-Transparent Perovskite Solar Cell Fabricated in Ambient Air. *Sustain. Energy Fuels* **2017**, *1* (10), 2120–2127. https://doi.org/10.1039/C7SE00383H.

(141)   Guo, F.; Azimi, H.; Hou, Y.; Przybilla, T.; Hu, M.; Bronnbauer, C.; Langner, S.; Spiecker, E.; Forberich, K.; Brabec, C. J. High-Performance Semitransparent Perovskite Solar Cells with Solution-Processed Silver Nanowires as Top Electrodes. *Nanoscale* **2015**, *7* (5), 1642–1649. https://doi.org/10.1039/C4NR06033D.

(142)   Zhang, Y.; Wu, Z.; Li, P.; Ono, L. K.; Qi, Y.; Zhou, J.; Shen, H.; Surya, C.; Zheng, Z. Fully Solution-Processed TCO-Free Semitransparent Perovskite Solar Cells for Tandem and Flexible Applications. *Adv. Energy Mater.* **2018**, *8* (1), 1701569. https://doi.org/10.1002/aenm.201701569.

(143)   You, P.; Liu, Z.; Tai, Q.; Liu, S.; Yan, F. Efficient Semitransparent Perovskite Solar Cells with Graphene Electrodes. *Adv. Mater.* **2015**, *27* (24), 3632–3638. https://doi.org/10.1002/adma.201501145.

(144)   Jeon, I.; Seo, S.; Sato, Y.; Delacou, C.; Anisimov, A.; Suenaga, K.; Kauppinen, E. I.; Maruyama, S.; Matsuo, Y. Perovskite Solar Cells Using Carbon Nanotubes Both as Cathode and as Anode. *J. Phys. Chem. C* **2017**, *121* (46), 25743–25749. https://doi.org/10.1021/acs.jpcc.7b10334.

(145)   Eperon, G. E.; Hörantner, M. T.; Snaith, H. J. Metal Halide Perovskite Tandem and Multiple-Junction Photovoltaics. *Nat. Rev. Chem.* **2017**, *1* (12), 0095. https://doi.org/10.1038/s41570-017-0095.

(146)   Eperon, G. E.; Leijtens, T.; Bush, K. A.; Prasanna, R.; Green, T.; Wang, J. T.-W.; McMeekin, D. P.; Volonakis, G.; Milot, R. L.; May, R.; et al. Perovskite-Perovskite Tandem Photovoltaics with Optimized Band Gaps. *Science* **2016**, *354* (6314), 861–865. https://doi.org/10.1126/science.aaf9717.

(147)   Wang, R.; Mujahid, M.; Duan, Y.; Wang, Z.-K.; Xue, J.; Yang, Y. A Review of Perovskites Solar Cell Stability. *Adv. Funct. Mater.* **2019**, 1808843. https://doi.org/10.1002/adfm.201808843.

(148)   Meng, L.; You, J.; Yang, Y. Addressing the Stability Issue of Perovskite Solar Cells for Commercial Applications. *Nat. Commun.* **2018**, *9* (1), 1–4. https://doi.org/10.1038/s41467-018-07255-1.

(149)   You, J.; Yang, Y. (Michael); Hong, Z.; Song, T.-B.; Meng, L.; Liu, Y.; Jiang, C.; Zhou, H.; Chang, W.-H.; Li, G.; et al. Moisture Assisted Perovskite Film Growth for High Performance Solar Cells. *Appl. Phys. Lett.* **2014**, *105* (18), 183902. https://doi.org/10.1063/1.4901510.

(150)   Pisoni, A.; Jaćimović, J.; Barišić, O. S.; Spina, M.; Gaál, R.; Forró, L.; Horváth, E. Ultra-Low Thermal Conductivity in Organic–Inorganic Hybrid Perovskite $CH_3NH_3PbI_3$. *J. Phys. Chem. Lett.* **2014**, *5* (14), 2488–2492. https://doi.org/10.1021/jz5012109.

(151)   Brunetti, B.; Cavallo, C.; Ciccioli, A.; Gigli, G.; Latini, A. On the Thermal and Thermodynamic (In)Stability of Methylammonium Lead Halide Perovskites. *Sci. Rep.* **2016**, *6*, 31896. https://doi.org/10.1038/srep31896.

(152)   Lee, S.-W.; Kim, S.; Bae, S.; Cho, K.; Chung, T.; Mundt, L. E.; Lee, S.; Park, S.; Park, H.; Schubert, M. C.; et al. UV Degradation and Recovery of Perovskite Solar Cells. *Sci. Rep.* **2016**, *6*, 38150. https://doi.org/10.1038/srep38150.

(153)   Tsai, C.-H.; Li, N.; Lee, C.-C.; Wu, H.-C.; Zhu, Z.; Wang, L.; Chen, W.-C.; Yan, H.; Chueh, C.-C. Efficient and UV-Stable Perovskite Solar Cells Enabled by Side Chain-Engineered Polymeric Hole-Transporting Layers. *J. Mater. Chem. A* **2018**, *6* (27), 12999–13004. https://doi.org/10.1039/C8TA03608J.

(154)   Kato, Y.; Ono, L. K.; Lee, M. V.; Wang, S.; Raga, S. R.; Qi, Y. Silver Iodide Formation in Methyl Ammonium Lead Iodide Perovskite Solar Cells with Silver Top Electrodes. *Adv. Mater. Interfaces* **2015**, *2* (13), 1500195. https://doi.org/10.1002/admi.201500195.

(155)   Sherkar, T. S.; Momblona, C.; Gil-Escrig, L.; Ávila, J.; Sessolo, M.; Bolink, H. J.; Koster, L. J. A. Recombination in Perovskite Solar Cells: Significance of Grain Boundaries, Interface

Traps, and Defect Ions. *ACS Energy Lett.* **2017**, *2* (5), 1214–1222. https://doi.org/10.1021/acsenergylett.7b00236.

(156) Fabini, D. Quantifying the Potential for Lead Pollution from Halide Perovskite Photovoltaics. *J. Phys. Chem. Lett.* **2015**, *6* (18), 3546–3548. https://doi.org/10.1021/acs.jpclett.5b01747.

(157) Chen, P.-Y.; Qi, J.; Klug, M. T.; Dang, X.; Hammond, P. T.; Belcher, A. M. Environmentally Responsible Fabrication of Efficient Perovskite Solar Cells from Recycled Car Batteries. *Energy Environ. Sci.* **2014**, *7* (11), 3659–3665. https://doi.org/10.1039/C4EE00965G.

(158) Xiao, Z.; Song, Z.; Yan, Y. From Lead Halide Perovskites to Lead-Free Metal Halide Perovskites and Perovskite Derivatives. *Adv. Mater. 0* (0), 1803792. https://doi.org/10.1002/adma.201803792.

(159) Pazoki, M.; Johansson, M. B.; Zhu, H.; Broqvist, P.; Edvinsson, T.; Boschloo, G.; Johansson, E. M. J. Bismuth Iodide Perovskite Materials for Solar Cell Applications: Electronic Structure, Optical Transitions, and Directional Charge Transport. *J. Phys. Chem. C* **2016**, *120* (51), 29039–29046. https://doi.org/10.1021/acs.jpcc.6b11745.

(160) Kopacic, I.; Friesenbichler, B.; Hoefler, S. F.; Kunert, B.; Plank, H.; Rath, T.; Trimmel, G. Enhanced Performance of Germanium Halide Perovskite Solar Cells through Compositional Engineering. *ACS Appl. Energy Mater.* **2018**, *1* (2), 343–347. https://doi.org/10.1021/acsaem.8b00007.

(161) Shai, X.; Zuo, L.; Sun, P.; Liao, P.; Huang, W.; Yao, E.-P.; Li, H.; Liu, S.; Shen, Y.; Yang, Y.; et al. Efficient Planar Perovskite Solar Cells Using Halide Sr-Substituted Pb Perovskite. *Nano Energy* **2017**, *36*, 213–222. https://doi.org/10.1016/j.nanoen.2017.04.047.

(162) Uribe, J. I.; Ramirez, D.; Osorio-Guillén, J. M.; Osorio, J.; Jaramillo, F. $CH_3NH_3CaI_3$ Perovskite: Synthesis, Characterization, and First-Principles Studies. *J. Phys. Chem. C* **2016**, *120* (30), 16393–16398. https://doi.org/10.1021/acs.jpcc.6b04207.

(163) Liao, W.; Zhao, D.; Yu, Y.; Grice, C. R.; Wang, C.; Cimaroli, A. J.; Schulz, P.; Meng, W.; Zhu, K.; Xiong, R.-G.; et al. Lead-Free Inverted Planar Formamidinium Tin Triiodide Perovskite Solar Cells Achieving Power Conversion Efficiencies up to 6.22%. *Adv. Mater.* **2016**, *28* (42), 9333–9340. https://doi.org/10.1002/adma.201602992.

(164) Dualeh, A.; Moehl, T.; Tétreault, N.; Teuscher, J.; Gao, P.; Nazeeruddin, M. K.; Grätzel, M. Impedance Spectroscopic Analysis of Lead Iodide Perovskite-Sensitized Solid-State Solar Cells. *ACS Nano* **2014**, *8* (1), 362–373. https://doi.org/10.1021/nn404323g.

(165) Liu, P.; Wang, W.; Liu, S.; Yang, H.; Shao, Z. Fundamental Understanding of Photocurrent Hysteresis in Perovskite Solar Cells. *Adv. Energy Mater.* **2019**, *9* (13), 1803017. https://doi.org/10.1002/aenm.201803017.

(166) Castro-Méndez, A.-F.; Hidalgo, J.; Correa-Baena, J.-P. The Role of Grain Boundaries in Perovskite Solar Cells. *Adv. Energy Mater.* **2019**, 1901489. https://doi.org/10.1002/aenm.201901489.

(167) Song, Z.; McElvany, C. L.; Phillips, A. B.; Celik, I.; Krantz, P. W.; Watthage, S. C.; Liyanage, G. K.; Apul, D.; Heben, M. J. A Technoeconomic Analysis of Perovskite Solar Module Manufacturing with Low-Cost Materials and Techniques. *Energy Environ. Sci.* **2017**, *10* (6), 1297–1305. https://doi.org/10.1039/C7EE00757D.

Chapter 2

Experimental Methods

This chapter introduces the various experimental methods used throughout this thesis. Specifically, Section 2.1 describes the thin-film deposition techniques used in the manufacture of solar cells. The fabrication procedures followed for the different cell architectures are detailed in Section 2.2. Section 2.3 is dedicated to the electrical characterization of the completed photovoltaic devices, while Section 2.4 provides background information on the techniques used to characterize the opto-electrical and morphological properties of thin films.

2.1. Thin-Film Deposition Techniques

The controlled deposition of materials as thin films is a fundamental step in the manufacture of perovskite solar cells. Proper understanding of thin-film deposition processes is crucial to fabricating high-efficiency devices. In this thesis, two main deposition techniques were used: spin-coating (to deposit perovskite and charge-transport layers) and vacuum thermal evaporation (to deposit metal top electrodes and electrode interlayers).

2.1.1. Spin-coating

Spin-coating is one of the most common techniques employed to deposit uniform thin films from solution. It is widely used in the manufacture of integrated circuits, optical mirrors, solar cells, detectors, sensors, photoresists, flat screen display coatings, *etc.*[1–7] In short, it is ubiquitous throughout the nanotechnology and semiconductor sectors. This technique simply utilizes centrifugal forces created by a spinning substrate to spread a coating solution evenly over the surface. In general, the spin mechanism requires a sample holder (typically connected to a vacuum pump), a motor and controller used to spin the substrate at a specified spin rate and time, and a spin bowl to catch excess material. The spin-coating setup is schematized in **Figure 2.1**.
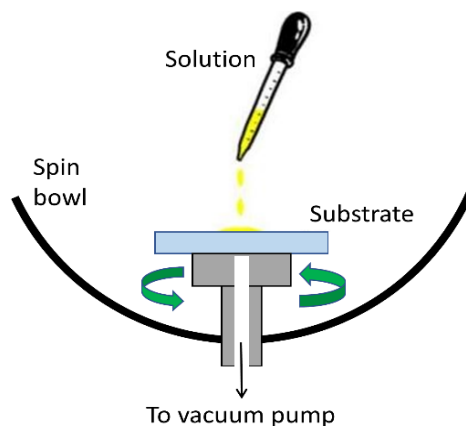
Figure 2.1. *Basic setup for spin-coating.*

The whole process of spin-coating can be divided into four key stages: deposition, spin-up, spin-off, and evaporation (see **Figure 2.2**). In the first stage, the desired material (or suitable precursors)

is dissolved in an appropriate solvent and the resulting solution is dispensed onto the substrate. Liquid dispensing can be static (the solution is placed upon the substrate while it is stationary) or dynamic (the solution is dispensed as the substrate is rotating). The latter is generally preferred as it is a more controlled and reproducible process. For this reason, a dynamic procedure was selected in this thesis for the deposition of perovskite films, as described in Section 2 of this chapter. The second stage, called spin-up stage, is when the substrate is accelerated up to its final, desired, rotation speed, typically between 1000 and 5000 rpm. This stage is characterized by aggressive expulsion of the excess fluid from the surface of the substrate due to centrifugal forces. In the spin-off stage, also known as flow-controlled stage, the substrate rotates at a constant rate and viscous forces dominate fluid thinning behavior. As the fluid thins down, the expulsion of the excess fluid decreases because the thinner the film, the higher its resistance to flow. The last stage is the drying stage, in which centrifugal outflow stops and evaporation becomes the main mechanism of solvent removal and thinning of the film (evaporation-controlled stage). The applied solvent is usually volatile, and hence evaporates relatively quickly (typically within 30 seconds). Complete evaporation results in the formation of a solid thin film on the substrate.
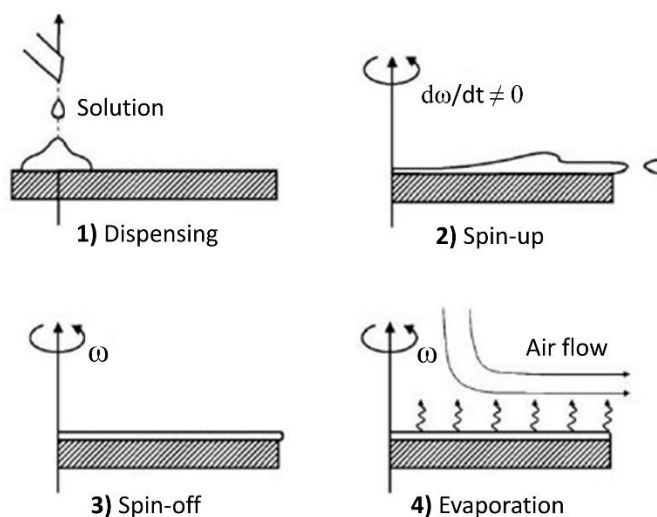
Figure 2.2. Stages of thin film deposition by the spin-coating method.

Several processing parameters are involved in the spin-coating method, including dispense volume, spin speed, acceleration rate, solution viscosity and concentration, spin time, *etc*. The spin speed of the substrate is one of the most important factors as it affects the degree of centrifugal

force applied to the liquid as well as the velocity and turbulence of the air immediately above it. In general, the thickness of a spin-coated film is proportional to the inverse of the spin speed squared as in the below equation, where t is the thickness and ω is the angular speed:

$$t \propto \frac{1}{\sqrt{\omega}}$$
{2.1}

The final thickness of the film will also depend upon the material concentration and solvent evaporation rate, which in turn depends upon the vapor pressure, viscosity, temperature, and humidity. Mathematically modeling the spin-coating process and predicting the resulting film thickness is extremely challenging because of the complex coupling of fluid rheology and solvent evaporation. For this reason, a test film is typically spin-coated and the thickness measured by surface profilometry, ellipsometry, or atomic force microscopy (see Appendix A).

The selection of appropriate solvent is crucial to the outcome of any spin-coating process. Low boiling point solvents such as chloroform, chlorobenzene, and isopropanol are typically used as they evaporate quickly to give good surface coverage. Contrarily, if a high boiling point solvent is used, surface coating is harder to be achieved because the liquid has time to dewet and is flung off the side. An interesting way to improve spin-coating uniformity is to use a mixture of solvents, whose major component has a low boiling point (fast evaporation rate), whereas the minor has a high boiling temperature (low evaporation rate). In this way, the fast evaporating solvent is removed quickly, ensuring a good surface coverage, and the remaining minor component leaves enough plasticity for atoms and molecules in the film to self-organize before the film itself is completely dried. A strategy of this type was developed as a part of this thesis and enabled perovskite films with enhanced uniformity and crystallinity to be obtained by using a mixture of dimethylformamide and α-terpineol (see Chapter 4).

Spin-coating is an incredibly effective technique for thin film research. It is simple, quick, low-cost, and extremely versatile as it can work with many types of coating solutions and can be controlled by a few parameters to yield a well-defined coating. The biggest disadvantage of spin-coating is its lack of material efficiency: typical spin-coating processes utilize only 5-10% of the material dispensed onto the substrate, while the remaining 95–90% is flung off the edge of the substrate and wasted. Moreover, it is an inherently batch-to-batch (single substrate) technique and therefore has a low throughput compared to other deposition processes. Despite these drawbacks, spin-coating is usually the starting point and benchmark for most research and industrial activities

that require a thin and uniform surface coating. In this thesis, spin-coating depositions were performed either in ambient conditions using a Laurell spin-coater (model WS-650S-6NPP/A1/AR1) or in an inert atmosphere using a spin-coater (model MB-SC-200) located inside a nitrogen-filled glove box system (MBRAUN, Germany).

2.1.2. Vacuum Thermal Evaporation

Vacuum thermal evaporation is a very well-known technology adopted in opto-electronics to produce thin films and surface coatings.[8–10] It is regarded as one of the traditional physical vapor deposition (PVD) techniques, a family of thin-film deposition methods which rely on the vaporization of material from a solid source and its subsequent condensation onto a substrate surface in a high vacuum environment. PVD technologies differ from one another basically in the methods used to form the coating vapor. In the thermal evaporation process, vaporization is accomplished by heating the source material above its evaporation (or sublimation) point using electrical energy. Most commonly, the required heat is provided by passing a high electrical current through a resistive element which contains the material to be deposited. The latter is thus intensively heated by the Joule effect until its evaporation (resistive thermal evaporation).

A simple evaporator diagram is shown in **Figure 2.3**. The deposition system consists of a vacuum chamber, which in typical laboratory equipment is designed to achieve high vacuum levels (10^{-6} mbar). The absence of other gas molecules in the chamber allows for a collision-free path of the evaporated material to the substrate and prevents unwanted reactions, heat transfer and contamination. Since heating is accomplished in a vacuum, the temperature required for vaporization is significantly lower than the corresponding temperature required at atmospheric pressure. In addition to a vacuum pump, any evaporation system includes a series of thermal sources, called evaporation sources, in order to allow either multiple or co-deposition processes. Each source can allocate a suitable resistive element where the target material is placed (in the form of powder, wire, or pellets) and which can be heated very simply by means of an external power supply. Typical resistive elements are made of refractory metals such as tungsten, tantalum, and molybdenum (capable of withstanding high temperatures) and are available in different shapes and configurations – filament, boat, crucible, basket – to allow for rapid heating and to realize a uniform distribution of the vapor flux. The two types of resistive elements used in this thesis are

shown in **Figure 2.4**. The substrate to be coated is loaded in a suitable substrate holder which is usually positioned above the sources and can be mechanically rotated so that all exposed surfaces of the sample are uniformly coated during the evaporation process. A shadow mask, also referred to as an evaporation mask, is typically installed below the deposition surface of the substrate in order to obtain a specific deposition pattern. The mask simply stops material from being deposited onto a sample in a desired pattern overlay, creating a 'shadow' area on the substrate on which no material is deposited (see Section 2.2). The evaporation chamber is also equipped with different mechanical shutters which allow to protect the sample from uncontrolled deposition during ramping up or cooling down of the sources.
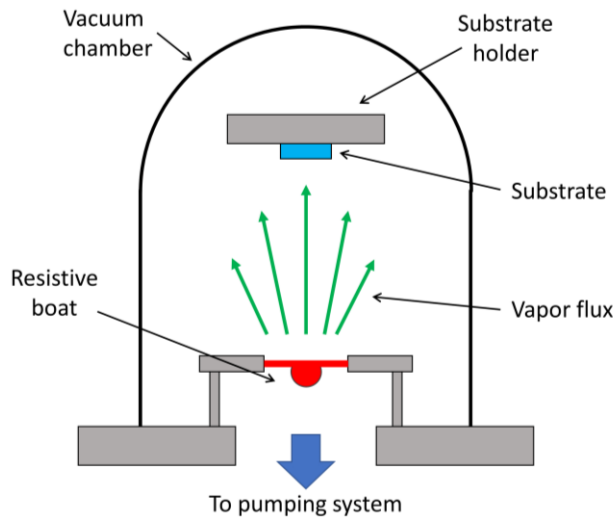
Figure 2.3. Schematic of a thermal evaporation system.

During the evaporation process, the input power is opportunely adjusted to reach the desired deposition rate, which is determined by the vapor pressure of the source material at the evaporation temperature. The deposition rate is commonly measured using a quartz crystal microbalance (QCM) located inside the chamber. This device consists of a resonator plate which mechanically oscillates when ac voltage is applied to it (thanks to the piezoelectric effect). As material is deposited onto the crystal, the resonance frequency of oscillations decreases, and this can be used to calculate the thickness of the deposited layer. The quartz crystal monitor must be opportunely programmed for each material (density, Z-ratio, and tooling factor). The Z-ratio is a parameter that corrects the frequency-change-to-thickness transfer function for the effects of acoustic impedance

mismatch between the crystal and the deposited material. The tooling factor is used to correct the geometrical difference between the position of the crystal sensor and the substrates.

Figure 2.4. Examples of resistive elements for thermal evaporation: spiral tungsten filament (left); dimpled boat in a resistive media (right).

Thermal evaporation represents a simple and versatile coating technology, applicable to a wide combination of coating substances (metals, alloys, ceramics) and substrate materials (metals, glass, plastics). It is most commonly used to deposit metallic contact layers for thin-film devices, including solar cells and transistors, but virtually anything that can be heated to vaporization can be deposited by resistive evaporation. Key advantages of this technique, with respect for example to solution-based processes, are the possibility of achieving a nanometer control of each layer thickness and the capability of easily stacking multilayers. These advantages were widely exploited in this thesis for the fabrication of multilayer transparent electrodes (see Chapter 3). On the other hand, one issue that has to be considered is the material usage, which may not be efficient due to lack of directionality of the evaporation cone. Control of uniformity requires relatively large chambers where the samples can be positioned far away from the sources, this resulting in a significant waste of material. In this thesis, a thermal evaporator (MB-EVAP) integrated in the glove box system and equipped with a turbo pump and a rate/thickness monitoring unit (SQM-160) was used.

2.2. Solar Cell Fabrication

In this thesis, solar cells were prepared by depositing a series of thin layers on top of FTO-coated glass substrates through the spin-coating and thermal evaporation techniques. Perovskite cells with two different architectures were fabricated: planar n-i-p (regular) architecture; mesoscopic n-i-p (regular) architecture. The planar n-i-p architecture was extensively used in the part of the thesis reported in Chapters 3 and 4 and focused on semitransparent design and additive engineering. On the other hand, mesoscopic structures were used in Chapter 5 to investigate the efficiency of new mesoporous titania scaffolds. The corresponding fabrication procedures are detailed here below.

2.2.1. Materials

The choice of material grade, material supplier and subsequent purification steps is vital to ensure reproducibility of cell performance. In this thesis, all chemicals were used as received without any further purification. Methylammonium iodide (MAI, 99.9%) was purchased from Ossila. Lead chloride ($PbCl_2$, 99.999%), gold wire (Au, 99.9%), silver wire (Ag, 99.99%), copper wire (Cu, 99.999%), and hydrochloric acid (HCl, 37 wt% in water) were obtained from Alfa Aesar. Titanium(IV) isopropoxide (99.999%, trace metals basis), titanium(IV) butoxide (97%, reagent grade), molybdenum (VI) oxide (MoO_3, 99.97%, trace metals basis), 4-*tert*-butylpyridine (TBP, 96%), bis(trifluoromethane)sulfonimide lithium salt (LiTFSI, 99.95%, trace metals basis), chlorobenzene (CB, anhydrous, 99.8%), acetonitrile (ACN, anhydrous, 99.8%), N,N-dimethylformamide (DMF, anhydrous, 99.8%), isopropyl alcohol (IPA, anhydrous, 99.5%), ethyl alcohol (≥99.8%), acetic acid (99%), 2-ethylimidazole (98%), α-terpineol (90%, technical grade), Triton X-100 (laboratory grade), ethyl cellulose (viscosity 22 cp, 5% in toluene/ethanol 80:20), urea (≥98%, reagent grade), and chloroplatinic acid hydrate (99.995%, trace metals basis) were supplied by Sigma Aldrich. 2,2',7,7'-tetrakis[N,N-di(4-methoxyphenyl)amino]-9,9-spirobifluorene (Spiro-OMeTAD) was obtained from Solaronix. Fluorine-doped tin oxide (FTO)-coated glass slides (TEC7) were purchased from two different suppliers: Dyesol (used in Chapter 3) and Visiontek Systems Ltd (used in Chapter 4 and 5). Both types of FTO provided a sheet resistance of 7 Ω sq^{-1}. Poly(3-hexylthiophene-2,5-dyil) (P3HT, regioregular 91-94%, average M_n 50-70K, electronic grade) was supplied by Rieke Metals. The three conjugated copolymers used

in Chapter 5 as alternative hole-transport layers were synthesized by Dr. Francesco Giacalone and co-workers from the Department of Biological, Chemical, and Pharmaceutical Sciences and Technologies (STeBiCeF) of the University of Palermo. More details about these three copolymers can be found on Chapter 5.

2.2.2. Planar n-i-p Architectures

Reference Protocol

Proper cleaning and preparation of substrate is critical to the success of the subsequent spin-coating deposition. FTO-coated glass substrates were cut into a required dimension (25 mm × 25 mm) and subjected to the following cleaning procedure:

- ultrasonic bath in acetone for 15 min;
- ultrasonic bath in isopropyl alcohol for 15 min;
- drying in nitrogen (N_2) flux.

The substrates were then kept at 110 °C for approximately 16 hours.

After the standard cleaning procedure, the substrates were exposed to ultraviolet-ozone (UVO) treatment for 40 minutes in order to remove any organic contamination and improve the wettability of the hydrophobic FTO layer. Immediately after UVO cleaning, a compact titania (c-TiO_2) hole-blocking layer was deposited by a sol-gel route: a mildly acidic solution of titanium(IV) isopropoxide in isopropanol (titanium isopropoxide / 2 M HCl / IPA = 175 µL / 17.5 µL / 2.5 mL) was spin-coated through a 0.2 µm PTFE filter onto the FTO substrate at 2000 rpm for 60 s, and then calcined in air at 500 °C for 45 min. During the spin-coating step, a small area in one edge of the substrate was masked by means of common adhesive tape in order to keep a portion of the FTO layer uncovered for subsequent electrical characterization.

The mixed-halide $CH_3NH_3PbI_{3-x}Cl_x$ perovskite was selected to be the absorber material. To prepare the $CH_3NH_3PbI_{3-x}Cl_x$ film, a 3:1 molar ratio of CH_3NH_3I and $PbCl_2$ was dissolved in anhydrous DMF at a concentration of 40 wt%. To ensure a complete dissolution, the mixture was stirred overnight at room temperature. The obtained precursor solution was spin-coated dynamically onto the TiO_2-coated FTO substrate at 2000 rpm for 20 s (one-step spin-coating; dispense volume = 140 µL), followed by thermal annealing on a hot plate at 105°C for 1.5 h. The

gradual formation of the desired perovskite phase during the thermal treatment was very obvious to the eye, involving a typical color transition from bright yellow to dark brown/black. Subsequently, a hole-transport layer was deposited from a solution consisting of 72.3 mg of spiro-OMeTAD dissolved in 1 mL of CB, 28.8 µL of TBP, and 17.5 µL of a LiTFSI solution (520 g/L in ACN). The solution was spin-coated on the perovskite layer at 4000 rpm for 45 s. The devices were then stored overnight inside a desiccator in air to allow the oxidation of spiro-OMeTAD. Lastly, the opaque top electrode, consisting of 6 nm thick MoO_x as anode buffer layer and 100 nm thick Ag or Au as rear contact, was thermally evaporated onto the $FTO/c\text{-}TiO_2/CH_3NH_3PbI_{3\text{-}x}Cl_x$/spiro-OMeTAD surface through a shadow mask under a vacuum of 5×10^{-6} mbar. The mask used in this work consists of a brass plate with holes drilled in it. The holes were of different diameters, namely 2, 3 and 4 mm, enabling the investigation of the effect of the increasing active area (3.14, 7.07 and 12.56 mm^2, respectively) on the device performance. The evaporation rate was set to be 0.3 Å/s for MoO_x and 2 Å/s for Ag or Au. Except for the $c\text{-}TiO_2$ deposition, all the processing steps were performed within a glove box system (MBraun, Germany) filled with N_2 (O_2, H_2O < 0.1 ppm). The complete fabrication procedure is schematized in **Figure 2.5**.
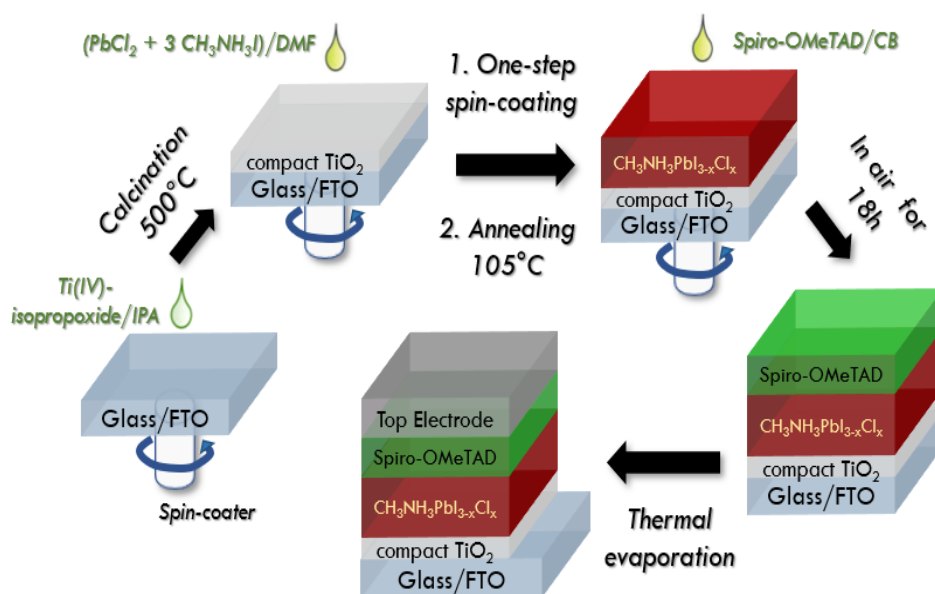

Figure 2.5. *Schematic of the fabrication procedure used in this work to prepare planar n-i-p PSCs with a glass/FTO/CH₃NH₃PbI₃₋ₓClₓ/spiro-OMeTAD/MoOₓ/Ag (or Au) architecture.*

Semitransparent Design

The semitransparent solar cells investigated in Chapter 3 were prepared with the same n-i-p planar architecture, but the opaque top electrode was replaced with opportunely designed DMD transparent electrodes. In particular, a novel multilayer MoO_x (6 nm)/Au-seed (1.5 nm)/Cu (9.5 nm)/MoO_x (20 nm) DMD transparent electrode was developed by thermal evaporation and used as a top anode. The evaporation rate was set to be 0.3 Å/s for MoO_x, 0.1 Å/s for Au, and 0.4 Å/s for Cu. For comparison purposes, MoO_x/Au/MoO_x and MoO_x/Cu/MoO_x transparent architectures were also prepared, where the gold-seeded Cu layer was replaced by a 11-nm-thick Au or Cu film respectively. All the layer thicknesses were monitored through the calibrated quartz crystal microbalance placed inside the evaporation chamber. Therefore, the very small thicknesses given in Chapter 3 must be interpreted in terms of equivalent thickness, indicating the amount of deposited material. In addition, the perovskite thickness was opportunely tuned by varying the precursor concentration in order to achieve acceptable transparency levels for practical ST applications. Four different concentrations of the precursor solution were used, namely 15, 20, 30 and 40 wt%. The active area of the devices was 3.14 mm^2.

α-Terpineol as Solvent Additive

In this thesis, the potential of α-terpineol as a solvent additive was also explored, as reported in Chapter 4. The additive was incorporated into the $CH_3NH_3PbI_{3-x}Cl_x$ precursor solution prior to the one-step spin-coating deposition. Two different concentrations of α-terpineol were used, namely 5 and 25 g/L, and the corresponding effect on the perovskite morphology was investigated.

Alternative Hole-Transport Layers

In Chapter 5 three different conjugated copolymers, as well as P3HT, were used as dopant-free HTMs in place of spiro-OMeTAD. For the spin-coating deposition of the hole-transport layers, the above materials were dissolved in CB at a concentration of 15 g/L, without the addition of any doping additive. The obtained solutions were spin-coated through a 0.2 μm PTFE filter onto the perovskite/c-TiO_2/FTO/glass substrates at 2000 rpm for 45 s.

2.2.3. Mesoporous n-i-p Architectures

The mesoporous n-i-p PSCs studied in Chapter 5 were fabricated with the same procedure as that used for planar devices, except for the incorporation of a mesoporous titania-based ETL between the c-TiO$_2$ film and the perovskite film. Both zero-dimensional (0D) and one-dimensional (1D) titania nanostructures were employed to prepare the mesoporous films. Specifically, reduced (blue) titania nanoparticles (undoped, Pt-doped, N-doped) were synthesized through a sol-gel route and opportunely dispersed for spin-coating, while titania nanorod arrays were grown directly on top of the c-TiO$_2$/FTO/glass substrates by hydrothermal method. The protocols are detailed here below.

Synthesis of Blue Titania Nanoparticles

Reduced (blue) titania was synthesized as reported by S. Hamdy et al.:[11] a solution composed of 12.6 mL of ethanol, 2 mL of HCl (37%), 2 mL of titanium(IV) isopropoxide, and 1.8 g of 2-ethylimidazole was stirred for a period of 15 min at 350 rpm and subsequently calcined at 500 °C for 5 h in a porcelain crucible inside a preheated oven. The obtained precipitation was opportunely washed and then dried at 80 °C overnight, resulting in a bluish/greyish powder. To obtain N-doped and Pt-doped blue titania nanoparticles, 0.4 g of urea or 0.02 g of chloroplatinic acid hydrate were added to the starting solution, respectively.

To fabricate the mesoporous layers, blue-TiO$_2$ pastes were prepared by dispersing 100 mg of the obtained blue-TiO$_2$ nanoparticles (undoped, N-doped, or Pt-doped) into a solution containing 2.53 mL of ethanol, 25 mg of ethyl cellulose, 20 μL of ultrapure water, 20 μL of acetic acid, 10 μL of Triton X-100 (used as a dispersing agent), and 324 μL of α-terpineol (used to provide proper viscosity). The pastes were vigorously stirred overnight and then left for a couple of hours to suppress the formation of bubbles. The as-prepared blue-TiO$_2$ slurries were deposited onto c-TiO$_2$/FTO/glass substrates by spin-coating at a rate of 5000 rpm for 30 s and then calcined at 500 °C for 30 min to obtain the desired mesoporous films.

Hydrothermal Growth of Titania Nanorod Arrays

TiO$_2$ NR arrays were grown by hydrothermal method as reported by W. Liu et al.:[12] 15 mL of HCl (37 wt% in water) was diluted with 15 mL deionized water, and then 260 μL of titanium (IV) butoxide was added dropwise into the above mixed solution under magnetic stirring. Subsequently, a c-TiO$_2$/FTO/glass substrate was submerged with face-down into the above precursor solution in

a Teflon-line stainless steel autoclave, heated at 150 °C for 2 h, and then cooled down to room temperature naturally. The obtained white film-coated FTO glass was washed with deionized water, dried in air, and finally calcined at 500 °C for 30 min to increase the crystallinity. The as-prepared TiO_2 NR film was used as a mesoporous scaffold in mesoscopic n-i-p PSCs. To achieve higher PCEs, the autoclaving time was reduced from 2 h to 1 h, and then from 1 h to 0.5 h.

2.3. Cell Characterization and Testing

In this section, the equipment required and methods used to test the electrical output performance of the solar cells are briefly described.

2.3.1. Solar Simulation

For a reliable photovoltaic testing, accurate illumination is critical to allow comparisons between samples of different designs from various manufacturers. Outdoor testing with sunlight under the natural ambient conditions would be an ideal circumstance as it represents reality. However, the incident solar radiation intensity, angle of incidence, direct-to-diffuse ratio, albedo, spectral distribution, ambient temperature and weather conditions vary so widely that the scientific requirement of repeatability cannot be achieved. This explains the need for solar simulation and standard indoor test conditions.[13]

In order to simulate a particular spectral response, we must first consider the solar spectrum and its specific features originating from the passing of photons through the Earth's atmosphere. The sun emits light with a spectrum approximately equal to that of a black body with a temperature of 5870 K. When photons travel through the Earth's atmosphere, absorption occurs due to O_2, O_3, H_2O, CO_2, and other molecules and particles. The Air Mass (AM) parameter defines the direct optical path length of photons through the atmosphere, expressed as a ratio relative to the path length vertically upwards, with the sun at the zenith. In other words, it refers to the mass of air through which solar radiation has passed, with AM0 corresponding to the solar irradiance just outside the atmosphere and AM1 corresponding to the light incident normal to the Earth's surface. Any deviation from AM1 will increase the path length, leading to higher AM values. **Figure 2.6** displays the dependence of AM on the zenith angle (θ), with the relative AM ratio calculated using the following equation:

$$AM = \frac{1}{\cos \theta} \qquad \qquad \{2.2\}$$

The convention for characterizing PV devices is to use the AM1.5G (Global) spectrum, with a total irradiance of 100 mW cm^{-2}, as shown in Figure 2.6, which corresponds to sunlight incident upon a sun-facing 37°-tilted surface at an angle of 48.2° relative to the normal to the Earth's surface

on a clear day. Contrarily to the AM1.5D (Direct) spectrum, the global spectrum also takes into account scattering, reflections and diffuse sources. This spectrum is representative of the solar spectrum encountered terrestrially at mid-latitudes, for example much of North America and Europe. The standard intensity of 100 mW cm^{-2} is usually chosen as a unit of solar irradiance "sun" (1 sun = 100 mW cm^{-2}), which is widely used in solar system research. In comparison, AM0 has an intensity of 135 mW cm^{-2} and is used to simulate the solar spectrum for space applications. In addition to the AM1.5G spectrum and 100 mW cm^{-2} irradiance, the Standard Test Conditions (STC) include a device operating temperature of 25 °C and the absence of wind.
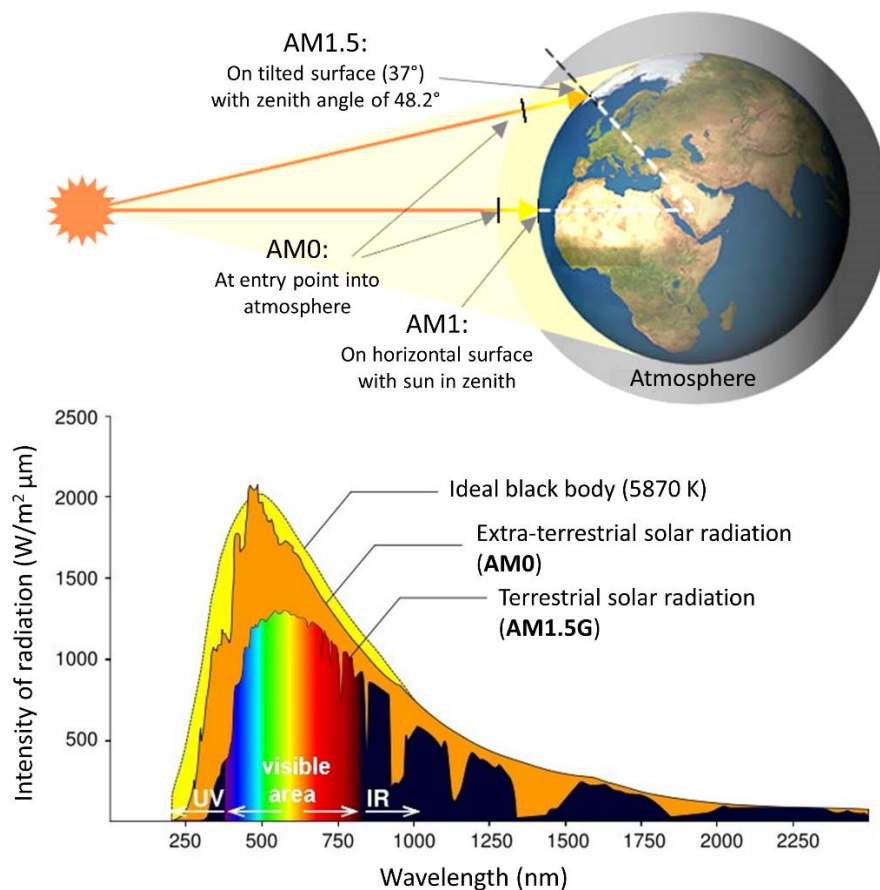
Figure 2.6. *Explanation of Air Mass (AM) notion (above). Ideal black body radiation (5870 °C), AM0 and AM1.5G solar irradiance spectra (below).*

Careful choice of the source of illumination is required in order to recreate the AM1.5G spectral profile under laboratory conditions. In this regard, solar simulators play an important part in PV research as they can offer illumination approximating natural sunlight, thus providing a

controllable indoor test facility. In general, a solar simulator consists of two main components: (1) light source and associated power supply; (2) any optical elements and filters used to modify the output beam in order to meet specific requirements. Regardless of the type, a solar simulator is currently evaluated based on three unique criteria: (1) spectral match to the reference spectrum over a certain wavelength range; (2) uniformity of the irradiance within the test plane; (3) temporal stability of the irradiance during the measurement. Based on these criteria, solar simulators can be classified in one of three classes: A, B or C. The specifications required for each class have been defined by different organizations such as the American Society for Testing and Materials (ASTM).[14]

Various lamps have been proposed for solar simulation, including xenon arc lamps, metal halide arc lamps, tungsten halogen lamps, and light emitting diodes (LEDs).[15] The xenon (Xe) arc lamp is the most widely used light source for almost all kinds of solar simulators, principally because of its stable spectral qualities and excellent continuum in the ultraviolet (UV) and visible regions. However, this type of lamp is also characterized by many undesirable emission peaks in the infrared (IR) between 800-1000 nm, which can be filtered by suitable filters, and it requires an expensive and complex power supply, which makes it nearly the most expensive commercial light source. A low-cost alternative to Xe lamps is represented by tungsten halogen lamps, with their inexpensive and excellent light output and consistency. But a key drawback of these lamps that must be considered is their relatively poor spectral match to the solar spectrum in the UV region, as evident from **Figure 2.7**. The brightest tungsten lamps operate at color temperatures of 3200K (lower than that of the sun of about 5900 K), and as a result, they radiate weaker in the shorter wavelengths (blue and UV portion) and stronger in the IR portion. Such a mismatch leaves a significant UV deficit and may invalidate quantitative data. However, this kind of light sources are a valid alternative to Xe lamps for qualitative or comparative studies with less restrictive spectrum requirements.

In this report, a halogen lamp (Osram 93592, 400 W, 3200 K) was used to characterize and compare the electrical performances of the solar cells fabricated in Chapter 3. In Chapters 4 and 5, the characterization of the devices was rather accomplished using a Sunlite Solar Simulator (model 11002, Class ABA, Abet Technologies) equipped with a 100 W xenon arc lamp and an AM1.5G filter. The simulators were calibrated using a commercial KG5-filtered Si reference cell

(model 15151, Abet Technologies) to obtain an incident light power of 100 mW cm^{-2} and to normalize the output from the device under test.
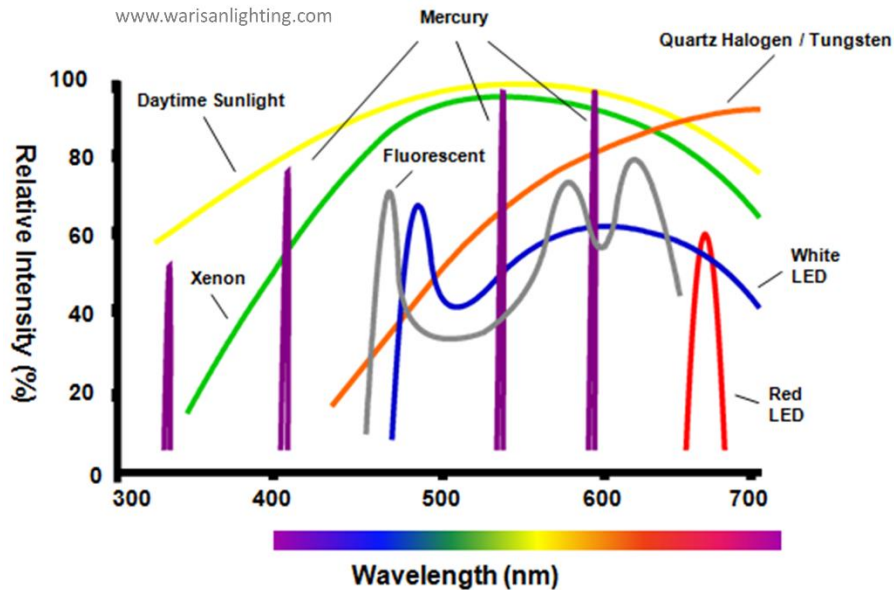
Figure 2.7. Simplified spectral profiles of several common light sources.

2.3.2. Current-Voltage Measurements

Solar cells are typically characterized by measuring their current-voltage (I-V) response under standard illumination conditions.[16] A source-measure unit is used to apply a source voltage across the device and measure the resulting current flow whilst the device is illuminated with a known spectrum of light. Analysis of the I-V curve allows for the extraction of the PCE and other useful metrics which give an insight on the workings of the solar cell under test. An example of this can be seen in **Figure 2.8**. It should be noted that current density (J) is generally used instead of current when characterizing solar cells, as the active area of the cell will have an impact on the output current (the larger the cell, the higher the current).

To understand the electrical behavior of a solar cell, it is useful to create a model which is electrically equivalent. A solar cell in the dark acts as a diode, a device which enables the flow of current only under direct polarization (with the anode positively polarized with respect to the cathode). Therefore, the electrical behavior of an ideal device in the dark can be modelled using the Shockley diode equation:

$$J_D = J_0 \left(e^{\frac{qV}{kT}} - 1 \right) \qquad \{2.3\}$$

where J_D is the diode current density, J_0 the reverse saturation current density, q the elementary charge, k the Boltzmann's constant, and T the absolute temperature. The current density J_0, observed while working in reverse polarization, is orders of magnitude lower than that flowing in direct polarization. When the cell is illuminated, a photocurrent J_{ph} is delivered thanks to the photovoltaic effect. As a result, the J-V curve is shifted downward into the fourth quadrant of the J-V plane (see Figure 2.8), where electric power (P = JV) is negative, meaning that it can be extracted from the device. An ideal solar cell can thus be modelled as a current source connected in parallel with a diode. Equation 2.3 transforms in:

$$J = J_D - J_{ph} = J_0 \left(e^{\frac{qV}{kT}} - 1 \right) - J_{ph} \qquad \{2.4\}$$

where J is the output current density of the cell.

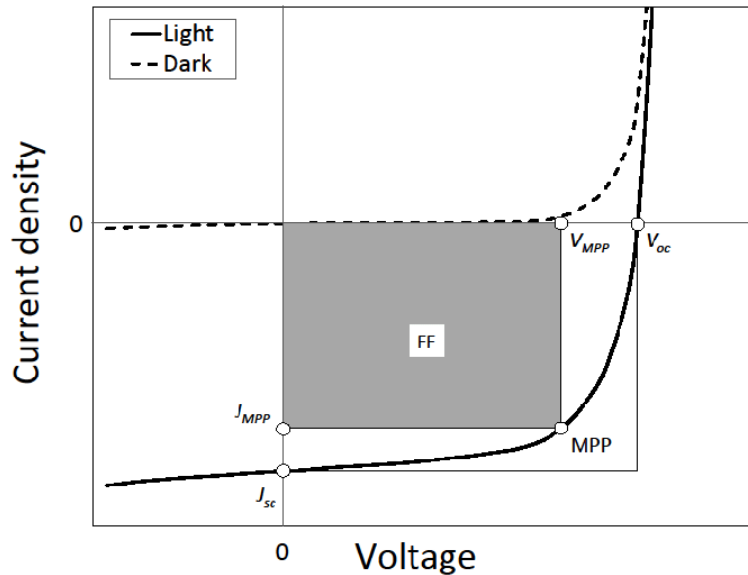**Figure 2.8.** *Typical current density-voltage (J-V) curves of a solar cell in the dark (dashed line) and under illumination (solid line). The relevant points on the curve are also indicated.*

Since the cell is generating power, the convention is to invert the current axis. The corresponding equation for the JV curve in the first quadrant is:

$$J = J_{ph} - J_0 \left(e^{\frac{qV}{kT}} - 1 \right) \qquad \{2.5\}$$

However, in reality, no device is ideal, and so Equation 2.5 must be modified to account for potential losses:

$$J = J_{ph} - J_0\left[e^{\frac{q(V+JR_S)}{nkT}} - 1\right] - \frac{V+JR_S}{R_{sh}} \qquad \{2.6\}$$

where n is the diode ideality factor, R_{sh} the shunt resistance, and R_s the series resistance. R_s accounts for resistances that may arise from energetic barriers at contacts and bulk resistances within the layers constituting the solar cell. Ideally, R_s should be close to $0\,\Omega$ to prevent efficiency losses due to increased charge carrier recombination, and this can be achieved by ensuring good energy level alignment of the materials. On the other hand, R_{sh} accounts for the existence of alternate current pathways (pinholes in the cell, non-ideal leaky contacts, etc.), and unlike R_s, it is ideally as high as possible to prevent current leakage. An estimate of R_s and R_{sh} can be obtained from the inverse of the slope of the J-V curve at $J = 0$ and at $V = 0$, respectively. Based on Equation 2.6, a solar cell can be modelled using the equivalent circuit diagram shown in **Figure 2.9**.
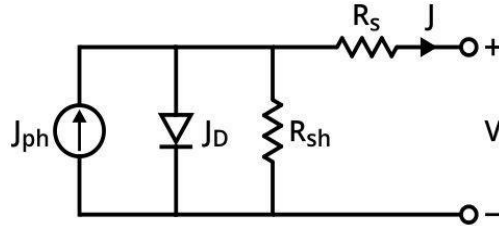
Figure 2.9. *The equivalent circuit of a solar cell.*

When the cell is operated at open-circuit condition ($J = 0$), the voltage across the output terminals is defined as the open-circuit voltage (V_{oc}, see Figure 2.7). Using Equation 2.6, and assuming R_{sh} is high enough to neglect the final term, V_{oc} can be expressed as:

$$V_{oc} \approx \frac{nkT}{q}\ln\left(\frac{J_{ph}}{J_0} + 1\right) \qquad \{2.7\}$$

Similarly, when the cell is operated at short-circuit condition ($V = 0$), the current flowing through the output terminals is defined as the short-circuit current (I_{sc}), and the corresponding current density as the short-circuit current density (J_{sc}, see Figure 2.7). For a high-quality solar cell (low R_s and J_0, and high R_{sh}), J_{sc} is:

$$J_{sc} \approx J_{ph} \qquad \{2.8\}$$

However, a solar cell neither works in short-circuit nor in open-circuit condition. It is rather connected to an external load, to which it delivers electric power. The maximum output power (P_{MPP}) that can be delivered by the cell is related to the fill factor (FF) of the J-V curve, which is defined as:

$$FF = \frac{P_{MPP}}{J_{sc}V_{oc}} = \frac{J_{MPP}V_{MPP}}{J_{sc}V_{oc}} \qquad \{2.9\}$$

where J_{MPP} and V_{MPP} are the current density and the voltage at maximum power point (MPP), respectively (see Figure 2.8).

These key cell parameters (V_{oc}, J_{sc}, FF) reflect the intrinsic behavior and quality of the device. J_{sc} is mainly determined by the number of absorbed photons and by the efficiency of exciton dissociation in free charge carriers. V_{oc} depends on J_0 (see Equation 2.7), which in turn depends on recombination in the solar cell, and therefore it is a measure of the amount of recombination in the device. FF is strictly linked to charge transport and recombination as well as shunt and series resistances. Once extracted from the J-V curve, these metrics can be used to calculate the power conversion efficiency, which is usually expressed in percentage and is defined as the ratio between the maximum electric power provided by the cell and the incident light power (P_{in}):

$$PCE = \frac{P_{MPP}}{P_{in}} = \frac{J_{sc}V_{oc}FF}{P_{in}} \qquad \{2.10\}$$

In this work of thesis, all the J-V measurements were performed in glove box at room temperature. A computer-controlled Keithley 4200 source-measure unit was used to apply a DC voltage ramp to the sample and measure the resulting output current. Specifically, the J-V characterization consisted in the following steps:

- J-V characterization in the dark: a voltage scan from −2 V to +2 V was applied to the cell, and the dark current was recorded. The analysis of the dark J-V curve provides useful information about the device quality in the dark (rectification properties of the diode, presence of short-circuits, etc.);

- J-V characterization under illumination (100 mW cm^{-2}, 1 sun). The fourth quadrant portion of the J-V characteristic was obtained by applying a voltage scan from -0.25 V to +1.75 V under standard illumination conditions. The cells were illuminated across the transparent TCO contact, using one of the two solar simulators previously described. The simulator is located out of the glove box, but light can hit the samples inside the glove box across a suitable quartz

window. The values of V_{oc}, J_{sc}, and FF were extracted from each curve, and the corresponding PCE was calculated at one sun.

- J-V characterization by varying the voltage scan direction. All J-V curves were acquired both in the forward (from -0.25 V to $+1.75$ V) and reverse (from $+1.75$ V to -0.25 V) scan direction, in order to assess any hysteresis effect in the solar cell under test.

- J-V characterization over time. The solar cells of interest were subjected to repeated J-V measurements over a certain period of time while stored in glove box, in order to assess their intrinsic stability.

In the following chapters, all the J-V curves will be reported with the current axis inverted (in the first quadrant), as dictated by convention.

2.4. Material and Thin Film Analysis

In addition to the J-V analysis, an in-depth characterization of the employed materials and thin films was performed in order to further understand the behavior and trends observed in solar cells. Their opto-electrical, morphological, and structural properties were investigated through a number of analytical techniques, including UV/vis spectroscopy, steady-state fluorescence spectroscopy, scanning electron microscopy (SEM), energy-dispersive X-ray spectroscopy (EDS), atomic force microscopy (AFM), X-ray diffraction (XRD), X-ray photoelectron spectroscopy (XPS), and four-probe method for resistivity measurements. Basic information about each of these techniques is provided in Appendix A. Optical absorption and transmission spectra of the perovskite films, the titania mesoporous films, the semitransparent electrodes, and the semitransparent solar cells fabricated in this thesis were acquired using a SPECORD S600 UV/vis spectrophotometer (Analytic Jena), equipped with a diode array detector and a combination of halogen and deuterium lamps as the light source. The spectra were taken over the spectral range 350-1020 nm and referenced to either air or glass slide. Fluorescence quenching experiments were carried out using a Fluoromax-4 spectrofluorimeter (HORIBA Jobin Yvon, Edison, USA); the excitation wavelength was fixed at 525 nm, and the spectra were normalized with respect to the absorbance. The SEM and AFM techniques were employed to investigate the surface morphology of the fabricated thin films. SEM imaging was performed using a FEI Quanta 200 microscope equipped with standard SE and BSE detectors and operated at an accelerating voltage of 30 kV. EDX spectra of the perovskite films were acquired with an EDAX Genesis XM4i detector (Link Analytical, Oxford Instruments, UK) in order to evaluate their elemental composition. AFM imaging was performed by using a Dimension Icon Instrument (Bruker, Germany). All images were acquired in AM tapping mode, using commercially available silicon probes (RTESP type; Bruker, Germany) and collecting 512×512 points per image at a scan rate of about 1 line s^{-1} or less. Surface roughness was calculated as the root-mean-square roughness R_q from 5×5 μm^2 or 2×2 μm^2 AFM images. In Chapter 3, AFM was also used to measure the thicknesses of the perovskite films and those of the multilayers constituting the DMD electrode. For this purpose, a sharp scratch was operated on each film using a blade, and the height of the obtained step was measured by scanning the corresponding area. XRD patterns of the perovskite and titania films were collected using a Philips PW 1050/39 diffractometer, in the Bragg Brentano geometry, equipped with a Ni-

filtered Cu Kα radiation source and operating at 40 kV and 30 mA. The XPS technique was mainly used to acquire compositional depth profiles of the multilayer transparent electrodes fabricated in Chapter 3. The depth-profiling XPS analysis was carried out with a PHI 5000 VersaProbe II system equipped with a monochromatic Al K_α source and a hemispherical analyser, using Ar^+ as the sputtering source (ULVAC-PHI). Sheet resistances of the multilayer transparent electrodes were measured through the four-probe method using a Summit 1100 probe station (Cascade Microtech, Inc.), and they were averaged over at least nine measurements per sample. The structures to be tested were deposited on plain glass substrates as well as on polyethylene terephthalate (PET) substrates for mechanical stability testing.

2.5. References

(1) Larson, R. G.; Rehg, T. J. Spin Coating. In *Liquid Film Coating: Scientific principles and their technological implications*; Kistler, S. F., Schweizer, P. M., Eds.; Springer Netherlands: Dordrecht, 1997; pp 709–734. https://doi.org/10.1007/978-94-011-5342-3_20.

(2) Spin Coating: A Complete Guide to Theory and Techniques. https://www.ossila.com/pages/spin-coating (accessed Sep 19, 2019).

(3) Taylor, J. F. Spin Coating: An Overview. *Met. Finish.* **2001**, *99* (1), 16–21. https://doi.org/10.1016/S0026-0576(01)80527-4.

(4) Sahu, N.; Parija, B.; Panigrahi, S. Fundamental Understanding and Modeling of Spin Coating Process: A Review. *Indian J. Phys.* **2009**, *83* (4), 493–502.

(5) Tyona, M. D. A Comprehensive Study of Spin Coating as a Thin Film Deposition Technique and Spin Coating Equipment. *Adv. Mater. Res.* **2013**, *2* (4), 181–193.

(6) Tyona, M. D. A Theoritical Study on Spin Coating Technique. *Adv. Mater. Res.* **2013**, *2* (4), 195–208.

(7) Aguilar, R. G.; López, J. O. Low Cost Instrumentation for Spin-Coating Deposition of Thin Films in an Undergraduate Laboratory. **2011**, *5* (2), 6.

(8) Mattox, D. M. Deposition Processes. In *The Foundations of Vacuum Coating Technology*; Mattox, D. M., Ed.; William Andrew Publishing: Norwich, NY, 2003; pp 11–33. https://doi.org/10.1016/B978-081551495-4.50009-7.

(9) Mattox, D. M. Vacuum Evaporation and Vacuum Deposition. In *Handbook of Physical Vapor Deposition (PVD) Processing (Second Edition)*; Mattox, D. M., Ed.; William Andrew Publishing: Boston, 2010; pp 195–235. https://doi.org/10.1016/B978-0-8155-2037-5.00006-X.

(10) Sarangan, A. Physical and Chemical Vapor Deposition. In *Nanofabrication: Principles to Laboratory Practice*; Routledge Handbooks Online, 2016. https://doi.org/10.1201/9781315370514-4.

(11) Hamdy, M. S.; Amrollahi, R.; Mul, G. Surface Ti3+-Containing (Blue) Titania: A Unique Photocatalyst with High Activity and Selectivity in Visible Light-Stimulated Selective Oxidation. *ACS Catal.* **2012**, *2* (12), 2641–2647. https://doi.org/10.1021/cs300593d.

(12) Liu, W.; Chu, L.; Hu, R.; Zhang, R.; Ma, Y.; Pu, Y.; Zhang, J.; Yang, J.; Li, X.; Huang, W. Diameter Engineering on TiO2 Nanorod Arrays for Improved Hole-Conductor-Free Perovskite Solar Cells. *Sol. Energy* **2018**, *166*, 42–49. https://doi.org/10.1016/j.solener.2018.03.037.

(13) Wujun Wang. *Simulate a 'Sun' for Solar Research: A Literature Review of Solar Simulator Technology*; KTH Energy and Environmental Technology, 2014.

(14) ASTM E927-10. *Standard Specification for Solar Simulation for Terrestrial Photovoltaic Testing*; ASTM International: West Conshohocken, PA, 2010. https://doi.org/10.1520/E0927-10.

(15) Esen, V.; Sağlam, Ş.; Oral, B. Light Sources of Solar Simulators for Photovoltaic Devices: A Review. *Renew. Sustain. Energy Rev.* **2017**, *77*, 1240–1250. https://doi.org/10.1016/j.rser.2017.03.062.

(16) Field, H. Methods and Instruments for the Characterization of Solar Cells. In *Photovoltaic Solar Energy*; John Wiley & Sons, Ltd, 2017; pp 303–321. https://doi.org/10.1002/9781118927496.ch29.

Chapter 3

High-Performance, Semitransparent PSCs using Nonprecious DMD Top Electrodes

In this chapter, a novel DMD transparent electrode based on nonprecious, less-reactive copper is developed via thermal evaporation and used as a top anode in the fabrication of high-performance semitransparent n-i-p perovskite solar cells, the best device yielding a power conversion efficiency as high as 12.5%. The DMD architecture consists of a gold-seeded Cu thin film sandwiched between two MoO_x dielectric layers. It is demonstrated that Cu self-aggregation and diffusion into MoO_x can be substantially limited by introducing an ultra-thin (1.5 nm) Au seed layer, and conductive Cu films as thin as 9.5 nm can be achieved. A fine tuning of the perovskite layer thickness is also carried out to further enhance the device transparency up to a maximum average visible transmittance of 24%. The following results have been object of a publication in the journal of Advanced Materials Technologies (Wiley).[1]
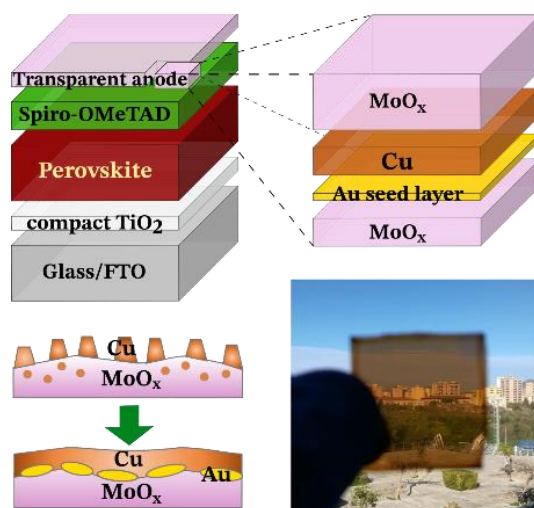
3.1. Motivation of the study

In recent years, a significant emphasis has been placed on developing multi-functional solar cells that integrate new features such as color and transparency, thereby opening up the possibility of unconventional PV applications, including building-integrated photovoltaic (BIPV) systems, tandem solar cells, and wearable electronics.[2–6] In particular, the integration of semitransparent (ST) solar cells into buildings as power-generating windows, facades or other aesthetic architectural elements constitutes one of the most intriguing perspectives, but it requires a proper balance between electricity generation and optical transparency, which involves careful selection of materials and sophisticated design of the corresponding device architecture.[7] The color perception is another crucial factor that should be considered. Colourful ST devices may be favorable for decoration purposes, whereas neutral-color ST solar cells are generally preferred for solar window applications. Since silicon-based panels are generally opaque and anaesthetic, there has been a growing research interest in emerging thin-film solar cells that can be made truly semitransparent, display different colors, and be easily adapted to any type and surface of buildings.[8] Among third-generation PVs, perovskite solar cells (PSCs) are particularly attractive for these applications owing to their superior performances.[9]

Over the past few years, tremendous efforts have been applied to develop esthetic semitransparent perovskite solar cells (ST-PSCs) by exploring various kinds of transparent electrodes, controlling the morphology, and engineering the bandgap of the perovskite absorbers. [4,5,10–19] In Chapter 1, the key requirements for transparent top electrodes (TTEs) were introduced, together with the motivation for investigating alternatives to the ubiquitous TCOs.[20] In addition, a brief introduction was given to dielectric/metal/dielectric (DMD) multilayer electrodes as one promising candidate.[21–24] These composite electrodes are made of an ultrathin metal layer (<12 nm) sandwiched between two dielectric materials with high refractive indexes. Compared with other transparent electrodes, DMD electrodes exhibit ideal characteristics to serve as TTEs, such as high electrical conductivity, enhanced transparency compared with ultrathin metal films, mechanical and thermal stability, simple evaporation process, and tunable opto-electrical properties. Their electrical conductivity mainly depends on the intermediate metal film, whose thickness must be high enough to provide electrical percolation but also minimized to avoid significant optical losses; their optical transparency can be easily tuned by varying the nature and thickness of the dielectric

layers. The materials integrated in the DMD stack also determine the carrier collection polarity of the entire structure and must be carefully selected according to the specific device architecture. In particular, the bottom dielectric layer would act as an electrode buffer layer, facilitating charge extraction and charge blocking in the device.

To fabricate ST-PSCs with a regular n-i-p configuration, whose performances are typically higher than those of inverted devices, hole-collecting top electrodes are required. Traditional hole-collecting DMD electrodes mostly employ precious metals (Ag, Au) to form the intermediate layer, and high-work-function transition metal oxides like molybdenum oxide (MoO$_3$) and tungsten oxide (WO$_3$) as the dielectric material.[14,25–27] As an example, Della Gaspera and co-workers applied a MoO$_x$/Au/MoO$_x$ DMD top electrode to the fabrication of regular ST-PSCs in 2015, and their devices showed PCEs of 5.3-13.6% with the corresponding average visible transmittances (AVTs) of 31-7%.[14] Silver and gold are commonly preferred over other metals for their excellent electrical conductivity and high work function, well matched with the light absorber and hole-transport layers. However, the employment of such expensive metals could represent a quite substantial obstacle to the large-scale commercialization of perovskite-based solar cells. Moreover, stability issues may be encountered when using silver. As already mentioned in Chapter 1, Ag atoms can diffuse in the underlayers and severely react with the decomposition products of perovskite (e.g. HI), forming silver halides (e.g. AgI) and accelerating the degradation of PSCs.[28] A solution to these problems relies on finding alternative metals that are much cheaper than Au and more stable than Ag, this being the key motivation of the present study.

Nonprecious copper, whose cost is about 1/6000 than that of gold, has recently been reported as an effective and cheaper alternative to high-value metals in opaque PSCs.[29–31] Thanks to its better corrosion resistance compared to Ag (especially in non-oxidizing acids such as HI), Cu undergoes no chemical reaction with perovskite under inert conditions, providing long-term intrinsic stability to the devices.[29] Nevertheless, only few investigations have been dedicated to Cu-based TTEs for semitransparent PSCs,[32] even though a series of transparent electrodes made of Cu thin films have been used in the past decade to replace ITO as the bottom electrode in OSCs.[33–36] The limited attention paid to the development of D/Cu/D structures is justified by their poor stability: Cu atoms tend to self-aggregate and strongly diffuse into the oxides that are typically used to form the dielectric films, with detrimental effects on the opto-electrical properties. Particularly poor results have been obtained by evaporating Cu directly on top of the hole-selective MoO$_x$ and WO$_x$, making

it necessary to deposit relatively thick Cu layers (at least 32 nm on MoO_x) for achieving the electrical conductivity, at the expense of transparency.[37,38] Further investigations are strongly needed to enhance the performance and stability of these structures, with the aim of developing new hole-collecting Cu-based DMD electrodes to be used in place of the traditional Au-/Ag-based ones.

This chapter explores the potential of copper as a non-precious, perovskite-compatible metal layer in DMD architectures used as hole-collecting TTEs for ST-PSCs. Specifically, a multilayer transparent electrode based on a MoO_x/Au-seed/Cu/MoO_x stack is developed via thermal evaporation and applied for the first time as a top anode to the fabrication of planar n-i-p perovskite solar cells. It is demonstrated that an ultrathin (1.5 nm) gold layer can act as an effective wetting inducer and diffusion barrier for copper, thus allowing conductive structures to be obtained with gold-seeded Cu films as thin as 9.5 nm. By combining this strategy with a careful control of the perovskite layer thickness, high-performance Cu-based ST-PSCs covering a broad range of efficiency vs. transparency values are successfully fabricated. A perspective of the opportunities of the fabricated devices in the context of BIPVs is also provided.

3.2. Results and Discussion

3.2.1. Opaque Reference Solar Cells

The first step of this study was the fabrication of a highly efficient opaque PSC to be used as a reference. For this purpose, the mixed-halide perovskite $CH_3NH_3PbI_{3-x}Cl_x$ (or $MAPbI_{3-x}Cl_x$) was selected to be the absorber material for its well-known and superior opto-electronic properties, including the broad and strong light absorption (see **Figure 3.1**a). The perovskite films were deposited by a one-step spin-coating procedure starting from a solution of MAI and $PbCl_2$ in DMF (40 wt%) at 3:1 molar ratio (see Chapter 2, Section 2). In Chapter 1 the advantages of such a simple deposition approach were introduced. Dark brown/black films with good uniformity and reproducibility were obtained, as shown in Figure 3.1b. The thickness was found to be ~390 nm by AFM. The full surface coverage revealed by SEM, together with the strong XRD peaks along the (110) and (220) lattice planes characteristic of the $MAPbI_{3-x}Cl_x$ tetragonal phase,[39] confirmed the identity and quality of the fabricated perovskite films (see Figure 3.1c and d).

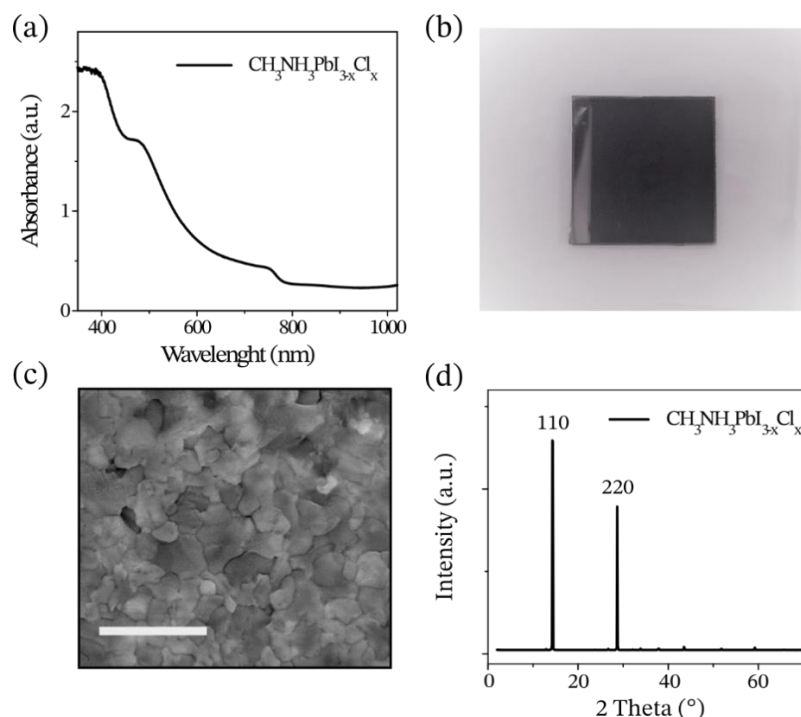***Figure 3.1.*** *(a) Absorption spectrum, (b) photograph, (c) top-view SEM image (scale bar: 5 um), and (d) XRD pattern of a $CH_3NH_3PbI_{3-x}Cl_x$ film deposited by one-step spin-coating technique on top of a c-TiO₂/FTO/glass substrate.*

The widely used n-i-p planar configuration, with compact-TiO₂ as the electron-transport layer and spiro-OMeTAD as the hole-transport material, was adopted in this work due to its simplicity and capacity to provide reduced optical losses compared with the traditional perovskite solar cells having a mesoscopic TiO₂ scaffold (see **Figure 3.2**a).[40] The device was completed by thermally evaporating 6 nm of MoO_x as anode buffer layer and 100 nm of Au as rear contact on top of the spiro-OMeTAD. The energy band diagram of the complete device is sketched in Figure 3.2b. Currently, most of the high-efficiency n-i-p PSCs reported in the literature use gold as the counter electrode material due to its high electrical conductivity, ideal work function (5.1 eV),[41] and excellent chemical stability. The presence of iodide in the perovskite layer limits the possibility of employing less expensive metals (Ag, Al), which can react with iodide and lead to poor device stability.[28,42] MoO_3 has been widely used and proved to be effective as anode buffer layer in OSCs and PSCs thanks to its wide bandgap, high work function (WF = 5.3 ~ 6.9 eV depending on the fabrication method), excellent environmental stability, and easy processing.[14,25–27,43] Among the other transition metal oxides, MoO_3 has the additional advantage of a low melting point, so that it can be easily processed by vacuum thermal evaporation resulting in a slightly sub-stoichiometric MoO_x (x < 3) film. Thermally evaporated MoO_x films were found to have WF at 5.4 eV,[43] which aligns well with the HOMO level of the spiro-OMeTAD (see Figure 3.2b). Despite the strong n-type nature and very low-lying valence band, MoO_x can extract holes from the adjacent organic semiconductor through oxygen-vacancy-induced gap states close to its Fermi level, leading to a better contact.[44] More details about the fabrication procedure were provided in Chapter 2.
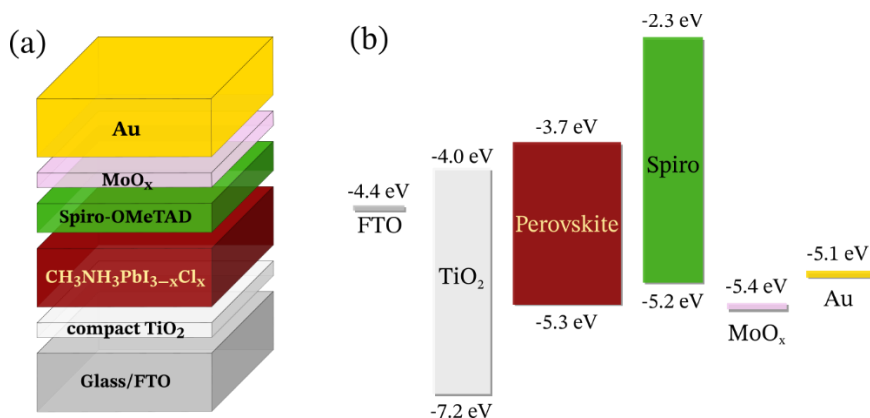

Figure 3.2. *(a) Schematic illustration of the opaque PSC planar architecture. (b) Energy band diagram of the complete n-i-p photovoltaic device. Literature reports for band edges and Fermi levels were used.*[40,41,43]

The J-V characterization of the fabricated solar cells was performed as described in Chapter 2, using a calibrated halogen lamp as the light source. The best-performance opaque PSC delivered a PCE as high as 14.2% under standard (1 sun) illumination. This efficiency is comparable with that shown by other opaque perovskite-based solar cells with similar characteristics reported in the literature.[14] The corresponding J-V curve is shown in **Figure 3.3**, while the relative photovoltaic parameters, together with the mean values obtained from at least 8 devices, are summarized in **Table 3.1**. The high values of J_{sc} (19.7 mA cm^{-2}), V_{oc} (1002 mV), and FF (72.3%) are indicative of an efficient light absorption and excellent interface and charge transport properties with restrained recombination losses.
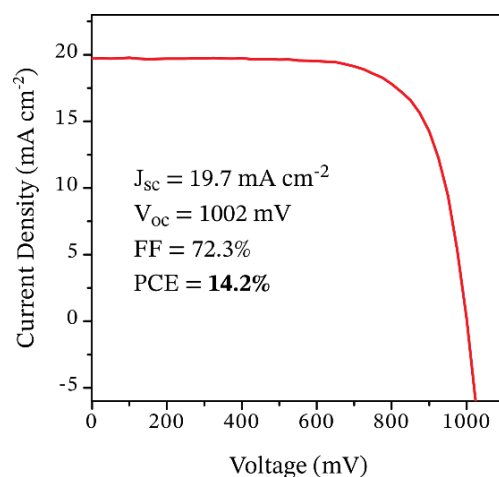
Figure 3.3. *Reverse scanning current density-voltage (J-V) curve of the best-performance opaque PSC featuring a MoO$_x$ (6 nm)/ Au (100 nm) top electrode, measured under standard (1 sun) illumination using a halogen lamp. The device parameters are reported as an inset.*

Table 3.1. *Summary of PSC performances (short-circuit current, J$_{sc}$; open circuit voltage, V$_{oc}$; fill factor, FF; power conversion efficiency, PCE) for opaque control cells having 390 nm thick perovskite film and 100 nm thick Au top contact, measured under standard (1 sun) illumination.*

	J_{sc} [mA cm^{-2}]	V_{oc} [mV]	FF [%]	PCE [%]
Best[a]	19.7	1002	72.3	**14.2**
Mean[b]	18.8 (±0.8)	976 (±20)	70.8 (±3.4)	12.9 (±0.8)

[a]Values obtained for the best performing device. [b]Mean values obtained from at least 8 individual cells; the standard deviation around the mean is given in brackets.

Since it has been reported that the scanning direction has a significant impact on the PSC performance,[45] the J-V characteristics of the solar cells were acquired both in the forward (from short circuit to forward bias, SC-FB) and reverse direction (from forward bias to short circuit, FB-SC). A typical but contained hysteresis effect was observed, as shown in **Figure 3.4**a, with the lowest PCE (12.3%) corresponding to the forward scan. On the other hand, the J-V curves acquired at dark conditions provided indication of an excellent rectification behavior, showing a large current in forward bias and a negligible current in reverse bias (see Figure 3.4b).
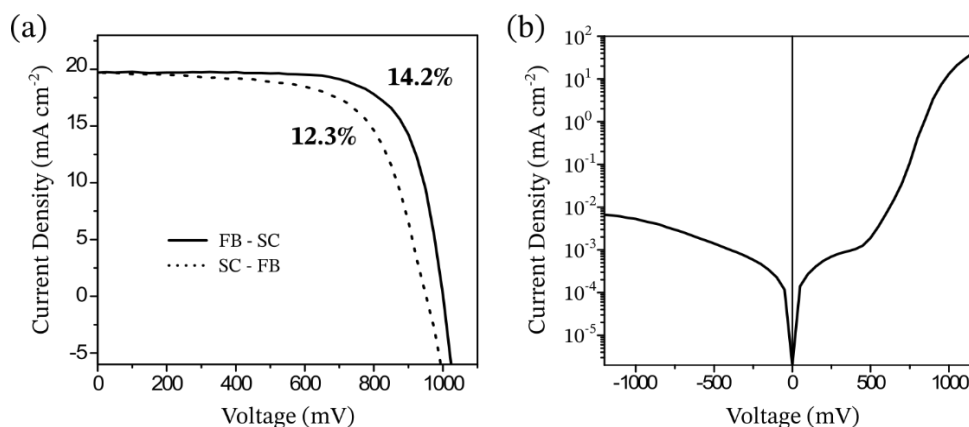
Figure 3.4. *(a) Hysteresis effect in the J-V curves of the top opaque control PSC by varying the scanning direction. (b) Dark J-V curve (semilog plot) of the top opaque control PSC.*

3.2.2. Design of a Novel Cu-based DMD Transparent Electrode

The second step of this work consisted in developing a novel, cost-effective transparent DMD electrode to be used as a top anode in ST-PSCs in the prospect of practical ST applications. For this purpose, Cu and MoO_x were selected to be the metal and the dielectric material, respectively. In addition to its hole-selective nature, the wide bandgap and visible-light transparency of MoO_x make it well suited for integration into a hole-collecting DMD transparent structure. Concerning the metal layer, Cu was employed instead of the conventional precious metals (Au, Ag) in order to develop a cost-effective DMD structure that is also intrinsically stable with perovskite unlike Ag-based contacts. The proper work function (~4.53 eV),[41] good electrical conductivity and stability, as well as the low cost of Cu make it a suitable metal candidate.

A careful design of the DMD electrode was carried out to achieve a simultaneous optimization of electrical conductance and optical transmittance. First, a 6-nm-thick MoO_x film was chosen to be

the bottom dielectric layer (b-MoO$_x$) after being proven effective as anode buffer layer in opaque reference Au-based PSCs (see Figure 3.3). Then, various attempts were made to deposit continuous and smooth metal films onto the MoO$_x$ surface at the minimum thickness, in order to provide electrical percolation pathways with minimized transmittance losses. Uniform and conductive Au films as thin as 11 nm were easily grown onto MoO$_x$ (**Figure 3.5**a), as already demonstrated in the literature.[25] On the contrary, in a first attempt to replace gold with nonprecious copper, isolated granular metal clusters were formed when Cu was directly deposited on the molybdenum oxide layer at the same thickness (Figure 3.5b). This indicates a typical 3D (Volmer-Weber) growth mode, which is universally observed with high-surface-free-energy metal films on low-surface-free-energy oxides during the very early stages of growth.[46] A particularly vigorous coalescence between the fast-migrating nanoscopic Cu clusters evidently occurs, leading to a delay in the formation of a percolative film over the thickness of 11 nm. The different behavior of Au and Cu atoms on the MoO$_x$ surface can be explained as follows: since the surface free energy of Cu (1.8 J m^{-2}) is higher than that of Au (1.5 J m^{-2}), the thermodynamic driving force for surface diffusion and self-aggregation is stronger in the case of copper because of the higher energy mismatch with the MoO$_x$ substrate (0.06 J m^{-2});[47,48] moreover, the small atomic radius of the Cu atoms enables them to travel much more quickly than the Au ones, facilitating surface diffusion and 3D clustering. Such a discontinuous morphology shown by the Cu film (Figure 3.5b), deriving from the poor wetting of copper on the substrate, is clearly undesirable for electrode purposes since it allows no efficient charge carrier transport.

To fabricate continuous and ultrathin Cu layers, the Volmer-Weber growth mode must be suppressed. Current strategies for improving the wettability of oxide substrates by noble metals consist on applying chemically different transition metals as either a seed layer[25,48] or an alloy.[38] Interestingly, it was found that a very thin (1.5 nm) Au layer inserted between Cu and MoO$_x$ was sufficient to enhance the interfacial adhesion and reduce the electrical percolation threshold (equivalent thickness at which electrical paths are developed), thus acting as an effective wetting inducer. Since the surface free energy of Au is much higher than that of MoO$_x$, the energy difference between Cu and the substrate is reduced upon deposition of gold, and it becomes thermodynamically more favorable for the Cu atoms to bound to the surface. Moreover, the high degree of interfacial alloying (Au and Cu are completely miscible) corresponds to a more negative interfacial free energy which drives copper to grow more smoothly on the gold surface.[49] From a

kinetic point of view, the activation energy barrier for surface diffusion of Cu is expected to increase on the Au seed layer compared to pristine oxide, thanks to strong cohesion between the two metals, leading to a diffusion-limited scenario. As a result, a drastic transition to a more two-dimensional (Frank-van der Merwe) growth mode is promoted: Cu adatoms tend to form a 2D continuous film rather than diffuse and aggregate into disconnected island-like clusters (see Figure 3.5c).
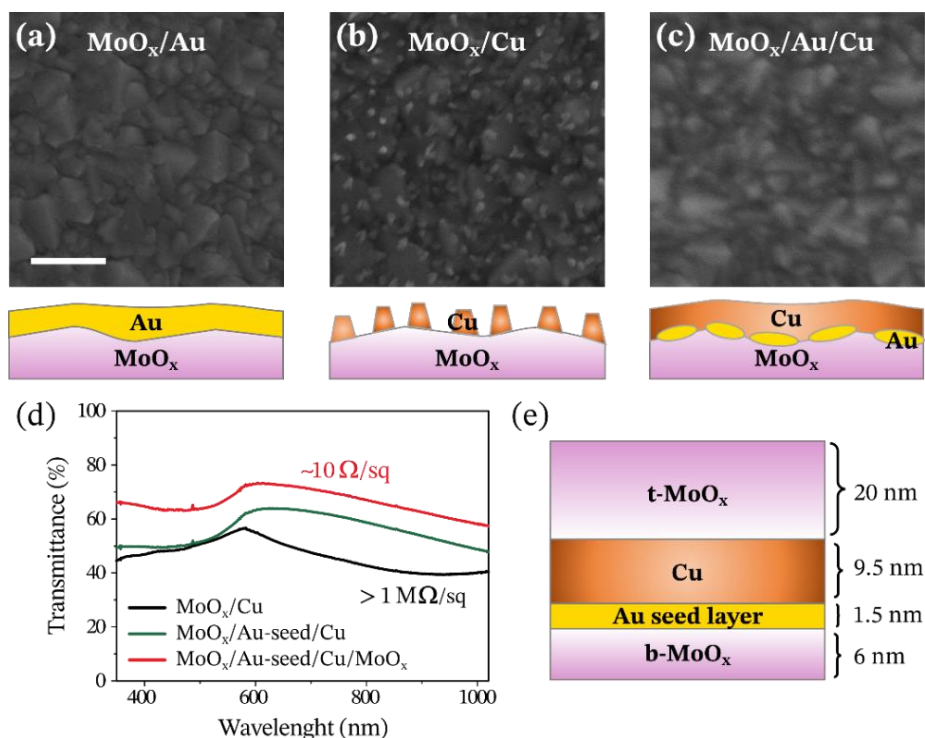
Figure 3.5. *Top-view SEM images and schematics of (a) pristine Au, (b) pristine Cu, and (c) gold-seeded Cu deposited onto MoO$_x$-coated FTO/glass substrates at the same metal thickness of 11 nm. Scale bar: 1 µm. (d) Transmittance spectra of b-MoO$_x$/Cu (11 nm), b-MoO$_x$/Au-seed (1.5 nm)/Cu (9.5 nm), and b-MoO$_x$/Au-seed (1.5 nm)/Cu (9.5 nm)/t-MoO$_x$ multilayer structures; the bottom and top MoO$_x$ films are of 6 and 20 nm respectively. The corresponding values of sheet resistance are also reported. (e) The final architecture of the Cu-based DMD electrode.*

This strategy allowed to get a continuous and percolative Cu film as thin as 9.5 nm with enhanced electrical and optical properties. With the same metal thickness (11 nm), the gold-seeded Cu layer exhibited a higher transmittance compared with the pristine Cu film in the whole range of 380-1020 nm, as shown in Figure 3.5d. This result suggests that Rayleigh-scattering and absorption effects of the surface plasmon resonance (SPR) in the nanoscopic Cu clusters are successfully

suppressed by the formation of a continuous film, thereby leading to enhanced transparency. The sheet resistance of the metal layer decreased by several orders of magnitude from a value higher than 1 MΩ/sq (11 nm Cu) to 10 Ω/sq (1.5 nm Au + 9.5 nm Cu). confirming the achievement of electrical percolation. The conductivity achievement can be entirely attributed to the substantial change in the morphology of the Cu film. Indeed, the b-MoO$_x$ (6 nm)/Au-seed (1.5 nm) substrate taken alone is highly resistive and shows a typical 3D morphology (see the AFM images in **Figure 3.6**), suggesting a nanoscale discontinuity that prevents gold from reaching the electrical percolation by itself at such a low thickness.
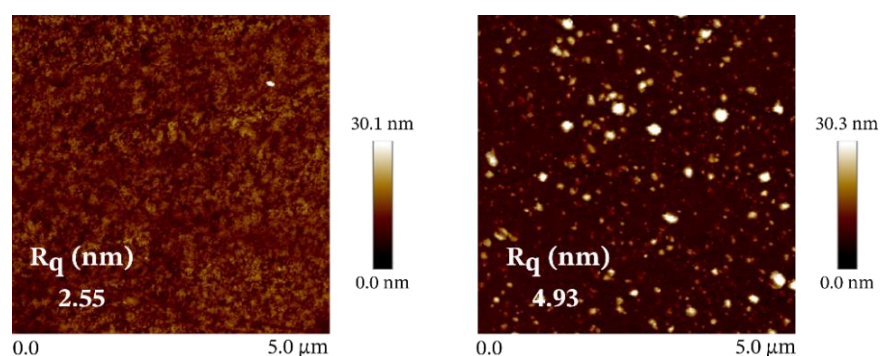
Figure 3.6. *Top-view AFM images of MoO$_x$ (6 nm) (left) and MoO$_x$ (6 nm)/ Au-seed (1.5 nm) (right) deposited on plain glass substrates. The surface roughness is noted as the root mean-square value (R$_q$).*

Once the metal film was optimized, the multilayer electrode was completed by subsequent deposition of an additional MoO$_x$ top layer (t-MoO$_x$) to further enhance the transparency according to the DMD approach: by embedding a metal thin film with a low refractive index (gold-seeded Cu) between two dielectric materials with high refractive indexes (b-MoO$_x$ and t-MoO$_x$), surface plasmon suppression and optical interference effects are promoted at the metal-dielectric interfaces, leading to an enhanced optical transmittance.[21] The molybdenum oxide was once again selected over other candidates to simplify the fabrication process without changing the thermal evaporation source. Following previous studies, the thickness of t-MoO$_x$ was fixed at 20 nm.[35] As expected, a significant increase in the overall transmittance was observed upon deposition of t-MoO$_x$ (Figure 2d), up to a maximum T$_{max}$ = 73% at the visible wavelength of 604 nm. A schematic cross section of the final b-MoO$_x$/Au-seed/Cu/t-MoO$_x$ architecture is depicted in Figure 3.5e. The actual thicknesses of the constituent layers were measured by AFM and were found to be quite

consistent with the values indicated by the quartz crystal microbalance (see **Figure 3.7**). A figure of merit (FoM) for transparent electrodes has been defined by Haacke[50] as:

$$FoM = \frac{T^{10}}{R_S} \qquad \qquad \{3.1\}$$

where T is the optical transmittance and R_s is the sheet resistance. Using T_{max}, the figure of merit obtained for the MoO$_x$/Au-seed/Cu/MoO$_x$ electrode was 4.3 10^{-3} Ω^{-1}, which is appropriate for the role of TTE and of the same order of magnitude than that achieved by other DMD structures reported in the literature.[37,38]
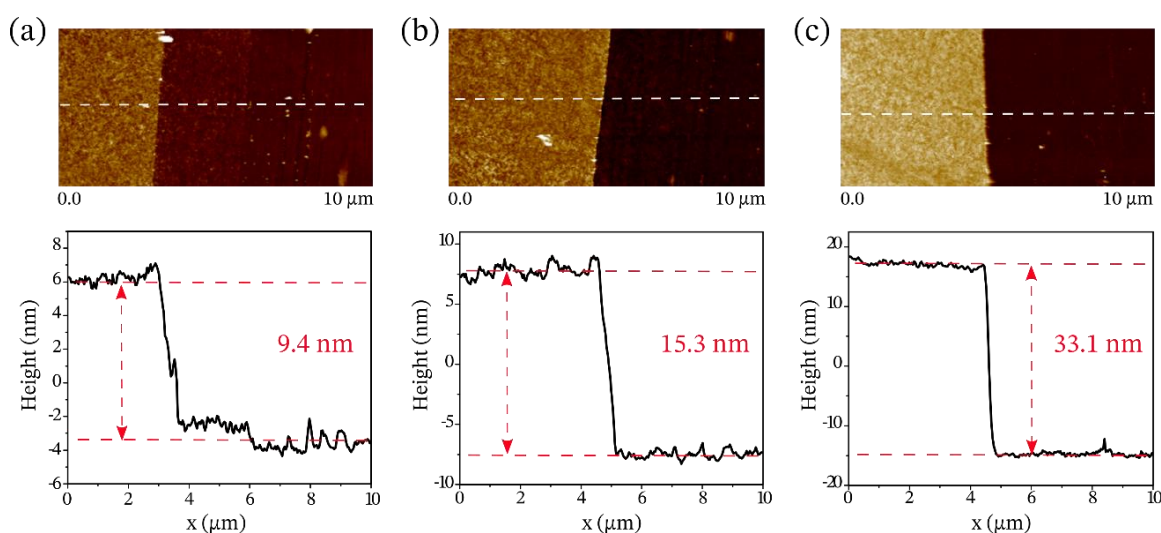
Figure 3.7. Top-view AFM images and thickness profiles along the white dashed lines for the following multilayers (the thickness values monitored by the quartz crystal microbalance are indicated in brackets): (a) b-MoO$_x$ (6 nm)/ Au-seed (1.5 nm); (b) b-MoO$_x$ (6 nm)/ Au-seed (1.5 nm)/ Cu (9.5 nm); (c) b-MoO$_x$ (6 nm)/ Au-seed (1.5 nm)/ Cu (9.5 nm)/ t-MoO$_x$ (20 nm). The AFM thicknesses are reported in the figures. As expected, the obtained values are slightly different from those indicated by the quartz crystal microbalance, since the latter provides only a theoretical estimation by considering the films as ideally smooth.

The value of FoM was found to be strongly dependent on the thickness of the intermediate metal layer. **Figure 3.8** displays the trends of R_s, T_{max}, and FoM as a function of the Cu film thickness, which was varied from 8 nm to 11 nm while keeping all other parameters constant. It was found that the thickness of 9.5 nm corresponds to the highest value of FoM, and hence to the best trade-off between transparency and conductivity. Indeed, Cu films thinner than 9.5 nm showed R_s higher than 40 Ω/sq, while those thicker than 9.5 nm were significantly less transparent, both cases

resulting in a lower FoM. The effect of the thickness of the Au seed layer on the electrode performance was also investigated. A detrimental impact on the electrical conductivity was observed when the thickness was reduced from 1.5 nm (R_s = 10 Ω/sq) to 1 nm (R_s = 82 Ω/sq), and then from 1 nm to 0.5 nm (R_s = 450 Ω/sq), as presented in Figure 3.8. The AFM images in **Figure 3.9** show the evolution of the morphology of the Cu film, which grows three-dimensionally and appears rougher as the Au thickness decreases (the root mean-square surface roughness R_q of the Cu film is 5.9 onto 1.5-nm-thick Au, 6.4 onto 0.5-nm-thick Au, and 13.9 without a gold seed layer). This is indicative of a poorer Cu wetting on the substrate, that can explain the gradual loss of electrical percolation. Structures featuring Au seed layers thicker than 1.5 nm were not investigated as they would not meet the objective of minimizing the amount of expensive gold. Therefore, the thicknesses of Au and Cu were fixed at 1.5 nm and 9.5 nm respectively in order to guarantee the best compromise between performance and cost of the electrode.
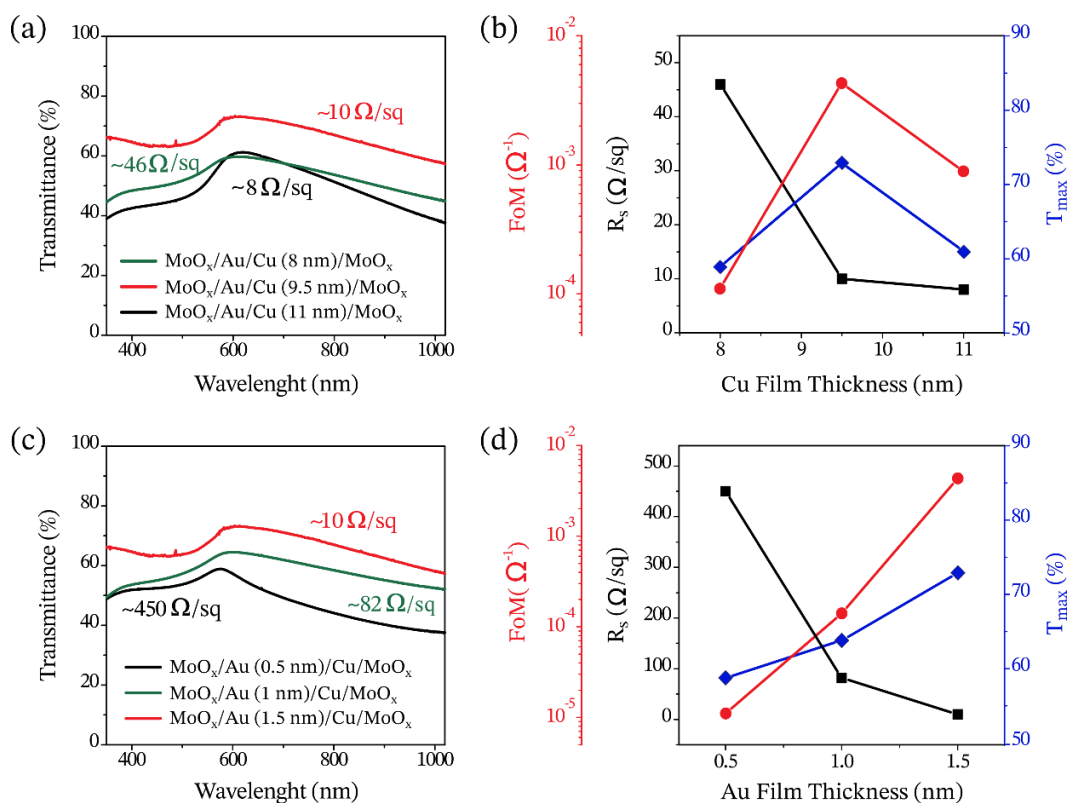
Figure 3.8. *Transmittance spectra of the MoO$_x$/Au-seed/Cu/MoO$_x$ structure as a function of the thickness of the Cu film (a) and of the Au seed layer (c). Sheet resistance (R$_s$), maximum optical transmittance (T$_{max}$), and figure of merit (FoM) of the MoO$_x$/Au-seed/Cu/MoO$_x$ structure as a function of the thickness of the Cu film (b) and of the Au seed layer (d).*
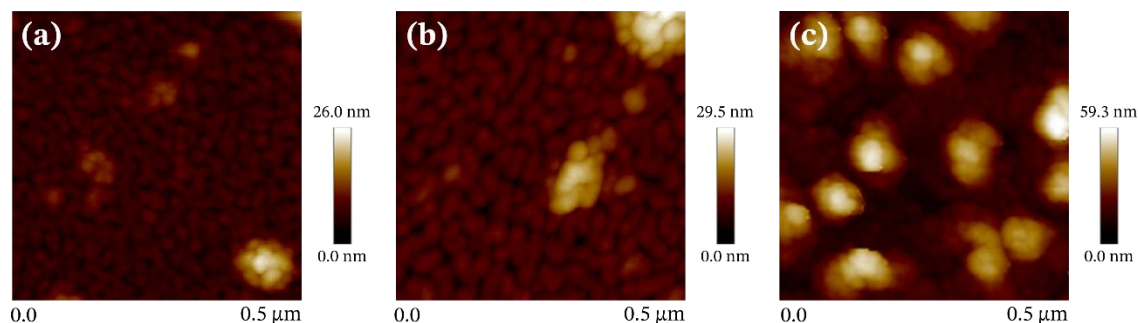
Figure 3.9. *Top-view AFM images of 9.5-nm-thick copper films deposited onto Au-seed/MoO$_x$-coated glass substrates with different thicknesses of the gold seed layer: 1.5 nm (a), 0.5 nm (b), and 0 nm (c).*

3.2.3. Depth-Profiling XPS Characterization

Since Cu can diffuse into the bulk MoO$_x$ with detrimental effects on the electrical conductivity and stability,[37] the study proceeded with an in-depth compositional analysis of the DMD structure to investigate the role of the ultrathin Au seed layer with respect to this phenomenon. The DMD electrode under investigation (Figure 3.5e), as well as the MoO$_x$ (6 nm)/Cu (11 nm)/MoO$_x$ (20 nm) analogue structure without the gold seed layer, were deposited on plain glass substrates for depth-profiling XPS characterization. The relative composition profiles are shown in **Figure 3.10**.
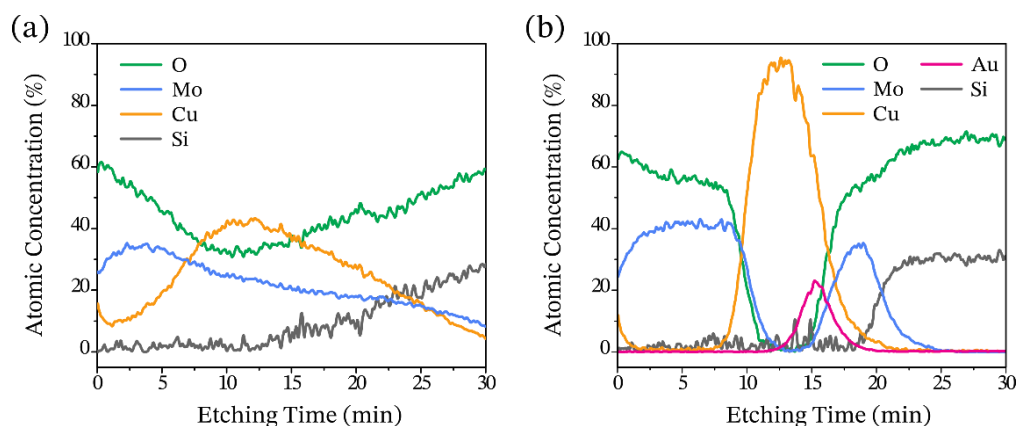
Figure 3.10. *XPS depth profiles of the (a) MoO$_x$ (6 nm)/Cu (11 nm)/MoO$_x$ (20 nm) and (b) MoO$_x$ (6 nm)/Au-seed (1.5 nm)/Cu (9.5 nm)/MoO$_x$ (20 nm) structures deposited on glass substrates.*

As expected, a strong diffusion of copper was observed throughout the MoO$_x$/Cu/MoO$_x$ stack (Figure 3.10a), especially within the MoO$_x$ bottom layer. Given the thermally activated nature of

diffusivity, the Cu diffusion within the b-MoO$_x$ is assisted by the high energy of the incoming Cu atoms during thermal evaporation. As shown in Figure 3.9a, the atomic concentration of Cu remains quite elevated all along the structure and is even higher than that of Mo for the entire thickness of b-MoO$_x$ up to the glass surface. On the contrary, the MoO$_x$/Au-seed/Cu/MoO$_x$ structure showed a spatially-defined stacking of the constituent layers, indicating a very limited Cu diffusion (Figure 3.10b). In this case, we found prevalent concentrations of Mo and O within both the t-MoO$_x$ and b-MoO$_x$ layers, and a practically zero amount of copper at the b-MoO$_x$/glass interface. The clear predominance of the Cu atoms in a region of sufficient thickness (etching time between 10 and 16 min), up to a maximum of 95 at%, confirmed the presence of a smooth and uniform copper film at the center of the structure.

A direct comparison between the Cu depth profiles of the two structures clearly suggests that the Au seed layer contributes substantially to the limitation of Cu diffusion, thus allowing ultra-thin and spatially-defined Cu films to be grown onto the MoO$_x$ surface. This result should not surprise since the insertion of ultra-thin metal layers is often used as a strategy to circumvent inter-diffusion.[37] Even if discontinuous at such a low thickness, the pre-deposited gold film can prevent or retard the diffusion of copper in the b-MoO$_x$ by acting as a physical barrier to the incoming high-energy Cu atoms during thermal evaporation (reduced number of free adsorption sites at the MoO$_x$/air interface) as well as by favoring the adhesion of copper to the surface (higher activation energy for bulk diffusion of Cu) as previously discussed. On the other hand, the apparent suppression of Cu diffusion within the outer t-MoO$_x$, which is in direct contact with the copper layer, could be attributed to the improved uniformity and smoothness of the gold-seeded Cu film. Indeed, the topography of the Cu/t-MoO$_x$ interface can strongly influence the kinetics of inter-diffusion (inter-diffusion rates are expected to decrease with decreasing interface area and structural defects) as well as the results of the XPS depth analysis (the more the interface is sharp and smooth, the more accurately the two layers are resolved). In any case, the Cu diffusion into the t-MoO$_x$ would not be as detrimental for the electrode performance as that occurring within the b-MoO$_x$. While the latter would compete with the growth of a thin percolative Cu film and potentially proceed in the underlayers of the solar cell, the diffusion into the t-MoO$_x$ is expected to saturate and give rise to a conductive Cu-MoO$_x$ blend if the thickness of t-MoO$_x$ does not exceed 20 nm, as in the present case.[35] Therefore, it was assumed that the use of an additional diffusion barrier between Cu and t-MoO$_x$ was not necessary to obtain a long-term performance electrode.

3.2.4. Thermal and Mechanical Stability

In order to test the performance stability of the proposed MoO_x/Au-seed/Cu/MoO_x electrode, the evolution of its electrical properties with time and under thermal stress was monitored. The electrode aging was carried out both in glove box (inert atmosphere), to probe aging mechanisms that are intrinsic to the architecture, and in the ambient environment, to investigate the additional effects of oxygen and moisture. The corresponding variation in the sheet resistance $R_s - R_{s(0)}$, normalized to the $R_{s(0)}$ initial value, was plotted as a function of time. As can be seen in **Figure 3.11**a, the sample stored in glove box showed no significant changes in resistance, even when aged at 85 °C for up to 1000 h. The multilayer structure appears inherently stable within this time frame, with no evident intrinsic mechanism occurring at the expense of electrical conductivity. On the other hand, a gradual increase in R_s from 10 Ω/sq to around 300 Ω/sq was observed under ambient conditions. This can be attributed to the fact that Cu can be easily oxidized by oxygen and moisture from the ambient environment. The possible oxidation products can induce the release of Cu ions into the dielectric and negatively affect the electrical properties of the multilayer structure. To investigate the stability of the Cu-based electrode also at elevated temperature, other samples were subjected to thermal cycles of 30 min at 100, 150, 200, and 300 °C, and the corresponding sheet resistance was measured after each cycle. In ambient air, an abrupt increase in R_s due to oxidation was observed above 200°C (Figure 3.11b). On the contrary, the sample stored in inert atmosphere exhibited high thermal stability, with a change in resistance of less than 5% at 300°C. These results suggest that removing oxygen and moisture, for example by encapsulation, would prevent the Cu oxidation and stabilize the electrode performance in the perspective of practical use.

A more recent requirement for transparent electrodes is mechanical flexibility for applications in modern opto-electronics. To determine the performance of the MoO_x/Au-seed/Cu/MoO_x electrode under external mechanical stress, the DMD architecture was deposited on a PET substrate (Figure 3.11c), and the changes in the sheet resistance after repeated bending cycles were monitored. Commercial ITO-coated PET (Sigma Aldrich, 60 Ω/sq) was subjected to the same characterization for comparison. The samples were flexed manually to a radius of curvature of 4 mm, and the R_s was measured after a certain number of bending cycles. The bending test results are presented in Figure 3.11d. As expected, the ITO film failed to maintain the flexibility: R_s changed by 314% as early as after the first 10 cycles. Indeed, ITO is brittle and tends to form cracks that block the

electrical pathways upon bending.[51] In contrast, the resistance of MoO_x/Au-seed/Cu/MoO_x remained nearly unchanged even after 1000 bending cycles. The excellent flexibility shown by the multilayer structure is a feature common to all the DMD architectures and can be associated to the ductile nature of the metal thin film. Such a mechanical stability is a great advantage over existing technologies like TCOs, as it extends the possibilities of application to flexible devices.
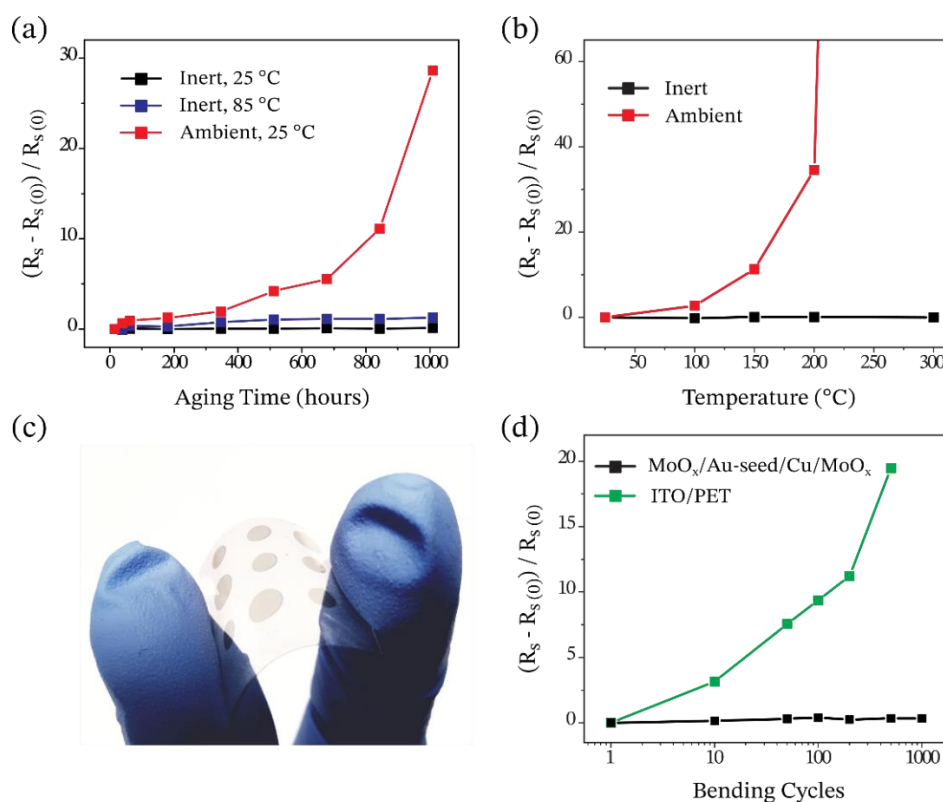
Figure 3.11. (a) Change in sheet resistance ($R_s − R_{s(0)}$)/$R_{s(0)}$ of the MoO_x/Au-seed/Cu/MoO_x electrode according to the aging time and temperature, under inert and ambient conditions. (b) Effect of strong thermal stress on the sheet resistance of the Cu-based DMD electrode, under inert and ambient conditions. Annealing time per thermal cycle = 30 min. (c) Photograph of a PET substrate on which circular MoO_x/Au-seed/Cu/MoO_x electrodes were thermally evaporated. (d) Effect of repeated bending cycles on the sheet resistance of MoO_x/Au-seed/Cu/MoO_x and ITO films on PET. Bending radius = 4 mm.

3.2.5. Application as Hole-Collecting Top Electrode in ST-PSCs

In order to demonstrate the practical use of the proposed Cu-based DMD electrode as well as the real effectiveness of the seed layer approach, semitransparent perovskite solar cells based on the

same planar architecture of Figure 3.2a and featuring a 390-nm-thick $CH_3NH_3PbI_{3-x}Cl_x$ film were prepared with both the MoO_x (6 nm)/Au-seed (1.5 nm)/Cu (9.5 nm)/MoO_x (20 nm) and MoO_x (6 nm)/Cu (11 nm)/MoO_x (20 nm) structures as the top electrode in place of the opaque 100 nm thick Au. **Figure 3.12** shows the schematic structure of a ST-PSC having MoO_x/Au-seed/Cu/MoO_x as the top transparent electrode, as well as a photograph of a fabricated device. As a reference, ST-PSCs having MoO_x (6 nm)/Au (11 nm)/MoO_x (20 nm) top electrodes were also fabricated. The performances of the devices are summarized **Table 3.2**.
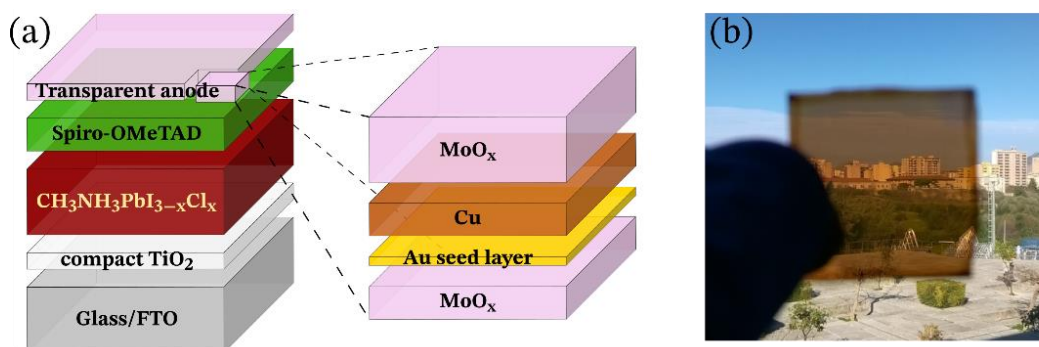
Figure 3.12. *(a) Schematic illustration of the ST-PSC planar architecture with an enlarged view of the DMD transparent top electrode. (b) Photograph of a fabricated ST perovskite solar cell.*

The Au-based control ST solar cells exhibited a maximum PCE of 13% when illuminated from the FTO side (see Table 3.2). This efficiency is lower than that of the Au-based opaque reference (PCE = 14.2%, Figure 3.3), as expected, since the opaque metallic contact always leads to enhanced light absorption due to back-reflection of unabsorbed photons into the perovskite layer. Regarding the performance of the Cu-based ST-PSCs, **Figure 3.13** highlights the huge impact of the seed layer approach on the J-V characteristics. When Cu was evaporated directly on top of MoO_x, the devices exhibited non-ideal J-V curves and very poor power conversion efficiencies (PCE < 0.001%), indicating no efficient charge collection at the MoO_x/Cu/MoO_x electrode. This is consistent with the results presented in Figure 3.5 and 3.10, which show that a non-homogeneous and highly resistive Cu film is formed onto MoO_x without a proper wetting inducer. On the contrary, the insertion of the ultra-thin Au seed layer in the DMD stack enabled solar cells with much higher performances to be fabricated. The best solar cell delivered a very good PCE of 12.5%, which is slightly lower than that of the top control ST device based on MoO_x/Au/MoO_x (see Table 3.2). To the best of our knowledge, this is the highest efficiency reported to date for a

semitransparent regular PSC with a top electrode based on a copper thin film. The high values of fill factor (FF = 76%), short-circuit current density (J_{sc} = 16.6 mA cm^{-2}), and open-circuit voltage (V_{oc} = 993 mV) indicate that the MoO_x/Au-seed/Cu/MoO_x electrode acts as an effective hole-extracting TTE by preventing significant resistive losses and providing efficient charge carrier transport. These results prove that gold can be replaced almost entirely by non-precious copper (the thickness of Au was reduced by a factor of 7.3) in the MoO_x/M/MoO_x structure without sacrificing the device performance.
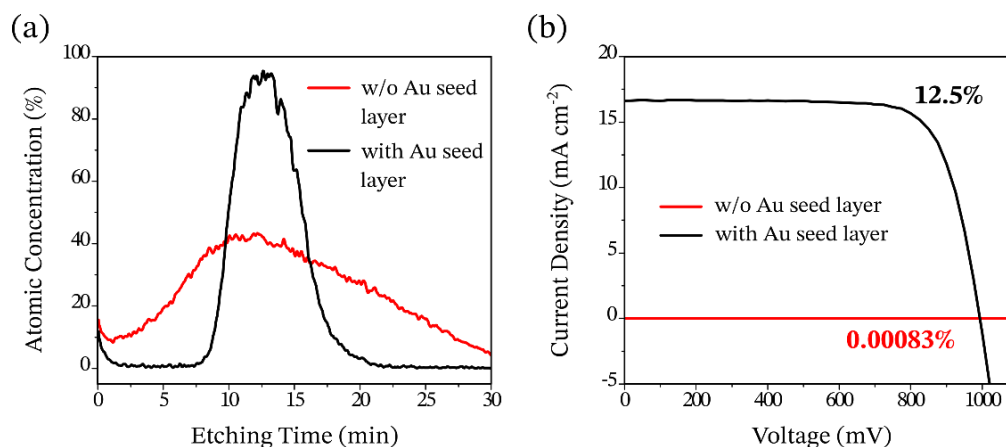
Figure 3.13. (a) Cu depth profile of the two DMD structures with/without the Au seed layer. (b) Reverse scanning J-V curves of the best-performance Cu-based ST-PSCs with/without the Au seed layer, measured under standard (1 sun) illumination from the FTO side. The calculated power conversion efficiencies are also reported.

A non-negligible hysteresis was observed in the J-V curves of the Cu-based ST devices, as shown in **Figure 3.14**a, with the lowest PCE (9.9%) corresponding to the forward scan. The same hysteretic behavior was also exhibited by the Au-based reference solar cells (Figure 3.14b), indicating that this phenomenon is related to a feature common to all the samples, independently from the nature of the counter electrode material. Indeed, the hysteresis effect is generally attributed to intrinsic properties and mechanisms that are beyond the objective of this study, such as the ferroelectricity of perovskite, the formation and release of interfacial charges, and the migration of mobile ions in the absorber material.[52] Similar and very good rectification properties were observed for both Au-based and Cu-based solar cells, as evident from the dark J-V curves in Figure 3.14c. This means that both types of solar cells satisfy the essential condition of acting as a good diode in the dark to obtain good performance under illumination.

In addition to the J-V output, the Cu-based ST-PSCs also exhibited stability comparable to that of the control Au-based ST devices when stored in the glove box. Figure 3.14d compares the PCE degradation of solar cells having MoO_x/Au-seed$/Cu/MoO_x$ and $MoO_x/Au/MoO_x$ as the top electrode respectively. After over 500 hours of storage, the power conversion efficiency degraded only to around 70% of its initial value in both cases, indicating that the intrinsic aging mechanisms (mainly attributed to the perovskite decomposition) are not aggravated by replacing Au with Cu. This analogous behavior of the Au-based and Cu-based solar cells seems to suggest that copper, in the same way as gold, could provide greater inherent stability to the devices compared to other metals typically used in PSCs such as Ag and Al, whose corrosion and reaction with perovskite are recognized as a major origin of self-degradation in perovskite solar cells (see Chapter 1, Section 2.7).[28,42] However, this interpretation should be subject to further scrutiny, even though recent reports on semitransparent Ag-based PSCs with poorer stability under inert conditions seem to support our hypothesis.

Table 3.2. *Summary of ST-PSC performances (short-circuit current, J_{sc}; open circuit voltage, V_{oc}; fill factor, FF; power conversion efficiency, PCE) for solar cells having 390 nm thick perovskite films and different top electrodes, measured under standard (1 sun) illumination.*

Top electrode		J_{sc} [mA cm^{-2}]	V_{oc} [mV]	FF [%]	PCE [%]
MoO_x (6 nm)/Au (11 nm)/MoO_x (20 nm) (*ST control*)	Best[a]	17.1	977	77.8	**13.0**
	Mean[b]	15.9 (±1.4)	976 (±14)	74.9 (±2.1)	11.6 (±0.9)
MoO_x (6 nm)/Au (1.5 nm)/Cu (9.5 nm)/ MoO_x (20 nm)	Best[a]	16.6	993	76.0	**12.5**
	Mean[b]	15.7 (±0.8)	977 (±17)	73.6 (±3.9)	11.3 (±0.7)
MoO_x (6 nm)/Cu (11 nm)/MoO_x (20 nm)	Best[a]	0.0026	947	33.9	**0.00083**
	Mean[b]	-	-	-	-

[a]*Values obtained for the best performing device.* [b]*Mean values obtained from at least 8 individual cells; the standard deviation around the mean is given in brackets.*
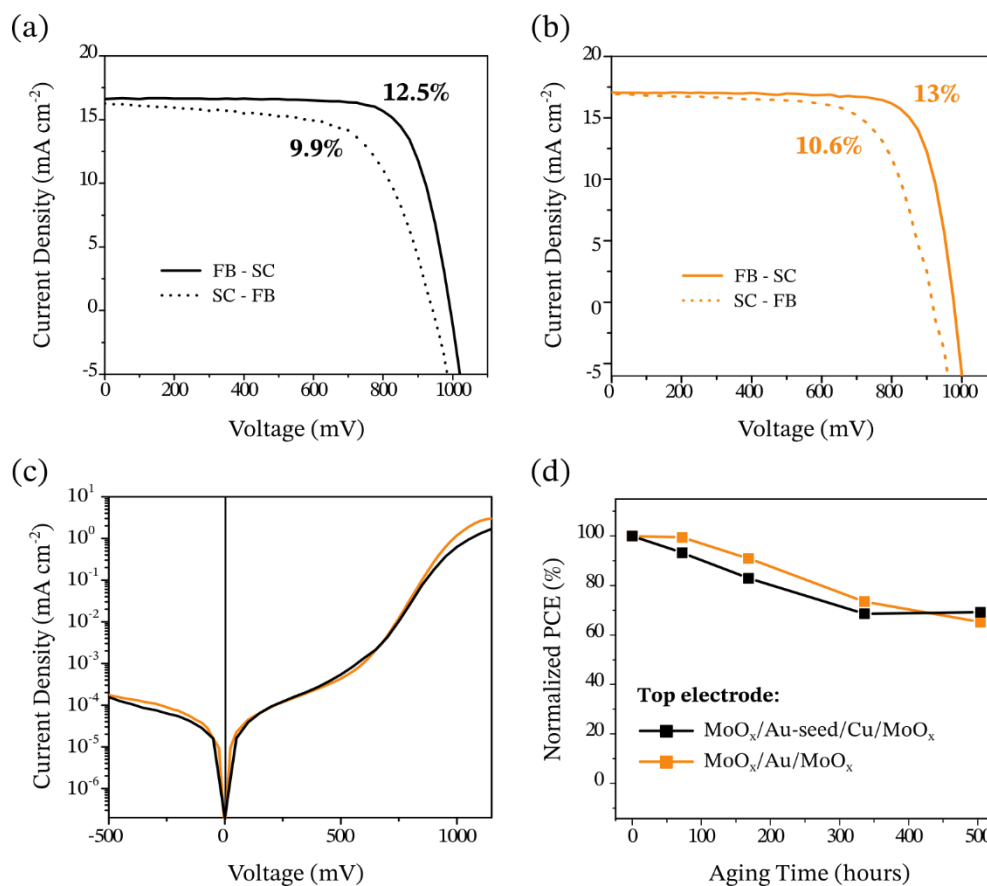
Figure 3.14. *Hysteresis effect in the J-V curves of the best-performance ST-PSCs having (a) MoO_x/Au-seed/Cu/MoO_x and (b) MoO_x/Au/MoO_x as the transparent top electrode, respectively, measured from forward bias to short circuit (FB-SC) and from short circuit to forward bias (SC-FB). (c) Dark J-V curves (semilog plot) of the top Au-based and Cu-based ST devices (d) PCE degradation of two representative solar cells having MoO_x/Au-seed/Cu/MoO_x and MoO_x/Au/MoO_x as the top electrode, respectively, stored in a N_2-filled glove box.*

3.2.6. Effect of Increasing the Perovskite Film Thickness

After having demonstrated the effectiveness of MoO_x/Au-seed/Cu/MoO_x as a transparent top electrode for ST-PSCs, the attention was focused on the perovskite layer. The very strong light absorption of $CH_3NH_3PbI_{3-x}Cl_x$ in the visible spectral region (Figure 3.1) is certainly desirable for PV application, but can also be inappropriate for semitransparent purposes, since even relatively thin films (~390 nm) absorb almost all visible light. It is worth considering that specific transparency requirements must be fulfilled to enable practical ST applications. For example, an AVT of at least 25% is generally taken as a benchmark for solar windows.[53] Therefore, a fine

tuning of the perovskite layer thickness was performed in order to achieve acceptable transparency levels. Specifically, a series of semitransparent devices based on the MoO_x/Au-seed/Cu/MoO_x top electrode were prepared in which the perovskite thickness was progressively reduced from 390 nm to 100 nm by reducing the precursor concentration (see Chapter 2, Section 2). The J-V characteristics and transmission spectra of the top devices are reported in **Figure 3.15**a and b, while the corresponding photovoltaic parameters and average transmittances are summarized in **Table 3.3**.
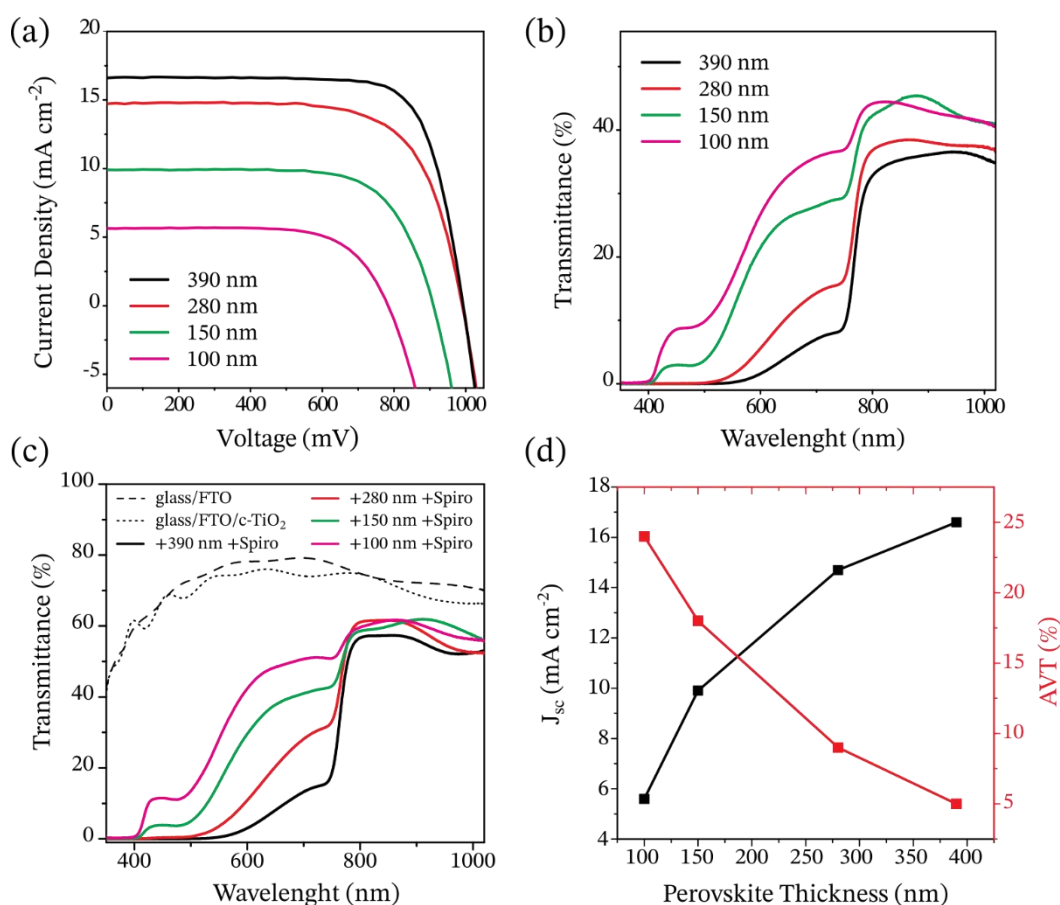
Figure 3.15. *(a) Reverse scanning J-V curves of the best-performance copper-based ST-PSCs with different $CH_3NH_3PbI_{3-x}Cl_x$ thicknesses, acquired under 1 sun illumination from the FTO side. (b) Transmittance spectra through the complete devices with different perovskite thicknesses. (c) Transmittance spectra through the devices without top electrodes, featuring perovskite films of different thicknesses and a spiro-OMeTAD top layer. The spectra of the FTO/glass and c-TiO₂/FTO/glass substrates are also reported. (d) Short-circuit current density (J_{sc}) and average visible transmittance (AVT) of the Cu-based ST devices, plotted with respect to the thickness of the $CH_3NH_3PbI_{3-x}Cl_x$ layer.*

As expected, decreasing the active layer thickness brought to a considerable enhancement in the device transparency, notably in the visible spectral range where $CH_3NH_3PbI_{3-x}Cl_x$ absorbs. The contribution of each layer on the overall transmittance of the complete devices is presented in Figure 3.15c. The average visible transmittance (calculated between 400 nm and 800 nm) increased from 5% (for 390-nm-thick films) to 24% (for 100-nm-thick films), thus approaching the benchmark of 25% for solar window applications. A substantial shift in the chromaticity coordinates was also observed, with thinner devices having a color closer to the desired neutrality (see **Figure 3.16**). Inevitably, thinner solar cells also displayed lower power conversion efficiencies (PCE = 12.5% for 390-nm-thick films, 10.2% for 280-nm-thick films, 6.4% for 150-nm-thick films, and 3.1% for 100-nm-thick films) because of poorer light absorption. The short-circuit current density (J_{sc}) declined steeply from 16.6 mA cm^{-2} to 5.6 mA cm^{-2}, showing exactly the opposite trend of AVT as a function of the perovskite thickness (see Figure 3.15d). On the other hand, the FF and V_{oc} parameters underwent minor reductions. Except for the thinnest solar cell, all the devices exhibited a high V_{oc} between 910 mV and 993 mV and FF above 70%, indicating excellent interface and charge transport properties.
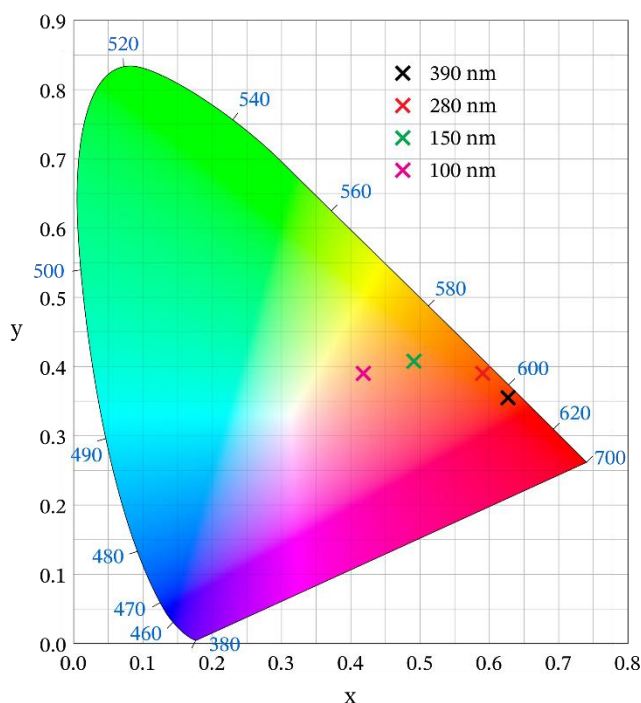
Figure 3.16. *CIE 1931 color space chromaticity diagram showing the (x, y) coordinates obtained for the ST-PSCs with different perovskite thicknesses, calculated from the XYZ tristimulus values using the transmittance spectra of the devices and the AM 1.5 solar spectrum.*

Table 3.3. Summary of ST-PSC performances under standard (1 sun) illumination from the FTO side as a function of the $CH_3NH_3PbI_{3-x}Cl_x$ thickness, using the MoO_x (6 nm)/Au-seed (1.5 nm)/Cu (9.5 nm)/MoO_x (20 nm) DMD structure as the transparent top electrode. The corresponding average visible transmittance (AVT) calculated between 400 and 800 nm is also reported.

Perovskite Thickness		J_{sc} [mA cm^{-2}]	V_{oc} [mV]	FF [%]	PCE [%]	AVT [%]
390 nm	Best[a)]	16.6	993	76.0	**12.5**	5
	Mean[b)]	15.7 (±0.8)	977 (±17)	73.6 (±3.9)	11.3 (±0.7)	-
280 nm	Best[a)]	14.7	991	70.1	**10.2**	9
	Mean[b)]	13.3 (±0.7)	992 (±10)	71.1 (±1.7)	9.4 (±0.4)	-
150 nm	Best[a)]	9.9	910	70.5	**6.4**	18
	Mean[b)]	9.2 (±0.7)	910 (±8)	70.5 (±2.8)	5.9 (±0.3)	-
100 nm	Best[a)]	5.6	784	69.3	**3.1**	24
	Mean[b)]	6.1 (±0.4)	764 (±21)	61.5 (±4.5)	2.9 (±0.2)	-

[a)]Values obtained for the best performing device. [b)]Mean values obtained from at least 8 individual cells; the standard deviation around the mean is given in brackets.

The Cu-based ST-PSCs displayed performances and transparency levels comparable to those of control ST devices based on MoO_x (6 nm)/Au (11 nm)/MoO_x (20 nm) at the same perovskite thickness, as schematized in **Figure 3.17**. This further confirms that the gold-seeded Cu film acts as an effective alternative to the pristine Au film in the hole-collecting DMD structure. The J-V characteristics and transmittance measurements of the top control Au-based solar cells are summarized in Figure 3.17 and **Table 3.4**. In **Table 3.5**, the best devices are also compared with other ST-PSCs taken from the literature and based on high-value metals. This comparative analysis demonstrates that the MoO_x/Au-seed/Cu/MoO_x architecture can be conveniently used as a cost-effective, perovskite-compatible alternative to the common Au- and Ag-based DMD electrodes in the fabrication of high-performing and relatively stable regular ST-PSCs for BIPV systems.
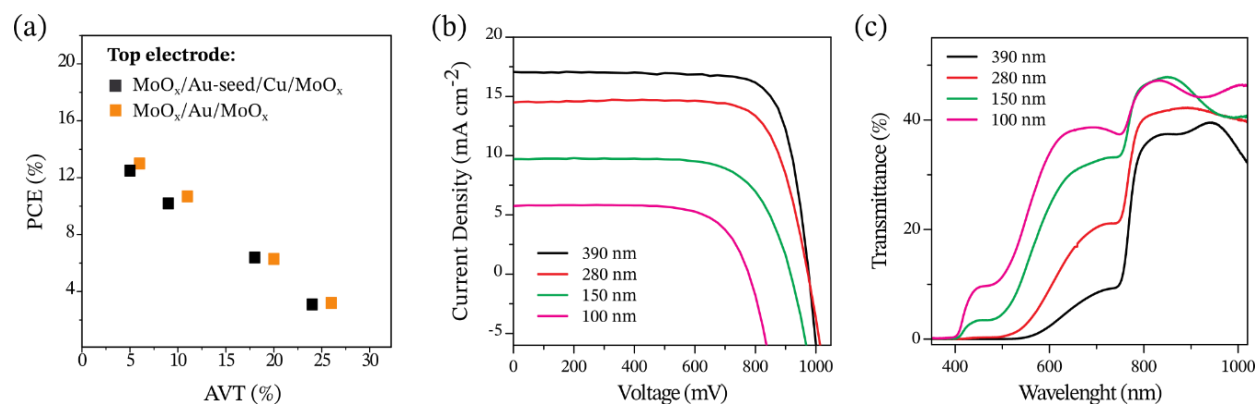
Figure 3.17. *(a) Best-performance comparison between the Cu-based ST-PSCs and the control devices based on MoO$_x$/Au/MoO$_x$ at different perovskite thicknesses (b) Reverse scanning J-V curves of the top control Au-based ST-PSCs with different CH$_3$NH$_3$PbI$_{3-x}$Cl$_x$ thicknesses, acquired under 1 sun illumination from the FTO side. (c) Transmittance spectra through the complete Au-based devices with different perovskite thicknesses.*

Table 3.4. *Summary of ST-PSC performances under standard (1 sun) illumination from the FTO side as a function of the CH$_3$NH$_3$PbI$_{3-x}$Cl$_x$ thickness, using the MoO$_x$ (6 nm)/Au (11 nm)/MoO$_x$ (20 nm) DMD structure as the transparent top electrode. The corresponding average visible transmittance (AVT) calculated between 400 and 800 nm is also reported.*

Perovskite Thickness		J$_{sc}$ [mA cm^{-2}]	V$_{oc}$ [mV]	FF [%]	PCE [%]	AVT [%]
390 nm	Best[a)]	17.2	977	77.8	**13.0**	6
	Mean[b)]	15.9 (±1.4)	976 (±14)	74.9 (2.1)	11.6 (±0.9)	-
280 nm	Best[a)]	14.5	974	75.9	**10.7**	11
	Mean[b)]	13.5 (±0.6)	983 (±12)	72.4 (±3.4)	9.6 (±0.7)	-
150 nm	Best[a)]	9.7	917	70.2	**6.3**	20
	Mean[b)]	9.3 (±0.8)	905 (±12)	66.6 (±2.3)	5.6 (±0.4)	-
100 nm	Best[a)]	5.8	778	70.7	**3.2**	26
	Mean[b)]	6.2 (±0.4)	763 (±23)	64.0 (±3.6)	3.0 (±0.2)	-

[a)]*Values obtained for the best performing device.* [b)]*Mean values obtained from at least 8 individual cells; the standard deviation around the mean is given in brackets.*

Table 3.5. Recently reported performances of ST-PSCs based on ultra-thin metal films, and comparison with the proposed best-efficiency Cu-based devices. The power conversion efficiencies (PCEs) and average visible transmittances (AVTs) are tabulated basing on data available in each reference.

Device Architecture	PCE [%]	AVT [%]	Reference
ITO/PEDOT:PSS/MAPbI$_3$/PCBM/Au	12.2	3	[11]
Au/PEDOT:PSS/ MAPbI$_{3-x}$Cl$_x$/PCBM/MoO$_3$/Au/Ag/MoO$_3$/Alq$_3$	8.6	4	[12]
ITO/PTAA/MAPbI$_3$/PCBM/C$_{60}$/BCP/Cu-seed/Au	16.5	5	[13]
FTO/TiO$_2$/MAPbI$_3$/spiro-OMeTAD/MoO$_x$/Au/MoO$_x$	13.6	7	[14]
	8.8	19	
	5.3	31	
FTO/TiO$_2$/MAPbI$_{3-x}$Cl$_x$/spiro-OMeTAD/MoO$_x$/Au/Ag/MoO$_x$	11.5	-	[25]
ITO/TiO$_2$/MAPbI$_3$/spiro-OMeTAD/MoO$_x$/Ag/ZnS	13.1	8	[15]
ITO/PEDOT:PSS/MAPbI$_3$/Ag nanocubes/BCP/Ag/MoO$_3$	9.6	18	[16]
FTO/TiO$_2$/microstructured-MAPbI$_{3-x}$Cl$_x$/spiro-OMeTAD/Au	7.0	7	[17]
	6.5	18	
	4.5	32	
ITO/PEDOT:PSS/polyTPD/MAPbI$_3$/PCBM/Au/LiF	7.73	10	[18]
	3.39	35	
FTO/TiO$_2$/mp-TiO$_2$/MAPbI$_3$ grid/spiro-OMeTAD/Au	4.98	19	[19]
	0.38	67	
ITO/PEDOT:PSS/MAPbI$_3$/PCBM/AZO/SnO$_x$/Cu/SnO$_x$	9.6	-	[32]
FTO/TiO$_2$/MAPbI$_{3-x}$Cl$_x$/spiro-OMeTAD/MoO$_x$/Au-seed/Cu/MoO$_x$	12.5	5	This work
	10.2	9	
	6.4	18	
	3.1	24	

The relatively low V_{oc} and FF values corresponding to the thinnest device (see Table 3.3) are indicative of some recombination losses occurring at very small perovskite thicknesses. To assess any effect of reducing the thickness on the quality of the perovskite layer, an in-depth morphological and structural characterization was performed. No relevant differences in the structural and compositional properties were observed between perovskite layers of different thickness (see the XRD patterns and EDX spectra in **Figure 3.18** and **Figure 3.19**). In particular, XRD measurements confirmed the deposition of tetragonal $CH_3NH_3PbI_{3-x}Cl_x$, without any contaminant phases. The only difference observed in XRD patterns between samples of different thicknesses was a variation in intensity of the diffraction peaks, which scales proportionally with the amount of material (thickness). The EDX analysis confirmed the presence of chloride in the perovskite films and revealed reasonably comparable Pb/I and I/Cl atomic ratios between layers of different thicknesses. On the other hand, SEM and AFM images disclosed an increasing number of morphological defects and pinholes in thinner $CH_3NH_3PbI_{3-x}Cl_x$ films, as shown in **Figure 3.20** and **Figure 3.21**. As discussed in Chapter 1, the presence of pinholes and a low surface coverage of the perovskite layer can cause interface charge recombination and shunts through direct electrical contact between the HTL and the ETL, leading to a decay in the PV parameters.[54] The deposition of thin perovskite films with higher quality would probably be the key to enhancing the performance and stability of the proposed devices. Further efforts in this direction are planned.
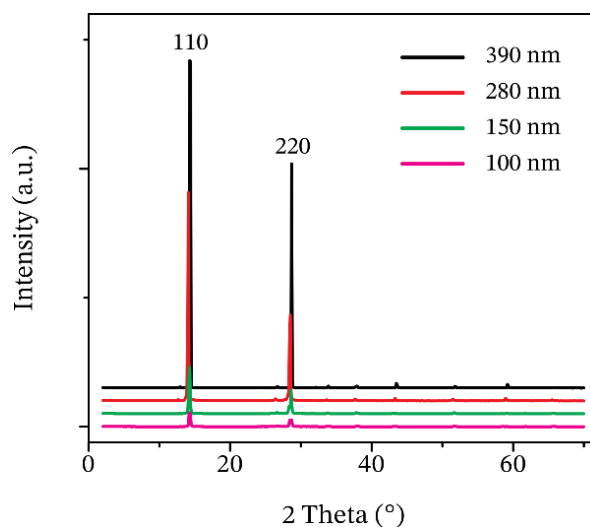
Figure 3.18. *XRD patterns of the perovskite films with different thicknesses, showing the characteristic peaks of the $CH_3NH_3PbI_{3-x}Cl_x$ tetragonal phase with predominant crystallization along the (110) and (220) planes.*
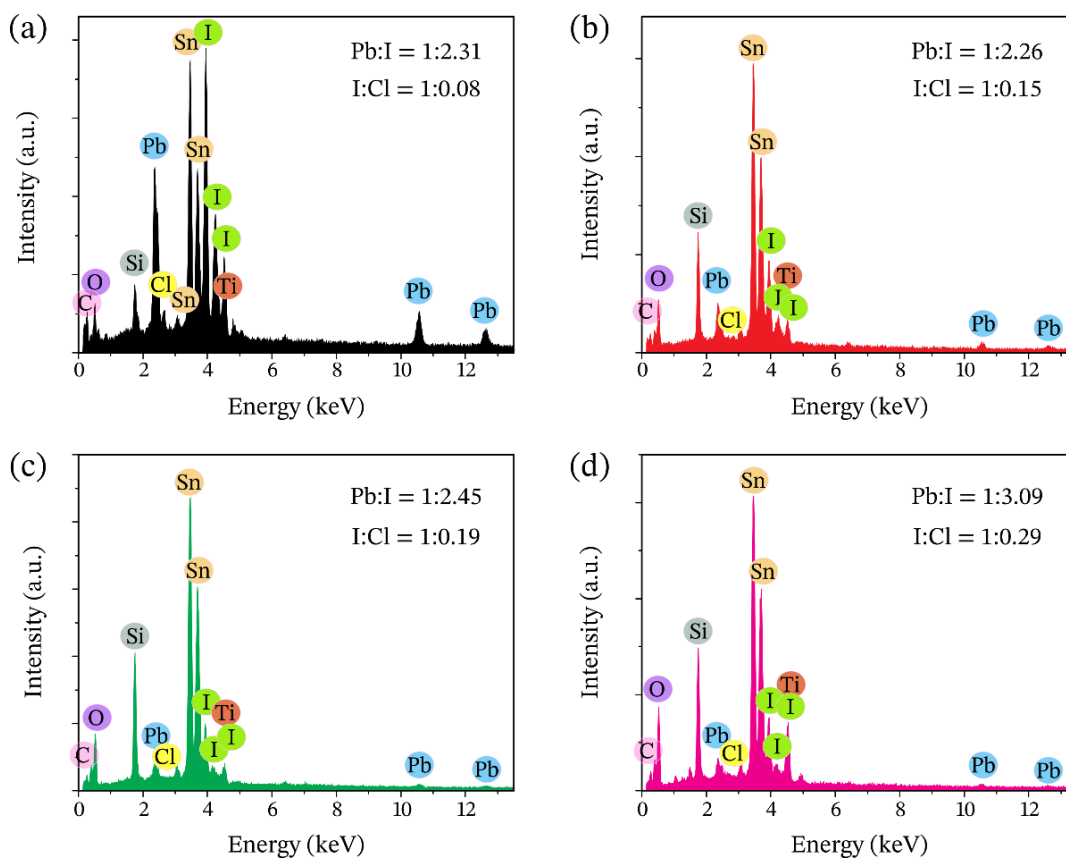
Figure 3.19. *EDX spectra acquired in scanning electron microscopy (SEM) at the top-view samples of CH₃NH₃PbI₃₋ₓClₓ deposited onto c-TiO₂-coated FTO/glass substrates at different thicknesses: (a) 390 nm; (b) 280 nm; (c) 150 nm; (d) 100 nm. The obtained Pb:I and I:Cl atomic ratios are reported as an inset.*
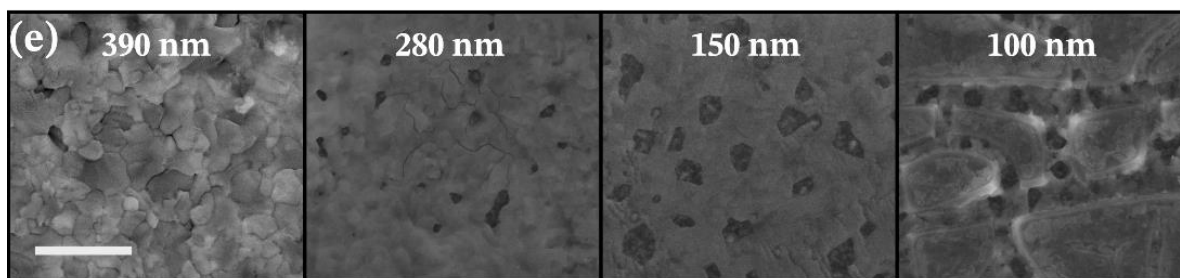
Figure 3.20. *Top-view SEM images of CH₃NH₃PbI₃₋ₓClₓ films deposited onto c-TiO₂-coated FTO/glass substrates. The corresponding thickness is shown at the top of each image. Scale bar: 5 μm.*
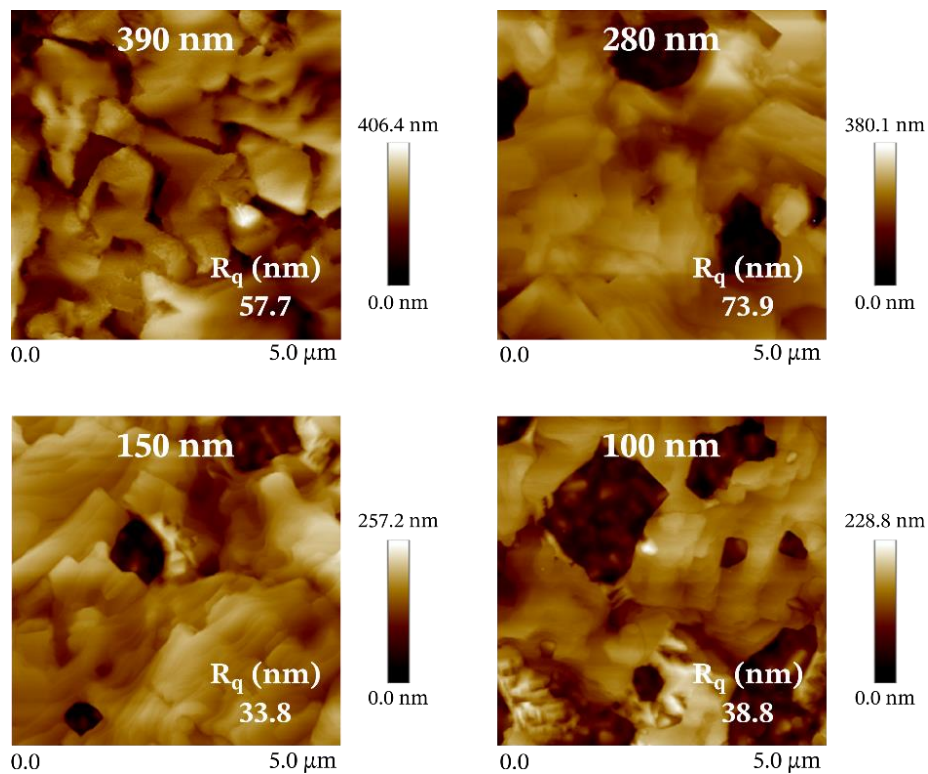
Figure 3.21. *Top-view AFM images of the mixed-halide perovskite films deposited onto c-TiO₂-coated FTO/glass substrates. The corresponding thickness is shown at the top of each image. The surface roughness of each film is noted as the root mean-square value (R_q).*

3.3. Conclusions

In summary, a novel DMD multilayer top electrode with high transparency and conductivity was developed using copper as metal and molybdenum suboxide as dielectric. Uniform and conductive Cu films as thin as 9.5 nm were successfully grown on the MoO_x substrate by means of an ultrathin (1.5 nm) Au seed layer, which was also proved to act as an effective Cu diffusion barrier. This strategy provided great thermal and mechanical stability to the MoO_x/Au-seed/Cu/MoO_x structure, making it appealing for applications in modern opto-electronics. High-performance semitransparent mixed-halide perovskite solar cells were manufactured by combining the proposed Cu-based transparent electrode with perovskite layers of different thicknesses. The thickest solar cell yielded the best PCE of 12.5%, with an average transmittance of 5% in the range 400-800 nm. In the prospect of BIPV applications, solar cells with thinner perovskite films and enhanced visible transparency were also prepared, showing AVTs of 9, 18 and 24% with the corresponding PCEs of 10.2, 6.4 and 3.1%. The use of copper allowed a substantial reduction in material costs compared to other DMD structures reported in literature and based on expensive gold, without sacrificing the device performance. Moreover, the devices showed acceptable stability under inert conditions, proving to be a reliable alternative to the more common and intrinsically unstable Ag-based PSCs. Therefore, this work demonstrates that the traditional high-value metals (Au, Ag) can be effectively replaced by non-precious copper in the fabrication of high-performing, perovskite-compatible DMD architectures to serve as hole-selective contacts in ST-PSCs. These findings open up new possibilities for high-performance, cost-effective semitransparent perovskite solar cells for BIPV systems. The feasibility of using less expensive metal in place of Au as a wetting inducer will be investigated in the future to further reduce material costs, even though gold remains one of the most promising materials for this role in terms of chemical stability, work function, and easy processing. Moreover, there is room for further improvement in the electrode performance by optimizing thickness, processing conditions and structural properties of each constituent layer in order to achieve higher efficiency as well as transparency for practical ST applications, including tandem solar cells.

3.4. References

(1)   Giuliano, G.; Cataldo, S.; Scopelliti, M.; Principato, F.; Martino, D. C.; Fiore, T.; Pignataro, B. Nonprecious Copper-Based Transparent Top Electrode via Seed Layer–Assisted Thermal Evaporation for High-Performance Semitransparent n-i-p Perovskite Solar Cells. *Adv. Mater. Technol.* **2019**, *4* (5), 1800688. https://doi.org/10.1002/admt.201800688.

(2)   Traverse, C. J.; Pandey, R.; Barr, M. C.; Lunt, R. R. Emergence of Highly Transparent Photovoltaics for Distributed Applications. *Nat. Energy* **2017**, *2* (11), 849. https://doi.org/10.1038/s41560-017-0016-9.

(3)   Xue, Q.; Xia, R.; Brabec, C. J.; Yip, H.-L. Recent Advances in Semi-Transparent Polymer and Perovskite Solar Cells for Power Generating Window Applications. *Energy Environ. Sci.* **2018**, *11* (7), 1688–1709. https://doi.org/10.1039/C8EE00154E.

(4)   Bailie, C. D.; Christoforo, M. G.; Mailoa, J. P.; Bowring, A. R.; Unger, E. L.; Nguyen, W. H.; Burschka, J.; Pellet, N.; Lee, J. Z.; Grätzel, M.; et al. Semi-Transparent Perovskite Solar Cells for Tandems with Silicon and CIGS. *Energy Environ. Sci.* **2015**, *8* (3), 956–963. https://doi.org/10.1039/C4EE03322A.

(5)   Lee, K.-T.; Guo, L.; Park, H. Neutral- and Multi-Colored Semitransparent Perovskite Solar Cells. *Molecules* **2016**, *21* (4), 475. https://doi.org/10.3390/molecules21040475.

(6)   Hu, X.; Huang, Z.; Zhou, X.; Li, P.; Wang, Y.; Huang, Z.; Su, M.; Ren, W.; Li, F.; Li, M.; et al. Wearable Large-Scale Perovskite Solar-Power Source via Nanocellular Scaffold. *Adv. Mater.* **2017**, *29* (42), 1703236. https://doi.org/10.1002/adma.201703236.

(7)   Saifullah, M.; Gwak, J.; Yun, J. H. Comprehensive Review on Material Requirements, Present Status, and Future Prospects for Building-Integrated Semitransparent Photovoltaics (BISTPV). *J. Mater. Chem. A* **2016**, *4* (22), 8512–8540. https://doi.org/10.1039/C6TA01016D.

(8)   Tai, Q.; Yan, F. Emerging Semitransparent Solar Cells: Materials and Device Design. *Adv. Mater.* **2017**, *29* (34), 1700192. https://doi.org/10.1002/adma.201700192.

(9)   National Renewable Energy Laboratory (NREL). Best Research-Cell Efficiency Chart. https://www.nrel.gov/pv/assets/pdfs/best-research-cell-efficiencies.20190802.pdf (accessed Sep 18, 2019).

(10)   Shi, B.; Duan, L.; Zhao, Y.; Luo, J.; Zhang, X. Semitransparent Perovskite Solar Cells: From Materials and Devices to Applications. *Adv. Mater.* 1806474. https://doi.org/10.1002/adma.201806474.

(11)   Li, C.; Sleppy, J.; Dhasmana, N.; Soliman, M.; Tetard, L.; Thomas, J. A PCBM-Assisted Perovskite Growth Process to Fabricate High Efficiency Semitransparent Solar Cells. *J. Mater. Chem. A* **2016**, *4* (30), 11648–11655. https://doi.org/10.1039/C6TA04790D.

(12)   Ou, X.-L.; Xu, M.; Feng, J.; Sun, H.-B. Flexible and Efficient ITO-Free Semitransparent Perovskite Solar Cells. *Sol. Energy Mater. Sol. Cells* **2016**, *157*, 660–665. https://doi.org/10.1016/j.solmat.2016.07.010.

(13)   Chen, B.; Bai, Y.; Yu, Z.; Li, T.; Zheng, X.; Dong, Q.; Shen, L.; Boccard, M.; Gruverman, A.; Holman, Z.; et al. Efficient Semitransparent Perovskite Solar Cells for 23.0%-Efficiency Perovskite/Silicon Four-Terminal Tandem Cells. *Adv. Energy Mater.* **2016**, *6* (19), 1601128. https://doi.org/10.1002/aenm.201601128.

(14) Della Gaspera, E.; Peng, Y.; Hou, Q.; Spiccia, L.; Bach, U.; Jasieniak, J. J.; Cheng, Y.-B. Ultra-Thin High Efficiency Semitransparent Perovskite Solar Cells. *Nano Energy* **2015**, *13*, 249–257. https://doi.org/10.1016/j.nanoen.2015.02.028.

(15) Kim, H.; Kim, H.-S.; Ha, J.; Park, N.-G.; Yoo, S. Empowering Semi-Transparent Solar Cells with Thermal-Mirror Functionality. *Adv. Energy Mater.* **2016**, *6* (14), 1502466. https://doi.org/10.1002/aenm.201502466.

(16) Kim, G. M.; Tatsuma, T. Semi-Transparent Perovskite Solar Cells Developed by Considering Human Luminosity Function. *Sci. Rep.* **2017**, *7* (1). https://doi.org/10.1038/s41598-017-11193-1.

(17) Eperon, G. E.; Burlakov, V. M.; Goriely, A.; Snaith, H. J. Neutral Color Semitransparent Microstructured Perovskite Solar Cells. *ACS Nano* **2014**, *8* (1), 591–597. https://doi.org/10.1021/nn4052309.

(18) Roldán-Carmona, C.; Malinkiewicz, O.; Betancur, R.; Longo, G.; Momblona, C.; Jaramillo, F.; Camacho, L.; Bolink, H. J. High Efficiency Single-Junction Semitransparent Perovskite Solar Cells. *Energy Env. Sci* **2014**, *7* (9), 2968–2973. https://doi.org/10.1039/C4EE01389A.

(19) Aharon, S.; Layani, M.; Cohen, B.-E.; Shukrun, E.; Magdassi, S.; Etgar, L. Self-Assembly of Perovskite for Fabrication of Semitransparent Perovskite Solar Cells. *Adv. Mater. Interfaces* **2015**, *2* (12), 1500118. https://doi.org/10.1002/admi.201500118.

(20) Cao, W.; Li, J.; Chen, H.; Xue, J. Transparent Electrodes for Organic Optoelectronic Devices: A Review. *J. Photonics Energy* **2014**, *4* (1), 040990. https://doi.org/10.1117/1.JPE.4.040990.

(21) Kim, S.; Lee, J.-L. Design of Dielectric/Metal/Dielectric Transparent Electrodes for Flexible Electronics. *J. Photonics Energy* **2012**, *2* (1), 021215. https://doi.org/10.1117/1.JPE.2.021215.

(22) Cattin, L.; Bernède, J. C.; Morsli, M. Toward Indium-Free Optoelectronic Devices: Dielectric/Metal/Dielectric Alternative Transparent Conductive Electrode in Organic Photovoltaic Cells. *Phys. Status Solidi A* **2013**, *210* (6), 1047–1061. https://doi.org/10.1002/pssa.201228089.

(23) Cattin, L.; Jouad, E.; Stephant, N.; Louarn, G.; Morsli, M.; Hssein, M.; Mouchaal, Y.; Thouiri, S.; Addou, M.; Khelil, A.; et al. Dielectric/Metal/Dielectric Alternative Transparent Electrode: Observations on Stability/Degradation. *J. Phys. Appl. Phys.* **2017**, *50* (37), 375502. https://doi.org/10.1088/1361-6463/aa7dfd.

(24) Bernède, J. C.; Cattin, L. Dielectric/Metal/Dielectric Flexible Transparent Electrodes, from Smart Window to Semi-Transparent Solar Cells. *Asian J. Eng. Technol.* **2019**, *7* (3). https://doi.org/10.24203/ajet.v7i3.5710.

(25) Yang, Y. (Michael); Chen, Q.; Hsieh, Y.-T.; Song, T.-B.; Marco, N. D.; Zhou, H.; Yang, Y. Multilayer Transparent Top Electrode for Solution Processed Perovskite/Cu(In,Ga)(Se,S) $_2$ Four Terminal Tandem Solar Cells. *ACS Nano* **2015**, *9* (7), 7714–7721. https://doi.org/10.1021/acsnano.5b03189.

(26) Rahmany, S.; Layani, M.; Magdassi, S.; Etgar, L. Fully Functional Semi-Transparent Perovskite Solar Cell Fabricated in Ambient Air. *Sustain. Energy Fuels* **2017**, *1* (10), 2120–2127. https://doi.org/10.1039/C7SE00383H.

(27) Han, G. S.; Lee, S.; Duff, M. L.; Qin, F.; Jiang, M.; Li, G.; Lee, J.-K. Multi-Functional Transparent Electrode for Reliable Flexible Perovskite Solar Cells. *J. Power Sources* **2019**, *435*, 226768. https://doi.org/10.1016/j.jpowsour.2019.226768.

(28) Kato, Y.; Ono, L. K.; Lee, M. V.; Wang, S.; Raga, S. R.; Qi, Y. Silver Iodide Formation in Methyl Ammonium Lead Iodide Perovskite Solar Cells with Silver Top Electrodes. *Adv. Mater. Interfaces* **2015**, *2* (13), 1500195. https://doi.org/10.1002/admi.201500195.

(29) Zhao, J.; Zheng, X.; Deng, Y.; Li, T.; Shao, Y.; Gruverman, A.; Shield, J.; Huang, J. Is Cu a Stable Electrode Material in Hybrid Perovskite Solar Cells for a 30-Year Lifetime? *Energy Environ. Sci.* **2016**, *9* (12), 3650–3656. https://doi.org/10.1039/C6EE02980A.

(30) Deng, Y.; Dong, Q.; Bi, C.; Yuan, Y.; Huang, J. Air-Stable, Efficient Mixed-Cation Perovskite Solar Cells with Cu Electrode by Scalable Fabrication of Active Layer. *Adv. Energy Mater.* **2016**, *6* (11), 1600372. https://doi.org/10.1002/aenm.201600372.

(31) Wang, L.; Li, G.-R.; Zhao, Q.; Gao, X.-P. Non-Precious Transition Metals as Counter Electrode of Perovskite Solar Cells. *Energy Storage Mater.* **2017**, *7*, 40–47. https://doi.org/10.1016/j.ensm.2016.11.007.

(32) Zhao, J.; Brinkmann, K. O.; Hu, T.; Pourdavoud, N.; Becker, T.; Gahlmann, T.; Heiderhoff, R.; Polywka, A.; Görrn, P.; Chen, Y.; et al. Self-Encapsulating Thermostable and Air-Resilient Semitransparent Perovskite Solar Cells. *Adv. Energy Mater.* **2017**, *7* (14), 1602599. https://doi.org/10.1002/aenm.201602599.

(33) Lim, S.; Han, D.; Kim, H.; Lee, S.; Yoo, S. Cu-Based Multilayer Transparent Electrodes: A Low-Cost Alternative to ITO Electrodes in Organic Solar Cells. *Sol. Energy Mater. Sol. Cells* **2012**, *101*, 170–175. https://doi.org/10.1016/j.solmat.2012.01.016.

(34) Zhao, G.; Wang, W.; Bae, T.-S.; Lee, S.-G.; Mun, C.; Lee, S.; Yu, H.; Lee, G.-H.; Song, M.; Yun, J. Stable Ultrathin Partially Oxidized Copper Film Electrode for Highly Efficient Flexible Solar Cells. *Nat. Commun.* **2015**, *6* (1). https://doi.org/10.1038/ncomms9830.

(35) Hssein, M.; Cattin, L.; Morsli, M.; Addou, M.; Bernède, J.-C. Copper:Molybdenum Sub-Oxide Blend as Transparent Conductive Electrode (TCE) Indium Free. *Eur. Phys. J. Appl. Phys.* **2016**, *74* (2), 24604. https://doi.org/10.1051/epjap/2015150336.

(36) Zhao, G.; Song, M.; Chung, H.-S.; Kim, S. M.; Lee, S.-G.; Bae, J.-S.; Bae, T.-S.; Kim, D.; Lee, G.-H.; Han, S. Z.; et al. Optical Transmittance Enhancement of Flexible Copper Film Electrodes with a Wetting Layer for Organic Solar Cells. *ACS Appl. Mater. Interfaces* **2017**, *9* (44), 38695–38705. https://doi.org/10.1021/acsami.7b10234.

(37) Lopéz, I. P.; Cattin, L.; Nguyen, D.-T.; Morsli, M.; Bernède, J. C. Dielectric/Metal/Dielectric Structures Using Copper as Metal and MoO3 as Dielectric for Use as Transparent Electrode. *Thin Solid Films* **2012**, *520* (20), 6419–6423. https://doi.org/10.1016/j.tsf.2012.06.056.

(38) Tuo, S.; Cattin, L.; Essaidi, H.; Peres, L.; Louarn, G.; El Jouad, Z.; Hssein, M.; Touihri, S.; Yapi Abbe, S.; Torchio, P.; et al. Stabilisation of the Electrical and Optical Properties of Dielectric/Cu/Dielectric Structures through the Use of Efficient Dielectric and Cu:Ni Alloy. *J. Alloys Compd.* **2017**, *729*, 109–116. https://doi.org/10.1016/j.jallcom.2017.09.087.

(39) Luo, S.; Daoud, W. A. Crystal Structure Formation of CH3NH3PbI3-XClx Perovskite. *Materials* **2016**, *9* (3). https://doi.org/10.3390/ma9030123.

(40) Ye, M.; He, C.; Iocozzia, J.; Liu, X.; Cui, X.; Meng, X.; Rager, M.; Xiaodan Hong; Liu, X.; Lin, Z. Recent Advances in Interfacial Engineering of Perovskite Solar Cells. *J. Phys. Appl. Phys.* **2017**, *50* (37), 373002. https://doi.org/10.1088/1361-6463/aa7cb0.

(41) Hölzl, J.; Schulte, F. K. Work Function of Metals. In *Solid Surface Physics*; Hölzl, J., Schulte, F. K., Wagner, H., Eds.; Springer Tracts in Modern Physics; Springer Berlin Heidelberg: Berlin, Heidelberg, 1979; pp 1–150. https://doi.org/10.1007/BFb0048919.

(42) Guerrero, A.; You, J.; Aranda, C.; Kang, Y. S.; Garcia-Belmonte, G.; Zhou, H.; Bisquert, J.; Yang, Y. Interfacial Degradation of Planar Lead Halide Perovskite Solar Cells. *ACS Nano* **2016**, *10* (1), 218–224. https://doi.org/10.1021/acsnano.5b03687.

(43) Sun, Y.; Takacs, C. J.; Cowan, S. R.; Seo, J. H.; Gong, X.; Roy, A.; Heeger, A. J. Efficient, Air-Stable Bulk Heterojunction Polymer Solar Cells Using MoOx as the Anode Interfacial Layer. *Adv. Mater.* **2011**, *23* (19), 2226–2230. https://doi.org/10.1002/adma.201100038.

(44) Dasgupta, B.; Goh, W. P.; Ooi, Z. E.; Wong, L. M.; Jiang, C. Y.; Ren, Y.; Tok, E. S.; Pan, J.; Zhang, J.; Chiam, S. Y. Enhanced Extraction Rates through Gap States of Molybdenum Oxide Anode Buffer. *J. Phys. Chem. C* **2013**, *117* (18), 9206–9211. https://doi.org/10.1021/jp3114013.

(45) Snaith, H. J.; Abate, A.; Ball, J. M.; Eperon, G. E.; Leijtens, T.; Noel, N. K.; Stranks, S. D.; Wang, J. T.-W.; Wojciechowski, K.; Zhang, W. Anomalous Hysteresis in Perovskite Solar Cells. *J. Phys. Chem. Lett.* **2014**, *5* (9), 1511–1515. https://doi.org/10.1021/jz500113x.

(46) Yun, J. Ultrathin Metal Films for Transparent Electrodes of Flexible Optoelectronic Devices. *Adv. Funct. Mater.* **2017**, *27* (18), 1606641. https://doi.org/10.1002/adfm.201606641.

(47) Vitos, L.; Ruban, A. V.; Skriver, H. L.; Kollár, J. The Surface Energy of Metals. *Surf. Sci.* **1998**, *411* (1–2), 186–202.

(48) Schubert, S.; Meiss, J.; Müller-Meskamp, L.; Leo, K. Improvement of Transparent Metal Top Electrodes for Organic Solar Cells by Introducing a High Surface Energy Seed Layer. *Adv. Energy Mater.* **2013**, *3* (4), 438–443. https://doi.org/10.1002/aenm.201200903.

(49) Bauer, E. Epitaxy of Metals on Metals. *Appl. Surf. Sci.* **1982**, *11–12*, 479–494. https://doi.org/10.1016/0378-5963(82)90094-0.

(50) Haacke, G. New Figure of Merit for Transparent Conductors. *J. Appl. Phys.* **1976**, *47* (9), 4086–4089. https://doi.org/10.1063/1.323240.

(51) Leppänen, K.; Augustine, B.; Saarela, J.; Myllylä, R.; Fabritius, T. Breaking Mechanism of Indium Tin Oxide and Its Effect on Organic Photovoltaic Cells. *Sol. Energy Mater. Sol. Cells* **2013**, *117*, 512–518. https://doi.org/10.1016/j.solmat.2013.07.010.

(52) Elumalai, N. K.; Uddin, A. Hysteresis in Organic-Inorganic Hybrid Perovskite Solar Cells. *Sol. Energy Mater. Sol. Cells* **2016**, *157*, 476–509. https://doi.org/10.1016/j.solmat.2016.06.025.

(53) Chen, K.-S.; Salinas, J.-F.; Yip, H.-L.; Huo, L.; Hou, J.; Jen, A. K.-Y. Semi-Transparent Polymer Solar Cells with 6% PCE, 25% Average Visible Transmittance and a Color Rendering Index Close to 100 for Power Generating Window Applications. *Energy Environ. Sci.* **2012**, *5* (11), 9551. https://doi.org/10.1039/c2ee22623e.

(54) Agarwal, S.; Nair, P. R. Pinhole Induced Efficiency Variation in Perovskite Solar Cells. *J. Appl. Phys.* **2017**, *122* (16), 163104. https://doi.org/10.1063/1.4996315.

Chapter 4

Rational Additive Engineering for More Efficient and Stable n-i-p PSCs

---

The perovskite film is at the core of a PSC, and its quality is crucial to device performance. In particular, the uniformity, crystallinity, and coverage of the perovskite layer greatly affect PCE, hysteresis, and long-term stability of devices. Additive engineering is an effective way to control film morphology and to reduce defect density. In this chapter, α-terpineol, a non-toxic and easily accessible monoterpene alcohol, is incorporated into one-step perovskite precursor solution as an effective solvent additive to improve the quality of perovskite films and to restrain non-radiative recombination in the corresponding devices. It is demonstrated that the incorporation of α-terpineol at a concentration of 5 g/L is capable of generating uniform and highly crystalline perovskite films with fewer trap states. Through this approach, the PCE of PSCs is boosted from 13.9% to 15.4% with reduced hysteresis and improved stability.

4.1. Motivation of the study

At present, one of the main challenges in PSC fabrication is the control of the perovskite film formation and crystallization. In Chapter 1 the importance of depositing uniform, dense, highly crystalline and pinhole-free perovskite layers for obtaining higher PCEs was introduced. It is well-known that poor perovskite morphology can deleteriously impact the efficiency of charge dissociation, transport, and collection in the devices. In particular, a high concentration of defects and grain boundaries in the perovskite film would create severe shorting and trapping sites for non-radiative recombination, which is recognized as one of the main causes of PCE losses in PSCs. As already discussed in Chapter 1, defect- and grain-boundary-assisted charge recombination is also related to anomalous hysteresis phenomena and long-term stability issues. Therefore, optimizing the perovskite layer by passivating defects and improving crystal quality has become an important strategy to reduce recombination losses, remove adverse hysteresis, prolong device lifetime, and boost PCE towards the theoretical SQ limit.[1–5]

To date, numerous approaches have been proposed to manipulate the nucleation and growth of the perovskite grains. Among them, additive engineering is the simplest and easiest technique, which has often proved effective in enhancing the film quality and minimizing the recombination losses.[6,7] The mechanism behind this strategy is generally related to the passivation of defects and trap states and modulation of the crystallization kinetics. Some additives can trigger the fast crystallization, while others can delay the nucleation process, depending on their nature. Additives with high coordination power can also play a key role in perovskite film formation if used in suitable deposition routes. Various types of additives have been applied, including fullerene derivatives,[8,9] inorganic acids,[10–12] metal halide salts,[13,14] organic solvents and polymers,[15,16] which have been incorporated into perovskite film in several ways, for example by simply adding them to the one-step precursor solution or to the solution of organic sources in two-step deposition.

Recently published work has demonstrated that interactions between organic solvents and components of perovskite can be utilized to control the morphology and crystallinity of solution-processed perovskite films.[17] For example, 1,8-diiodiooctane (DIO) and 1-chloronaphtalene (CN) have been reported by several groups as effective solvent additives in the one-step precursor solution.[18–22] Their halogen atoms can coordinate with Pb^{2+} during crystal growth, thus effectively decreasing the density of defect states and altering the crystallization kinetics of the perovskite

film. Moreover, as they possess higher boiling points compared with the major solvent (DMF, b.p. 153 °C), they are retained in the film for a longer time, which is beneficial to merge small grains during the annealing treatment and form a uniform perovskite film with large grains. A significant PCE enhancement from 9.0% to 11.8% has been demonstrated by Liang et al.,[19] who introduced 1 wt% DIO in the precursor solution prior to thin-film deposition. High-quality perovskite films can also be fabricated via the addition of some strong Lewis base solvents, such as N-methyl-2-pyrrolidone (NMP), dimethyl sulfoxide (DMSO), and hexamethylphosphoramide (HMPA), which can interact strongly with Pb^{2+} to form Lewis acid-base adducts.[23–26] However, these solvents generally show high toxicity, which can harm health and environment.

Aiming at the commercialization of PSCs, non-toxicity, low-cost and easy accessibility should be addressed in seeking for the appropriate additives. In this direction, Chang et al.[15] and Zhao et al.[16] reported the incorporation of poly(ethylene glycol) (PEG) as an effective and harmless additive in the perovskite precursor solution. Apparently, PEG can retard the growth and aggregation of perovskite crystals and can reduce the voids between perovskite domains during thermal annealing at 100 °C. The strong hydrogen bonding between O atoms in PEG and H atoms in MA^+ contribute to a desirable perovskite morphology and an improved device stability. More recently, Zhi et al.[27] proposed the use of 1,3-Dimethyl-2-imidazolidinone (DMI) solvent additive as a less-toxic, environmentally friendly alternative to the carcinogen HMPA and reproductively toxic NMP. In their work, the efficiency of the solar cells was significantly enhanced from 10.72% to 14.54% by adding 10 vol% DMI in the precursor solution and annealing at 130 °C.

Inspired by the abovementioned works, the study reported in this chapter explores the potential of α-terpineol, a naturally occurring monoterpene alcohol (see the chemical structure in **Figure 4.1**), as a solvent additive to improve the morphology and crystallinity of one-step solution-processed perovskite films. α-terpineol can be isolated from a variety of natural sources such as pine oil, cajeput oil, and petitgrain oil. It plays an important role in the industrial field as a popular fragrance ingredient used in perfumes and cosmetics, but also in the medical ad biological fields as an antioxidant, anticancer, antiulcer, anticonvulsant, pesticide, etc.[28–32] In addition, α-terpineol is frequently used as a high viscosity solvent along with ethyl cellulose as a resin to prepare printable pastes.[33] Its low toxicity, easy accessibility, and high boiling point (b.p. 219 °C), as well as its well-known capacity to act as a good solvent in printing media make it very attractive for applications as solvent additive into perovskite precursor solution. Moreover, the −OH group in α-

terpineol can interact with MA^+ and I^- ions, as reported by Guo et al. in a recently published work,[34] or with Pb^{2+} through Pb−O coordination bonds, and this may lead to an effective defect passivation in resultant perovskite films.
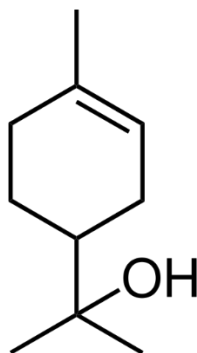
Figure 4.1. *Chemical structure of α-terpineol.*

4.2. Results and Discussion

4.2.1. Reference Solar Cells without Additive

As a reference, PSCs processed from pristine precursor solution (without additive) were first fabricated. The same planar n-i-p configuration as that used in Chapter 3 was adopted in this work, with c-TiO$_2$ as the ETL, CH$_3$NH$_3$PbI$_{3-x}$Cl$_x$ as the absorber layer, and spiro-OMeTAD as the HTL. However, less-expensive Ag (100 nm thick, WF = 4.3 eV) was used instead of Au as the top electrode material. The architecture as well as the energy level diagram of the complete device are illustrated in **Figure 4.2**. The CH$_3$NH$_3$PbI$_{3-x}$Cl$_x$ films were deposited through the same one-step spin-coating technique as that used in Chapter 3. Detailed information regarding the fabrication procedure was provided in Chapter 2, while the results obtained from the morphological and structural characterization of the fabricated perovskite films were reported in Chapter 3.
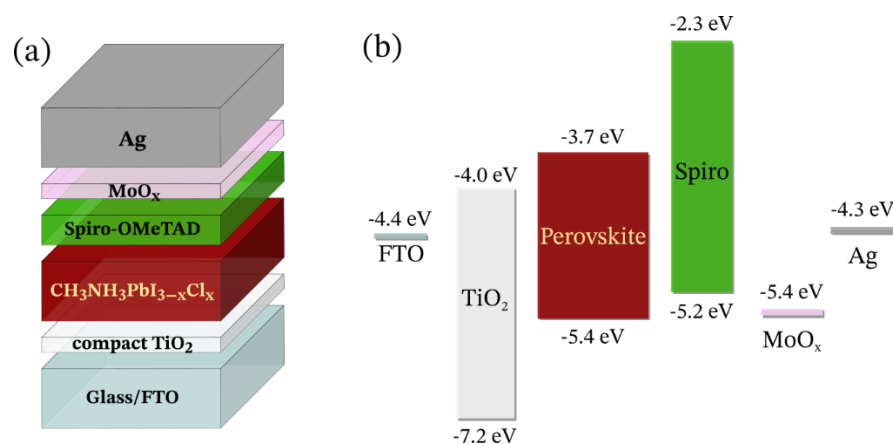
Figure 4.2. *(a) Schematic illustration of the PSC planar architecture. (b) Energy band diagram of the complete n-i-p photovoltaic device. Literature reports for band edges and Fermi levels were used.*

In this chapter, the electrical characterization of the devices was performed using a xenon arc lamp solar simulator (Sunlite, model 11002, class ABA, Abet Technologies) instead of the halogen lamp used in Chapter 3. As the halogen lamp inevitably leaves a significant UV deficit with respect to the solar spectrum, this evolution in the instrumental equipment allowed for a more correct extraction and interpretation of the photovoltaic parameters. The control Ag-based devices prepared from the pristine precursor solution (without additive) exhibited PCEs as high as 13.9%

under standard 1 sun illumination (see **Figure 4.3**a), an efficiency comparable to that extracted from the J-V curve of the best opaque Au-based reference cell fabricated in Chapter 3 (14.2%). It is well known from the literature that gold generally leads to the best-performance devices owing to its high work function (5.1 eV) and excellent chemical stability.[35] To confirm this, reference solar cells with 100 nm thick Au top electrodes were also prepared in this work, but this time they were characterized using the xenon arc lamp solar simulator. A record high PCE of 17.7% was achieved under reverse scan (see Figure 4.3b), confirming the superiority of gold as a counter electrode material and the importance of the UV spectral region for a more accurate PSC characterization. The corresponding photovoltaic parameters are summarized in **Table 4.1**. The higher FF and V_{oc} values obtained for the Au-based devices are indicative of an improved interface contact and reduced charge carrier recombination compared with the Ag-based cells, as expected.

Figure 4.3. Reverse scanning J-V curves of the best-performance control PSCs featuring (a) MoO_x (6 nm)/ Ag (100 nm) and (b) MoO_x (6 nm)/ Au (100 nm) as the top electrode, respectively, measured under standard (1 sun) illumination using a xenon arc lamp solar simulator. The device parameters are reported as an inset. Active area: 3.14 mm^2.
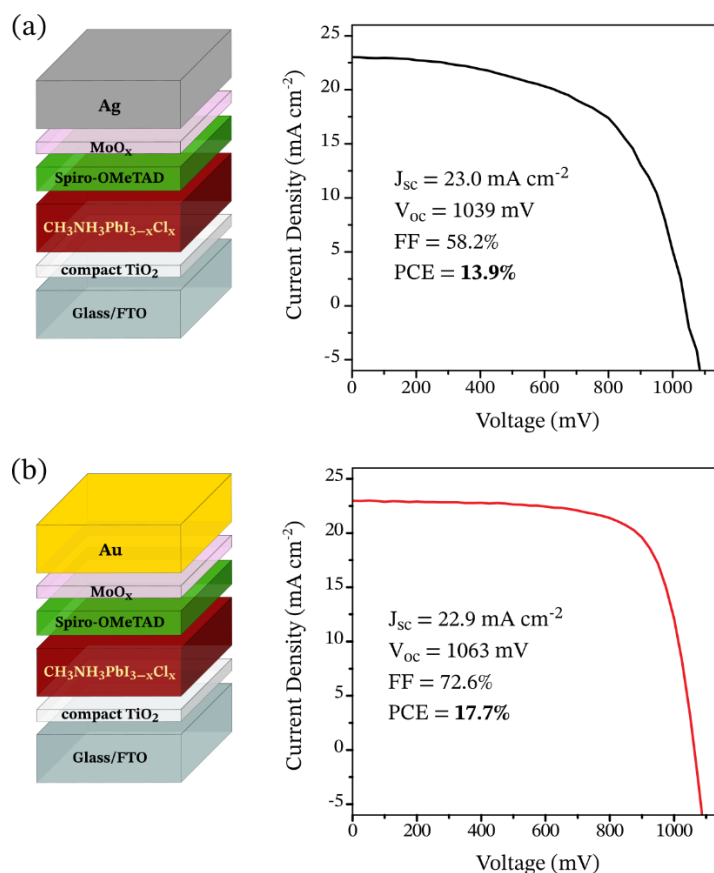
Table 4.1. *Summary of PSC performances (short-circuit current, J$_{sc}$; open-circuit voltage, V$_{oc}$; fill factor, FF; power conversion efficiency, PCE) for control (additive-free) solar cells having 100 nm thick Ag or Au as the top contact, measured under standard (1 sun) illumination.*

Top electrode		J$_{sc}$ [mA cm^{-2}]	V$_{oc}$ [mV]	FF [%]	PCE [%]
MoO$_x$ (6 nm)/Ag (100 nm)	Best[a]	23.0	1039	58.2	**13.9**
	Mean[b]	21.3 (±1.7)	1017 (±32)	57.9 (±5.1)	12.5 (±0.9)
MoO$_x$ (6 nm)/Au (100 nm)	Best[a]	22.9	1063	72.6	**17.7**
	Mean[b]	23.1 (±1.1)	1041 (±37)	70.3 (±2.2)	16.9 (±0.6)

[a] Values obtained for the best performing device. [b] Mean values obtained from at least 8 individual cells; the standard deviation around the mean is given in brackets.

4.2.2. Impact of α-Terpineol Additive on the J-V Curves

After the control solar cells were optimized, the study proceeded with the investigation of the effect on the device performance of introducing α-terpineol as a solvent additive into the perovskite precursor solution. α-terpineol was selected among other compounds for its low-cost, non-toxicity, and easy accessibility, and because it is frequently used as a solvent in printing media. Moreover, it was chosen for its higher boiling point (219 °C) compared to that of DMF (153 °C), since it is known that high-boiling-point additives can lead to a retarded crystallization of perovskite, which in turn produces more uniform films with smooth coverage.[17] Although the best-performance control devices were obtained using gold as the counter electrode material, the optimization of the solar cells processed from α-terpineol-based solutions was carried out using less-expensive silver in the perspective of future PSC commercialization.

As a first attempt, a relatively high concentration of α-terpineol was added to the precursor solution of MAI and PbCl$_2$ in DMF, namely 25 g/L. Then, the as-prepared solution was spin-coated onto c-TiO$_2$/FTO/glass substrates according to the reference protocol (see Chapter 2, Section 2). Discouragingly, the as-deposited films (before thermal annealing) showed non-uniform coverage with a high density of striation defects (see the picture in **Figure 4.4**). The occurrence of such

radial striated inhomogeneities typically arises from unfavourable surface tension effects during the spin-coating process and is indicative of an inappropriate solvent system.[36]

Figure 4.4. *Striation defects in perovskite precursor films obtained by adding 25 g/L of α-terpineol to the precursor solution.*

Based on the previous results, it was decided to opportunely reduce the concentration of the α-terpineol additive from 25 to 5 g/L. As a result, uniform and homogeneous perovskite films were achieved on top of the c-TiO$_2$/FTO/glass substrates, looking completely similar to those obtained from pristine precursor solutions at the naked-eye level (see **Figure 4.5**).
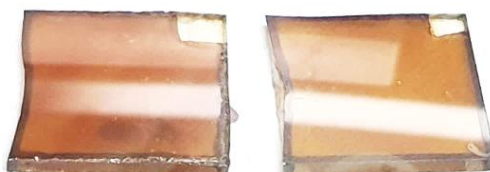
Figure 4.5. *As-deposited perovskite precursor films obtained by adding 5 g/L of α-terpineol to the precursor solution.*

The optimized films were then subject to the standard annealing treatment at 105°C for 1.5 h to promote the conversion of precursors into CH$_3$NH$_3$PbI$_{3-x}$Cl$_x$ crystals. Since α-terpineol has a boiling point comparable to that of other processing solvents commonly used in PSC fabrication (e.g. GBL, b.p. 204 °C), it is supposed to be completely removed from the samples through evaporation at the end of the annealing step, leading to high-purity perovskite layers with negligible residues. Further characterizations of the CH$_3$NH$_3$PbI$_{3-x}$Cl$_x$ films are planned in order to confirm this possibility. After the annealing process, the devices were completed by sequential deposition of the spiro-OMeTAD HTL and the MoO$_x$/Ag top electrode.

Surprisingly, the devices processed from the precursor solution containing 5 g/L α-terpineol showed a significant PCE enhancement (~11%) compared to the control solar cells, as presented in **Figure 4.6**a. The best-performance device possessed a PCE of 15.4% with a V$_{oc}$ of 1.05 V, a J$_{sc}$

of 23.2 mA cm^{-2}, and a FF of 63.1%, compared to the 13.9% PCE of the top control device with a V_{oc} of 1.04 V, a J_{sc} of 23.0 mA cm^{-2}, and a FF of 58.2%. The results of the J-V analysis are summarized in **Table 4.1**. The overall increase in the PV parameters, particularly in the FF, indicates that the interface and charge-transport properties are enhanced by the use of α-terpineol in the perovskite layer. Decreased series resistance and increased shunt resistance, which can be estimated from the inverse of the slope of the J-V curve at J = 0 and at J = J_{sc} (see Chapter 2, Section 3), reveal faster charge transport and less carrier recombination and suggest an improved morphology of the perovskite film in terms of coverage, uniformity, and crystallinity.
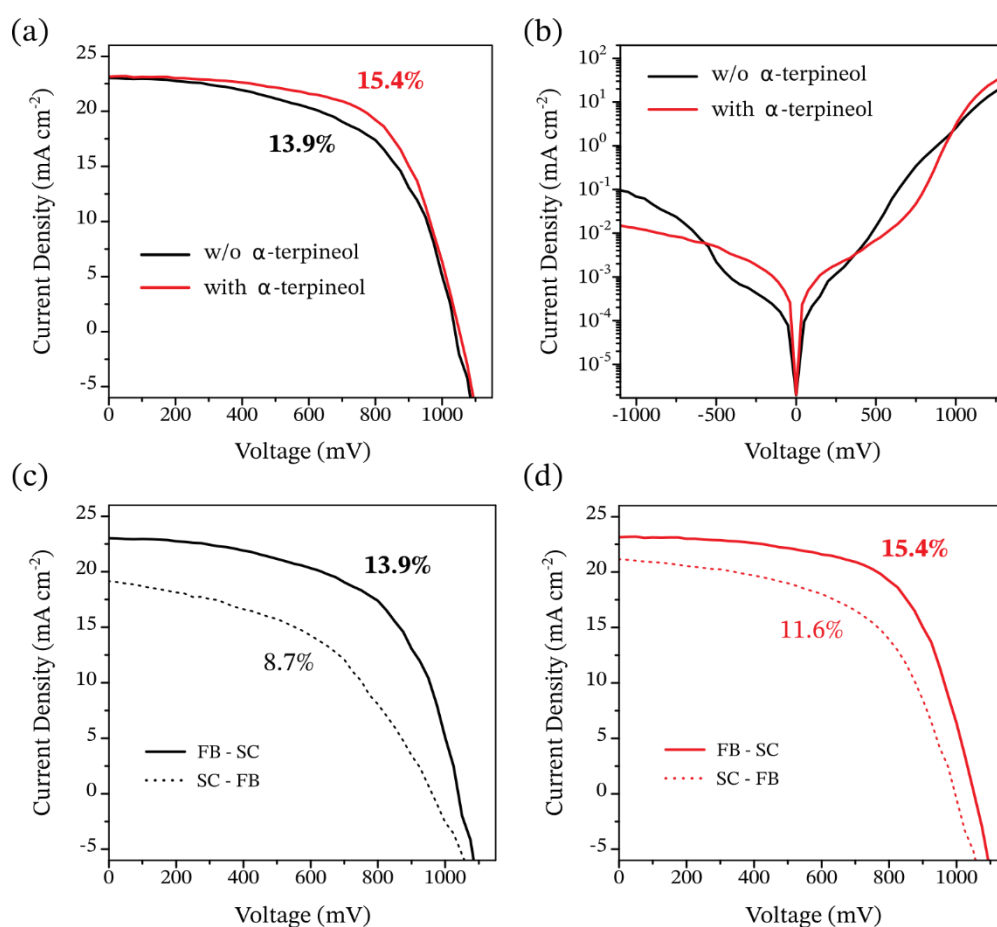
Figure 4.6. *(a) Reverse scanning J-V curves of the best-performance PSCs processed from solutions with/without α-terpineol, measured under standard 1 sun illumination. Active area: 3.14 mm². (b) Dark J-V curves (semilog plot) of the best-performance PSCs processed from solutions with/without α-terpineol. Hysteresis effect in the J-V curves of the top devices processed from solutions (c) without α-terpineol and (d) with α-terpineol by varying the voltage scanning direction.*

The dark JV curves of the PSCs with and without α-terpineol are reported in Figure 4.6b. It is observed that the dark current density of the device with α-terpineol is lower than that of the control cell in the reverse bias region between −0.5 V and −1.2 V, indicating that the leakage current is reduced with the addition of α-terpineol. On the other hand, the dark current density is higher for the α-terpineol-based device under the forward bias (voltages higher than 1 V), suggesting a lower injection barrier at the TiO_2/perovskite interface. These results account for the increase in V_{oc} and FF observed under standard illumination conditions.

Figure 4.6c-d compares the hysteretic behavior of the control PSCs and the PSCs treated with α-terpineol depending on the voltage scanning direction. The control device showed a relatively large degree of hysteresis, with the lowest PCE (8.7%) corresponding to the forward scan. As discussed in Chapter 1, such hysteresis effects may arise from charge trapping/detrapping dynamics resulting from a large defect density in the perovskite film, as well as from injection barriers at the perovskite/charge-transport layers interfaces. Interestingly, the cell using the perovskite absorber with α-terpineol in the precursor yielded a PCE of 11.6% under forward voltage scanning, revealing a significantly reduced hysteresis and a much-improved FF. These results further suggest a reduced density of defects and trapping sites for non-radiative recombination in the α-terpineol-modified perovskite film and lower carrier injection barriers at the interfaces, which translate into higher performances and lower hysteresis.

The reproducibility of the photovoltaic performances was also investigated. The values shown in Table 4.1 are average values and standard deviations of eight devices fabricated under identical conditions, with or without α-terpineol. The average V_{oc}, J_{sc}, FF, and PCE for the eight control cells are 1017 ± 32 mV, 21.3 ± 1.7 mA cm^{-2}, $57.9 \pm 5.1\%$, and $12.5 \pm 0.9\%$, respectively, measured under reverse voltage scanning. On the other hand, the average V_{oc}, J_{sc}, FF, and PCE for the eight devices prepared from α-terpineol-based solutions are 1028 ± 26 V, 22.1 ± 1.6 mA cm^{-2}, $62.9 \pm 3.8\%$, and $14.3 \pm 0.6\%$, respectively, extracted from the reverse scanning J-V curves. It is clear from the lower standard deviations that adding 5 g/L α-terpineol in the precursor solution significantly improves the reproducibility of PSCs. This means that the proposed deposition method is capable of generating compact and highly repeatable perovskite films. Considering that a very simple one-step spin-coated technique was used in this work, the achieved PCEs, along with the high reproducibility of the fabricated PSCs, are very promising and highly competitive with those of other systems reported in the literature.[18–21]

Table 4.2. Summary of PSC performances (short-circuit current, J_{sc}; open-circuit voltage, V_{oc}; fill factor, FF; power conversion efficiency, PCE) for solar cells processed from solutions with/without α-terpineol, measured under standard (1 sun) illumination.

Sample	Scan Direction		J_{sc} [mA cm^{-2}]	V_{oc} [mV]	FF [%]	PCE [%]
Without α-terpineol	Reverse	Best[a]	23.0	1039	58.2	**13.9**
	Reverse	Mean[b]	21.3 (±1.7)	1017 (±32)	57.9 (±5.1)	12.5 (±0.9)
	Forward	Best[a]	19.1	961	47.0	8.7
With α-terpineol	Reverse	Best[a]	23.2	1053	63.1	**15.4**
	Reverse	Mean[b]	22.1 (±1.6)	1028 (±26)	62.9 (±3.8)	14.3 (±0.6)
	Forward	Best[b]	21.2	996	55.1	11.6

[a] Values obtained for the best performing device. [b] Mean values obtained from at least 8 individual cells; the standard deviation around the mean is given in brackets.

4.2.3. Effect of Increasing the Active Area

As introduced in Chapter 1, one of the major challenges in PSC manufacturing is the scaling up. In large-area PSC devices, surfaces, bulk defects, and interfaces introduce charge recombination centers that lead to fast non-radiative losses and consequent decrease in the PV parameters.[37] The dilemma with fabricating large-area devices is that the perovskite layer should be thin enough to minimize resistive losses, while at the same time, it should cover the entire area in a contiguous and uniform manner. However, the deposition of uniform and pinhole-free perovskite films over a large area using a simple solution-based technique such as spin-coating is typically arduous.
In this work, solar cells with an increasing active area (3.14, 7.07, and 12.56 mm^2) were fabricated in order to evaluate the impact of the α-terpineol additive on the device performance while scaling up. The active-area-dependent J-V curves of the top devices with and without additive are shown in **Figure 4.7**, together with the trends of the corresponding power conversion efficiencies. The PV parameters are summarized in **Table 4.3**. A significant decrease in the conversion efficiency with the increase of the active area was observed for the control devices. The decrease in FF (from

58.2% to 50.6%) was the most significant influence, as often found in the literature. Indeed, the FF parameter is strictly linked to charge transport and recombination, which in turn depend on the morphology of the perovskite film over the entire active area. Conversely to the control devices, the solar cells processed using α-terpineol as a solvent-additive showed a minor reduction of the PV parameters as the active area increased. The FF decreased only from 63.1% to 60.7% when the active area was increased from 3.14 to 12.56 mm^2. A PCE as high as 14.0% was achieved for the α-terpineol-based PSC with 12.56 mm^2 active area. This implies that the incorporation of α-terpineol into the precursor solution improves the quality of the perovskite film over a large area.

Figure 4.7. *Reverse scanning J-V curves of the best-performance PSCs processed from solutions (a) without α-terpineol and (b) with α-terpineol with increasing of the active area, measured under standard 1 sun illumination. (c) Photograph of a fabricated sample with nine cells defined on it and featuring different active areas. (d) Variation in PCE with increasing of the active area for solar cells processed from solutions with/without α-terpineol.*

Table 4.3. Summary of PSC performances (short-circuit current, J_{sc}; open-circuit voltage, V_{oc}; fill factor, FF; power conversion efficiency, PCE) for solar cells processed from solutions with/without α-terpineol and featuring different active areas, measured under 1 sun illumination.

Sample	Active Area (mm^2)	J_{sc} [mA cm^{-2}]	V_{oc} [mV]	FF [%]	PCE [%]
Without α-terpineol	3.14	23.0	1039	58.2	**13.9**
	7.07	21.9	1018	56.3	**12.5**
	12.56	21.8	1009	50.6	**11.1**
With α-terpineol	3.14	23.2	1053	63.1	**15.4**
	7.07	22.8	1043	63.6	**15.1**
	12.56	22.7	1018	60.7	**14.0**

4.2.4. Stability Testing

In this study, the inherent stability of the PSC devices with and without the α-terpineol additive was also investigated. The solar cells were stored in a N$_2$-filled glove box (inert atmosphere) in the dark, and their PV performance was measured at different time intervals at room temperature. The results reported in **Table 4.3** and **Figure 4.8** show that, after more than 500 h of storage, the PCE of the best α-terpineol-based device degraded only to around 76% of its initial value. On the other hand, the control device merely retained 58% of its original efficiency, mainly due to a fast decrease in the J$_{sc}$ (Figure 4.8e). Since the control and modified devices were processed and stored under identical conditions, this discrepancy can be entirely attributed to the effect of α-terpineol on the intrinsic properties of the perovskite layer. It is known from the literature that the perovskite materials can undergo several decomposition mechanisms (see Chapter 1, Section 7), and that the latter are favoured by a high density of lattice defects and grain boundaries in the perovskite film.[38] Therefore, the enhanced stability observed in the α-terpineol-based devices suggests that the incorporation of this additive in the precursor solution can effectively prevent or retard the degradation of perovskite by passivating the defects and favourably altering the kinetics of crystallization. These results are promising for stability also under ambient humidity conditions.

More measurements will be carried out to evaluate the PCE degradation of α-terpineol-based devices exposed to ambient air. In this regard, the hydrophobicity of α-terpineol could help to enhance the perovskite resistance against oxygen and moisture and to prolong the device lifetime.
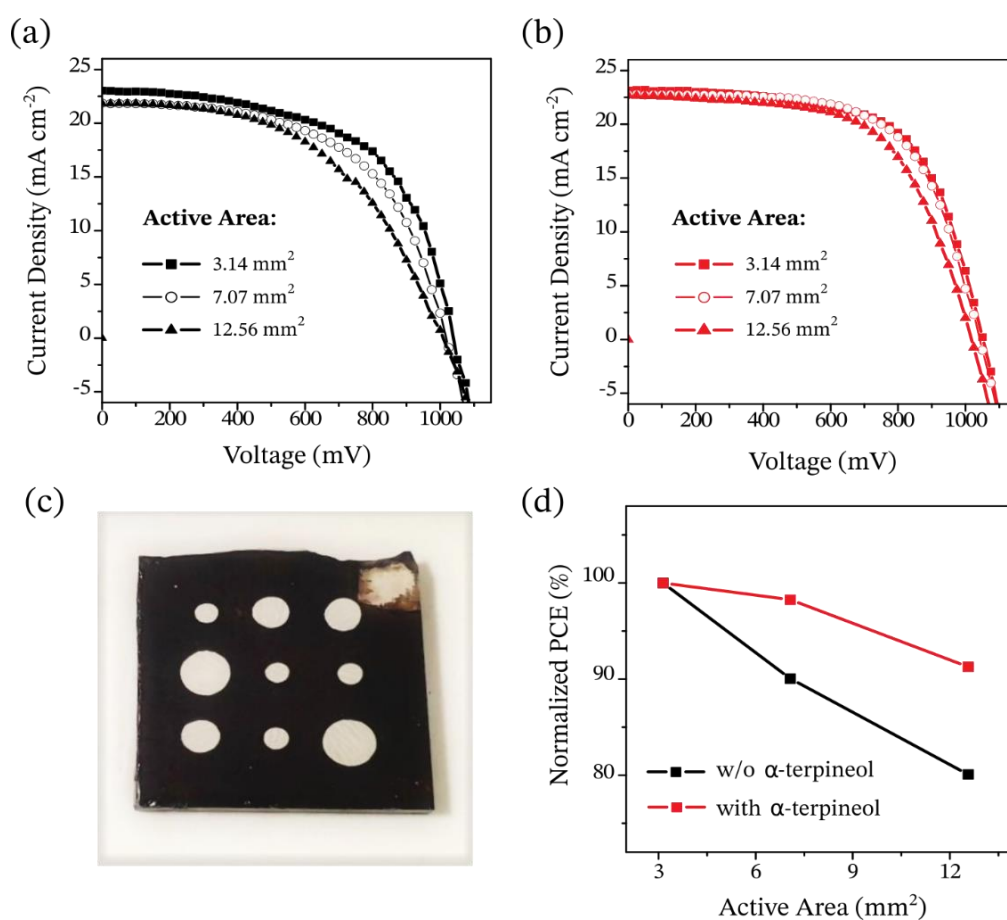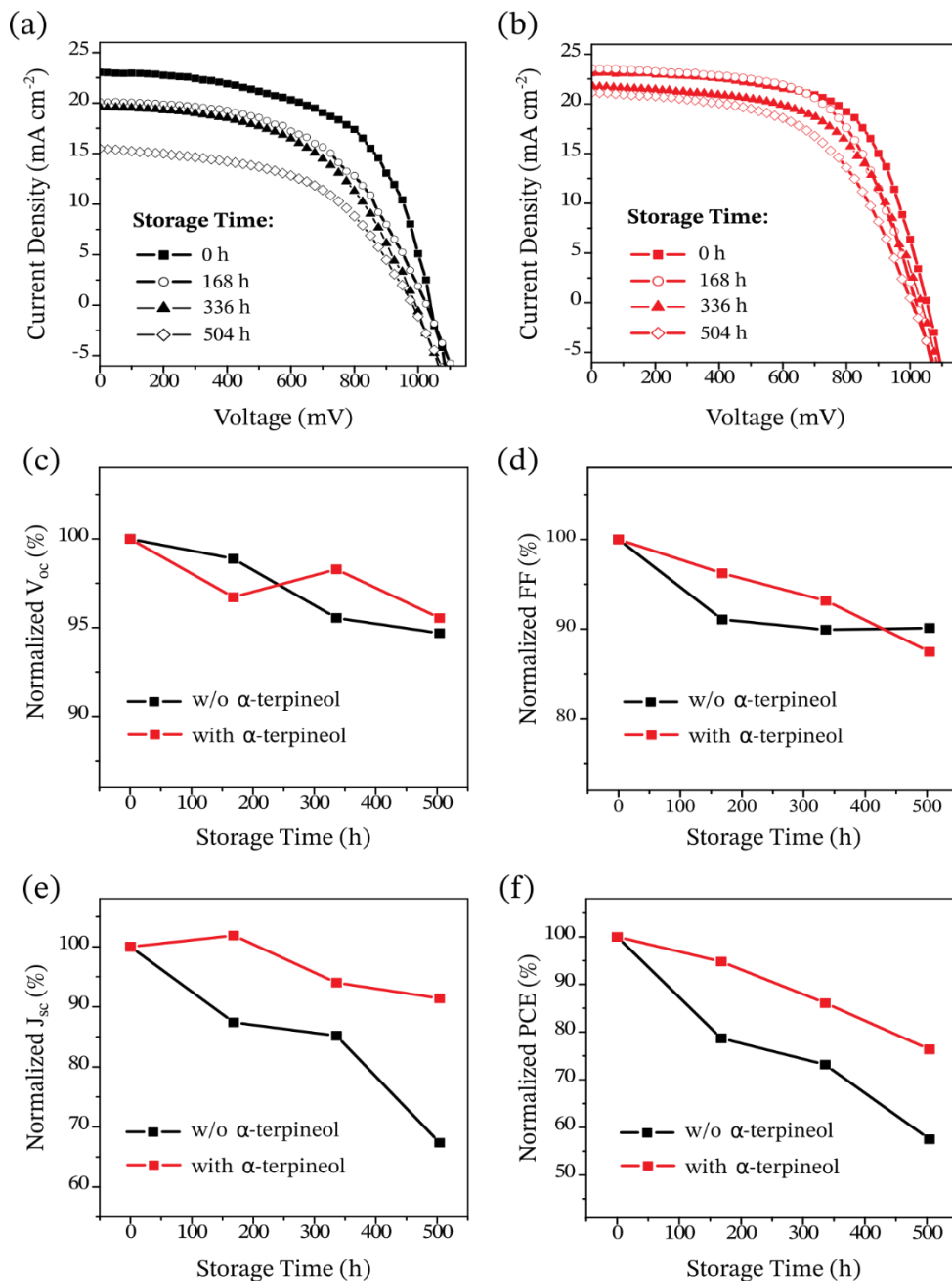

Figure 4.8. *Reverse scanning J-V curves of the best-performance PSCs processed from solutions (a) without α-terpineol and (b) with α-terpineol over time, measured under standard 1 sun illumination. (c) Degradation of the (c) V_{oc}, (d) FF, (e) J_{sc}, and (f) PCE parameters of solar cells processed from solutions with/without α-terpineol and stored in a N_2-filled glove box.*

Table 4.3. *Degradation of the PV parameters (short-circuit current, J_{sc}; open-circuit voltage, V_{oc}; fill factor, FF; power conversion efficiency, PCE) for solar cells processed from solutions with/without α-terpineol and stored in a N_2-filled glove box.*

Sample	Storage Time (h)	J_{sc} [mA cm^{-2}]	V_{oc} [mV]	FF [%]	PCE [%]
Without α-terpineol	0	23.0	1039	58.2	**13.9**
	168	20.1	1027	53.0	**11.0**
	336	19.6	993	52.3	**10.2**
	504	15.5	984	52.4	**8.0**
With α-terpineol	0	23.2	1053	63.1	**15.4**
	168	23.6	1018	60.7	**14.6**
	336	21.8	1035	58.8	**13.2**
	504	21.1	1006	55.2	**11.7**

4.2.5. Structural and Morphological Analysis

From the results shown so far, the incorporation of α-terpineol into the perovskite precursor solution generates a significant enhancement in the photovoltaic performance of the devices. To explore the mechanism behind this improvement, the structural and morphological properties of the perovskite films with and without the α-terpineol additive were opportunely analyzed and compared. First, XRD measurements were conducted to investigate the role of α-terpineol in perovskite crystallization. The analysis results are reported in **Figure 4.9**. Both control and modified films exhibited prominent peaks at 14.1° and 28.5°, which can be ascribed to the (110) and (220) lattice planes of the typical $CH_3NH_3PbI_{3-x}Cl_x$ tetragonal phase, respectively.[39] The unchanged positions of the peaks suggest that the solvent additive does not modify the crystal structure of the perovskite. On the other hand, the higher intensities of the diffraction peaks are indicative of a higher degree of crystallinity, which is beneficial for charge carrier transport in the perovskite layer. Since the α-terpineol can be retained in the film for a longer time compared to DMF due to its higher boiling point, it is supposed that the residual α-terpineol can balance the

dissolution and recrystallization processes during the annealing treatment, thus promoting the formation of high-quality perovskite grains. An enhanced crystallinity of the perovskite film generally leads to higher PCEs, reduced hysteresis and improved stability of PSCs, as reported in numerous works,[18,21,22] and this is in perfect agreement with the results of the J-V analysis conducted in this study. The chemical interactions between the −OH group in α-terpineol and the MA^+ and I^- ions in the perovskite precursors,[34] as well as the possible Pb−O coordination bonds may also be responsible for the improved perovskite crystallization. However, further characterizations are required to confirm this possibility.
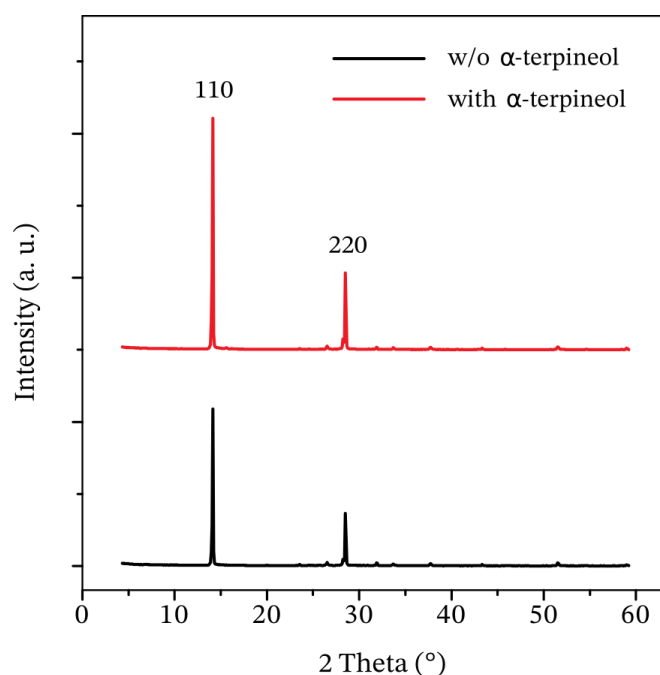
Figure 4.9. *XRD patterns of the perovskite films processed from solutions with/without α-terpineol, showing the characteristic peaks of the CH₃NH₃PbI₃₋ₓClₓ tetragonal phase with predominant crystallization along the (110) and (220) lattice planes.*

This study next analyzed the morphology of the perovskite films by AFM. The corresponding results are shown in **Figure 4.10**. The control films appeared relatively rough (R_q =53.6 nm) and unshaped, as frequently reported in the literature for one-step spin-coated perovskite layers. On the other hand, the films prepared from α-terpineol-based solution displayed better surface coverage, lower roughness (R_q = 43.5 nm), and more regular shaped crystallites. This is consistent with a reduced nucleation rate of the perovskite induced by the residual α-terpineol during the

thermal treatment, which helps to get a more uniform crystallization and a smoother morphology. Such improvements in the morphological properties of the perovskite films are typically advantageous to the performance of PSCs and thus provide a further explanation for the higher PCEs observed for the α-terpineol-treated solar cells in the previous sections.
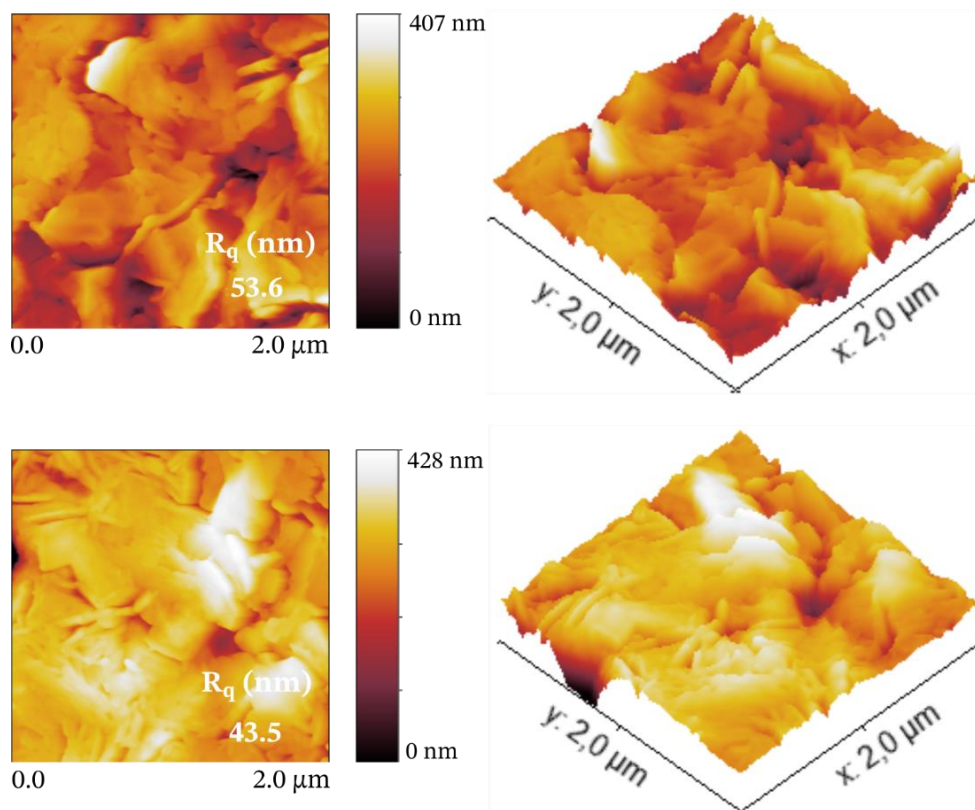
Figure 4.10. *Top-view (left) and 3D (right) AFM images of the pristine perovskite film (above) and of the perovskite film prepared using the a-terpineol additive (below), deposited on top of c-TiO₂/FTO/glass substrates.*

4.2.6. Spectroscopic Characterization

To further understand how the α-terpineol additive influences the performances of PSCs, steady-state fluorescence measurements were performed for both the control samples and the α-terpineol-treated samples. As described in Appendix A, steady-state fluorescence spectra can provide useful information about the quality of thin films and interfaces in perovskite solar cells. By monitoring the variations in fluorescence intensity, it is possible to evaluate the entity of non-radiative recombination losses in pristine perovskite films as well as the efficiency of charge transfer

processes at the interfaces. The schematic structures of the samples used for PL measurements are shown in **Figure 4.11**, together with the corresponding steady-state PL spectra. The excitation wavelength was fixed at 525 nm to incident from the FTO/glass side.
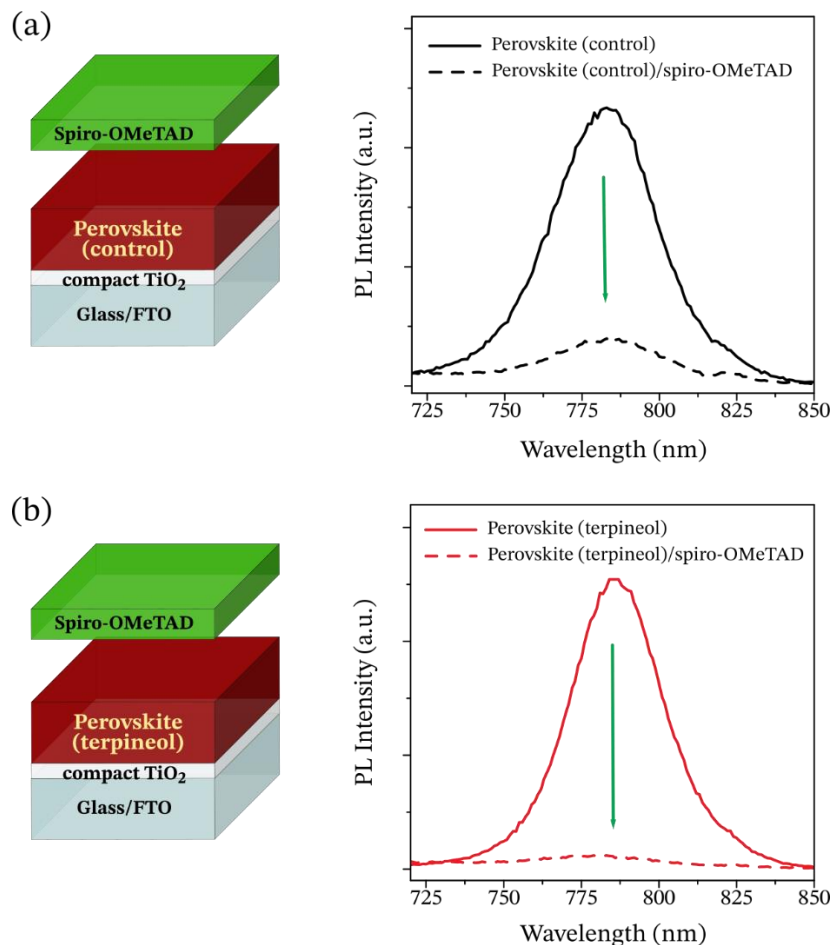
Figure 4.11. Structures (left) and steady-state fluorescence spectra (right) of the control samples (a) and α-terpineol-treated samples (b) with/without spiro-OMeTAD.

Both control and α-terpineol-treated perovskite films exhibited a prominent emission band centered at ~783 nm, corresponding to the characteristic fluorescence of $CH_3NH_3PbI_{3-x}Cl_x$. It is observed from Figure 4.11 that there is a clear fluorescence quenching caused by deposition of spiro-OMeTAD on top of the perovskite films. This quenching is more pronounced in the case of α-terpineol-treated sample (92%) compared to pristine sample (79%). This is indicative of a better interface contact and a more efficient charge transfer process (which competes with radiative recombination) at the perovskite/spiro-OMeTAD junction. Therefore, the enhanced quality of the

α-terpineol-treated perovskite film seems to positively impact the interface and charge transport properties of the device, as expected. This further explains the improved PV performance and enhanced stability of PSCs previously observed.

Figure 4.12 directly compares the optical (absorption + fluorescence) properties of control and α-terpineol-treated perovskite films. No relevant differences in the absorption spectra were found (Figure 4.12a). Both samples exhibited an absorption band edge at about 780 nm, which is consistent with the optical bandgap of $CH_3NH_3PbI_{3-x}Cl_x$ (~1.6 eV), and comparable absorption intensities in the measured wavelength range. This implies that the discrepancy of the J_{sc} and V_{oc} values between control devices and α-terpineol-processed devices is not due to an enhanced light absorption or to a variation of the bandgap, but it is more related to charge recombination. On the other hand, the addition of α-terpineol apparently improves the fluorescence efficiency of the pristine $CH_3NH_3PbI_{3-x}Cl_x$ film, as evident from Figure 4.12b. This may indicate a reduced density of defects (where emission might be quenched) and trapping sites for non-radiative recombination within the perovskite film, which would be consistent with the improved quality of the perovskite crystals revealed by XRD and with the enhanced performance and stability exhibited by the α-terpineol-treated devices. This interpretation is in agreement with recently published work by Guo et al.,[34] who demonstrated that α-terpineol can act as an effective defect passivating agent in perovskite films as a consequence of chemical interactions with MA^+ and I^- ions. Therefore, the results of the steady-state PL analysis further demonstrate the effective defect passivation induced by the α-terpineol additive in this PV system.
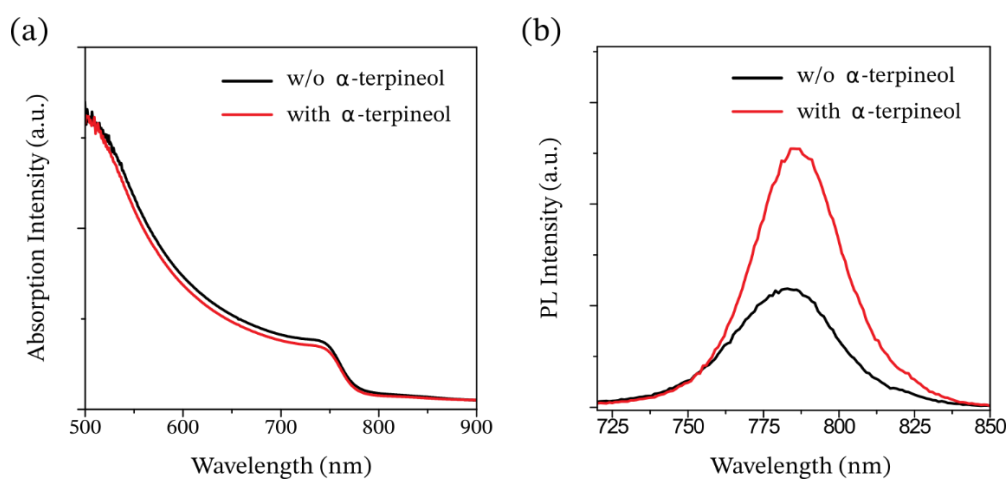

Figure 4.12. *(a) Absorption spectra and (b) steady-state PL spectra of the pristine perovskite films with/without α-terpineol deposited onto c-TiO$_2$/FTO/glass substrates.*

4.3. Conclusions and Future Work

In this work, non-toxic, easily accessible α-terpineol was successfully employed as a solvent-additive in the fabrication of high-performance planar n-i-p PSCs. It was demonstrated that the incorporation of α-terpineol into the one-step perovskite precursor solution at a concentration of 5 g/L can lead to perovskite films with improved crystallinity, lower roughness, and reduced density of defects and trap states. The higher boiling point of α-terpineol compared to the major solvent (DMF) can moderate the growth rate of $CH_3NH_3PbI_{3-x}Cl_x$, thus favoring the formation of continuous and homogenous films with a smoother morphology. Planar n-i-p PSCs processed from solutions containing the α-terpineol additive achieved PCEs as high as 15.4%, significantly higher than those yielded by control devices without additive (13.9%). The PV parameters (V_{oc}, J_{sc}, FF) were all improved due to reduced non-radiative recombination, and the hysteresis effect was partially eliminated by trap passivation. Contrarily to the reference cells, the α-terpineol-treated devices exhibited high performances also after having increased the active area from 3.14 mm^2 to 12.56 mm^2 (14.0% PCE), suggesting that the proposed strategy is effective in forming uniform and high-quality perovskite layers over a larger area. This result is encouraging with respect to the scaling up of PSCs in the prospect of a future commercialization. Additionally, the best device processed from 5 g/L α-terpineol solution displayed relatively high stability under inert conditions, retaining more than 75% of its original efficiency after more than 500 h of storage (against 58% of the control device). This was attributed to the effective defect/trap passivation induced by α-terpineol, which can retard the degradation of perovskite. The significantly enhanced PL intensity of the α-terpineol-modified perovskite films was a powerful testament to the efficient defect passivation, while the higher fluorescence quenching observed after the deposition of spiro-OMeTAD highlighted a more efficient charge extraction at the perovskite/HTL interface, which was in agreement with the J-V analysis results. The passivation effect, along with the hydrophobicity of the α-terpineol additive, could provide the devices with long-term stability also under ambient humidity conditions. This possibility will be investigated in the future. To this end, α-terpineol-treated devices with gold top electrodes will be opportunely fabricated, and their performances will be compared with those of reference gold-based solar cells, in order to prevent stability issues related to the use of silver under ambient atmosphere.

In summary, this work provided a facile and very effective method to promote the formation and growth of high-quality perovskite films using a simple one-step solution technique for integration in highly efficient and stable PV devices.

4.4. References

(1) Dubey, A.; Adhikari, N.; Mabrouk, S.; Wu, F.; Chen, K.; Yang, S.; Qiao, Q. A Strategic Review on Processing Routes towards Highly Efficient Perovskite Solar Cells. *J. Mater. Chem. A* **2018**, *6* (6), 2406–2431. https://doi.org/10.1039/C7TA08277K.

(2) Li, Y.; Ji, L.; Liu, R.; Zhang, C.; Mak, C. H.; Zou, X.; Shen, H.-H.; Leu, S.-Y.; Hsu, H.-Y. A Review on Morphology Engineering for Highly Efficient and Stable Hybrid Perovskite Solar Cells. *J. Mater. Chem. A* **2018**, *6* (27), 12842–12875. https://doi.org/10.1039/C8TA04120B.

(3) Aydin, E.; Bastiani, M. D.; Wolf, S. D. Defect and Contact Passivation for Perovskite Solar Cells. *Adv. Mater.* **2019**, *31* (25), 1900428. https://doi.org/10.1002/adma.201900428.

(4) Kim, J.; Ho-Baillie, A.; Huang, S. Review of Novel Passivation Techniques for Efficient and Stable Perovskite Solar Cells. *Sol. RRL* **2019**, *3* (4), 1800302. https://doi.org/10.1002/solr.201800302.

(5) Chen, J.; Park, N.-G. Causes and Solutions of Recombination in Perovskite Solar Cells. *Adv. Mater.* **2019**, 1803019. https://doi.org/10.1002/adma.201803019.

(6) Li, T.; Pan, Y.; Wang, Z.; Xia, Y.; Chen, Y.; Huang, W. Additive Engineering for Highly Efficient Organic–Inorganic Halide Perovskite Solar Cells: Recent Advances and Perspectives. *J. Mater. Chem. A* **2017**, *5* (25), 12602–12652. https://doi.org/10.1039/C7TA01798G.

(7) Li, H.; Wu, G.; Li, W.; Zhang, Y.; Liu, Z.; Wang, D.; Liu, S. (Frank). Additive Engineering to Grow Micron-Sized Grains for Stable High Efficiency Perovskite Solar Cells. *Adv. Sci.* **2019**, *6* (18), 1901241. https://doi.org/10.1002/advs.201901241.

(8) Guan, Y.; Mei, A.; Rong, Y.; Duan, M.; Hou, X.; Hu, Y.; Han, H. Fullerene Derivative as an Additive for Highly Efficient Printable Mesoscopic Perovskite Solar Cells. *Org. Electron.* **2018**, *62*, 653–659. https://doi.org/10.1016/j.orgel.2018.07.002.

(9) Zhen, J.; Zhou, W.; Chen, M.; Li, B.; Jia, L.; Wang, M.; Yang, S. Pyridine-Functionalized Fullerene Additive Enabling Coordination Interactions with $CH_3NH_3PbI_3$ Perovskite towards Highly Efficient Bulk Heterojunction Solar Cells. *J. Mater. Chem. A* **2019**, *7* (6), 2754–2763. https://doi.org/10.1039/C8TA12206G.

(10) Zhang, W.; Pathak, S.; Sakai, N.; Stergiopoulos, T.; Nayak, P. K.; Noel, N. K.; Haghighirad, A. A.; Burlakov, V. M.; deQuilettes, D. W.; Sadhanala, A.; et al. Enhanced Optoelectronic Quality of Perovskite Thin Films with Hypophosphorous Acid for Planar Heterojunction Solar Cells. *Nat. Commun.* **2015**, *6* (1), 1–9. https://doi.org/10.1038/ncomms10030.

(11) Huang, J.; Wang, M.; Ding, L.; Yang, Z.; Zhang, K. Hydrobromic Acid Assisted Crystallization of $MAPbI_{3−x}Cl_x$ for Enhanced Power Conversion Efficiency in Perovskite Solar Cells. *RSC Adv.* **2016**, *6* (61), 55720–55725. https://doi.org/10.1039/C6RA07536C.

(12) Li, G.; Zhang, T.; Zhao, Y. Hydrochloric Acid Accelerated Formation of Planar CH3NH3PbI3 Perovskite with High Humidity Tolerance. *J. Mater. Chem. A* **2015**, *3* (39), 19674–19678. https://doi.org/10.1039/C5TA06172E.

(13) Wang, L.; Moghe, D.; Hafezian, S.; Chen, P.; Young, M.; Elinski, M.; Martinu, L.; Kéna-Cohen, S.; Lunt, R. R. Alkali Metal Halide Salts as Interface Additives to Fabricate Hysteresis-Free Hybrid Perovskite-Based Photovoltaic Devices. *ACS Appl. Mater. Interfaces* **2016**, *8* (35), 23086–23094. https://doi.org/10.1021/acsami.6b07368.

(14) Boopathi, K. M.; Mohan, R.; Huang, T.-Y.; Budiawan, W.; Lin, M.-Y.; Lee, C.-H.; Ho, K.-C.; Chu, C.-W. Synergistic Improvements in Stability and Performance of Lead Iodide Perovskite Solar Cells Incorporating Salt Additives. *J. Mater. Chem. A* **2016**, *4* (5), 1591–1597. https://doi.org/10.1039/C5TA10288J.

(15) Chang, C.-Y.; Chu, C.-Y.; Huang, Y.-C.; Huang, C.-W.; Chang, S.-Y.; Chen, C.-A.; Chao, C.-Y.; Su, W.-F. Tuning Perovskite Morphology by Polymer Additive for High Efficiency Solar Cell. *ACS Appl. Mater. Interfaces* **2015**, *7* (8), 4955–4961. https://doi.org/10.1021/acsami.5b00052.

(16) Zhao, Y.; Wei, J.; Li, H.; Yan, Y.; Zhou, W.; Yu, D.; Zhao, Q. A Polymer Scaffold for Self-Healing Perovskite Solar Cells. *Nat. Commun.* **2016**, *7* (1), 1–9. https://doi.org/10.1038/ncomms10228.

(17) Arain, Z.; Liu, C.; Yang, Y.; Mateen, M.; Ren, Y.; Ding, Y.; Liu, X.; Ali, Z.; Kumar, M.; Dai, S. Elucidating the Dynamics of Solvent Engineering for Perovskite Solar Cells. *Sci. China Mater.* **2019**, *62* (2), 161–172. https://doi.org/10.1007/s40843-018-9336-1.

(18) Tsai, C.-H.; Lin, C.-M.; Kuei, C.-H. Improving the Performance of Perovskite Solar Cells by Adding 1,8-Diiodooctane in the $CH_3NH_3PbI_3$ Perovskite Layer. *Sol. Energy* **2018**, *176*, 178–185. https://doi.org/10.1016/j.solener.2018.10.037.

(19) Liang, P.-W.; Liao, C.-Y.; Chueh, C.-C.; Zuo, F.; Williams, S. T.; Xin, X.-K.; Lin, J.; Jen, A. K.-Y. Additive Enhanced Crystallization of Solution-Processed Perovskite for Highly Efficient Planar-Heterojunction Solar Cells. *Adv. Mater.* **2014**, *26* (22), 3748–3754. https://doi.org/10.1002/adma.201400231.

(20) Peng, L.; Xie, W.; Yang, C. Study of the Effect of DIO Additive on Charge Extraction and Recombination in Organic–Inorganic Hybrid $MAPbI_{3-x}Cl_x$ Perovskite Solar Cell. *RSC Adv.* **2018**, *8* (70), 40298–40307. https://doi.org/10.1039/C8RA08563C.

(21) Song, X.; Wang, W.; Sun, P.; Ma, W.; Chen, Z.-K. Additive to Regulate the Perovskite Crystal Film Growth in Planar Heterojunction Solar Cells. *Appl. Phys. Lett.* **2015**, *106* (3), 033901. https://doi.org/10.1063/1.4906073.

(22) Wei, Q.; Yang, D.; Yang, Z.; Ren, X.; Liu, Y.; Feng, J.; Zhu, X.; Liu, S. Effective Solvent-Additive Enhanced Crystallization and Coverage of Absorber Layers for High Efficiency Formamidinium Perovskite Solar Cells. *RSC Adv.* **2016**, *6* (62), 56807–56811. https://doi.org/10.1039/c6ra10007d.

(23) Cao, X.; Zhi, L.; Li, Y.; Fang, F.; Cui, X.; Yao, Y.; Ci, L.; Ding, K.; Wei, J. Elucidating the Key Role of a Lewis Base Solvent in the Formation of Perovskite Films Fabricated from the Lewis Adduct Approach. *ACS Appl. Mater. Interfaces* **2017**, *9* (38), 32868–32875. https://doi.org/10.1021/acsami.7b07216.

(24) Cao, X. B.; Li, C. L.; Zhi, L. L.; Li, Y. H.; Cui, X.; Yao, Y. W.; Ci, L. J.; Wei, J. Q. Fabrication of High Quality Perovskite Films by Modulating the Pb–O Bonds in Lewis Acid–Base Adducts. *J. Mater. Chem. A* **2017**, *5* (18), 8416–8422. https://doi.org/10.1039/C7TA00539C.

(25) Ahn, N.; Son, D.-Y.; Jang, I.-H.; Kang, S. M.; Choi, M.; Park, N.-G. Highly Reproducible Perovskite Solar Cells with Average Efficiency of 18.3% and Best Efficiency of 19.7% Fabricated via Lewis Base Adduct of Lead(II) Iodide. *J. Am. Chem. Soc.* **2015**, *137* (27), 8696–8699. https://doi.org/10.1021/jacs.5b04930.

(26) Zhang, Y.; Gao, P.; Oveisi, E.; Lee, Y.; Jeangros, Q.; Grancini, G.; Paek, S.; Feng, Y.; Nazeeruddin, M. K. PbI_2–HMPA Complex Pretreatment for Highly Reproducible and Efficient $CH_3NH_3PbI_3$ Perovskite Solar Cells. *J. Am. Chem. Soc.* **2016**, *138* (43), 14380–14387. https://doi.org/10.1021/jacs.6b08347.

(27) Zhi, L.; Li, Y.; Cao, X.; Li, Y.; Cui, X.; Ci, L.; Wei, J. Perovskite Solar Cells Fabricated by Using an Environmental Friendly Aprotic Polar Additive of 1,3-Dimethyl-2-Imidazolidinone. *Nanoscale Res. Lett.* **2017**, *12* (1), 632. https://doi.org/10.1186/s11671-017-2391-3.

(28) Khaleel, C.; Tabanca, N.; Buchbauer, G. α-Terpineol, a Natural Monoterpene: A Review of Its Biological Properties. *Open Chem.* **2018**, *16* (1), 349–361. https://doi.org/10.1515/chem-2018-0040.

(29) Bhatia, S. P.; Letizia, C. S.; Api, A. M. Fragrance Material Review on (-)-α-Terpineol. *Food Chem. Toxicol.* **2008**, *46* (11, Supplement), S204–S205. https://doi.org/10.1016/j.fct.2008.06.081.

(30) Hassan, S. B.; Gali-Muhtasib, H.; Göransson, H.; Larsson, R. Alpha Terpineol: A Potential Anticancer Agent Which Acts through Suppressing NF-KappaB Signalling. *Anticancer Res.* **2010**, *30* (6), 1911–1919.

(31) Li, L.; Shi, C.; Yin, Z.; Jia, R.; Peng, L.; Kang, S.; Li, Z. Antibacterial Activity of α-Terpineol May Induce Morphostructural Alterations in Escherichia Coli. *Braz. J. Microbiol.* **2015**, *45* (4), 1409–1413.

(32) Sousa, D. P. de; Jr, L. Q.; Almeida, R. N. de. Evolution of the Anticonvulsant Activity of α-Terpineol. *Pharm. Biol.* **2007**, *45* (1), 69–70. https://doi.org/10.1080/13880200601028388.

(33) Nam, J.-G.; Lee, E.-S.; Jung, W.-C.; Park, Y.-J.; Sohn, B.-H.; Park, S.-C.; Kim, J. S.; Bae, J.-Y. Photovoltaic Enhancement of Dye-Sensitized Solar Cell Prepared from [TiO$_2$/Ethyl Cellulose/Terpineol] Paste Employing TRITON^{TM} X-Based Surfactant with Carboxylic Acid Group in the Oxyethylene Chain End. *Mater. Chem. Phys.* **2009**, *116* (1), 46–51. https://doi.org/10.1016/j.matchemphys.2009.02.037.

(34) Guo, X.; McCleese, C.; Gao, W.; Wang, M.; Sang, L.; Burda, C. Investigation of Moisture Stability and PL Characteristics of Terpineol-Passivated Organic–Inorganic Hybrid Perovskite. *Mater. Renew. Sustain. Energy* **2016**, *5* (4), 17. https://doi.org/10.1007/s40243-016-0081-1.

(35) Uhl, A. R. Metal Counter Electrodes for Perovskite Solar Cells. In *Counter Electrodes for Dye-sensitized and Perovskite Solar Cells*; John Wiley & Sons, Ltd, 2018; pp 421–456. https://doi.org/10.1002/9783527813636.ch17.

(36) Kozuka, H. Radiative Striations in Spin-Coating Films. In *Handbook of Sol-Gel Science and Technology*; Klein, L., Aparicio, M., Jitianu, A., Eds.; Springer International Publishing: Cham, 2017; pp 1–19. https://doi.org/10.1007/978-3-319-19454-7_148-1.

(37) Liu, W.-W.; Wu, T.-H.; Liu, M.-C.; Niu, W.-J.; Chueh, Y.-L. Recent Challenges in Perovskite Solar Cells Toward Enhanced Stability, Less Toxicity, and Large-Area Mass Production. *Adv. Mater. Interfaces* **2019**, *6* (9), 1801758. https://doi.org/10.1002/admi.201801758.

(38) Boyd, C. C.; Cheacharoen, R.; Leijtens, T.; McGehee, M. D. Understanding Degradation Mechanisms and Improving Stability of Perovskite Photovoltaics. *Chem. Rev.* **2019**, *119* (5), 3418–3451. https://doi.org/10.1021/acs.chemrev.8b00336.

(39) Luo, S.; Daoud, W. A. Crystal Structure Formation of CH$_3$NH$_3$PbI$_{3-x}$Cl$_x$ Perovskite. *Materials* **2016**, *9* (3). https://doi.org/10.3390/ma9030123.

Chapter 5

Novel Charge-Transport Layers for Planar and Mesoscopic n-i-p PSCs

The electron-transport and hole-transport layers play a crucial role for charge extraction in PSCs. Spiro-OMeTAD and PTAA are the most widely used HTMs in regular device structures due to their superior photovoltaic performances. However, their high commercial prices due to synthesis complexity, as well as the requirement of stability-adverse dopants, necessitate the development of alternative materials. In the first part of this chapter, three novel conjugated copolymers are tested for the first time as dopant-free HTLs in planar n-i-p PSCs. It is demonstrated that one of the three copolymers can lead to efficient hole extraction from the perovskite layer to the anode without the addition of any doping additive, resulting in a maximum PCE of 10.4%, much higher than that of pristine spiro-OMeTAD-based device (0.77%). In the second part of this chapter, preliminary studies on the development and optimization of mesoporous TiO_2-based ETLs are presented. Specifically, Ti^{3+}-containing blue-titania nanoparticulate (NP) films are successfully prepared and used as mesoporous scaffolds in mesoscopic n-i-p PSCs. The best device yielded a PCE of 6.0%, significantly higher than that of solar cells fabricated using commercial TiO_2 NPs (4.8%). A further 10% PCE enhancement is demonstrated by doping the blue titania with nitrogen element. In parallel, TiO_2 nanorod (NR) arrays are grown onto c-TiO_2/FTO/glass substrates by hydrothermal method at different autoclaving times. The best efficiency is achieved with an autoclaving time of 0.5 h (8.9% PCE).

5.1. Part I –Dopant-Free Polymeric HTLs

5.1.1. Motivation of the Study

Although hybrid perovskites show excellent ambipolar transport properties (see Chapter 1), recent reports of HTL-free PSCs have resulted in PCEs much lower than those of HTL-based devices.[1–4] This indicates the necessity of introducing a proper hole-transport material to obtain efficient hole extraction from the perovskite layer to the anode. To date, HTL-based PSCs with record efficiencies (> 20%) have been achieved by a regular n-i-p device architecture, wherein spiro-OMeTAD or PTAA was used as the HTM.[5–8] These arylamine-based HTMs exhibit ideal properties in terms of energy level alignment and electron-blocking ability. However, both pristine spiro-OMeTAD and PTAA films suffer from poor hole mobility ($\sim 10^{-4}$ cm^2 V^{-1} s^{-1}) and low conductivity ($\sim 10^{-5}$ S cm^{-2}) on account of their amorphous nature. Thus, appropriate additives and p-type dopants such as Li-TFSI and TBP have been commonly used to adjust their electrical properties, as introduced in Chapter 1. However, the doped arylamine-based HTLs have some apparent disadvantages from the viewpoint of long-term stability and industrial-scale fabrication: (i) they generally require complex synthesis and laborious purification steps, which involve high costs; (ii) the incorporation of dopants/additives complicates the device preparation process and increases the fabrication costs; (iii) the hygroscopic nature of Li-TFSI can cause a fast degradation of the perovskite layer when exposed to the ambient air; (iv) TBP slowly erodes the perovskite material; (v) a complex and uncontrollable air doping method is necessary for spiro-OMeTAD HTL to reach appreciable conductivity. In this regard, it is highly desirable to develop novel cost-effective, dopant-free HTMs in the perspective of a future PSC commercialization.[9–12]

In the design of alternative dopant-free HTMs, suitable energy levels (HOMO level well-matched with the VBM of perovskite) and excellent hole-transport properties should be guaranteed in order to minimize any resistive/recombination loss. Moreover, the top HTM should be soluble in solvents that are orthogonal to the perovskite material (e.g. CB, DCB, toluene), and it should not require any post-annealing step. Among other materials, conjugated polymers are promising HTM candidates for PSCs since they present many advantages such as excellent solution processability, tunable energy levels, thin film uniformity, mechanical flexibility, and thermal stability. Moreover, their hydrophobic nature is attractive for protecting the perovskite layer in ambient conditions. Numerous polymeric dopant-free HTMs have been explored in the past few years.[13–16] In 2013,

Conings et al.[17] reported P3HT HTL-based perovskite cells with PCE of 10.8%. PTB7, another polymer widely investigated in the organic solar cell literature, was incorporated into PSCs by Marin-Beloqui et al.,[18] and a PCE of 7.5% was achieved without the addition of any dopant. In 2015, Qiao and co-workers[19] applied PDPP3T, a polymer containing electron-donating thiophene and electron-accepting diketopyrrolopyrrole moieties, as HTM in perovskite solar cells. Their pristine PDPP3T-based PSCs exhibited a PCE of 12.32%, comparable to that of doped spiro-OMeTAD-based device (12.34%), and remarkable stability. More recently, other types of π-extended donor-acceptor (D-A) "push-pull" copolymers have been developed and proposed as dopant-free HTMs for PSCs. For instance, Cai et al. introduced a series of carbazole-benzothiadiazole copolymers as HTMs without any doping additive and achieved an impressive PCE of 19.1%.[20] Interestingly, the thiophene units in the backbone of these copolymers were found to act as Lewis bases and coordinate with the under-coordinated Pb atoms through the electron-donating sulphur atoms, thus partially passivating the trap states on the perovskite crystal surface. As widely discussed in the previous chapters, this passivation effect is highly beneficial for PSC performance as it results in a reduced non-radiative charge recombination.

Here, three different π-conjugated "push-pull" copolymers containing electron-accepting C_{60} units and electron-donating oligothiophene moieties of different lengths are tested for the first time as dopant-free HTMs in planar n-i-p PSC architectures within a project in collaboration with Eni S.p.A. The main attraction of these systems is that they can be easily synthesized by employing a simple and inexpensive one-step approach. It is anticipated that a maximum PCE of 10.4% was achieved (with much room for improvement) using one of the three copolymers, without the addition of any doping additive.

5.1.2. Material Properties and Device Structure

Figure 5.1a shows the PSC n-i-p planar architecture used in this work, in which the three copolymers under investigation were incorporated as dopant-free HTLs. The three copolymers, here called P1, P2, and P3, are conjugated "push-pull" copolymers containing C_{60} units and oligothiophene moieties with increasing length (P1 < P2 < P3). The electron-donating and electron-accepting functionalities are directly linked to each other without any additional insulating spacer, thus resulting in π-extended systems. The copolymers were designed and

synthesized by Dr. Francesco Giacalone and co-workers (SteBiCeF, University of Palermo) via a simple and low-cost one-step approach. Details on the synthesis procedure and chemical structures are not provided here as they are covered by the obligation of industrial secrecy.
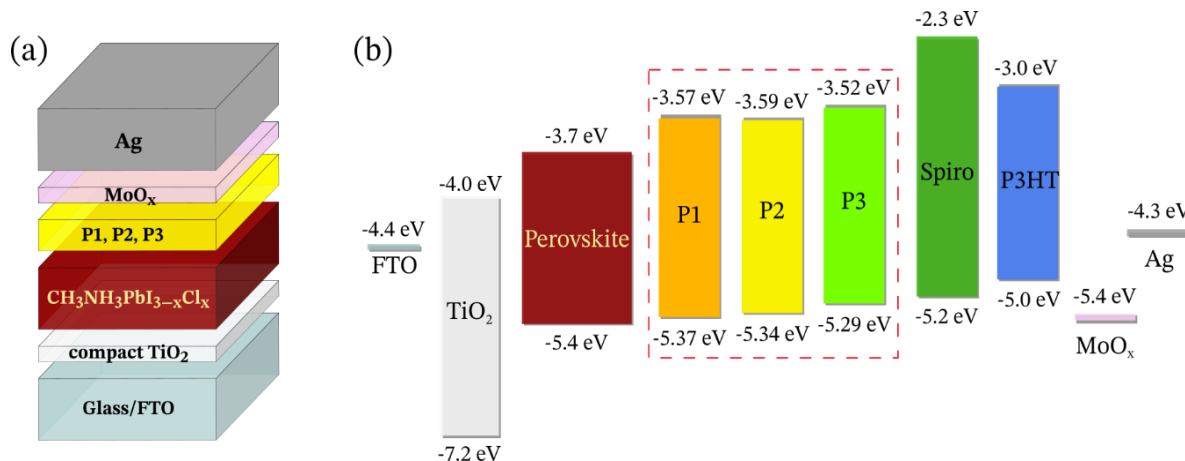

Figure 5.1. *(a) Schematic illustration of the PSC planar n-i-p architecture. (b) Energy band diagram showing the band edges and Fermi levels of the materials used in this work.*

The three copolymers are all soluble in common organic solvents such as chloroform, chlorobenzene, and dichlorobenzene, and they exhibit excellent film-forming ability. According to previously collected UV-visible spectra (not shown here), the spin-coated films show a large red shift of the band associated with the conjugated oligothiophenic chain compared with those in solution. This can be ascribed to the formation of a π-π stacked structure in the solid state, which would be beneficial for charge carrier transport in a PV device. A clear trend was also observed going from P1 to P3 (red shift + higher intensity), likely attributed to the increased extension of the conjugation. On the other hand, the intensities of the two major bands typical of the fullerene unit, with maxima in the wavelength range between 250 and 320 nm, appeared directly proportional to the content of the C_{60} derivative in the copolymers, as expected.

The UV-vis. absorption spectra, combined with the cyclovoltammetric (CV) characterization (not shown here), allowed to evaluate the HOMO and LUMO energy levels of the copolymers, which are schematized in Figure 5.1b and compared with those of traditional HTMs (spiro-OMeTAD and P3HT). A slight increase in the HOMO energy level can be observed going from P1 to P3 ($-5.37\,\text{eV} < -5.34\,\text{eV} < -5.29\,\text{eV}$), in accordance with the increasing oligothiophenic chain length, whereas the LUMO levels do not follow a particular trend (-3.57 eV for P1; -3.59 eV for P2;

−3.52 eV for P3). The positions of the energy levels are suitable to generate an i-p junction with the perovskite layer and to promote a hole extraction at the interface. In addition, the slightly higher HOMO levels of the three copolymers compared with spiro-OMeTAD (-5.2 eV) and P3HT (-5.0 eV) suggest a more favorable band alignment with the VBM of the perovskite, which in principle will reduce the energy loss during charge extraction. These results, along with the extended conjugation shown by these systems and the evidence of π-π stacking in the corresponding thin films, prompted the investigation of these copolymers as HTLs for PSCs.

5.1.3. Results and Discussion

The first step of this work was the fabrication of spiro-OMeTAD HTL-based PSCs having a regular planar architecture, with and without the addition of traditional LiTFSI and TBP dopants. This step was essential to demonstrate the requirement of stability-adverse doping for spiro-OMeTAD-based devices in order to reach appreciable conductivity and PCEs. Indeed, the devices without dopants exhibited non-ideal J-V curves and very poor conversion efficiencies (0.77%), indicating no efficient charge collection, against the 13.9% PCE of doped spiro-OMeTAD-based devices (see **Figure 5.2**). This is attributed to the low conductivity of the pristine spiro-OMeTAD film, which inevitably leads to a high series resistance and very low FF.
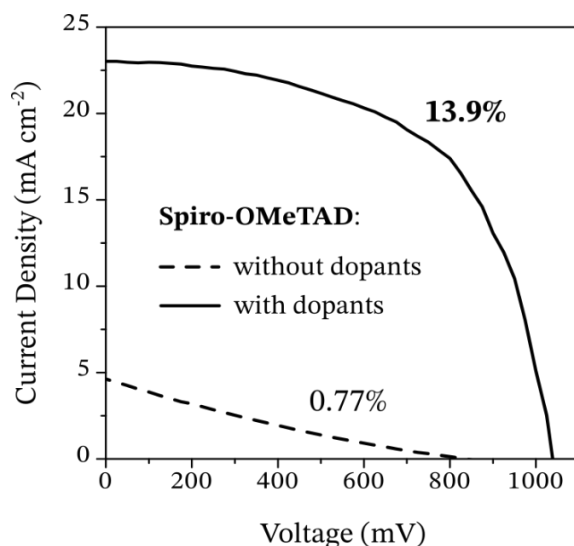

Figure 5.2. *Reverse scanning J-V curves of the best-performance PSCs having traditional spiro-OMeTAD as the HTM with/without dopants (TBP, LiTFSI), measured under standard 1 sun illumination. Active area: 3.14 mm².*

In order to develop novel dopant-free HTL-based PSCs, the pristine spiro-OMeTAD layer was replaced by thin films deposited from solutions of the three copolymers in CB (15 g/L), without the addition of any dopant. The excellent film-forming properties of these materials resulted in uniform and defect-free layers on top of the perovskite film. The J-V characteristics of the best-performance devices are reported in **Figure 5.3**a, while the corresponding PV parameters are summarized in **Table 5.1**. It is observed that the devices based on the copolymers P1 and P3 showed very poor efficiencies (0.98% PCE), with J-V curves similar to those of pristine spiro-OMeTAD-based PSCs. This suggests poor charge transport properties of the polymeric films, which impede an efficient charge collection at the anode and result in low FF (28.0% and 27.3%) and J_{sc} (4.4 mA cm^{-2}). On the other hand, an impressive PCE of 10.4% was achieved by using the P2 copolymer as a dopant-free HTM, with a J_{sc} of 20.4 mA cm^{-2}, a V_{oc} of 920 mV, and FF of 55.3%. The P2-based device displayed much smaller series resistance than solar cells with P1 and P3 and yielded much larger fill factor. This suggests better electrical properties and higher hole mobilities for P2 compared to P1 and P3. Such a difference in the electrical properties may result from a different aggregation mode of the polymeric chains in the solid state or from a different degree of crystallinity. Indeed, it is known that carrier transport strongly depends on the molecular orientation, crystallinity, and interchain π-π staking pattern, which may vary according to the length of the oligothiophenic chains. However, further characterization is required in order to confirm this possibility.

The results shown so far indicate that the P2 copolymer could be a promising candidate for replacing the costly and unstable spiro-OMeTAD as the HTM in PSCs (see Figure 5.3b). The relatively high hole mobility of P2 and the excellent thin-film formability are likely the main contributors to the efficient hole transport function of the layer. In addition, the electron-donating capability of the thiophene moieties can assist in extracting holes at the perovskite/HTL interface as well as in passivating the defects and trap states located at the perovskite surface, leading to an efficient charge transfer and reduced non-radiative recombination, as already demonstrated in the literature. In this regard, regioregular P3HT is a common thiophene-based organic polymer that has been widely investigated and used as the HTM in OSCs and PSCs. In this work, P3HT HTL-based PSCs were also fabricated and used as a polymeric reference. To do a fair comparison, the PSCs were prepared under the same conditions, using CB solutions of P3HT at a concentration of 15 g/L and spin-coating at a rate of 2000 rpm for 45 s (see Chapter 2, Section 2). Interestingly, the

P3HT-based devices exhibited lower efficiencies than those of P2-based solar cells, reaching a maximum PCE of 8.4% with a J_{sc} of 18.4 mA cm^{-2}, a V_{oc} of 888 mV, and FF of 51.2% (see Figure 5.3b and Table 5.1). This can be ascribed to the better energy level alignment between the VBM of the perovskite and the HOMO level of the P2 copolymer compared to that of P3HT (see Figure 5.1), which corresponds to a more favorable charge extraction at the interface. Further characterizations are planned to investigate other possible reasons for this improvement.
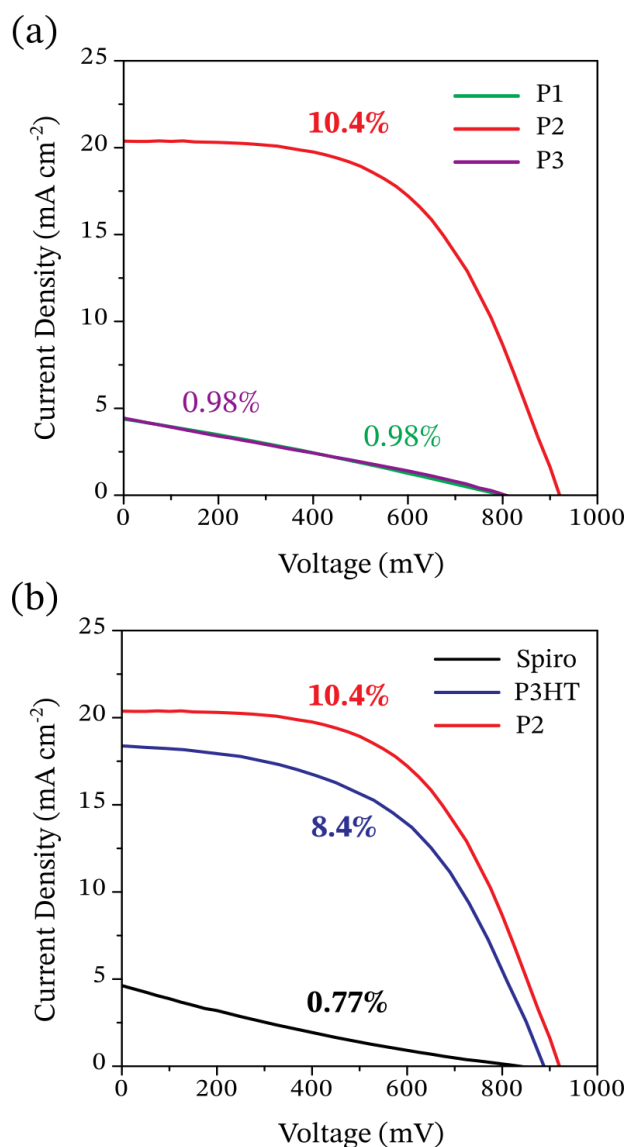

Figure 5.3. Reverse scanning J-V curves of the best-performance PSCs featuring different dopant-free HTLs: (a) P1, P2, and P3. (b) Spiro-OMeTAD, P3HT, and P2. The curves were measured under standard 1 sun illumination. Active area: 3.14 mm².

Table 5.1. Summary of best PSC performances (short-circuit current, J$_{sc}$; open-circuit voltage, V$_{oc}$; fill factor, FF; power conversion efficiency, PCE) for solar cells featuring different dopant-free HTLs, measured under standard (1 sun) illumination.

Dopant-free HTL	J$_{sc}$ [mA cm^{-2}]	V$_{oc}$ [mV]	FF [%]	PCE [%]
Spiro-OMeTAD	4.6	836	20.1	0.77
P3HT	18.4	888	51.2	8.4
P1	4.4	797	28.0	0.98
P2	20.4	920	55.3	**10.4**
P3	4.4	806	27.3	0.98

5.1.4. Conclusions and Future Work

In this work, three new π-conjugated copolymers with similar "push-pull" molecular structure, P1, P2, and P3, were tested as dopant-free HTMs in PSCs. The extended π conjugation, excellent film-forming ability, and suitable energy levels of these materials, as well as their simple and inexpensive synthetic procedure, make them attractive for this kind of application. Unfortunately, the solar cells based on P1 and P3 showed very low efficiencies, suggesting poor charge transport properties of these copolymers in the form of thin films. On the other hand, high-performance devices were obtained using the polymer P2 HTM, for which the PCE achieved a maximum of 10.4% without the addition of any dopant. Such a difference in the performances between the P2-based devices and the solar cells with P1 or P3 suggest that the spin-coated P2 films possess better structural and electrical properties which are beneficial for charge carrier transport and extraction. Further characterization will be carried out to explore these properties more in depth.

The main attraction of the proposed P2-based PV system is that it does not require processing HTL in air or adding any dopant such as LiTFSI and TBP, which are needed for the spiro-OMeTAD HTL preparation. This prevents exposure of the perovskite layer to the ambient conditions and avoids corrosion of the perovskite by dopants, which is promising for long-term stability of the devices. More measurements are planned in order to evaluate the PCE degradation of P2-based

PSCs over time. Moreover, it was shown that the PSCs based on the P2 copolymer exhibit higher efficiencies than those of P3HT-based devices (8.4% PCE), and this was mainly attributed to the better energy level alignment at the interface with the perovskite layer. This result indicates that the energy level tuning of the HTMs plays a key role in achieving highly efficient dopant-free HTLs for PSCs. Lastly, there is still much room for improving the P2 thin films by optimizing the solvent system, concentration, and spin-coating parameters towards higher photovoltaic performances. Further efforts are planned in this direction.

5.2. Part II – Titania Mesoporous ETLs

5.2.1. Motivation of the Study

As already introduced in Chapter 1, the state-of-the-art PSCs yielding the record PCEs are predominantly fabricated in the regular n-i-p mesoscopic configuration. The introduction of a proper mesoporous scaffold promotes an efficient electron extraction at the interface between perovskite layer and cathode, thus leading to J_{sc} and PCE higher than those of planar devices.[21–24] Since the early development stages of PSCs, TiO_2 has been widely used as the mesoporous ETM in mesoscopic PSCs owing to its excellent electron transport properties, well-matched energy levels, and suitable bandgap, as well as for its non-toxicity and low-cost. In particular, zero-dimensional (0D) titania nanoparticle (NP) films are the most widely studied and used as mesoporous ETLs.[25–29] However, these films generally suffer from a high density of surface defects and trap states, which provide numerous non-radiative recombination pathways at the ETL/perovskite interface and consequently reduce the voltage output and the electron injection rate in the corresponding device.[30] Various strategies have been developed to circumvent this issue and to improve the performance of the mesoporous TiO_2-based PSCs. For instance, an effective way of passivating the defects and improving the electronic properties of TiO_2 consists in doping the titania NPs by deliberately inserting impurities into the TiO_2 lattice. The Ti^{4+} cation and the O^{2-} anion can be replaced with other metal (Y, Nb, Li, Mg, Al, Ru)[31–34] or non-metal (F, N)[35,36] ions, respectively. Alternatively, one-dimensional (1D) TiO_2 nanostructures, including nanorods (NRs), nanowires (NWs), nanocones, and nanotubes, have also been applied and considered as promising ETLs for PSCs owing to their unique advantages compared to the TiO_2 NP films, such as facilitated electron transport and enhanced light harvesting.[36–47] For instance, Kim et al. reported PSCs based on 600 nm thick TiO_2 nanorod films that yielded a good PCE of 9.4%.[38] Extensive research has been done to control the morphology of the TiO_2 NR films with the aim of maximizing the photocurrent extraction and minimizing the interface losses. For instance, recent investigations of the effect of TiO_2 nanorod length on the device performance have revealed a decrease in the photovoltaic parameters with an increased nanorod length owing to the higher orientational disorder in the nanorod array and reduced pore-filling of the perovskite.[38,40,42] Various doping strategies of the TiO_2 NRs have also been reported by several groups. For example, Zhang et al.

synthesized N-doped titania nanorod arrays with hydrothermal method and used them as the ETL in mesoporous n-i-p PSCs.[36] Their best device yielded a PCE of 11.1%, which was 14.7% higher than that of devices based on undoped TiO$_2$. The efficiency enhancement was ascribed to faster electron transfer and lower resistance in the N-doped TiO$_2$-based device.

In this work, Ti^{3+}-containing (blue) TiO$_2$ NP films were prepared by a simple sol-gel route and doped with two different ionic species, namely N^{3-} and Pt^{4+}. The effect of the TiO$_2$ doping on the performance of mesoscopic n-i-p PSCs was investigated and discussed. Parallelly, 1D TiO$_2$ NR arrays were grown by hydrothermal method at different autoclaving times and used as mesoporous scaffolds in regular PSCs in order to evaluate the influence of the nanorod length and density on the electron extraction and power conversion efficiency of the devices. It is anticipated that the blue TiO$_2$ NP films doped with nitrogen element and the TiO$_2$ NR films grown at an autoclaving time of 0.5 h were found to correspond to the best PCEs, equal to 6.6% and 8.9%, respectively.

5.2.2. Doping of Titania Nanoparticles

The introduction of defects such as Ti^{3+} and oxygen vacancies in the TiO$_2$ lattice has been widely studied due to their close relationship with the electronic structure, charge transport, and surface activity of TiO$_2$. Numerous research groups have reported Ti^{3+}-containing (reduced, blue) TiO$_2$ NPs exhibiting excellent visible-light-driven photocatalytic activities thanks to the elevated valence band edge and consequently higher photoreactivity.[48–51] In general, the incorporation of Ti^{3+} defects efficiently narrow the band gap of TiO$_2$ and inhibit the fast recombination of electron-hole pairs, leading to enhanced photocatalytic performances. In the context of mesoscopic TiO$_2$-based n-i-p PSCs, a partial reduction of Ti^{4+} to Ti^{3+} within the TiO$_2$ lattice has been reported to improve the photovoltaic performance, mainly due to a faster electron injection and enhanced charge transport property, which can reduce electron accumulation at the TiO$_2$/perovskite interface.[52] Moreover, Pathak et al. have demonstrated that a small amount of species with valency +3 can effectively passivate the electronic defects and trap states within the TiO$_2$ film, thus making non-radiative recombination less favorable.[53]

In this work, Ti^{3+} defects were introduced into the TiO$_2$ NPs by reduction with 2-ethylimidazole during the sol-gel processing (see Chapter 2, Section 2).[48] The presence of Ti^{3+} in the TiO$_2$ lattice

was confirmed by electron paramagnetic resonance (EPR) measurements. The EPR spectrum reported in **Figure 5.4** clearly shows the characteristic signal of the Ti^{3+} species at g = 2.005.[49,54]
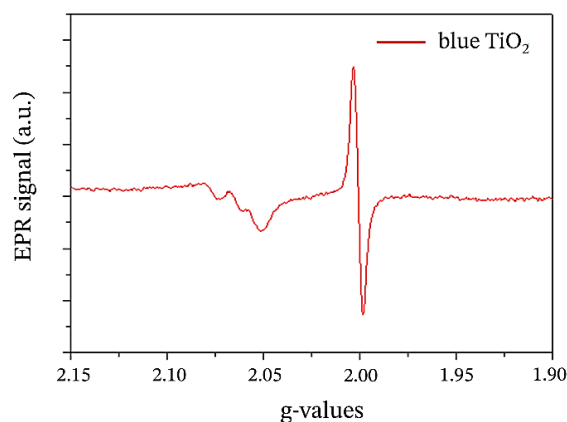
Figure 5.4. *EPR spectrum of the blue (Ti^{3+}-containing) TiO₂ nanoparticles.*

The as-synthesized blue TiO_2 NPs were also characterized by XRD. The XRD pattern shown in **Figure 5.5** reveals a clear prevalence of rutile phase in the sample. Based on literature reports, the rutile phase is not desirable for PV purposes since it generally suffers from inferior charge transport property and a lower CB compared to anatase, which can potentially lead to lower V_{oc} and J_{sc}.[55] However, there are some studies suggesting that rutile TiO_2-based solar cells can exhibit photovoltaic characteristics comparable to those of conventional anatase TiO_2-based devices.[56] The average crystallite size was also determined by XRD, and it was found to be 45.17 nm.

Figure 5.5. *XRD pattern of the blue TiO₂ NPs, showing the characteristic peaks of the rutile (R) and anatase (A) phases.*

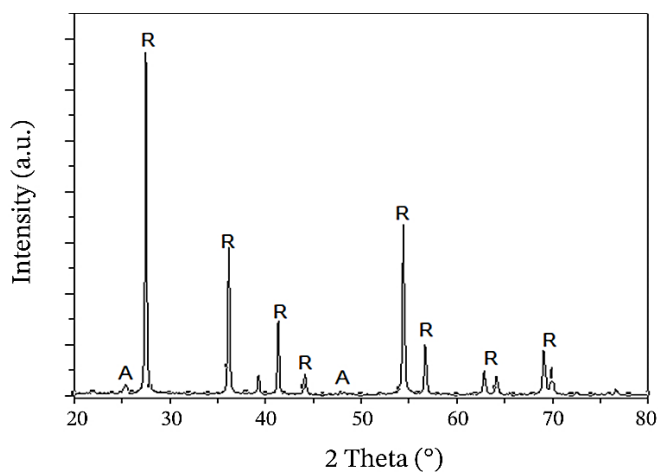As previously anticipated, N-doped and Pt-doped blue TiO₂ NPs were also prepared by adding specific amounts of urea and chloroplatinic acid hydrate to the starting precursor solution, respectively (see Chapter 2, Section 2). XPS measurements confirmed the presence of N and Pt ionic species in the surface of the corresponding samples. The doping concentrations were found to be 2.3% and 1.1%, respectively.

5.2.3. Growth of Titania Nanorod Arrays

Parallelly, 1D TiO₂ nanorod films were grown by hydrothermal method onto c-TiO₂/FTO/glass substrates, following the same procedure as that reported by Liu et al. (see Chapter 2, Section 2).[39] The as-prepared films were subjected to structural and morphological characterization prior to integration into PSCs. First, the crystal structure of the samples was examined by XRD. The typical diffraction pattern is presented in **Figure 5.6**. In addition to the characteristic peaks of the FTO, two other peaks can be observed, corresponding to the (101) and (211) planes of the rutile TiO₂.[57] The clear predominance of the rutile phase is in agreement with the results reported by Liu et al.[39]
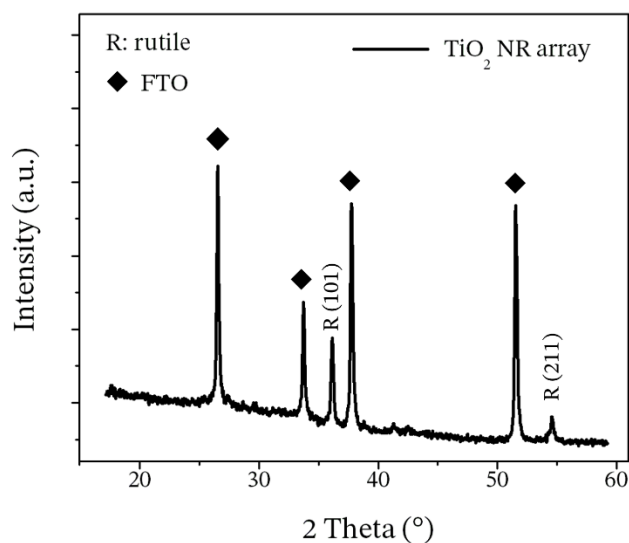
Figure 5.6. *XRD patter of the TiO₂ nanorod array grown onto a c-TiO₂/FTO/glass substrate, showing the characteristic peaks of the rutile (R) TiO₂ along the (101) and (211) planes.*

Figure 5.7 shows the SEM images of the obtained TiO₂ NR array, which exhibits the desired rod-like structure with sufficiently uniform orientation and thickness of around 1.7 µm (see the cross-

sectional SEM image in Figure 5.7c). Basing on recently published works,[38] such a thickness may be too high to allow for an efficient electron extraction at the cathode. Therefore, other films were prepared by gradually decreasing the autoclaving time with the aim of reducing the nanorod length/density and maximizing the PSC performance, as discussed in the next sub-section.

Figure 5.7. *Top view (a and b) and cross-sectional (c) SEM images of the TiO2 NR film grown by hydrothermal method with autoclaving time of 2 h.*

5.2.4. Application as Mesoporous Scaffolds in PSCs

Figure 5.8 shows the schematics of the mesoscopic n-i-p PSCs fabricated in this work, in which the synthesized TiO_2 nanostructures were incorporated as the mesoporous ETLs. As already described in Chapter 2, the blue TiO_2 NPs (undoped, Pt-doped,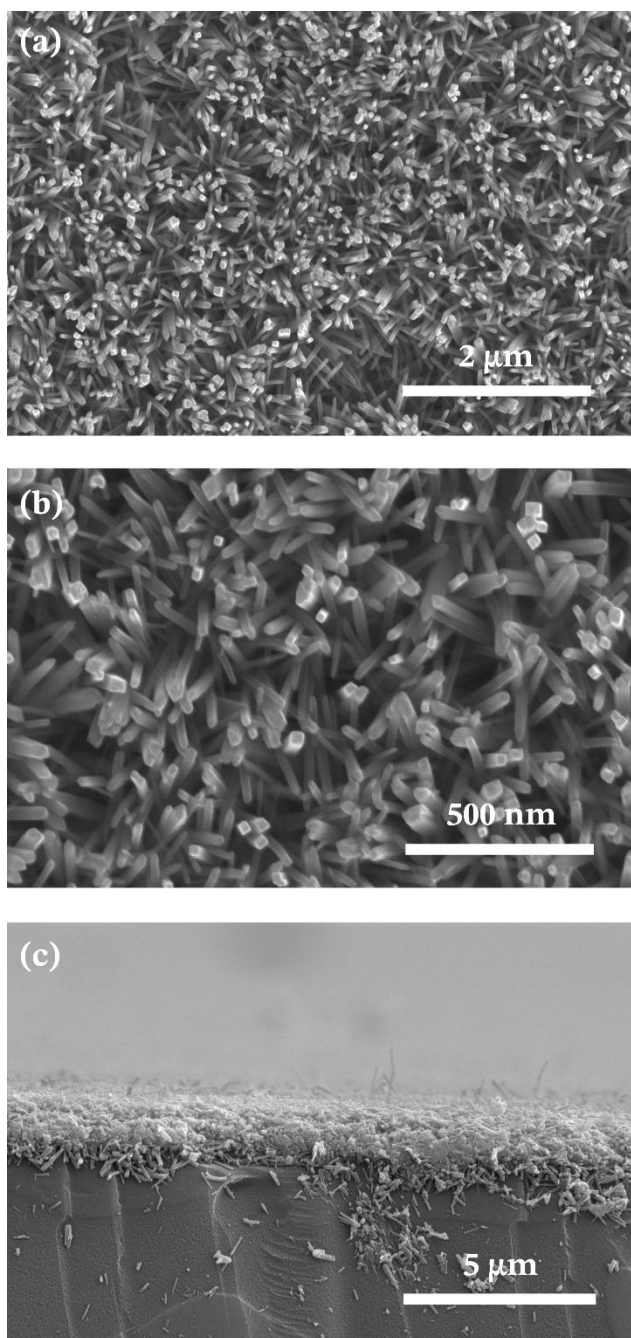 or N-doped) were dispersed in appropriate solutions and then deposited by spin-coating onto the c-TiO_2/FTO/glass substrates. Commercial TiO_2 P25 (Degussa) NPs were also used as a reference.
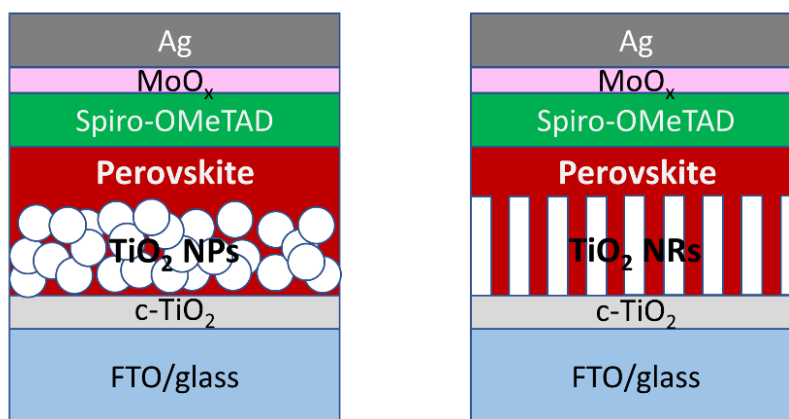
Figure 5.8. *Schematics of the fabricated mesoscopic n-i-p PSCs featuring TiO_2 NP films (left) or TiO_2 NR arrays (right) as mesoporous ETLs.*

Interestingly, the devices containing the undoped blue TiO_2 NPs showed a significant PCE enhancement compared to the solar cells based on commercial TiO_2 P25, as presented in **Figure 5.9**a. The best-performance device possessed a PCE of 6.0% with a V_{oc} of 769 mV, a J_{sc} of 15.7 mA cm^{-2}, and a FF of 49.9%, compared to the 4.8% PCE of the top control device with a V_{oc} of 612 mV, a J_{sc} of 17.0 mA cm^{-2}, and a FF of 46.0%. The results of the J-V analysis are summarized in **Table 5.2**. The significant increase in the V_{oc} and FF parameters indicates that the interface and charge-transport properties are enhanced by the use of the blue TiO_2 NPs compared to the commonly employed TiO_2 P25 NPs. This performance enhancement could be explained in terms of improved electronic properties and effective defect passivation induced by the incorporation of Ti^{3+} defects in the TiO_2 lattice, which would be in agreement with other published works.[52] However, there could be many other reasons, related to the crystallite size, film morphology, light absorption, etc. Further investigations will be carried out to investigate these aspects.

Figure 5.9. *Reverse scanning J-V curves of the best-performance PSCs featuring different mesoporous ETLs: (a) TiO₂ P25 (co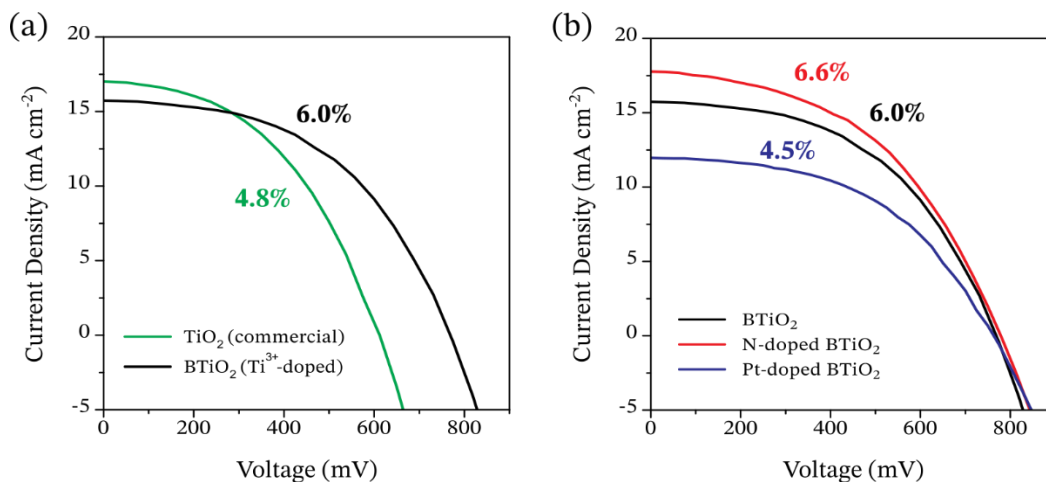mmercial) and blue-TiO₂ (BTiO₂) NP films. (b) BTiO₂, N-doped BTiO₂, and Pt-doped TiO₂ NP films. The curves were measured under standard 1 sun illumination. Active area: 3.14 mm².*

Subsequently, the performance of the undoped blue TiO_2-based PSCs was compared with that of solar cells containing N-doped and Pt-doped blue TiO_2 NP films as the mesoporous scaffolds. As can be seen from Figure 5.9b and Table 5.2, the devices exhibited comparable V_{oc} but significantly different J_{sc} and FF values. In particular, doping with nitrogen element resulted in a substantial PCE enhancement from 6.0% to 6.6.%, mainly due to a J_{sc} increase from 15.7 mA cm^{-2} to 17.8 mA cm^{-2}, suggesting an enhanced charge transport ability and a more effective electron transfer from $CH_3NH_3PbI_{3-x}Cl_x$ to N-doped blue TiO_2 than to undoped blue TiO_2. This result should not surprise since it has already been reported in the literature that N-doping can lead to faster charge transport and less carrier recombination in the device, as a consequence of the larger conduction band offset between $CH_3NH_3PbI_{3-x}Cl_x$ and N-doped TiO_2 and the effective passivation of the electronic trap states due to oxygen vacancy reduction.[36] On the contrary, platinum doping of blue TiO_2 was found to deteriorate the PSC performance, leading to a substantial reduction of the J_{sc} from 15.7 mA cm^{-2} to 12.0 mA cm^{-2}. The lower photogenerated current, together with the higher series resistance of the device compared with that of undoped blue TiO_2-based solar cells indicate inferior charge transport ability and less efficient charge extraction. This may be due to the formation of sub-band gap states arising from partially filled d-orbitals that act as recombination centers and result in an overall lower PV performance. Further characterizations are needed to confirm this hypothesis.

Table 5.2. *Summary of best PSC performances (short-circuit current, J_{sc}; open-circuit voltage, V_{oc}; fill factor, FF; power conversion efficiency, PCE) for solar cells featuring different mesoporous nanoparticulate ETMs, measured under standard (1 sun) illumination.*

Mesoporous ETM	J_{sc} [mA cm^{-2}]	V_{oc} [mV]	FF [%]	PCE [%]
TiO$_2$ P25 (commercial)	17.0	612	46.0	4.8
Blue TiO$_2$	15.7	769	49.9	6.0
N-doped Blue TiO$_2$	17.8	779	47.4	**6.6**
Pt-doped Blue TiO$_2$	12.0	763	49.7	4.5

Parallelly, the potential of the 1D TiO$_2$ nanorod films as mesoporous scaffolds for n-i-p PSCs was also investigated. As a first attempt, TiO$_2$ NR arrays grown at an autoclaving time of 2 h were used. However, the corresponding devices showed non-ideal J-V curves and poor power conversion efficiencies, with a maximum PCE of 1.9% (see **Figure 5.10**a). The extracted PV parameters are summarized in **Table 5.3**. The high series resistance and very low FF (27.2%) suggest poor charge transport and interface properties. Since it is known that too long and dense TiO$_2$ nanorods may impede an efficient electron extraction and perovskite pore-filling,[38] it was decided to reduce the autoclaving time (from 2 h to 1 h, and then from 1 h to 0.5 h) in order to stop the growth of the nanorods earlier, thus potentially obtaining less dense and thinner TiO$_2$ NR arrays. Through this approach, the efficiency was successfully enhanced from 1.9% to 7.3%, and then from 7.3% to 8.9% (see Figure 5.10a). Therefore, the optimal autoclaving time to fabricate high-performance perovskite solar cells was found to be 0.5 h. An in-depth characterization of the synthesized TiO$_2$ NRs (at different autoclaving times) will be performed in the future in order to find a precise correlation between their morphological properties and the corresponding device performances. Figure 5.10b shows the dark JV curves of the PSCs processed at different autoclaving times of the TiO$_2$ NR array. It is observed that the dark current density of the device corresponding to the shortest autoclaving time (0.5 h) is lower than that of the other solar cells in the reverse bias region (voltages lower than – 1 V), indicating that the leakage current is reduced by reducing the autoclaving time. On the other hand, the dark current density is higher at an

autoclaving time of 0.5 h under the forward bias (voltages higher than 1 V), suggesting a lower injection barrier at the TiO_2/perovskite interface. These results indicate a better rectifying behavior, which accounts for the increase in the PCE. It is worth noting that the best-performance TiO_2 NR-based device delivered a very high J_{sc}, equal to 23.6 mA cm^{-2}, which is much higher than that shown by the TiO_2 NP-based solar cells discussed above. This is in line with what is reported in the literature about the superior electron transport properties of the 1D TiO_2 nanostructures compared to 0D TiO_2 nanoparticles.[37] However, the voltage output of the device is still too low, limiting the overall PCE and indicating the need for further optimization.
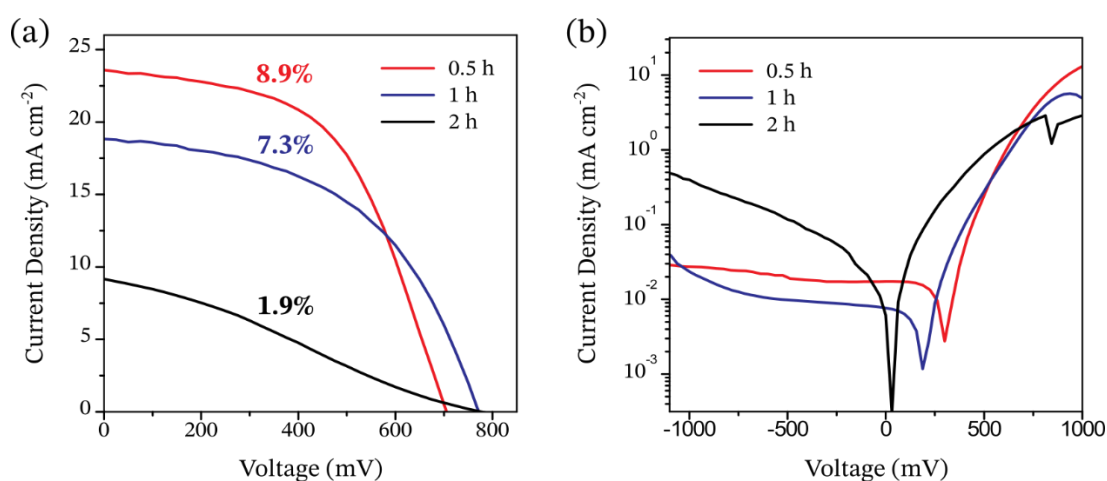
Figure 5.10. *Reverse scanning J-V curves of the best-performance PSCs featuring different mesoporous scaffolds of TiO_2 NR arrays, grown by hydrothermal method at different autoclaving times, measured (a) under standard (1 sun) illumination and (b) in the dark (semi-log plot).*

Table 5.3. *Summary of PSC performances (short-circuit current, J_{sc}; open-circuit voltage, V_{oc}; fill factor, FF; power conversion efficiency, PCE) for solar cells featuring mesoporous scaffolds of TiO2 NR arrays, grown by hydrothermal treatment at different autoclaving times.*

Autoclaving Time	J_{sc}	V_{oc}	FF	PCE
	[mA cm^{-2}]	[mV]	[%]	[%]
0.5 h	23.6	705	53.7	**8.9**
1 h	18.8	771	50.3	7.3
2 h	9.2	776	27.2	1.9

5.2.5. Conclusions and Future Work

In this work, various TiO$_2$-based nanostructures were synthesized and tested as mesoporous scaffolds in mesoscopic n-i-p PSCs. First, 0D TiO$_2$ NPs were prepared by a simple sol-gel method, and Ti^{3+} defects were successfully introduced into the TiO$_2$ lattice by reduction with 2-ethylimidazole, as confirmed by EPR. The as-synthesized blue TiO$_2$ nanoparticles were dispersed in appropriate solutions, spin-coated into c-TiO$_2$/FTO/glass substrates, and calcined at 500 °C to obtain the desired crystalline mesoporous layers. Interestingly, the PSCs containing the blue TiO$_2$ NPs showed a significant PCE enhancement (from 4.8% to 6.0%) compared to control solar cells prepared with commercial TiO$_2$ P25 NPs. This performance enhancement was explained in terms of improved electronic properties and effective defect passivation induced by the incorporation of Ti^{3+} defects in the TiO$_2$ lattice. Further investigations will be performed in order to investigate other possible reasons related to the different crystallite size, film morphology, and light absorption. N-doped and Pt-doped blue TiO$_2$ NPs were also prepared by adding specific amounts of urea and chloroplatinic acid hydrate to the starting precursor solution, respectively. Other mesoscopic n-i-p PSCs were fabricated by employing these novel doped blue TiO$_2$ NPs as mesoporous scaffolds, and their performances were compared with those of the devices containing undoped blue TiO$_2$ NPs. Interestingly, doping with nitrogen element resulted in a substantial PCE enhancement from 6.0% to 6.6%, mainly due to an increase in the J$_{sc}$, suggesting an enhanced charge transport ability and a more effective electron transfer at the perovskite/ETL interface. On the other hand, platinum doping of blue TiO$_2$ was found to deteriorate the PSC performance, probably caused by the formation of sub-band gap states that act as recombination centers. Further characterizations will be performed to confirm this possibility. Parallelly, 1D TiO$_2$ nanorod films were synthesized by hydrothermal method using different autoclaving times in order to tune the length and density of the TiO$_2$ nanorods, and then they were incorporated as mesoporous ETLs into n-i-p PSCs. The optimal autoclaving time was found to be 0.5 h, corresponding to the maximum PCE of 8.9%. The very high J$_{sc}$ (23.6 mA cm^{-2}) delivered by the best-performance device confirmed the superior electron transport properties of these 1D TiO$_2$ nanostructures compared to 0D TiO$_2$ NPs. However, much work has to be done to optimize the performance of these mesoscopic n-i-p PSCs in order to achieve PCEs higher than those of the planar n-i-p devices fabricated in the previous chapters and comparable to those of the state-of-the-art PSCs.

5.3. References

(1) Santhosh, N.; Sitaaraman, S. R.; Pounraj, P.; Govindaraj, R.; Pandian, M. S.; Ramasamy, P. Fabrication of Hole-Transport-Free Perovskite Solar Cells Using 5-Ammonium Valeric Acid Iodide as Additive and Carbon as Counter Electrode. *Mater. Lett.* **2019**, *236*, 706–709. https://doi.org/10.1016/j.matlet.2018.11.052.

(2) Xiong, Y.; Liu, Y.; Lan, K.; Mei, A.; Sheng, Y.; Zhao, D.; Han, H. Fully Printable Hole-Conductor-Free Mesoscopic Perovskite Solar Cells Based on Mesoporous Anatase Single Crystals. *New J. Chem.* **2018**, *42* (4), 2669–2674. https://doi.org/10.1039/C7NJ04448H.

(3) Sh. Atabaev, T. Stable HTM-Free Organohalide Perovskite-Based Solar Cells. *Mater. Today Proc.* **2017**, *4* (3, Part C), 4919–4923. https://doi.org/10.1016/j.matpr.2017.04.096.

(4) Zhou, J.; Ye, Z.; Hou, J.; Wu, J.; Zheng, Y.-Z.; Tao, X. Efficient Ambient-Air-Stable HTM-Free Carbon-Based Perovskite Solar Cells with Hybrid 2D–3D Lead Halide Photoabsorbers. *J. Mater. Chem. A* **2018**, *6* (45), 22626–22635. https://doi.org/10.1039/C8TA07836J.

(5) Yang, T.-Y.; Jeon, N. J.; Shin, H.-W.; Shin, S. S.; Kim, Y. Y.; Seo, J. Achieving Long-Term Operational Stability of Perovskite Solar Cells with a Stabilized Efficiency Exceeding 20% after 1000 h. *Adv. Sci.* **2019**, *6* (14), 1900528. https://doi.org/10.1002/advs.201900528.

(6) Matsui, T.; Yamamoto, T.; Nishihara, T.; Morisawa, R.; Yokoyama, T.; Sekiguchi, T.; Negami, T. Compositional Engineering for Thermally Stable, Highly Efficient Perovskite Solar Cells Exceeding 20% Power Conversion Efficiency with 85 °C/85% 1000 h Stability. *Adv. Mater.* **2019**, *31* (10), 1806823. https://doi.org/10.1002/adma.201806823.

(7) Alharbi, E. A.; Alyamani, A. Y.; Kubicki, D. J.; Uhl, A. R.; Walder, B. J.; Alanazi, A. Q.; Luo, J.; Burgos-Caminal, A.; Albadri, A.; Albrithen, H.; et al. Atomic-Level Passivation Mechanism of Ammonium Salts Enabling Highly Efficient Perovskite Solar Cells. *Nat. Commun.* **2019**, *10* (1), 1–9. https://doi.org/10.1038/s41467-019-10985-5.

(8) Yang, F.; Liu, J.; Wang, X.; Tanaka, K.; Shinokita, K.; Miyauchi, Y.; Wakamiya, A.; Matsuda, K. Planar Perovskite Solar Cells with High Efficiency and Fill Factor Obtained Using Two-Step Growth Process. *ACS Appl. Mater. Interfaces* **2019**, *11* (17), 15680–15687. https://doi.org/10.1021/acsami.9b02948.

(9) Wang, S.; Huang, Z.; Wang, X.; Li, Y.; Günther, M.; Valenzuela, S.; Parikh, P.; Cabreros, A.; Xiong, W.; Meng, Y. S. Unveiling the Role of TBP–LiTFSI Complexes in Perovskite Solar Cells. *J. Am. Chem. Soc.* **2018**, *140* (48), 16720–16730. https://doi.org/10.1021/jacs.8b09809.

(10) Dongxue, L.; Liu, Y. Recent Progress of Dopant-Free Organic Hole-Transporting Materials in Perovskite Solar Cells. *J. Semicond.* **2017**, *38* (1), 011005. https://doi.org/10.1088/1674-4926/38/1/011005.

(11) Rakstys, K.; Igci, C.; Nazeeruddin, M. K. Efficiency vs. Stability: Dopant-Free Hole Transporting Materials towards Stabilized Perovskite Solar Cells. *Chem. Sci.* **2019**, *10* (28), 6748–6769. https://doi.org/10.1039/C9SC01184F.

(12) Urieta-Mora, J.; García-Benito, I.; Molina-Ontoria, A.; Martín, N. Hole Transporting Materials for Perovskite Solar Cells: A Chemical Approach. *Chem. Soc. Rev.* **2018**, *47* (23), 8541–8571. https://doi.org/10.1039/C8CS00262B.

(13) Li, X.; Tang, X.; Yang, Y.; Ye, T.; Wu, D.; Wang, H.; Li, J.; Wang, X. A Dopant-Free Polymer as Hole-Transporting Material for Highly Efficient and Stable Perovskite Solar Cells. *Prog. Photovolt. Res. Appl.* **2018**, *26* (12), 994–1002. https://doi.org/10.1002/pip.3059.

(14) Valero, S.; Collavini, S.; Völker, S. F.; Saliba, M.; Tress, W. R.; Zakeeruddin, S. M.; Grätzel, M.; Delgado, J. L. Dopant-Free Hole-Transporting Polymers for Efficient and Stable Perovskite Solar Cells. *Macromolecules* **2019**, *52* (6), 2243–2254. https://doi.org/10.1021/acs.macromol.9b00165.

(15) Ruankham, P.; Sagawa, T. Dopant-Free π-Conjugated Polymers as Hole-Transporting Materials for Stable Perovskite Solar Cells. *J. Mater. Sci. Mater. Electron.* **2018**, *29* (11), 9058–9066. https://doi.org/10.1007/s10854-018-8932-4.

(16) Zhang, L.; Liu, C.; Wang, X.; Tian, Y.; Jen, A. K. Y.; Xu, B. Side-Chain Engineering on Dopant-Free Hole-Transporting Polymers toward Highly Efficient Perovskite Solar Cells (20.19%). *Adv. Funct. Mater.* 1904856. https://doi.org/10.1002/adfm.201904856.

(17) Conings, B.; Baeten, L.; Dobbelaere, C. D.; D'Haen, J.; Manca, J.; Boyen, H.-G. Perovskite-Based Hybrid Solar Cells Exceeding 10% Efficiency with High Reproducibility Using a Thin Film Sandwich Approach. *Adv. Mater.* **2014**, *26* (13), 2041–2046. https://doi.org/10.1002/adma.201304803.

(18) Marin-Beloqui, J. M.; Hernández, J. P.; Palomares, E. Photo-Induced Charge Recombination Kinetics in MAPbI$_{3-x}$Cl$_x$ Perovskite-like Solar Cells Using Low Band-Gap Polymers as Hole Conductors. *Chem. Commun.* **2014**, *50* (93), 14566–14569. https://doi.org/10.1039/C4CC06338D.

(19) Dubey, A.; Adhikari, N.; Venkatesan, S.; Gu, S.; Khatiwada, D.; Wang, Q.; Mohammad, L.; Kumar, M.; Qiao, Q. Solution Processed Pristine PDPP3T Polymer as Hole Transport Layer for Efficient Perovskite Solar Cells with Slower Degradation. *Sol. Energy Mater. Sol. Cells* **2016**, *145*, 193–199. https://doi.org/10.1016/j.solmat.2015.10.008.

(20) Cai, F.; Cai, J.; Yang, L.; Li, W.; Gurney, R. S.; Yi, H.; Iraqi, A.; Liu, D.; Wang, T. Molecular Engineering of Conjugated Polymers for Efficient Hole Transport and Defect Passivation in Perovskite Solar Cells. *Nano Energy* **2018**, *45*, 28–36. https://doi.org/10.1016/j.nanoen.2017.12.028.

(21) Islam, N.; Yang, M.; Zhu, K.; Fan, Z. Mesoporous Scaffolds Based on TiO$_2$ Nanorods and Nanoparticles for Efficient Hybrid Perovskite Solar Cells. *J. Mater. Chem. A* **2015**, *3* (48), 24315–24321. https://doi.org/10.1039/C5TA06727H.

(22) Robbiano, V.; Paternò, G. M.; Cotella, G. F.; Fiore, T.; Dianetti, M.; Scopelliti, M.; Brunetti, F.; Pignataro, B.; Cacialli, F. Polystyrene Nanoparticle-Templated Hollow Titania Nanosphere Monolayers as Ordered Scaffolds. *J. Mater. Chem. C* **2018**, *6* (10), 2502–2508. https://doi.org/10.1039/C7TC04070A.

(23) Noh, M. F. M.; Teh, C. H.; Daik, R.; Lim, E. L.; Yap, C. C.; Ibrahim, M. A.; Ludin, N. A.; Yusoff, A. R. bin M.; Jang, J.; Teridi, M. A. M. The Architecture of the Electron Transport Layer for a Perovskite Solar Cell. *J. Mater. Chem. C* **2018**, *6* (4), 682–712. https://doi.org/10.1039/C7TC04649A.

(24) Yang, G.; Tao, H.; Qin, P.; Ke, W.; Fang, G. Recent Progress in Electron Transport Layers for Efficient Perovskite Solar Cells. *J. Mater. Chem. A* **2016**, *4* (11), 3970–3990. https://doi.org/10.1039/C5TA09011C.

(25) Tanaka, Y.; Lim, S. L.; Goh, W. P.; Jiang, C.; Tee, S. Y.; Ye, T.; Li, X.; Nguyen, K. H.; Lee, C. J. J.; Ding, N.; et al. Fabrication of Mesoporous Titania Nanoparticles with Controlled Porosity and Connectivity for Studying the Photovoltaic Properties in Perovskite Solar Cells. *ChemNanoMat* **2018**, *4* (4), 394–400. https://doi.org/10.1002/cnma.201800009.

(26) Yang, H.-Y.; Rho, W.-Y.; Lee, S. K.; Kim, S. H.; Hahn, Y.-B. TiO$_2$ Nanoparticles/Nanotubes for Efficient Light Harvesting in Perovskite Solar Cells. *Nanomaterials* **2019**, *9* (3). https://doi.org/10.3390/nano9030326.

(27) Liu, Z.; Bi, S.; Hou, G.; Ying, C.; Su, X. Dual-Sized TiO$_2$ Nanoparticles as Scaffold Layers in Carbon-Based Mesoscopic Perovskite Solar Cells with Enhanced Performance. *J. Power Sources* **2019**, *430*, 12–19. https://doi.org/10.1016/j.jpowsour.2019.05.005.

(28) Hossain, I. M.; Hudry, D.; Mathies, F.; Abzieher, T.; Moghadamzadeh, S.; Rueda-Delgado, D.; Schackmar, F.; Bruns, M.; Andriessen, R.; Aernouts, T.; et al. Scalable Processing of Low-Temperature TiO$_2$ Nanoparticles for High-Efficiency Perovskite Solar Cells. *ACS Appl. Energy Mater.* **2019**, *2* (1), 47–58. https://doi.org/10.1021/acsaem.8b01567.

(29) Hu, W.; Zhou, W.; Lei, X.; Zhou, P.; Zhang, M.; Chen, T.; Zeng, H.; Zhu, J.; Dai, S.; Yang, S.; et al. Low-Temperature In Situ Amino Functionalization of TiO$_2$ Nanoparticles Sharpens Electron Management Achieving over 21% Efficient Planar Perovskite Solar Cells. *Adv. Mater.* **2019**, *31* (8), 1806095. https://doi.org/10.1002/adma.201806095.

(30) Abdi-Jalebi, M.; Dar, M. I.; Sadhanala, A.; Senanayak, S. P.; Giordano, F.; Zakeeruddin, S. M.; Grätzel, M.; Friend, R. H. Impact of a Mesoporous Titania–Perovskite Interface on the Performance of Hybrid Organic–Inorganic Perovskite Solar Cells. *J. Phys. Chem. Lett.* **2016**, *7* (16), 3264–3269. https://doi.org/10.1021/acs.jpclett.6b01617.

(31) Giordano, F.; Abate, A.; Baena, J. P. C.; Saliba, M.; Matsui, T.; Im, S. H.; Zakeeruddin, S. M.; Nazeeruddin, M. K.; Hagfeldt, A.; Graetzel, M. Enhanced Electronic Properties in Mesoporous TiO$_2$ via Lithium Doping for High-Efficiency Perovskite Solar Cells. *Nat. Commun.* **2016**, *7* (1), 1–6. https://doi.org/10.1038/ncomms10379.

(32) Chavan, R. D.; Yadav, P.; Nimbalkar, A.; Bhoite, S. P.; Bhosale, P. N.; Kook Hong, C. Ruthenium Doped Mesoporous Titanium Dioxide for Highly Efficient, Hysteresis-Free and Stable Perovskite Solar Cells. *Sol. Energy* **2019**, *186*, 156–165. https://doi.org/10.1016/j.solener.2019.04.098.

(33) Xiao, G.; Shi, C.; Lv, K.; Ying, C.; Wang, Y. Nb-Doping TiO$_2$ Electron Transporting Layer for Efficient Perovskite Solar Cells. *ACS Appl. Energy Mater.* **2018**, *1* (6), 2576–2581. https://doi.org/10.1021/acsaem.8b00286.

(34) Rafieh, A. I.; Ekanayake, P.; Wakamiya, A.; Nakajima, H.; Lim, C. M. Enhanced Performance of CH$_3$NH$_3$PbI$_3$-Based Perovskite Solar Cells by Tuning the Electrical and Structural Properties of Mesoporous TiO$_2$ Layer via Al and Mg Doping. *Sol. Energy* **2019**, *177*, 374–381. https://doi.org/10.1016/j.solener.2018.11.024.

(35) Zhang, X.; Wu, Y.; Huang, Y.; Zhou, Z.; Shen, S. Reduction of Oxygen Vacancy and Enhanced Efficiency of Perovskite Solar Cell by Doping Fluorine into TiO$_2$. *J. Alloys Compd.* **2016**, *681*, 191–196. https://doi.org/10.1016/j.jallcom.2016.04.194.

(36) Zhang, Z.-L.; Li, J.-F.; Wang, X.-L.; Qin, J.-Q.; Shi, W.-J.; Liu, Y.-F.; Gao, H.-P.; Mao, Y.-L. Enhancement of Perovskite Solar Cells Efficiency Using N-Doped TiO$_2$ Nanorod Arrays as Electron Transfer Layer. *Nanoscale Res. Lett.* **2017**, *12* (1), 43. https://doi.org/10.1186/s11671-016-1811-0.

(37) Thakur, U. K.; Kisslinger, R.; Shankar, K. One-Dimensional Electron Transport Layers for Perovskite Solar Cells. *Nanomater. Basel Switz.* **2017**, *7* (5). https://doi.org/10.3390/nano7050095.

(38) Kim, H.-S.; Lee, J.-W.; Yantara, N.; Boix, P. P.; Kulkarni, S. A.; Mhaisalkar, S.; Grätzel, M.; Park, N.-G. High Efficiency Solid-State Sensitized Solar Cell-Based on Submicrometer

Rutile TiO$_2$ Nanorod and CH$_3$NH$_3$PbI$_3$ Perovskite Sensitizer. *Nano Lett.* **2013**, *13* (6), 2412–2417. https://doi.org/10.1021/nl400286w.

(39) Liu, W.; Chu, L.; Hu, R.; Zhang, R.; Ma, Y.; Pu, Y.; Zhang, J.; Yang, J.; Li, X.; Huang, W. Diameter Engineering on TiO$_2$ Nanorod Arrays for Improved Hole-Conductor-Free Perovskite Solar Cells. *Sol. Energy* **2018**, *166*, 42–49. https://doi.org/10.1016/j.solener.2018.03.037.

(40) Xiao, G.; Shi, C.; Zhang, Z.; Li, N.; Li, L. Short-Length and High-Density TiO$_2$ Nanorod Arrays for the Efficient Charge Separation Interface in Perovskite Solar Cells. *J. Solid State Chem.* **2017**, *249*, 169–173. https://doi.org/10.1016/j.jssc.2017.03.005.

(41) Li, X.; Dai, S.-M.; Zhu, P.; Deng, L.-L.; Xie, S.-Y.; Cui, Q.; Chen, H.; Wang, N.; Lin, H. Efficient Perovskite Solar Cells Depending on TiO$_2$ Nanorod Arrays. *ACS Appl. Mater. Interfaces* **2016**, *8* (33), 21358–21365. https://doi.org/10.1021/acsami.6b05971.

(42) Chen, P.; Jin, Z.; Wang, Y.; Wang, M.; Chen, S.; Zhang, Y.; Wang, L.; Zhang, X.; Liu, Y. Interspace Modification of Titania-Nanorod Arrays for Efficient Mesoscopic Perovskite Solar Cells. *Appl. Surf. Sci.* **2017**, *402*, 86–91. https://doi.org/10.1016/j.apsusc.2017.01.037.

(43) Chen, W.; Luo, Q.; Deng, X.; Zheng, J.; Zhang, C.; Chen, X.; Huang, S. TiO$_2$ Nanorod Arrays Hydrothermally Grown on MgO-Coated Compact TiO$_2$ for Efficient Perovskite Solar Cells. *RSC Adv.* **2017**, *7* (85), 54068–54077. https://doi.org/10.1039/C7RA09824C.

(44) Liu, C.; Zhu, R.; Ng, A.; Ren, Z.; Cheung, S. H.; Du, L.; So, S. K.; Zapien, J. A.; Djurišić, A. B.; Phillips, D. L.; et al. Investigation of High Performance TiO$_2$ Nanorod Array Perovskite Solar Cells. *J. Mater. Chem. A* **2017**, *5* (30), 15970–15980. https://doi.org/10.1039/C7TA03710D.

(45) Jiang, Q.; Sheng, X.; Li, Y.; Feng, X.; Xu, T. Rutile TiO$_2$ Nanowire-Based Perovskite Solar Cells. *Chem. Commun.* **2014**, *50* (94), 14720–14723. https://doi.org/10.1039/C4CC07367C.

(46) Peng, G.; Wu, J.; Wu, S.; Xu, X.; Ellis, J. E.; Xu, G.; Star, A.; Gao, D. Perovskite Solar Cells Based on Bottom-Fused TiO$_2$ Nanocones. *J. Mater. Chem. A* **2016**, *4* (4), 1520–1530. https://doi.org/10.1039/C5TA08375C.

(47) Gao, X.; Li, J.; Gollon, S.; Qiu, M.; Guan, D.; Guo, X.; Chen, J.; Yuan, C. A TiO$_2$ Nanotube Network Electron Transport Layer for High Efficiency Perovskite Solar Cells. *Phys. Chem. Chem. Phys.* **2017**, *19* (7), 4956–4961. https://doi.org/10.1039/C6CP07733A.

(48) Hamdy, M. S.; Amrollahi, R.; Mul, G. Surface Ti3+-Containing (Blue) Titania: A Unique Photocatalyst with High Activity and Selectivity in Visible Light-Stimulated Selective Oxidation. *ACS Catal.* **2012**, *2* (12), 2641–2647. https://doi.org/10.1021/cs300593d.

(49) Zuo, F.; Wang, L.; Wu, T.; Zhang, Z.; Borchardt, D.; Feng, P. Self-Doped Ti3+ Enhanced Photocatalyst for Hydrogen Production under Visible Light. *J. Am. Chem. Soc.* **2010**, *132* (34), 11856–11857. https://doi.org/10.1021/ja103843d.

(50) Zhang, Y.; Xing, Z.; Liu, X.; Li, Z.; Wu, X.; Jiang, J.; Li, M.; Zhu, Q.; Zhou, W. Ti3+ Self-Doped Blue TiO$_2$(B) Single-Crystalline Nanorods for Efficient Solar-Driven Photocatalytic Performance. *ACS Appl. Mater. Interfaces* **2016**, *8* (40), 26851–26859. https://doi.org/10.1021/acsami.6b09061.

(51) Xu, Y.; Wu, S.; Wan, P.; Sun, J.; Hood, Z. D. Introducing Ti3+ Defects Based on Lattice Distortion for Enhanced Visible Light Photoreactivity in TiO$_2$ Microspheres. *RSC Adv.* **2017**, *7* (52), 32461–32467. https://doi.org/10.1039/C7RA04885H.

(52) Ma, X.; Tang, P.; Liu, D.; Zhang, J.; Feng, L.; Wu, L. Interface Engineering of Perovskite Solar Cells with Air Plasma Treatment for Improved Performance. *ChemPhysChem* **2017**, *18* (20), 2939–2946. https://doi.org/10.1002/cphc.201700536.

(53) Pathak, S. K.; Abate, A.; Ruckdeschel, P.; Roose, B.; Gödel, K. C.; Vaynzof, Y.; Santhala, A.; Watanabe, S.-I.; Hollman, D. J.; Noel, N.; et al. Performance and Stability Enhancement of Dye-Sensitized and Perovskite Solar Cells by Al Doping of TiO_2. *Adv. Funct. Mater.* **2014**, *24* (38), 6046–6055. https://doi.org/10.1002/adfm.201401658.

(54) Wang, Z.; Yang, C.; Lin, T.; Yin, H.; Chen, P.; Wan, D.; Xu, F.; Huang, F.; Lin, J.; Xie, X.; et al. H-Doped Black Titania with Very High Solar Absorption and Excellent Photocatalysis Enhanced by Localized Surface Plasmon Resonance. *Adv. Funct. Mater.* **2013**, *23* (43), 5444–5450. https://doi.org/10.1002/adfm.201300486.

(55) Bai, Y.; Mora-Seró, I.; De Angelis, F.; Bisquert, J.; Wang, P. Titanium Dioxide Nanomaterials for Photovoltaic Applications. *Chem. Rev.* **2014**, *114* (19), 10095–10130. https://doi.org/10.1021/cr400606n.

(56) Park, N.-G.; van de Lagemaat, J.; Frank, A. J. Comparison of Dye-Sensitized Rutile- and Anatase-Based TiO_2 Solar Cells. *J. Phys. Chem. B* **2000**, *104* (38), 8989–8994. https://doi.org/10.1021/jp994365l.

(57) Wang, J.; Qu, S.; Zhong, Z.; Wang, S.; Liu, K.; Hu, A. Fabrication of TiO_2 Nanoparticles/Nanorod Composite Arrays via a Two-Step Method for Efficient Dye-Sensitized Solar Cells. *Prog. Nat. Sci. Mater. Int.* **2014**, *24* (6), 588–592. https://doi.org/10.1016/j.pnsc.2014.10.013.

Concluding Remarks

From a sustainable development perspective, transforming the global energy sector by switching from fossil fuels to renewable energy sources constitutes an absolute priority. Among all the renewable technologies, solar photovoltaics offers one of the most effective strategy for producing clean and sustainable electric power. However, the expansion of solar PV on a Terawatt scale is still hindered by the high costs of production compared with other conventional fuels. Alternative thin-film PV technologies are continuously being developed to reduce the costs for a large-scale use. Among them, perovskite solar cells have recently gained much attention both from the scientific and industrial community mainly because perovskite absorbers have demonstrated very high PCEs, competitive with those of silicon-based PV devices. The high performance, low-cost processing, and great potential for unconventional PV applications (e.g. semitransparent BIPVs) make this kind of devices very appealing. However, the presence of still unsolved problems, such as the long-term stability of materials and interfaces, the high commercial prices of some components (e.g. spiro-OMeTAD HTL, Au top electrode), the current-voltage hysteresis, and the significant non-radiative charge recombination limiting the PCE with respect to the theoretical SQ limit, still constitute an obstacle to their massive commercialization. In this work of thesis, various strategies have been proposed to reduce the costs, increase the efficiency, and improve the stability of PSCs, with the ultimate goal of contributing to the advancement of this amazing PV technology. In further details, the chapters presented in this thesis have covered the following:

- In Chapter 3, I proposed a novel approach for fabricating high-performance semitransparent PSCs using nonprecious copper-based DMD transparent top electrodes. It was demonstrated that an ultrathin (1.5 nm) gold layer can act as an effective wetting inducer and diffusion barrier for copper, thus allowing conductive structure to be obtained with gold-seeded Cu films as thin as 9.5 nm evaporated on top of MoO_x. This strategy enabled planar n-i-p ST-PSCs with PCEs as high as 12.5% and acceptable transparency levels to be fabricated. A maximum AVT of 24% (corresponding to a PCE of 3.1%) was achieved after having decreased the perovskite layer thickness from 390 nm to 100 nm, thus approaching the benchmark of 25% for solar window applications. This work has been object of a publication in the journal of *Advanced Materials Technologies* (Elsevier) and is believed to be the first report of efficient planar n-i-

p PSCs containing Cu-based DMD top electrodes. The use of copper allows a substantial reduction in material costs compared to other DMD structures reported in the literature and based on expensive gold or silver, without sacrificing the device performance. Moreover, the less reactive nature of Cu compared to Ag makes it a valid metal candidate for the fabrication of highly stable and perovskite-compatible DMD structures. Future work will be focused on optimizing thickness, processing conditions and structural properties of each constituent layer of the proposed DMD electrode in order to achieve higher efficiency as well as transparency for practical ST applications, also in the field of tandem PV devices.

- In Chapter 4, I reported on an efficient way to deposit $CH_3NH_3PbI_{3-x}Cl_x$ films onto c-TiO_2/FTO/glass substrates, using a one-step spin-coating technique that involves the incorporation of α-terpineol as a solvent additive into the precursor solution ($PbCl_2$ and MAI in DMF). α-terpineol was selected among other compounds for its low-cost, non-toxicity, and easy accessibility, and because it is frequently used as a solvent in printing pastes. It was demonstrated that the addition of α-terpineol at a concentration of 5 g/L can improve the quality of perovskite films and restrain non-radiative charge recombination in the corresponding devices. The results of the XRD analysis revealed a higher degree of crystallinity for the α-terpineol-treated perovskite films, which is beneficial for charge carrier transport. Moreover, as observed by AFM, the perovskite films prepared from α-terpineol-based solution displayed better surface coverage, lower roughness, and more regular shaped crystallites. It was supposed that the higher boiling point of α-terpineol compared to the major solvent (DMF) can moderate the growth rate of $CH_3NH_3PbI_{3-x}Cl_x$, thus favoring the formation of continuous and homogenous films with smoother morphology and enhanced crystal quality. The chemical interactions between the −OH group in α-terpineol and the MA^+ and I^- ions, as well as the possible formation of PB−O coordination bonds, may also be responsible for the improved perovskite crystallization. This aspect will be investigated in the future. Through this strategy, the fabricated n-i-p PSCs achieved efficiencies as high as 15.4%, significantly higher than those yielded by control solar cells without additive (13.9%). This performance enhancement was ascribed to an effective defect/trap passivation induced by the α-terpineol additive, corresponding to a significantly reduced non-radiative recombination. The α-terpineol-treated devices also showed better reproducibility, reduced hysteresis, and higher stability under inert conditions. The defect passivation effect, together with the hydrophobic nature of α-terpineol,

may provide the devices with long-term stability also under ambient humidity conditions. More measurements are planned to verify this hypothesis.

- In Chapter 5, a novel conjugated push-pull copolymer containing C_{60} units and oligothiophene moieties was employed for the first time as a dopant-free HTM in planar n-i-p PSCs. A maximum PCE of 10.4% was successfully demonstrated, without the addition of any doping additive and with much room for improvement. In contrast to the traditional n-i-p PSCs based on spiro-OMeTAD, the proposed PV system does not require processing HTL in air or adding any dopant such as LiTFSI and TBP. This is encouraging with respect to the long-term stability of the devices, since this approach prevents exposure of the perovskite film to the ambient air and avoids corrosion of the perovskite by the common dopants. Further characterizations are planned in order to evaluate the PCE degradation over time. Moreover, it should be stressed that P2 can be easily synthesized by employing a simple and low-cost one-step approach, which makes it a promising candidate for replacing the expensive spiro-OMeTAD. Interestingly, the solar cells based on the P2 copolymer also exhibited higher efficiencies than those of P3HT-based devices (8.4% PCE), and this was mainly attributed to the better energy level alignment at the interface with the perovskite layer. A clear extension of this work will be the optimization of the P2 thin films by varying the solvent system, concentration, and spin-coating parameters in order to achieve higher photovoltaic performances. Parallelly, various doping strategies were attempted in the preparation of blue (Ti^{3+}-containing) TiO_2 nanoparticulate films to be used as mesoporous scaffolds in mesoscopic n-i-p PSCs. Doping with nitrogen element led to a significant PCE enhancement of 10%. Preliminary studies on mesoporous 1D TiO_2 nanorod films were also reported, and a maximum PCE of 8.9% was achieved. Future work will be dedicated to the optimization of such mesoporous films and to a more in-depth investigation of the role of the mesoporous ETL on the device performance.

To sum up, the studies documented in this thesis open up new scenarios for future development of PSCs by providing several strategies for the fabrication of cost-effective, semitransparent devices and for the optimization of materials and interfaces towards higher performance and stability. Further improvements of the technology in this direction will ultimately pave the way to PSCs with efficiencies close to the SQ limit and with long-term durability, ready to emerge as a leading technology in the global energy PV market.

Appendix A

Material and Thin Film Analysis

In this appendix, the techniques used for the characterization of materials and thin films are briefly outlined. These techniques are key for further understanding the behavior and trends observed in solar cells since they provide additional information on the opto-electrical, structural, morphological, and compositional properties of the constituent layers.

A.1. Absorption and Fluorescence Spectroscopy

The performance of a PV device strongly depends on the way in which the constituent layers interact with light. In particular, the ability to absorb light across the solar spectrum is a fundamental precondition for the proper functioning of a solar cell. For this reason, an in-depth optical characterization by means of spectroscopic techniques is probably the most obvious and routinely performed analysis in PV research.

Ultraviolet and visible (UV/vis) absorption spectroscopy is a very simple, accurate and cost-effective technique that readily allows to quantify the absorption of ultraviolet, visible and near-infrared electromagnetic radiation by a sample.[1] The instrument used in UV/vis spectroscopy, called UV/vis spectrophotometer, simply measures the attenuation of a beam of light when it passes through, or interacts with, an absorbing substance. The most straightforward approach is to generate UV/vis radiation with a light source (often a combination of tungsten/halogen and deuterium lamps), split that radiation into its component wavelengths by means of a diffraction grating (a monochromator or a prism), measure a reference spectrum of light intensity at different wavelengths with a photodetector (typically a photomultiplier tube, a photodiode, a photodiode array or a charge-coupled device CCD), and then re-measure the sample spectrum after placing the material under study in between the source and the detector (see **Figure A.1**). The ratio between the intensity of light transmitted by the sample (I_t) and the intensity of light before it passes through the sample (I_0) is called *transmittance* (T), usually expressed as a percentage (%T). The *absorbance* of a material, denoted A, can be expressed as a function of T as follows:

$$A = log_{10}\left(\frac{I_0}{I_t}\right) = -log_{10}T \qquad \{A.1\}$$

A spectrophotometer typically measures A (or T) as a function of wavelength λ (in nm) in the UV/vis spectral region, thus providing the optical absorption (or transmission) spectrum of the sample. Liquid samples are typically held in a flat and transparent container called cuvette, while thin films can be measured by depositing them onto transparent glass substrates. To calculate the actual absorption of the material under investigation, a reference spectrum of the solvent (for liquid samples) or substrate (for thin films) used, also referred to as the blank, has to be taken and subtracted to the sample spectrum. In a single-beam instrument the reference spectrum has to be measured first, while in a double-beam instrument blank and sample measurements can be made

at the same time. A spectrophotometer can also be configured to measure reflectance. In this case, the intensity of light reflected from the sample is measured and compared to the intensity of light reflected from a reference material. The ratio is called the *reflectance* (R), and is usually expressed as a percentage (%R).
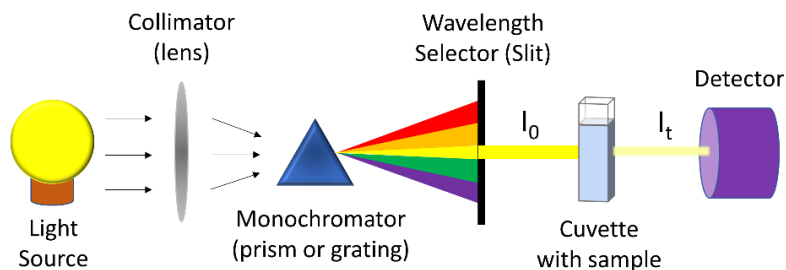

Figure A.1. *A schematic diagram of an UV/vis spectrophotometer.*

The UV/vis spectroscopy is most often used in analytical chemistry for the quantitative determination of an absorbing species in solution, using the Beer-Lambert law:

$$A = \varepsilon b c \qquad \{A.2\}$$

where ε is the molar absorptivity or extinction coefficient (specific for every species, and at every λ) with units of $L\ mol^{-1}\ cm^{-1}$, b is the path length of the beam of light through the sample expressed in cm, and c is the concentration of the attenuating species in the sample expressed in $mol\ L^{-1}$. According to this equation, for a fixed b, the measured absorbance can be used to calculate the concentration of an analyte in solution. However, it is necessary to know ε, which can be taken from references or can be determined from a calibration curve.

In PV research, the UV/vis spectroscopy is a useful tool for measuring the transmittance, reflectance, and absorbance of solar cells, as well as for investigating the optical and electronic properties of the constituent materials (e.g. for determining the optical HOMO-LUMO energy gap). Indeed, since the absorption of light in the UV/vis region is associated with excitation of electrons from lower to higher energy levels, this technique can also provide rich information on the electronic and vibrational states of the material under study, as well as on the interaction between different chemical species in the sample and on the presence and nature of defects and impurities. In the simplest instance, the technique is simply used to verify the identity of a chemical species by comparing the measured spectrum with those taken from the literature.
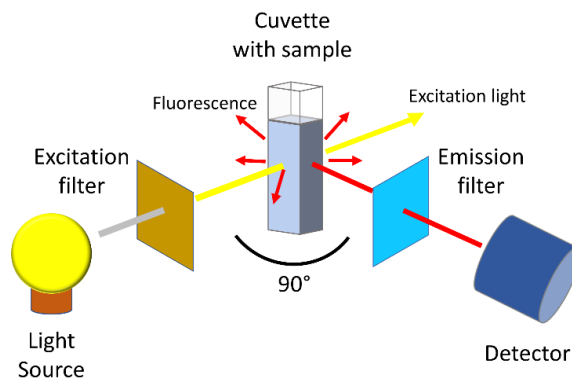
Figure A.2. *The optical set-up of a typical fluorimeter.*

Another spectroscopic technique commonly used in PV research is fluorescence spectroscopy.[2] This technique is complementary to absorption spectroscopy, in that absorption deals with electronic transitions from the ground state to the excited state, while fluorescence measures transitions from the excited state to the ground state. Once a molecule is excited by irradiation at a certain wavelength, relaxation can occur via several processes; fluorescence is one of these processes and results in the emission of light at a different wavelength (usually at a lower frequency) in all directions. Instruments designed to measure parameters of fluorescence are called fluorimeters. A typical fluorimeter includes a light source, a sample chamber with integrated optical components, and a high sensitivity photodetector. Fluorescence is typically measured at a 90° angle relative to the excitation light, as shown in **Figure A.2**, in order to ensure minimal leakage of excitation light in the detection system. Filters and/or monochromators are placed in the excitation and emission light paths to select a specific spectral region. The most versatile fluorimeters can record both emission and excitation spectra. The emission spectrum is defined as the fluorescence intensity measured as a function of emission wavelength at a fixed excitation wavelength (preferably a wavelength of high absorption). The excitation spectrum is the fluorescence intensity measured as a function of excitation wavelength at a constant emission wavelength and it is generally identical to the absorption spectrum as the fluorescence intensity is proportional to the absorption. Since the fluorescence signal is dependent on the type, concentration, and local environment of the fluorophore, fluorescence analysis can provide useful information for both qualitative and quantitative analysis.

In the context of solar PV research, photons emitted from a solar cell can be captured with a fluorimeter to obtain an image of the distribution of radiative recombination in the device. In a

solar cell, and more specifically in a perovskite solar cell, photogenerated excitons with a certain probability of recombining radiatively in the pristine perovskite material can become quenched at the interfaces with the HTL or the ETL. This is because the charge transfer (CT) process, from the perovskite layer to the HTL or from the perovskite layer to the ETL, competes with the radiative decay of the excitons, resulting in a lower intensity of fluorescence compared to that emitted from the pristine perovskite film. Such a decrease in intensity is called *fluorescence quenching* and is indicative of an efficient CT process at the interface, a desirable condition in a PV device.

A.2. Scanning Electron Microscopy

Scanning electron microscopy (SEM) is a powerful and versatile tool for material characterization that allows to observe surfaces at submicron and nano-level, providing information about the topography and composition of solid samples.[3] SEM imaging is achieved by probing the sample surface with a focused beam of accelerated electrons. By virtue of their smaller wavelength, electrons are able to resolve finer features and details of materials to a much greater extent compared with optical light (image resolutions of the order of 1 nm). The interaction between the electrons and the specimen result in the generation of many different signals, which are measured by different types of detectors and stored in computer memory. The intensity of the detected signal, combined with the position of the beam, is used to produce an image.

A schematic representation of the SEM technology is shown in **Figure A.3**. The SEM instrument consists of three basic components: electron column, specimen chamber, and detection system. Firstly, an electron beam is thermionically emitted from an electron gun, fitted with a tungsten filament cathode, placed at the top of the column. The generated electrons are then accelerated and attracted by a positively-charged anode. After that, a combination of electromagnetic lenses and apertures inside the column focus the beam into a fine spot (as small as 1 nm in diameter) on the surface of the specimen, which is located in a chamber at the end of the column. The gun, the column, and the specimen chamber are kept under vacuum since the presence of other atoms and molecules would cause the electron beam to deflect and would reduce the image quality. Before hitting the target, the small diameter probe passes through pairs of scanning coils which deflect the beam in the x and y directions, so that it scans the surface in a rectangular raster fashion (raster-scanning). The beam electrons, which typically have an energy ranging from 0.2 keV to 40 keV,

penetrate a few microns into the sample and interact with its atoms at various depths, generating a variety of signals such as secondary and backscattered electrons and characteristic X-rays, each of which can be detected by specialized detectors placed at the side of the electron column.
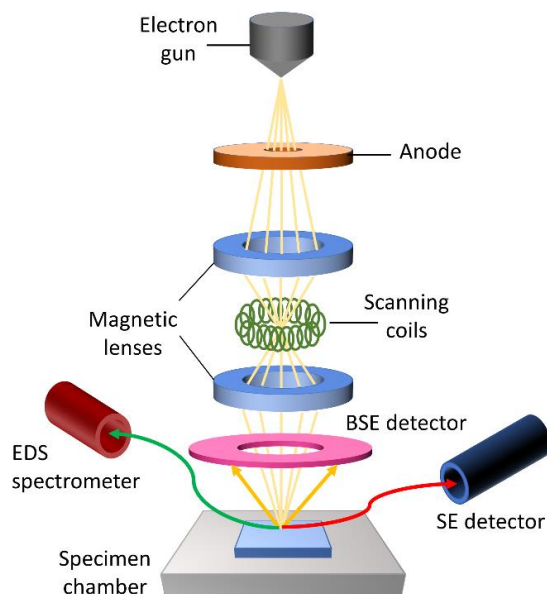

Figure A.3. *Schematic representation of the basic SEM components.*

Secondary electrons (SE) are low-energy electrons that are ejected from conduction or valence bands of the sample atoms by inelastic scattering interactions with the primary beam electrons. They originate from very close to the surface (within a few nanometers), and consequently, they can produce very high-resolution maps of the surface topography. All SEMs are standardly equipped with a SE detector. The Everhart-Thornley detector is the most commonly used and consists of a scintillator located inside a positively-charged Faraday cage. On the other hand, backscattered electrons (BSE) are beam electrons that are reflected or back-scattered out of the specimen by elastic scattering. Since BSE emerge from deeper locations within the sample, the resolution of BSE images is typically lower than that of SE images. However, BSE imaging is often used for analytical purposes since it can provide information about the distribution of different elements in the sample, the intensity of the BSE signal being strongly related to the atomic number Z. For the detection of BSE, solid-state detectors, usually either of scintillator or of semiconductor types, are placed above the sample, concentrically to the electron beam, in order to maximize the collection efficiency. Characteristic X-rays are also emitted when the incoming

electron beam dislodges an inner shell electron from the specimen, causing a higher-energy electron to fill the shell and release energy in the form of X-ray radiation. The energy of these characteristic X-rays can be measured by an energy-dispersive spectrometer and used to estimate the abundance of elements in the sample and map their distribution. This compositional characterization technique is called energy-dispersive X-ray spectroscopy (EDX).

A.3. Atomic Force Microscopy

Atomic force microscopy (AFM) is a type of scanning probe microscopy (SPM) that can provide three-dimensional images of virtually any surface at nanometer-scale resolution by means of a physical probe that scans the specimen.[4] Since its introduction in 1986,[5] AFM has evolved into a standard tool for high-resolution surface imaging in the fields of nanoscience and nanotechnology, also thanks to its several advantages over other competing technologies. Unlike optical microscopy and electron microscopy, it does not suffer from a limitation in spatial resolution due to diffraction and aberration. In addition, it does not require any special treatment of the specimen (such as metal coatings) or expensive vacuum environment for proper operation. As shown in **Figure A.4**, a typical AFM probe consists of a small spring-like cantilever that protrudes from a support (also called holder chip) and that has a sharp tip on its free-swinging end. The cantilever is typically made of silicon or silicon nitride and has dimensions in the micrometer scale, while the radius of the tip is usually on the scale of a few nanometers. When the tip is brought into proximity of a sample surface, forces between the tip and the surface lead to a deflection of the cantilever according to Hooke's law:

$$F = -ks_z \hspace{6cm} \text{\{A.3\}}$$

where s_z is the vertical displacement and k is the spring constant of the cantilever (k is typically between 0.01 and 100 N/m). In most AFM instruments, the cantilever deflection is indirectly monitored by reflecting a laser beam off the cantilever top side and measuring the movement of the reflected laser spot on a position-sensing detector, a split photodiode (laser beam deflection method). The displacement of the reflected laser spot is strictly dependent on the change of inclination of the cantilever near the tip end.

The tip-surface interactions that are measured in AFM include Van der Waals forces, electrostatic forces, dipole-dipole interactions, capillary forces, etc. These forces translate to changes in the

cantilever motion, and this can be used to create a spatial map of the surface topography at a high resolution (topographic imaging). In the traditional constant-force static AFM mode, this is achieved by raster-scanning the position of the sample with respect to the tip along an x-y grid and recording the z height of the probe that corresponds to a constant probe-sample interaction. A piezoelectric XY scanner is used to displace the sample stage in the x and y directions, while an electronic feedback loop is employed to continuously adjust the z position of the tip with respect to the surface so that the cantilever deflection (and thus the probe-sample force) is restored to a user-defined value. A Z scanner is used to vertically displace either the chip to which the cantilever is attached or the sample stage, depending on instrument design. The feedback output essentially represents the sample surface topography, which can then be displayed as a false-color image using an appropriate rendering software (e.g. Gwyddion).
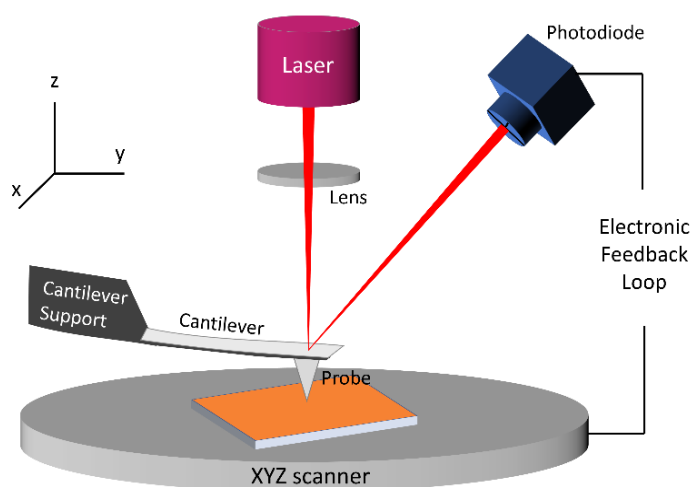

Figure A.4. *Scheme of a typical AFM probe.*

The conventional AFM static mode described above is also called "contact" mode because the tip and the sample are kept in close contact during scanning (repulsive region of the interatomic force curve). Despite the widespread success of contact mode AFM in various applications, its resolution was frequently found to be limited by lateral dragging forces exerted by the probe tip on the sample surface, especially when measuring soft samples like biological samples or organic thin films. To bypass this problem, a variety of dynamic ("non-contact" and "tapping") modes were developed in which the cantilever is deliberately oscillated in vertical direction above the sample surface, at

or near its natural resonance frequency, using a piezoelectric actuator. The non-contact mode is operated by moving the cantilever relatively far away from the sample surface (attractive region of the interatomic force curve). The tapping mode (also called "intermittent contact" mode) combines qualities of both the contact and non-contact modes, allowing the cantilever tip to impact the surface for a minimal amount of time during oscillation. In both operation modes, the cantilever dynamics are governed by the tip-sample interaction as well as by its driving method. Different detection schemes measuring either the changes in the oscillation amplitude ("amplitude-modulation", AM) or the changes in the resonance frequency of the cantilever ("frequency-modulation", FM) were proposed. Over the years, the AM tapping mode, where the oscillation amplitude is used as the parameter that goes into the feedback loop to control the tip-to-sample distance, has been established as the most widely applied AFM technique for soft samples in ambient conditions. When operating in tapping mode, changes in the phase of the cantilever oscillation with respect to the driving signal can be recorded as well and can be used to discriminate between different types of materials on the surface (phase imaging).

For AFM, the potential to extract quantitative information in post-processing is significant. The most common computations from AFM images are statistical metrics of the distribution of Ω, where Ω is the measured quantity (z height, phase, etc.). Indeed, the large number of measurements N contained in a conventional image ($N = 512^2$) provides for very-well determined distribution functions. Common statistical metrics include the mean value as well as various moments around the mean, which quantify deviations from the mean. For example, by analyzing z data, it is possible to quantify surface roughness (R_q) as the root-mean-square (rms) deviation of height distribution:

$$R_q = z_{rms} = \sqrt{\frac{1}{N}(z_1^2 + z_2^2 + \cdots + z_N^2)} \qquad \{A.4\}$$

A.4. X-ray Diffraction Analysis

X-ray diffraction, frequently abbreviated as XRD analysis, is a powerful non-destructive technique commonly used in laboratories to investigate the structural properties of a material.[6] Particularly, it is superior in elucidating the three-dimensional atomic structure of crystalline solids, providing information on crystalline phases, preferred crystal orientations (texture), and other structural parameters such as grain size, strain, and crystal defects.

In the simplest instance, an XRD experiment is performed by directing a monochromatic X-ray beam at a sample and detecting the intensities of the diffracted X-rays as a function of the outgoing direction (angle-resolved detection). The wavelengths of X-rays (between 10^{-3} and 10^{1} nm) are of the order of atomic distances in condensed matter, which qualifies their use as structural probes. When a crystalline sample is illuminated with X-rays, the regularly-spaced atoms in the crystal lattice cause the X-rays to be diffracted into very specific directions as a result of destructive and constructive interferences (analogous to diffraction of visible light by gratings), producing a characteristic XRD pattern. This diffraction pattern can be thought of as a chemical fingerprint containing information about the long-range orderly periodic arrangements of atoms within the sample. A geometrical interpretation of this phenomenon was provided by W. L. Bragg in 1913.[7] He considered the diffraction as the consequence of contemporaneous reflections of the X-ray beam by various lattice planes belonging to the same family. Bragg's law defines the condition for X-rays of wavelength λ to be diffracted by a family of parallel atomic planes in a crystal lattice:

$$n\lambda = 2d_{hkl} \sin \theta \qquad \text{\{A.5\}}$$

where d_{hkl} is the spacing between the Bragg planes, θ is the Bragg angle, and n is the diffraction order (see **Figure A.5**). Miller indices (hkl) are used to identify different planes of atoms in a crystal lattice. In most XRD measurements, λ is fixed, and consequently, a family of atomic planes produces a diffraction peak only at a specific angle 2θ. The intensity of this peak is related to the number of crystallites with the d_{hkl} spacing that are reflecting X-rays into the detector (crystallites with correct orientation) and may shed light on, for example, the degree of crystallinity. The dependency of the peak intensity on the crystallite orientation is also important in investigating crystallographic texture of the sample.
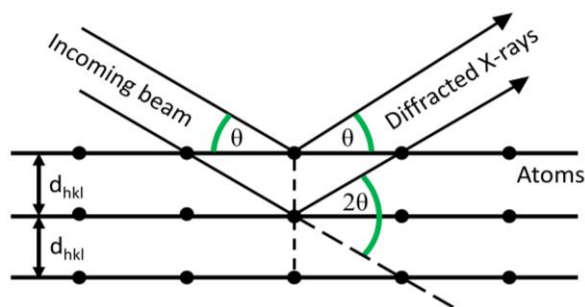

Figure A.5. *Geometrical condition for X-ray diffraction by lattice planes.*

The working principle of a conventional X-ray diffractometer in θ - 2θ (or Bragg-Brentano) symmetric reflection geometry is visualized in **Figure A.6**. The instrument consists of three basic elements: X-ray tube, sample holder, and X-ray detector. X-rays are generated in a cathode ray tube by heating a filament to produce electrons and accelerating these electrons towards a target by applying an appropriate acceleration voltage (in kV). The electron current between filament and target may be adjusted by tuning the filament current in the range of some 10 mA. When electrons have sufficient energy to displace inner shell electrons of the target material, characteristic X-ray spectra are produced. These spectra comprise a continuous part, called Bremsstrahlung, and some discrete spectral lines, the most common being K_α and K_β, which are characteristic of the target material (Cu, Fe, Mo, Cr). Appropriate filtering is required to select one of these lines and produce the monochromatic X-rays needed for diffraction. The most commonly used X-ray radiation is the Cu K_α radiation (λ = 1.5418 Å) filtered through Ni foil. The monochromatic X-rays are then collimated and directed to the flat surface of the sample (positioned in the center of the instrument) at an incident angle θ. At the same angle, the detector monitors the scattered radiation. During the scan, a goniometer is used to rotate the sample (by θ, scanning speed S) and the detector (by 2θ, double scanning speed 2S) with respect to the collimated X-ray beam. In this way, the angles of the incoming and exiting beam are continuously varied, but they also remain equal to each other throughout the whole scan. The diffraction pattern is collected by measuring the scattered intensity I(2θ) as a function of the scattering angle 2θ. When the geometry of the incident X-rays satisfies the Bragg's Equation, constructive interference occurs and a diffraction peak is observed.
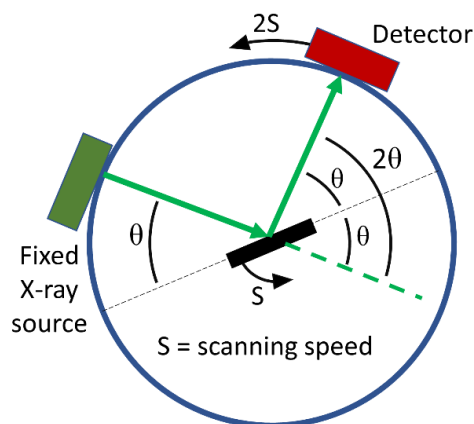

Figure A.6. *Schematic of an X-ray diffractometer in Bragg-Brentano geometry.*

The XRD method is traditionally employed on thick or powdered samples, but it can also be applied to the investigation of thin films. A primary task in thin-film analysis is the identification of chemical phases: in many thin-film projects, the prepared layers have to be checked whether an intended chemical phase has successfully been obtained. XRD yields different diffraction patterns for different chemical phases, and this selectivity makes it well suited for such an analytical task. In this work of thesis, XRD investigations were devoted to this type of qualitative phase analysis.

A.5. X-Ray Photoelectron Spectroscopy

X-ray photoelectron spectroscopy (XPS), also known as electron spectroscopy for chemical analysis (ESCA), is a surface-sensitive spectroscopic technique routinely used to investigate the elemental composition of solid surfaces.[8] It allows to determine the identity, chemical state, and quantity of a detected element in the sample. All elements can be identified and detected with sub-monolayer sensitivity, except for hydrogen and helium. This makes XPS a unique and effective tool for investigating the chemistry of any surface.

XPS experiments are typically accomplished by irradiating the sample with a beam of soft, monochromatic X-rays (1-3 keV) and simultaneously measuring the number and kinetic energy of electrons that escape from the topmost few nm of the sample surface into the vacuum of the instrument. A typical XPS spectrum is a plot of the number versus the binding energy (BE) of the electrons detected. BE can be calculated using the following equation:

$$BE = h\nu - (KE + \phi) \hspace{3cm} \text{\{A.6\}}$$

where $h\nu$ corresponds to the energy of the monochromatic X-ray photons, KE is the kinetic energy of the electron, and ϕ is an instrumental constant corresponding to the work function of the spectrometer. Each element produces characteristic XPS peaks which are identified by the shell from which electrons are emitted (1s, 2s, 2p, etc.) and whose intensity is directly related to the amount of element within the sampling volume. Atomic percentage values can be generated by dividing each XPS signal by a relative sensitivity factor (RSF) and normalizing over all the elements detected.

The logical components of an XPS system are shown in **Figure A.7** and include a source of monochromatic X-rays, an ultra-high vacuum (UHV, 10^{-8} - 10^{-9} Pa) chamber, a set of magnetic and/or electrostatic lens units, an electron energy analyser, and an electron detector system. During

XPS measurements, UHV is required to eliminate adsorption of contaminants on the sample and to increase the mean free path for electrons, photons, and ions. The source of X-rays used for irradiation is a standard X-ray tube, in which electrons are emitted from a heated filament and accelerated towards a solid anode. Al and Mg anodes are normally used. The generated X-rays are then monochromatized by reflection from a bent quartz crystal disperser. The most commonly used X-ray radiation is the Al K$_{\alpha}$ radiation (hv = 1486.7 eV). Energy analysis of the electrons emitted from the sample is typically performed using a hemispherical analyser (HSA), an electrostatic device which can disperse electrons as a function of their kinetic energy. The energy-dispersed electrons are then detected at the exit plane of the HDA, at 180° with respect to the entrance plane, by a multichannel detector system such as a microchannel plate (MCP) electron multiplier. Advanced XPS systems can also examine sample composition as a function of depth by ion beam etching (XPS depth profiling). These systems are equipped with an ion gun sputtering system (typically Ar$^+$ ion gun) which can be used to etch atoms from the surface in order to reveal subsurface information. The rate of removal of surface atoms will depend on both the kinetic energy of the ions and the nature of the sample atoms. During a typical depth-profiling analysis, XPS spectra are acquired after each ion beam etching cycle, and this sequence of etching and data acquisition is repeated until the desired depth is reached. This approach can be very useful in determining the composition and thickness of multilayer structures and thin films.
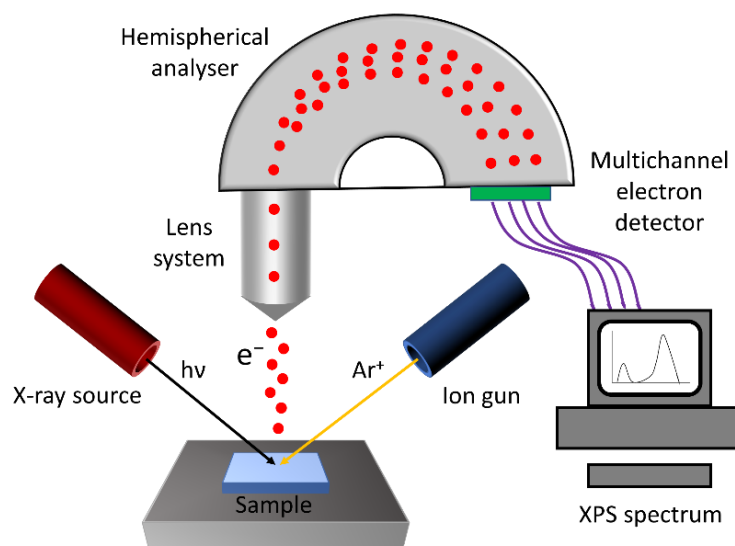

Figure A.7. *Basic scheme showing the main components of an XPS instrument.*

A.6. Sheet Resistance Measurements

Sheet resistance (R_s) is a common electrical property used to characterize thin films of conducting and semiconducting materials. Specifically, it is a measure of the lateral resistance through a thin square of material, and it is commonly defined as the bulk resistivity (ρ, in ohm $\cdot$ m) divided by the thickness (t, in m):

$$R_S = \frac{\rho}{t} \qquad \text{\{A.7\}}$$

The units of this equation resolve to ohms (Ω). However, since R_s represents a special case of resistance between opposite sides of a square film, it is generally expressed in "ohms per square" (denoted Ω/sq or Ω/□). Being independent of the size of the square film, it enables an easy comparison between different samples.
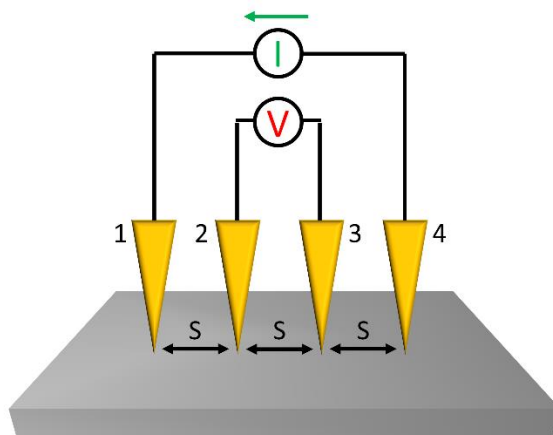

Figure A.8. *A schematic diagram of a four-point probe.*

Sheet resistance is a critical property for any thin film in which electrical charges are intended to travel along. For example, thin-film solar cells require conducting electrodes with low sheet resistances in order to transport electrical charges laterally with minimized power losses. Therefore, it may be useful to measure the R_s of a thin film in order to assess its suitability as an electrode material. A simple technique for measuring R_s is the four-probe method, which is performed using commercial four-point probes.[9] These probes consist of four equally spaced, collinear metal points that are pressed against the surface of the film, as shown in **Figure A.8**. A constant current I is applied between the outer two points, while the resultant voltage drop V across

the two inner points is measured with a high-impedance voltmeter. If the material being tested is no thicker than 40% of the spacing between probes, and if its lateral size is sufficiently large, the sheet resistance of the film can then be calculated using the equation:

$$R_S = \frac{\pi}{\ln(2)}\frac{V}{I} = 4.532\,\frac{V}{I} \qquad\qquad \{A.8\}$$

A.7. References

(1) Perkampus, H.-H. *UV-VIS Spectroscopy and Its Applications*; Springer Lab Manuals; Springer-Verlag: Berlin Heidelberg, 1992.

(2) Lakowicz, J. R. *Principles of Fluorescence Spectroscopy*, 3rd ed.; Springer US, 2006.

(3) Ul-Hamid, A. *A Beginners' Guide to Scanning Electron Microscopy*; Springer International Publishing, 2018.

(4) Greg Haugstad. *Atomic Force Microscopy: Understanding Basic Modes and Advanced Applications*; Wiley, 2012. https://doi.org/10.1002/9781118360668.

(5) Binnig, G.; Quate, C. F.; Gerber, Ch. Atomic Force Microscope. *Phys. Rev. Lett.* **1986**, *56* (9), 930–933. https://doi.org/10.1103/PhysRevLett.56.930.

(6) Mario Birkholz. *Thin Film Analysis by X-Ray Scattering*; Wiley-VCH Verlag GmbH & Co. KGa, Weinheim, 2006.

(7) Bragg, W. H.; Bragg, W. L. The Reflection of X-Rays by Crystals. *Proc. R. Soc. Lond. Ser. Contain. Pap. Math. Phys. Character* **1913**, *88* (605), 428–438. https://doi.org/10.1098/rspa.1913.0040.

(8) Heide, P. van der. *X-Ray Photoelectron Spectroscopy: An Introduction to Principles and Practices*; John Wiley & Sons, 2011.

(9) Smits, F. M. Measurement of Sheet Resistivities with the Four-Point Probe. *Bell Syst. Tech. J.* **1958**, *37* (3), 711–718. https://doi.org/10.1002/j.1538-7305.1958.tb03883.x.

Curriculum Vitae

Name: Giuliana Giuliano

Date of Birth: 11/10/1989

Place of Birth: Palermo

Full Career

- November 2016 – November 2019. **Ph.D. Student in Materials Science and Nanotechnologies** (University of Catania-University of Palermo)

- March 2016. **M.Sc. graduation in Photochemistry and Molecular Materials**, University of Bologna (110/110 *cum laude*)

  M.Sc. Thesis: "*Organic Solar Cells Based on Novel Fluorinated Copolymers*"

- June 2015 – March 2016. **Pre-graduation internship at CNR-ISOF**, Bologna.

- July 2013. **B.Sc. graduation in Chemistry**, University of Palermo. (110/110)

- March 2012 – June 2012. **Internship at CNR-ISMN**, Palermo.

List of Publications

- Giuliano, G.; Cataldo, S.; Scopelliti, M.; Principato, F.; Martino, D. C.; Fiore, T.; Pignataro, B. Nonprecious Copper-Based Transparent Top Electrode via Seed Layer–Assisted Thermal Evaporation for High-Performance Semitransparent n-i-p Perovskite Solar Cells. *Adv. Mater. Technol.* **2019**, *4* (5), 10800688.

Conferences (Presenting Author)

- Giuliano, G.; Cataldo, S.; Scopelliti, M.; Fiore, T.; Pignataro, B. Semitransparent Perovskite Solar Cells with Multilayered Metal Top Electrodes for BIPVs and Tandem Applications. 7th EuCheMS Chemistry Congress, 26-30 August 2018 (oral presentation)

- Giuliano, G.; Cataldo, S.; Fiore, T.; Scopelliti M.; Pignataro, B. Multilayer Copper-Rich Transparent Electrode as an Alternative Top Anode for High-Performance Semitransparent n-i-p Perovskite Solar Cells. 11th International Conference on Hybrid and Organic Photovoltaics (HOPV), 12-15 May 2019 (poster presentation)

Attended Schools

- 1st Enerchem School – Chemistry for the Energy Transition (20-24 February 2018, Firenze)

- 13th ISOPHOS International School on Hybrid and Organic Photovoltaics (2-6 September 2019, Castiglione della Pescaia)